Using Non-Small Cell Lung Cancer Organoids to Investigate Responses to Radiation

Maria del Carmen Velasco Martinez

Thesis submitted for the award of Doctor of Philosophy (Ph.D)

School of Biosciences, Cardiff University

October 2023

This thesis is the result of my own independent work, except where otherwise stated, and the views expressed are my own. Other sources are acknowledged by explicit references. The thesis has not been edited by a third party beyond what is permitted by Cardiff University's Use of Third Party Editors by Research Degree Students Procedure.

Statement 1

This thesis is being submitted in partial fulfilment of the requirements for the degree of *PhD.*

Statement 2

This work has not been submitted in substance for any other degree or award at this or any other university or place of learning, nor is it being submitted concurrently for any other degree or award (outside of any formal collaboration agreement between the University and a partner organisation)

Statement 3

I hereby give consent for my thesis, if accepted, to be available in the University's Open Access repository (or, where approved, to be available in the University's library and for inter-library loan), and for the title and summary to be made available to outside organisations, subject to the expiry of a University-approved bar on access if applicable.

Final words count: 45,994

Acknowledgements

I would like to first thank my supervisors Prof. Trevor Dale and Dr. Paul Shaw for giving me the opportunity to pursue this research. Thank you, Trevor, for your time and effort supporting me during this work and for all the scientifically stimulating conversations. Thank you, Paul, for your valuable clinical point of view for this work.

I also want to thank our collaborator Prof. Ming-Sound Tsao, at the University of Toronto, and the Princess Margaret Cancer Biobank for kindly providing some of their established NSCLC organoid-lines. I would also like to thank Prof. Alan Parker, at Cardiff University, for kindly providing a vial of the A549 line. I extend my gratitude to Prof. Anderson Ryan, at University of Oxford, for his advice on the radiation/drugs dosing and for kindly providing the shATM/shGFP NCI-H1299/COR-L105 lines. I would also like to thank Dr. Mark Jackson, at the University of Glasgow, for his generous advice on the surviving fraction calculations and for performing the statistical analysis in R for the IR-drug re-seeding experiments.

My gratitude is extended to all past members of the Dale laboratory: Dr. Andrew Hollins, Dr. Kenneth Ewan, Dr. Anika Offergeld. Dr. Nuria Abajo Lima, Dr. Eider Valle-Encinas and Matthew Zverev. I want to thank Matt Zverev for his contribution to this work by performing some of the PDX organoids establishment when only one of us was allowed in the laboratory, during the COVID pandemic. Thank you, Eider, for giving me the opportunity to come to Cardiff on the first place, and for all of our scientifically stimulating conversations. Gracias también tanto a Nuria como a Eider por las noches necesarias de bailoteo. Anika, thank you for all your scientific and professional advice, for your always interesting scientific questions and for our coffee breaks.

I would also like to thank my assessor, Dr. Catherine Hogan for her scientific input and for kindly letting me join their laboratory-meetings, which I highly enjoyed. My gratitude is extended to all present and past members of the Hogan laboratory (and to Dr. Anna Richards): Dr. Markella Alatsatianos, Dr. Beatriz Salvador, Liam Hill and Joshua D'Ambrogio. A Bea, a quien considero un modelo a seguir, gracias por todo tu apoyo y ayuda siempre (científica, técnica, intelectual y personal), y por esa semana tan calurosa en Sevilla.

I thank Cancer Research Wales for economically supporting this work. My gratitude is extended to every person that has ever economically contribute to a cancer research organisation for making research possible. I would like to thank all University Hospital of Wales patients that donated material for this work, for their understanding and kindness during difficult times.

I extend my gratitude to the companies that have contributed, economically or otherwise, to the providing of the PDX material for this work: Cellesce Ltd, Champions Oncolgy and TransCure bioServices.

I am grateful for the technical assistance provided by skilled individuals within Cardiff University, without whom much of the work presented in this thesis would not have been possible. In particular, Mark bishop provided training with the flow cytometer and irradiator. Angela Marchbank performed the library preparation for the scRNAseq experiment. Dr. Sarah Christofides performed the bioinformatics analysis of the scRNAseq experiment.

I would personally like to thank Dr. Laura Thomas and Alethea Tang, at Swansea University, for giving me the opportunity to work with them. Not only this was personally and scientifically highly stimulating, but also economically allowed me to write this work.

I would also like to thank every person (inside and outside Cardiff University) I ever had a scientific discussion with during this period, for reminding me why I love research.

Thanks to everybody at the 3rd floor east, Biosciences, Cardiff University, for the everyday stories. I would like to especially thank here Dr. Peter Watson for his support with all the time-complications during this work.

On a personal note, I want to specially thank the 'Sunday' group, for the shared moments and the scientific discussions and memes. Thank you for making me feel at home. To Rhod, for always supporting me. To Elena, for your endless positivism and wise resolutions. To Marti, for the telepathic connexion that always made me laugh. To Nicole, for always knowing exactly how to fill my needs.

I also want to thank all my Cardiff friends; it is impossible to list everyone here. Thanks to the girls' group for always encouraging me and to the little Margot, whose funny videos have cheer me up during the writing period. Special thanks to Sophie, for making the idea

of doing this PhD at Cardiff possible. To Amy, for being such a kind and wholesome human being. To Huw and James, for always listening and supporting me whilst we lived together.

Eskerrik asko a toda mi familia. A mi abu, por ser tú abu, con eso siempre será más que suficiente. Eskerrik asko también a mis amigas de casa (Hegoa, Cristina, Oihane, Iñigo, Ainara, Beli, Aitziber, Laura…) por asegurarse de que el tiempo y los kilómetros no importen. Gracias a Ainara, por entenderme y apoyarme y quererme siempre, aunque hablemos diferentes lenguajes. Eskerrik asko Hegoa, necesitaría una tesis entera para explicar el por qué: beti.

Finalmente, y muy importante, gracias a mi hermana, que por suerte me ha tocado pero a la que elegiría para siempre. Gracias a mis padres. A mi aita, por saber escuchar como solo un sabio con mucha sensibilidad podría. A mi ama, por tanto, sobre todo por conseguir calmarme siempre. Gracias por el apoyo incondicional.

Abstract

Background

Cancer organoids preserve the histological, genetic, cellular, spatial, and functional diversity of the tumours from which they are derived and have been shown to accurately reproduce clinical responses to drug treatments. In addition, organoids represent relatively simple cultures that can be adapted for high-throughput research purposes. The first Non-Small Cell Lung Cancer (NSCLC) long-term organoids were described in 2019 and at the time this work was started, only this one protocol had been published. A range of cancers including NSCLC are treated in the clinic by radiotherapy and at the start of this project, it was unknown whether organoids would be able to model tumour responses to radiation. In this work, I aimed to examine the response of NSCLC organoids to radiation while investigating the potential of organoid systems to emulate combination therapies, specifically combining radiotherapy with DNA damage response inhibitors (DDRis) to enhance the therapeutic effects of radiation-induced DNA damage.

Methods

Adapting a range of novel assay formats (i.e. ATP-based, image-based), I established radiation-responses assays in 3D formats (including organoids and spheroids) and analysed responses to radiation and DDRi combination therapies.

Results

The direct evaluation of post-irradiation reproductive cell death through 3D re-plating assays emerged as a pivotal assay for radiation organoid-response assessment. This could be combined with less sensitive but more rapid methodologies, such as ATP assays, when results were regularly cross-verified. Furthermore, a preliminary investigation corroborated the existence of intra-organoid 'cell type' variability within NSCLC organoids. This intra-organoid heterogeneity may have profound implications for comprehending intra-tumoral NSCLC variability *in vivo*, a phenomenon often implicated in cancer recurrence and patient mortality.

Conclusions

My findings highlight the need for employing a combination of techniques to accurately assess organoid responses to radiation. Specifically, the re-plating assay stands out as a critically sensitive method for evaluating organoid radiation-response.

Abbreviations

^{O}C	Celsius degrees
2D	Two Dimension
3D	Three Dimension
53BP1	Tumour protein p53 binding protein 1
8-oxoG	8-oxoguanine

A

ACTB	Actin Beta
AdDF	Advanced DMEM/F12
ADP	Adenosine Diphosphate
ALI	Air-Liquid Interphase
ALK	Anaplastic Lymphoma Kinase
ALK1	Anaplastic Lymphoma Kinase 1
ALK5	Anaplastic Lymphoma Kinase 5
ANOVA	Analysis of variance
AO	Airway Organoid
ASCL4	Achaete-Scute Family BHLH Transcription Factor 4
ATC0	Alveolar Type 0 cells
ATC1	Alveolar Type I Cells
ATC2	Alveolar Type II Cells
ATCC	American Type Culture Collection
ATM	Ataxia Telangiectasia Mutated
ATMi	Ataxia Telangiectasia Mutated inhibitor
ATP	Adenosine Triphosphate
ATR	Ataxia Telangiectasia and Rad3-related
ATRi	Ataxia Telangiectasia and Rad3-related inhibitor

B

BADJ	Bronchioalveolar Junction
BASC	Bronchioalveolar Stem Cell
BLM	Bloom syndrome RecQ like helicase
BMP	Bone Morphogenic Protein
BRAF	Serine/threonine-protein kinase B-raf
BRCA1	Breast cancer protein 1
BRCA2	Breast cancer protein 2
BSA	Bovine serum albumin

C

CDC25 A	Cell division cycle 25 A
CDC25C	Cell division cycle 25 C
CDK1	Cyclin dependant kinase 1
CDK2	Cyclin dependant kinase 2
CDK4	Cyclin dependant kinase 4
CDKN2 A	Cyclin Dependent Kinase Inhibitor 2A

CDX	Cell Line-Derived Xenograft
CellAgg	Cell Agreggate
CFA	Colony Formation Assay
Chk1	Checkpoint kinase 1
Chk2	Checkpoint kinase 2
CI	Combination Index
CK	Cytokeratin
CK1	Cytokeratin 1
CK20	Cytokeratin 20
CK5	Cytokeratin 5
CK6	Cytokeratin 6
CK7	Cytokeratin 7
CNA	Copy Number Alteration
CNV	Copy Number Variation
COPD	Chronic Obstructive Pulmonary Disease
CPM	Counts per million
CRC	Colorectal cancer
cre-ERT2	Cre recombinase-mutated estrogen receptor
CRIPSR-Cas9	Clustered regularly interspaced short palindromic repeats and CRISPR-associated protein 9
CRPC	Castration Resistant Prostate Cancer
CSC	Cancer Stem Cell
CtIP	C-terminal binding protein interacting protein
CU	Cardiff University
CUL3	Cullin 3

D

DAPI	4′,6-diamidino-2-phenylindole
DDR	DNA Damage and Response
DDRi	DNA Damage and Response Inhubitor
DE	Differentially expressed
DMEM	Dulbecco's Modified Eagle Medium
DMSO	Dimethyl sulfoxide
DNA	Deoxyribonucleic acid
DNA-PK	DNA-dependent protein kinase
DSB	Double Strand Break

E

ECACC	European Collection of Authenticated Cell Cultures
ECM	Extra-cellular Matrix
EDTA	Ethylenediaminetetraacetic acid
EGF	Epidermal Growth Factor
EGFR	Epidermal Growth Factor Receptor
EMT	Epithelial-Mesenchymal Transition
EpCAM	Epithelial cell adhesion molecule
ERBB2	Receptor tyrosine-protein kinase erbB-2
ERBB4	Receptor tyrosine-protein kinase erbB-4

ERCC1	Excision repair cross complementation group 1
Exo1	Exonuclease 1

F

FACS	Fluorescence-activated cell sorting
FBS	Fetal bovine serum
FC	Fold-change
FDR	False Discovery Rate
FGF	Fifroblast growth factor
FGF10	Fibroblast growth factor 10
FGF7	Fibroblast growth factor 7
FGFR	Fibroblast growth factor receptor 1
FIJI	FIJI Is Just ImageJ
FSC	Forward scatter

G

G_1	Gap 1 (Cell cycle)
G_2	Gap 2 (Cell cycle)
GDCFP	Gross cystic disease fluid protein 15
M	Mitosis (Cell cycle)
GEM	Gel Beads-in-emulsion
GEMM	Genetically Engineered Mouse Model
GFP	Green Fluorescent Protein
GO	Gene Ontology
GSH	Glutathione
GSK-3	Glycogen synthase kinase 3

H

H&E	Heamaoxylin and Eosin
H2AX	H2A histone family member
HEPES	4-(2-hydroxyethyl)-1-piperazineethanesulfonic acid
HES1	Hairy and enhancer of split-1
hESC	Human Embryonic Stem Cell
Hif1a	Hypoxia-inducible factor 1a
HLCA	Human Lung Cell Atlas
HR	homologous Recombination
HRAS	HRas proto-oncogene
HTA	Human Tissue Authority

I

ID	Identity
IF	Immunofluorescence
IHC	Immunohistochemistry
IMRT	Intensity-modulated radiotherapy
IR	Ionising Radiation
ISO *X*	Isolation X
ITH	Intra-tumour heterogeneity

K

KEAP1	Kelch-like ECH-associated protein 1
KRAS	Kirsten Rat Sarcoma viral oncogene homolog

L

Lgr5	leucine-rich repeat-containing G-protein coupled receptor 5
LNEP	Lineage-negative epithelial progenitor cell
LSPC	lung epithelial stem/progenitor cell
LUAD	Lung Adenocarcinoma
LUSC	Lung Squamous Cell Carcinoma

M

MACS	Magnetic affinity cell sorting
MAPK	Mitogen-activated protein kinase
MDC1	Mediator of DNA damage checkpoint protein 1
MDM2	Mouse double minute 2 homolog
MEM	Minimum Essential Medium Eagle
MET	Mesenchymal Epithelial Transition
MGA	MAX Dimerization protein MGA
MTA	Material Transfer Agreement
MTOR	Mammalian target of rapamycin
MYC	MYC Proto-Oncogene

N

NBS1	Nijmegen breakage syndrome 1
NCBI	Nationl Cnter for Biotechnology Information
NEAA	Non-Essential Amino Acids
NF1	Neurofibromatosis type 1
NFE2L2	Nuclear factor erythroid 2-related factor 2
NHEJ	Non-Homologous End Joining
NHS	National Health Service
NICE	National Institute for Health and Care Excellence
NOTCH 1	Neurogenic locus notch homolog protein 1
NOTCH 2	Neurogenic locus notch homolog protein 2
NRAS	Neuroblastoma RAS viral oncogene homolog
NRG1	Neuregulin 1
NSCLC	Non-Small Cell Lung Cancer
NTRK1	Neurotrophic tyrosine receptor kinase 1

P

PARP	Poly (ADP-ribose) Polimerase

PARP1	Poly (ADP-ribose) Polimerase 1
PARPi	Poly (ADP-ribose) Polimerase inhbitor
PBS	Phosphate-buffered saline
PCR	Polymerase chain reaction
PD-1	Programmed cell death protein 1
PD-L1	Programmed death-ligand 1
PDMS	poly(dimethylsioloxane
PDX	Patient-Derived Xenograft
PDXO	Patient-derived Xenograft Organoid
PE	Plating efficiency
PFA	Paraformaldehyde
PI	Propidium Iodide
PI3K	Phosphatidylinositol-3-kinase
PIK3CA	Phosphatidylinositol-4,5-bisphosphate 3-kinase catalytic subunit alpha
PNEC	Pulmonary Neuroendocrine Cell
PTEN	Phosphatase and tensin homolog

Q

QC	Quality Control

R

RAD51	RAD51 recombinase
RAD52	RAD52 recombinase
RASC	Respiratory Airway Secretory Cell
Rb	Retinoblastoma protein
RB1	Retinoblastoma 1
RBM10	RNA Binding Motif Protein 10
REC	Research Ethics Committee
RET	Ret Proto-Oncogene
RIF1	Replication regulatory timing factor 1
RIT1	Ras like without CAAX 1
RLU	Relative Luminescense
RNA	Ribonucleic acid
RNAseq	RNA sequencing
RNF168	Ring finger protein 168
RNF8	Ring finger protein 8
ROCK	Rho-associated coiled-coil containing kinase
ROS	Reactive Oxygen Species
ROS1	ROS Proto-Oncogene, Receptor Kinase
RP2D	Recommended phase II dose
RPA	Replication Protein A
RPMI	Roswell Park Memorial Institute medium
RT	Room Temperature
RTK	Receptor Tyrosine Kinase

S

S	Interphase (Cell cycle)
SAG	Smoothened Agonist

	SCGB1A1	Secretoglobin Family 1A Member 1
	SCGB3A1	Secretoglobin Family 3A Member 1
	SCGB3A2	Secretoglobin Family 3A Member 2
	SCLC	Small Cell Lung Cancer
	scRNAseq	single-cell RNA sequencing
	SD	Standard Deviation
	SF	Survival Fraction
	SFTPB	Pulmonary surfactant-associated protein B
	SFTPC	Pulmonary surfactant-associated protein C
	shATM	Short hairpin ATM
	shGFP	Short hairpin GFP
	SMC1	Structural maintenance of chromosomes protein 1
	SNV	Single Nucleotide Variant
	SOX2	SRY-Box Transcription Factor 2
	SSA	Single Strand Annealing
	SSB	Single Strand Break
	SSC	Side Scatter
	ssDNA	Single strand DNA
	STK11	Serine/Threonine Kinase 11
	STR	Short Tandem Repeats
	SV	Structural variation
T	TAE	Tris-acetate-EDTA
	TERT	Telomerase reverse transcriptase
	TGF-b	Transforming growth factor beta1
	TGI	Tumour growth inhibition
	TIL	Tumour-infiltrating lymphocyte
	TNM	Tumour, Node, Metastasis
	TP53	Tumour Protein 53
	TP63	Tumour Protein 63
	TTF1	Thyroid Transcription Factor 1
U	U2AF1	U2 small nuclear RNA auxiliary factor 1
	UHW	University Hospital of Wales
	UK	United Kingdom
	UMI	Unique Molecular Identifier
	UV	Ultraviolet
W	WCB	Wales Cancer Bank
	WES	Whole Exome Sequencing
	WGS	Whole Genome Sequencing
	WHO	World Health Organization
	Wnt	Wingless and Int-1
	WT	Wild-type

X

XLF	XRCC4-like factor
XPF	Xeroderma pigmentosun group F
XRCC1	x-ray repair cross complementing 1
XRCC4	x-ray repair cross complementing 4

List of contents

2. Materials and Methods

3. Results - NSCLC CellAggs: cell-line derived 3D models for radiation-response

6. General discussion

List of figures

List of tables

1. Introduction

1.1. Cell types within the normal and cancerous lung

1.1.1. General anatomy and function of the lung

The lung is the main organ of respiration responsible for oxygen transfer and carbon dioxide release. It has a complex structure consisting of two primary zones - the airway and the alveolar zone. To understand respiratory health maintenance and treatment options, like tumour resection in lung cancer, it is crucial to comprehend the relationship between lung structure and function. Macroscopically, the lungs are enclosed by a double-layered membrane called the pleura, that helps protect and lubricate the lungs as they expand and contract during breathing. The diaphragm is a muscular sheet located in the base of the thoracic cavity that helps with these contractions. Each lung is divided into lobes (3 in the right lung and 2 in the left, for the human lungs) (Chaundry and Bordoni 2023).

Air enters the lungs through a structure known as the trachea, which originates from the larynx in the upper neck. The trachea then splits into two main bronchi, one for each lung. These primary bronchi subsequently give rise to smaller branches that divide further, forming a tree-like structure (general diagram in Figure 1.1.). The branching pattern of the airways in the lungs is highly complex and serves to decrease resistance to airflow, thereby slowing down the entry of breath into the respiratory system. The airways can be categorized into two main groups: the proximal airways or bronchi, which are comprised of cartilage and submucosal glands, and the smaller bronchioles that do not possess these characteristics. The terminal respiratory units or lung parenchyma, found at the end of bronchioles, are composed of various structures including respiratory bronchioles, alveolar ducts and alveoli. The structure of the alveoli is vital for efficient gas exchange in the lungs. Alveoli have a thin and extensive surface area, which facilitates the exchange of gases by allowing them to easily diffuse across from the air to the blood in capillaries (Murray 2010).

1.1.2. Organisation of the lung airway epithelium

The airways (Figure 1.1.) consist of a pseudostratified columnar epithelium composed of various cell types, including basal, ciliated, secretory (club/club-like or serous/globet/mucous), brush/tuft cells, pulmonary neuroendocrine cells (PNECs), and hillock cells/ionocytes (which have been recently discovered by single-cell RNA sequencing (scRNAseq) experiments). These cell types are found in varying proportions and densities across the proximal-distal areas of the lung (Mindt et al. 2018; Montoro et al. 2018;

Plasschaert et al. 2018). Ciliated and secretory cells serve as a protective barrier against inhaled pathogens and particles within the respiratory system. Brush cells seem to have a chemosensory role to detect bacterial infections, while PNECs are hypoxia-sensitive cells, and both represent less than 1 % of the airway epithelium (Krasteva et al. 2012; Cutz et al. 2013). Historically, basal cells have been considered the stem cells of the lung stratified epithelium; they self-renew and differentiate into other lineages in homeostasis and repair. In the mouse they are only present in the trachea, whilst human small airways still contain basal cells (Michael J. Evans 2009; Rock et al. 2009; Teixeira et al. 2013). During homeostasis, basal cells are believed to give rise to club cells initially, which subsequently undergo trans-differentiation into ciliated cells (Rock et al. 2009; Montoro et al. 2018).

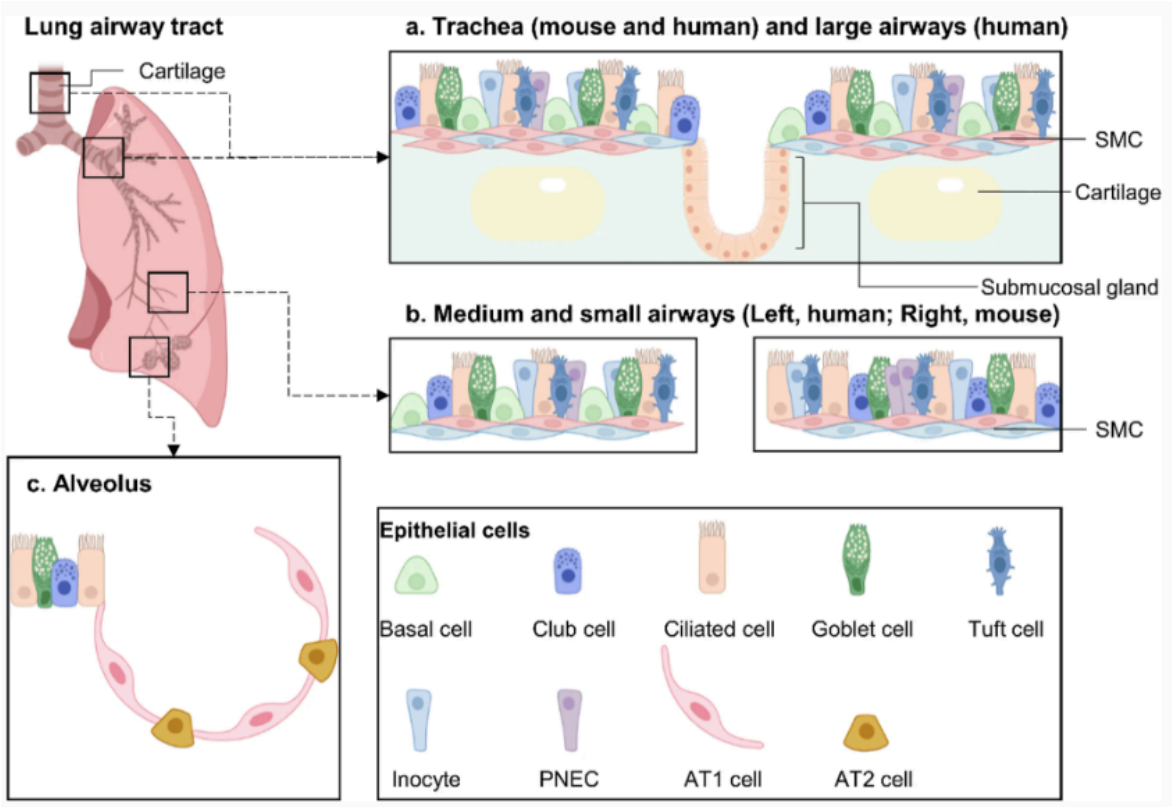

Figure 1.1. (Meng et al. 2023). The lung epitheliums. The anatomy and cellular composition in mammalian lung. **a, b** The architecture of epithelial cells within mouse and human airways. The basal cells, club cells, ciliated cells, goblet cells, tuft cells, pulmonary neuroendocrine cells and pulmonary ionocytes are observed in the proximal airways both in human and mouse. Basal cells are resident stem cells for trachea and main bronchi in mouse lung and trachea and proximal airways in human lung. **b** Mouse small airways don't contain basal cells comparing to human. **c** Cellular composition of alveoli. The alveoli include the alveolar type 1 epithelial cells and the alveolar type 2 cells. Figure and figure legend from Meng et al. 2023.

1.1.3. The lung alveoli

The alveolar region (Figure 1.1.) is composed of type I alveolar cells (ATC1), type II alveolar cells (ATC2), alveolar fibroblasts and macrophages. ATC1 are flat and specialised for gas exchange, while ATC2 cuboidal cells produce surfactant to decrease the surface tension in the alveolar region (Weibel 2015). In addition, ATC2 can both self-renew and differentiate into ATC1 after naphthalene injury, as demonstrated in promoter-driven *cre* recombinases lineage tracing studies (Desai et al. 2014). In a nine-month lineage tracing experiment done using $Axin2^{creERT2\text{-}tdT}$; $R26^{eYFP}$ mice to define alveolar epithelial progenitor dynamics during adult homeostasis, it was suggested that a population of Axin2 responsive ATC2 cells could be the alveolar stem cells during steady-state turnover, even though in lung homeostasis cellular turnover is normally very low (Zacharias et al. 2018). An ATC2-signalling cell subset (selectively expressing genes involved in Wnt signalling genes) was also detected in a scRNAseq study in which 75,000 human lung cells were transcriptionally profiled (Travaglini et al. 2020).

1.1.4. Lung stem cells: cell identity and plasticity

The previous two sections represent the classic overview of the airway epithelium and alveolar region. However, recent advances in single-cell RNA sequencing have allowed for a more detailed characterization of rare airway lineages and cell states. This, together with previous functional studies on the role of different cell types in lung regeneration (especially after injury) have produced a more detailed description of lung epithelial composition, cell and stem cell identity and cell plasticity.

There seems to be significant variability within the population of basal cells. In fact, four different basal cell types or cell states were detected in a scRNAseq study in which 75,000 human lung cells were transcriptionally profiled. These were classified as basal ($CK5^{+}$), proximal basal, proliferating basal (enriched in cell cycle genes) and differentiating basal (these were characterised by reduced expression of CK5 and the increased expression of cytokeratin 7 (CK7), Hairy and enhancer of split-1 (HES1) – Notch signalling possibly indicating club fate - and Secretoglobin Family 3A Member 2 (SCGB3A2) – suggesting secretory fate -) (Travaglini et al. 2020). In addition, various cell-lineage tracing experiments in mice have indicated that it cannot be discarded the possibility that most types of lung epithelial airway cells, excluding ciliated cells (Rawlins et al. 2007), can proliferate and expand after injury by naphthalene, inhaled oxidants or bleomycin (Rawlins and Hogan 2006).

Several other cell groups with self-renewal and/or differentiation capability have also been reported. Lineage-negative epithelial progenitor cells (LNEPs) were seen to arise in acute alveolar injury models, in which Notch suppression, the deletion of hypoxia-inducible factor 1a (Hif1a) or continuous Wingless and Int-1 (Wnt) activation drove LNEPs into ATC2 cells in mice (Vaughan et al. 2015; Xi et al. 2017). A group of cells named bronchioalveolar stem cells (BASCs) have also been previously reported by fluorescence-activated cell sorting (FACS) and immunofluorescence in the bronchioalveolar junction (BADJ), expressing both Secretoglobin Family 1A Member 1 (SCGB1A1) club cell marker and pulmonary surfactant-associated protein C (SFTPC) ATC2 marker (Kim et al. 2005). By lineage tracing in mice expressing both BASCs markers, these cells have also shown to differentiate into multiple epithelial lineages including club, ciliated, ATC1 and ATC2 cells after airway (naphthalene) or alveolar (bleomycin) injury (Liu et al. 2019; Salwig et al. 2019). Integration of proximal and distal single cell transcriptomes defined a group of cells that resided in the bronchioles and expressed both SCGB1A1 (club cell marker) and SCGB3A2 (secretory marker in distal airways) as respiratory airway secretory cells (RASCs). FACS sorted and *organoid* grown $SCGB3A2^{+}$ human embryonic stem cells (hESCs) were found to differentiate into ATC2 ($SFTPC^{+}$) when cultured in alveolar medium. This response was partially regulated by Notch and Wnt signalling, and it was disrupted in COPD patients (Basil et al. 2022).

Recently, the Human Lung Cell Atlas (HLCA) project has created an integrated single-cell transcriptomic atlas combining data from 486 donors and 49 datasets, including 2.4 million cells which have been re-annotated to create a consensus cell reference. The study identified six cell identities that were either not previously known in the human lung or only recently described. These include alveolar type 0 cells (ATC0) (recently described (Kadur Lakshminarasimha Murthy et al. 2022)) marked by expression of Pulmonary surfactant-associated protein C $(SFTPB)^{+}$, $SCGB3A2^{+}$, $SFTPC^{High}$ and Secretoglobin Family 3A Member 1 $(SCGB3A1)^{Low}$. The team also discovered 'predeterminal bronchiole secretory cells', closely related to ATC0s (together called transitional club-ATC2s), marked by expression of $SFTPB^{+}$, $SCGB3A2^{+}$, $SFTPC^{Low}$ and $SCGB3A1^{High}$ (Sikkema et al. 2023).

Overall, the lung epithelia maintains a high degree of phenotypical and physiological heterogeneity. Here there is some degree of regional and temporal cell plasticity with a broad range of cell lineages capable of proliferating, de-differentiating, or trans-differentiating in response to a variety of injuries, depending on the severity, type, and location of the insult.

1.1.5. NSCLC tumour initiation and evolution

Non-Small Cell Lung Cancer, the most common form of lung cancer, will be later described later described in depth in *section 1.2*. However, we will focus here on the initiation and evolution of the tumour from 'normal cells' in a cell-by-cell basis. The pathogenesis of NSCLC is a multifaceted and a poorly understood process. It has been hypothesised that prolonged exposure to carcinogens promotes mutations in critical genes (e.g. involved in cell cycle regulation, DNA repair, and tumour suppressor genes like Ataxia-telangiectasia mutated (ATM) or TP53) causing disruption of certain pathways (e.g. Receptor Tyrosine Kinase (RTK)-RAS or phosphatidylinositol-3-kinase – mammalian target of rapamycin (PI3K-MTOR) signalling) that lead to the formation of preneoplastic lesions in the lung, such as atypical adenomatous hyperplasia and squamous metaplasia. We will be focusing on alterations on the DNA Damage Response (DDR) pathway (for its potential antitumour therapeutic opportunities) in this thesis (section 1.3.). However, several others have investigated the mutational evolutionary trajectory and pathway alterations in NSCLC (Swanton and Govindan 2016; Jamal-Hanjani et al. 2017). After not yet fully understood series of alterations, preneoplastic lesions show abnormal cellular growth and are considered precursors to NSCLC. Further genetic changes and clonal expansion of preneoplastic cells can lead to the development of dysplastic lesions (abnormal cell multiplication that implies evolution towards malignity but with phenotype expression limited to the epithelia) and carcinoma *in situ*. The tumours can then invade nearby tissues and organs, as well as spread to distant sites in the body causing metastasis (Siddiqui et al. 2023).

At the cellular level, the cell of origin of the tumour, whether differentiated or stem, because of the mentioned alterations, undergoes a malignant transformation. This can perturb pathways that also activate stemness-associated genetic programs. As a consequence, as per the Cancer Stem Cell (CSC) theory (Schofield 1978), a subset of transformed cells acquires the capacity for self-renewal and pluripotency, giving rise to CSCs. These represent a subpopulation within a tumour with distinct properties reminiscent of stem cells. These cells possess the remarkable ability to self-renew and differentiate into various cell types found within the tumour (Schofield 1978).

Certain populations of transformed ATC2s (for lung adenocarcinoma: LUAD) and transformed basal cells (for lung squamous cell carcinoma: LUSC) are considered the cancer stem cells of NSCLC, mainly due to CSCs with tumour growth capacity co-expressing both adult stem cell and ATC2/basal cell makers (Heng et al. 2019). Interestingly, a recent study

that integrated 52 single-cell RNA sequencing and 2342 public bulk RNA sequencing human LUAD and LUSC data revealed stemness-related subclusters (expressing proliferating/differentiating markers) in both LUAD (in ATC2s) and LUSC (in basal cells) (Zhang et al. 2022).

In any case, the reality of NSCLC is that there is great heterogeneity and cellular interaction within tumours. Tissues with intrinsic heterogeneity (as the lung) provide a greater spectrum of cell types susceptible to transformation, potentially leading to a wider repertoire of cancer cell phenotypes. Hence, it could be that the greater the inherent diversity of cell types in the normal tissue, the more pronounced the tumour's heterogeneity tends to be, especially when many cell types in the lung have shown to have proliferative, differentiating and de-differentiating capacity as commented earlier. This interplay between tissue heterogeneity, the origin of the tumour cell, and the subsequent emergence of CSCs collectively shapes the multifaceted landscape of tumour heterogeneity.

1.1.6. Intra-tumour heterogeneity and tumour microenvironment

Intra-tumour heterogeneity (ITH) refers to the coexistence of diverse subpopulations of cells within a single tumour, each displaying distinct characteristics. This diversity can arise from genetic and epigenetic alterations and is very important for the understanding of how cancers will respond to therapies.

Genetic heterogeneity can occur due to somatic mutations, chromosomal rearrangements, and copy number variations. Subclones of cells within the tumour may have distinct genetic alterations, leading to variability in drug sensitivity and treatment resistance. The relationship between NSCLC's mutational landscape and its treatment is later commented in relation to targeted therapies in section 1.4.3. Epigenetic heterogeneity contributes to differences in cellular phenotype, behaviour, and response to environmental cues. Epigenetic changes include DNA methylation, histone modifications, and non-coding RNA expression (Ansari et al. 2016).

Cellular tumour heterogeneity includes both cancer cell diversity and diversity in non-mutant cell types in the tumour microenvironment, including immune cells, fibroblasts, endothelial cells, and stromal components, which critically influence tumour progression, immune responses, and treatment resistance. Based on scRNAseq copy number alteration (CNA) analyses of 42 tissue biopsy samples from stage III/IV NSCLC patients, LUSC was

reported to have a higher inter- and intra-tumour heterogeneity than LUAD (Wu et al. 2021). Spatial heterogeneity refers to variations in the distribution of cell types and molecular features within tumours. Tumours can have regions with different levels of oxygenation (hypoxia), nutrient availability, immune cell infiltration, and extracellular matrix composition, resulting in distinct microenvironments that affect tumour progression and therapy response (e.g. hypoxic cells are more resistant to radiation treatment (Bouleftour et al. 2021; Menegakis et al. 2021)). Functional heterogeneity describes differences in the biological behaviours of tumour cells, with some being more proliferative, invasive, resistant to cell death, or capable of inducing angiogenesis. This diversity of functions significantly impacts treatment outcomes and contributes to therapy resistance, often attributed to distinct cellular subtypes within the tumour.

1.2. Non-small cell lung cancer (NSCLC)

1.2.1. Lung cancer and NSCLC

Lung Cancer remains the leading cause of cancer death worldwide, with an estimated 1.8 million deaths (18 % of all cancer-related deaths) as per the GLOBOCAN 2020 report, produced by the International Agency for Research on Cancer, that includes 26 cancers in 185 countries (Sung et al. 2021). The vast majority (85 %) of lung cancer are Non-Small Cell Lung Cancer (NSCLC) with a larger proportion with later stage disease (Clark and Alsubait 2023). Lung cancer was also the second most commonly diagnosed cancer (11.4 % of all cancers – 2.2. million new cases in 2020), topped recently only by female breast cancer (11.7 %) (Sung et al. 2021). Lung cancer incidence and mortality rates are twice as high in men than in women, although the male/female ratio varies widely regionally ranging from 1.2 in North America to 4.6 in North Africa (Sung et al. 2021). Incidence and mortality rates also vary between *transitioned* and *transitioning* countries, being 3 to 4 times higher in *transitioned* ones (Sung et al. 2021).

However, these numbers do not represent the impact of SARS-CoV-2, as derive from data collected before the pandemic. Although the full extent of the impact of the COVID-19 pandemic in different regions around the world is unknown yet, delays in diagnosis and treatments are evident, including the suspension of screening programs and reduced availability to healthcare systems. As a result, a short-term decrease in incidence, followed by an increase in advanced-stage diagnoses and cancer mortality could be expected.

NSCLC patients' prognosis depends on several factors such as the stage and subtype of cancer, the patient's age and general health, genetical mutations, an adequate diagnosis and treatment plan and access.

1.2.2. Environmental risk factors

It is well established that smoking is the primary environmental risk factor associated with lung cancer, especially with Lung Squamous Cell Carcinoma (LUSC) and Small Cell Lung Cancer (SCLC). Differences across worldwide regions / sex and lung cancer rates, reflect the patterns of the tobacco epidemic, with similar patterns in mortality and incidence reflecting the high lethality (Sung et al. 2021).

Lung cancer in never smokers is more frequent among women and in East Asia. Outdoor and indoor air pollution, chemical exposures, second-hand smoking, asbestos, certain metals (e.g., arsenic), ionising radiation and others are also considered important causes of lung cancer (Shankar et al. 2019).

Pre-existing lung diseases can also increase the risk of developing lung cancer. Chronic lung conditions, such as chronic obstructive pulmonary disease (COPD) (Durham and Adcock 2015), pulmonary fibrosis (Ballester et al. 2019) and bronchiectasis (Chung et al. 2015) can create an environment within the lungs that is characterised by chronic inflammation, tissue damage and impaired lung function. These conditions can lead to persistent irritation and stress, promoting a tissue environment that is conducive to the growth of mutated cells and cancer development. Moreover, the compromised lung functions in these diseases may reduce the body's ability to effectively clear harmful substances from the respiratory tract, increasing exposure to potential carcinogens. Interestingly, exposure to fine particulate matter with a diameter of 2.5 μm or less in the environment has also been found to contribute to the development of lung cancer by affecting cells that already have oncogenic mutations in healthy lung tissue. Research conducted using functional mouse models has shown that air pollutants lead to increased numbers of macrophages entering the lungs and releasing interleukin-1β, which prompted Epidermal Growth Factor Receptor (EGFR) mutant lung alveolar type II epithelial cells to adopt a progenitor-like state that supported tumour growth (Hill et al. 2023).

Therefore, all these factors, together with family history or genetic predisposition (that will be addressed in section 1.2.4), synergistically elevate the chances of developing lung cancer,

emphasising the necessity of comprehensive preventive policy, healthcare strategies and biological research to address the aetiology of the disease.

1.2.3. Tumour staging and histopathology classification

The Tumour, Node, Metastasis (TNM) staging system is a fundamental framework used in clinical oncology to categorise the extent of cancer progression. 'T' represents the primary tumour's size and extent within the lung, along with its invasion into surrounding tissues. 'N' indicates the extent of regional lymph node involvement. Lastly, 'M' signifies the presence or absence of distant metastasis, indicating whether the cancer has spread to distant organs or tissues beyond the lungs. A more comprehensive explanation of each category can be found in Table 1.1. The combination of these three factors yields a comprehensive stage designation that assists clinicians in assessing disease progression, prognosis, and treatment planning (see Figure 1.2.) (Lababede and Meziane 2018):

- Stage I indicates and early, localised tumour with limited spread.
- Stage II suggests further invasion or lymph node involvement on the same side of the chest.
- Stage III reflects more extensive local spread and lymph node involvement on the opposite side of the chest.
- Stage IV represents advanced disease with distant metastasis.

Table 1.1. TNM staging (Lababede and Meziane 2018).

T	**T1**	Small tumours confined to the lung. T1a: tumour < 1 cm. T1b: Tumour between 1-2 cm across. T1c: tumour between 2-3 cm across.
	T2	Larger tumours that may involve nearby structures (e.g. diaphragm).
	T3	Tumours spread to adjacent structures (e.g. major blood vessels) or is between 5-7 cm across
	T4	Extensive local invasion to the trachea, oesophagus or spine or the tumour is < 7 cm across.
N	**N0**	No evidence of lymph node involvement
	N1	Involvement of nearby nodes
	N2	Spread to lymph nodes withing the chest but on the same side as primary tumour
	N3	Presence of cancer in lymph nodes on the opposite side of the chest or above the collarbone
M	**MX**	Metastasis could not be assessed
	M0	No distant metastasis detected
	M1	Distant metastasis has occurred (often to the brain, bones, or liver)

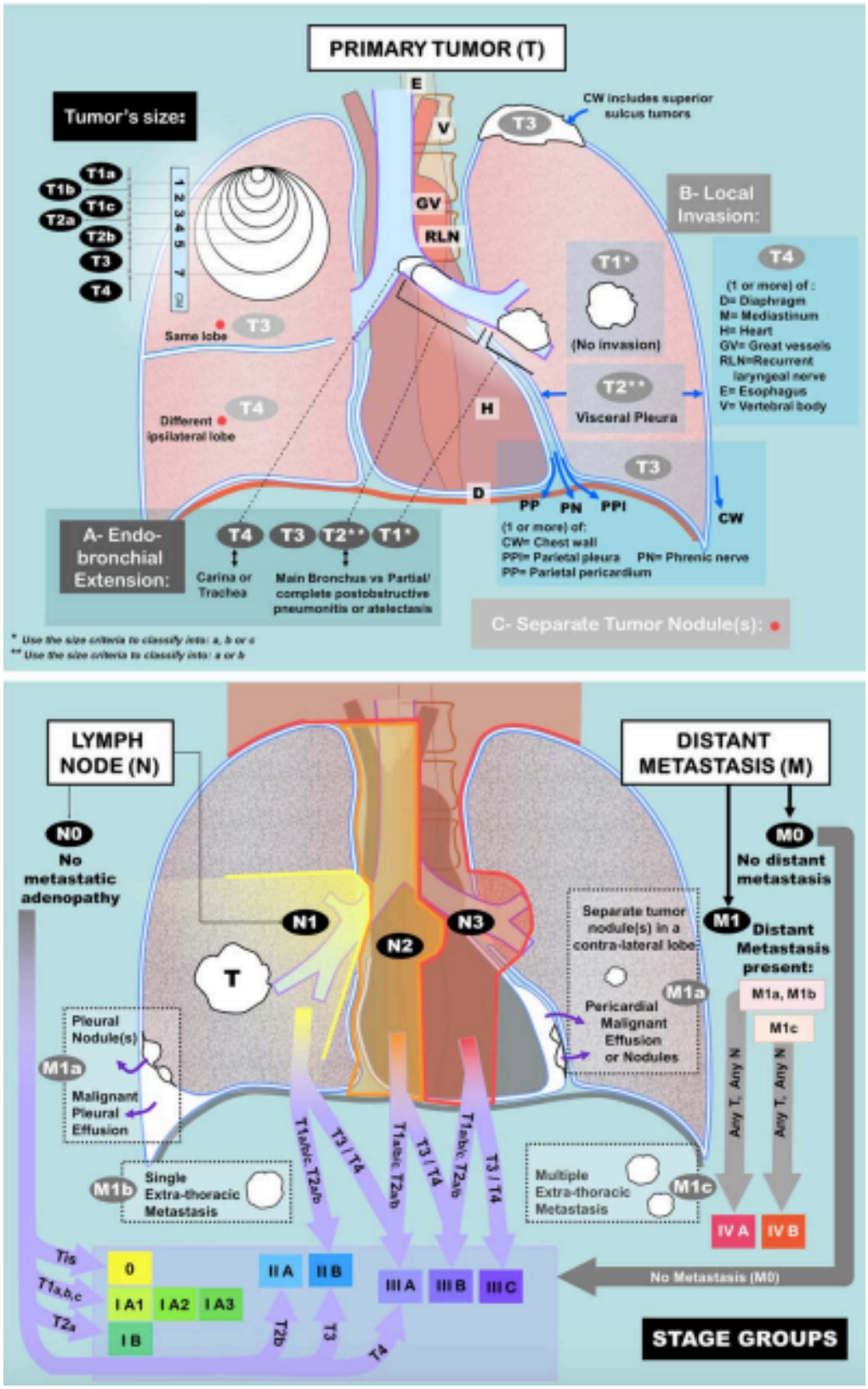

Figure 1.2. Reference diagrams depicting the eighth edition of TNM staging classification of lung cancer (Lababede and Meziane 2018). First, define T category by matching the greatest dimension and the appropriate T category. Second, upgrade the classification based on the other criteria of primary tumor invasion/extent if applicable (use the criteria of invasion/extent [endobronchial extension (A), local invasion (B), and separate tumor nodule(s)(C)] only to assign a higher, not lesser, T classification). Finally, use the lower diagram to assign N and M classifications then combine that with the T category to define the corresponding stage. In the lower illustration, N1, N2, N3, and the separate tumor nodule(s) of M1a were described based on right-sided primary neoplasm (marked with letter T). Use a mirror image in the case of leftsided lung neoplasm. Figure and figure legend adapted from Lababede and Meziane 2018.

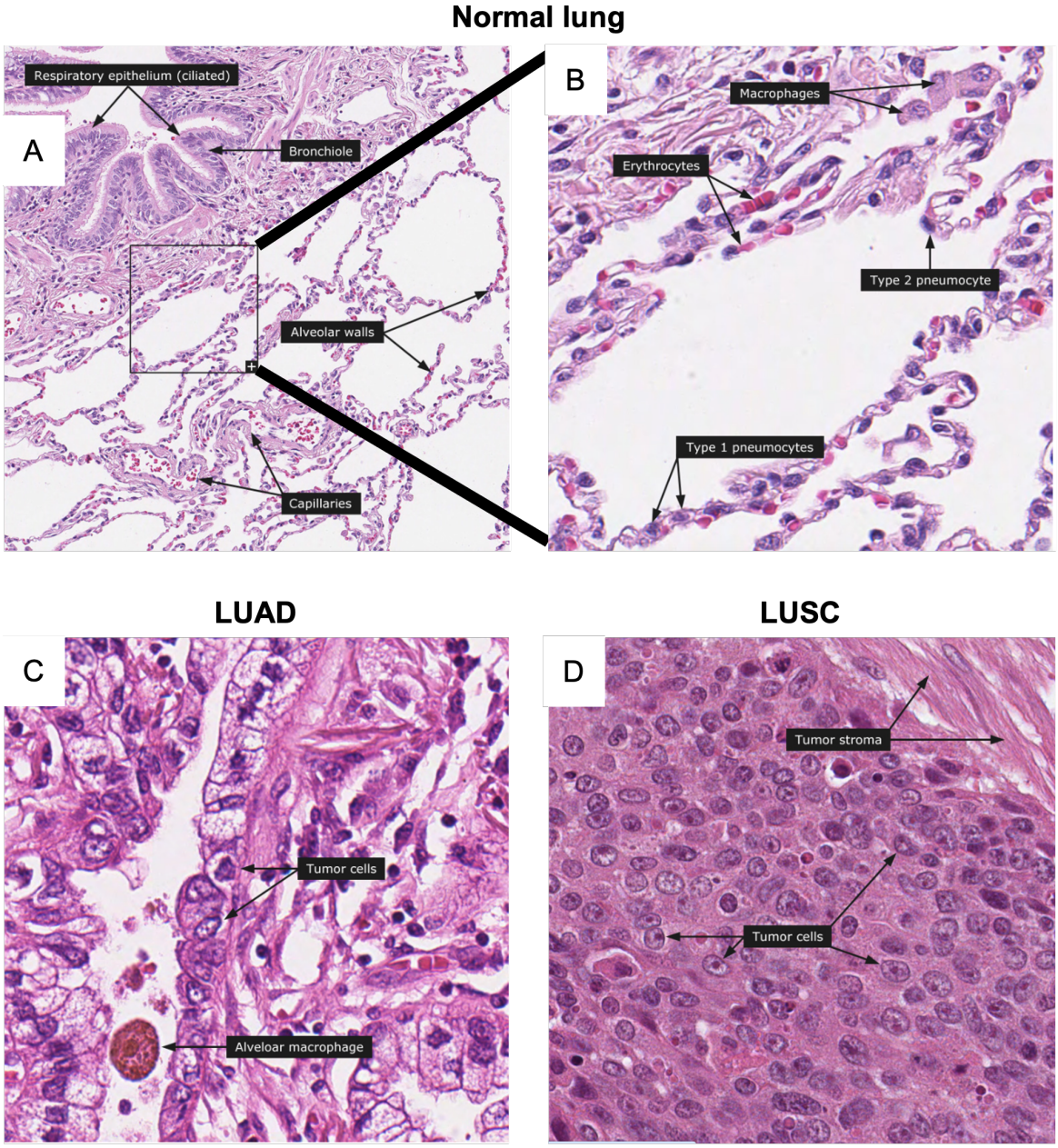

Figure 1.3. Normal lung and lung cancer histology. A) H&E staining of normal lung tissue showing differencial lung structures: respiratory epithelium, bronchioles, alveolar walls, capillaries. **B)** Magnification of image "A)" that shows normal lung alveolar cells: Type 1 and 2 pneumocytes, erythrocytes and macrophages. **C)** H&E staining of lung adenocarcinoma, pointing out tumour cells and alveolar macrophages. **D)** H&E staining of lung squamous cell carcinoma, pointing out tumour cells and tumour stroma. Images from the Human Protein Atlas (https://v15.proteinatlas.org/).

NSCLC encompasses a diverse spectrum of subtypes, each characterised by distinct histological and molecular features that have implications for the prognosis and treatment strategies of patients. The primary subtypes of NSCLC include Lung Adenocarcinoma (LUAD; ~ 50 %), Lung Squamous Cell Carcinoma (LUSC; ~ 25 %) and Large Cell Carcinoma. In addition, 10 % of all lung carcinomas have also a combined histology (Osmani et al. 2018). LUAD, the most prevalent subtype, often arises in the peripheral lung

and has glandular histology (characterised by irregularly shaped, mucous secreting structures lined with cancerous epithelial cells) (Figure 1.3.). LUSC typically originates in the central airways and is characterised by squamous differentiation, in line with the nature of the pseudostratified columnar epithelium (Figure 1.3.). Keratinization and intercellular bridges are common features of LUSC (Clark and Alsubait 2023).

In the clinical setting, while a proportion of NSCLC cases are categorised into subtypes though analysis of histomorphological characteristics using haematoxylin and eosin (H&E) staining, precise classification of tumours is often achieved by employing immunohistochemical (IHC) markers that are distinct to each subtype, especially in the case of poorly differentiated carcinomas, which often lack the morphological phenotypes and features of either glandular or squamous differentiation that are typically used to identify subtypes. The specific markers to subcategorise NSCLCs vary depending on each hospital's pipeline, although the World Health Organization (WHO) has issued general guidelines: the most common IHC markers for categorising NSCLCs are thyroid transcription factor 1 (TTF1) and Napsin A for LUADs and cytokeratin 5/6 (CK5/6), p63 and p40 for LUSCs ((Figure 1.4. for staining patterns) (Osmani et al. 2018; Nicholson et al. 2022).

TTF-1 and Napsin A are present in alveolar cells and are particularly valuable for recognising glandular differentiation in LUADs. The expression of TTF-1, which belongs to the Nkx2 family of transcription factors, is inversely linked with the level of tumour differentiation, which implies that poorly differentiated LUADs are less inclined to express TTF-1 when compared with well-differentiated LUAD tumours. Napsin A functions as an aspartic proteinase, aiding in the maturation of surfactant protein B in lung tissue. It is substantially expressed in the cytoplasm of type II alveolar cells (ATC2) and club cells, as well as in LUAD. P40 and p63 are both products of the p63 gene and they are produced by the basal cell layer of the bronchial epithelium. CK 5 / 6 are also expressed in basal cells. However, limitations exist with current IHC markers due to the potential for cross-reactivity with other cell types and tumours. For instance, TTF-1 displays immunoreactivity with normal alveolar macrophages, whereas both p40 and p63 exhibit immunoreactivity with normal bronchial basal epithelial cells, as commented above. Overall, the final pathohistological diagnosis of the tumours is performed by a trained professional histopathologist, considering both morphology and marker expression (Osmani et al. 2018; Nicholson et al. 2022)

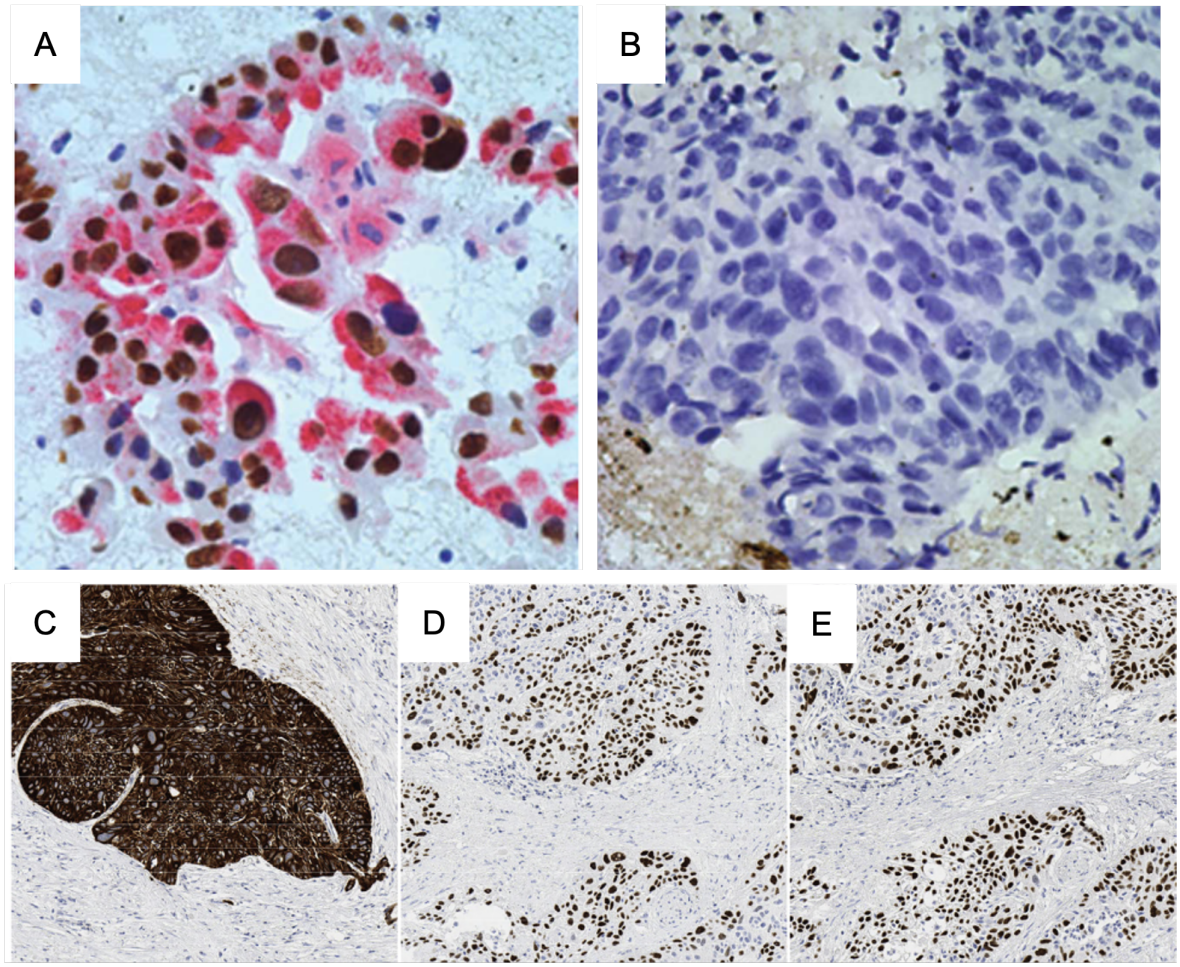

Figure 1.4. Specific marker patterns to subcategorise NSCLC. A) High magnification of malignant lung adenocarcinoma shows TTF-1 nuclear staining and Napsin A cytoplasmic staining, x60 (images from (Fatima et al. 2011)). **B)** High magnification of lung squamous cell carcinoma is shown with negative staining for TTF-1/Napsin A, x60 (images from (Fatima et al. 2011)). LUSC showing positivity for **C)** CK5/6, **D)** p40 and **E)** p63 (images from (Kriegsmann et al. 2019)).

1.2.4. General mutational landscape of NSCLC

The Cancer Genome Atlas project (https://www.cancer.gov/tcga) has helped elucidating genomic alterations in the different NSCLC subtypes that can, sometimes, be related to prognosis and are currently being investigated due to their ability to be therapeutically targeted (mentioned later in section 1.4.3).

The genomic profiles of lung cancer show clear differences between never smokers and smokers. Smokers exhibit a much higher mutation frequency, with more cytosine to adenine (C>A) nucleotide changes, along with mutations in genes like Kirsten Rat Sarcoma viral oncogene homolog (KRAS) and tumour protein 53 (TP53) (Swanton and Govindan 2016). Never smokers, who are more likely to suffer from LUAD, typically have a mutational spectrum in which cytosine to thymine (C>T) transition predominates together with a higher

occurrence of activating EGFR mutations, and ROS Proto-Oncogene, Receptor Kinase (ROS1) and Anaplastic Lymphoma Kinase (ALK) translocations (Swanton and Govindan 2016). Recurrent molecular alterations are indicated in Table 1.2., and these could be related to tumour initiation and evolution and tumour treatment, discussed in sections 1.1.5 and 1.4.3.

Table 1.2. (Swanton and Govindan 2016). Recurrent molecular alterations in NSCLC. All gene definitions are included in the list of abbreviations at the beginning of this thesis.

Type of alteration	Lung Adenocarcinoma (LUAD)	Lung Squamous Cell Carcinoma (LUSC)
Cell cycle mutations	TP53 (46%), CDKN2A(4%), KRAS (33%), EGFR (14%), BRAF (10%), STK11 (17%), MET (8%), NF1 (11%), PIK3CA (7%), RIT1 (2%)	TP53 (91%), CDKN2A (17%), RB1 (7%), PIK3CA (16%), PTEN (8%), HRAS (3%).
Other mutations	Oxidative stress response: KEAP1 (17%), MYC pathway; MGA (8%). Aberrant splicing: U2AF1 (3%), RBM10 (8%)	Oxidative stress response: CUL3 (6%), KEAP1 (12%), NFE2L2 (15%). Squamous differentiation: NOTCH1 (8%), ASCL4 (3%), NOTCH2 (5%).
Rearrangements	ALK (3–8%), ROS1 (2%), RET (1%), NTRK1 (3%), NRG1 (2%), BRAF (3% in those who never smoked), ERBB4 (1%).	FGFRs (rare).
Amplifications	TTF1 (14%), TERT (18%), EGFR (7%), MET (4%), KRAS (6%), ERBB2 (3%), MDM2 (8%)	Chr3q: SOX2 (43%), TP63 (29%), PIK3CA (38%), HES1 (26%).
Deletions	CDKN2A (20%).	CDKN2A (27%), PTEN (3%).
Commonly altered pathways	MAPK and PI3K signalling, oxidative stress response, cell-cycle progression, RNA splicing and processing, nucleosome remodelling	Squamous-cell differentiation, oxidative stress response, MAPK and PI3K signalling.

1.3. Biology of DNA damage and response

1.3.1. The DNA damage and response pathway

One of the key therapies used for treating patients with lung cancer is radiotherapy. To link the cellular mechanisms of lung cancer cells to the tumour responses, it is necessary to understand some background on DNA damage responses. The DNA Damage Response (DDR) pathway monitors DNA integrity and, in the presence of any type of DNA damage, activates transient cell cycle arrest and repair pathways to ensure maintenance of genomic stability and cell viability. When normal cells cannot repair their DNA, they undergo senescence or cell death.

In a general overview, DNA damage is recognised by sensor proteins (e.g. MRN complex, Ku70/80) that recruit and activate the transducer kinases (e.g. ATM, Ataxia Telangiextasia and Rad3-related (ATR), DNA-dependent protein kinase catalytic subunit (DNA-PKcs)), these transmit the signal to the upstream kinases (e.g. Checkpoint kinase 1/2 (Chk1/2)), which phosphorylate their substrates, the downstream effectors (e.g. p53, RAD51, cell division cycle 25 A/C (CDC25A/C)), that recruit the appropriate DNA repair module (including cell cycle control) depending on the type of DNA lesion (Hakem 2008).

1.3.2. Types of DNA damage

DNA damage can originate due to endogenous or exogenous factors. Both metabolic (reactive oxygen species in general, lipid peroxidation, endogenous oestrogens, endogenous alkylating agents, reactive carbonyl species…), hydrolytic processes and replication errors cause endogenous DNA damage naturally (De Bont and van Larebeke 2004) (Figure 1.5.). Among exogenous DNA damaging agents, UV light, ionising radiation (IR) and genotoxic chemicals are the most common. DNA damage response depends on the amount and type of damage (Hakem 2008). IR can cause damage to the DNA molecule by ionisation of reactive species that will indirectly cause DNA damage. IR can also directly damage the DNA molecule causing double strand breaks (DSBs) or single strand breaks (SSB) and also bulky lesions or intra- and inter- strand crosslinks (Figure 1.5.). Henceforth, this work will focus on DSBs-responses as these are the most deleterious type of damage caused by IR (next section 1.3.3), which is a Standard-of-Care (SoC) treatment for NSCLC (Iyama and Wilson 2013; Chatterjee and Walker 2017; Huang and Zhou 2021).

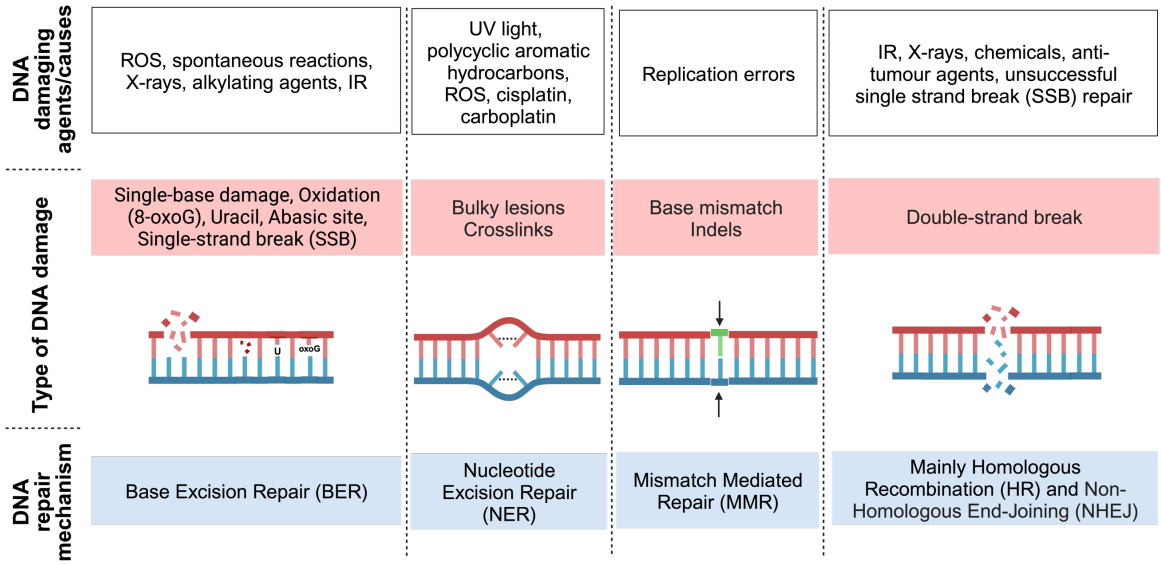

Figure 1.5. Types of DNA damage causes and repair pathways. Diagram of general DNA repair mechanisms depending on the type of DNA damage caused by different agents (De Bont and van Larebeke 2004; Hakem 2008; Iyama and Wilson 2013; Chatterjee and Walker 2017; Huang and Zhou 2021). ROS: reactive oxygen species. IR: ionising radiation. 8-oxoG: 8-oxoguanine, usually caused by interaction of ROS with guanine base. Bulky lesion are helix-distorting DNA lesions. Indels: Insertions / deletions of DNA bases. Figure created in BioRender.

1.3.3. Double strand breaks

Double-strand breaks (DSBs) are a severe form of DNA damage that can be induced by ionising radiation. Unlike other DNA lesions, DSBs result in the complete separation of both DNA strands, leading to potential loss of critical genetic information. The repair involves complex mechanisms such as non-homologous end joining (NHEJ) or homologous recombination (HR), which can introduce errors or require accurate sequence alignment. Unrepaired or improperly repaired DSBs can trigger DNA mutations and chromosomal rearrangements. Cells recognise the gravity of DSBs and often arrest the cell cycle and initiate apoptosis to prevent the propagation of genetic instability. Overall, DSBs are a great threat to genome integrity and cellular viability (Lomax et al. 2013).

Ionising radiation, such as gamma rays, is one of the few DNA damaging agents with sufficient energy to cause direct ionisation. Direct ionisation is a process by which ionising radiation directly interacts with a molecule, particularly DNA, in a cell. This interaction gives enough energy to the DNA molecule to break chemical bonds and cause DNA damage. This energy can be high enough to break the chemical bonds in both strands of the DNA helix at the same time, creating a physical gap in the DNA. Ionising radiation can also indirectly cause DSBs by interacting with water molecules in the cellular environment. This

interaction generates reactive oxygen species (ROS) such as hydroxyl radicals, which can diffuse into cells and damage DNA by causing oxidative stress and inducing DSBs (Ward 1988; Lomax et al. 2013).

Once DSBs have been detected (explained later on section 1.3.5), a whole downstream mechanism begins, which can be divided on the cell cycle response (e.g. ideally temporarily arresting cells which are actively cycling, in order that they have time to repair) and the DNA repair response. The physiological outcome for the cell will depend on the interaction of these two mechanisms.

1.3.4. Cell cycle arrest

The cell cycle duplicates the genome at interphase (S) and divides it during mitosis (M). In between, there are 3 mayor checkpoints (G_1, intraS and G_2) (Figure 1.6.). The cell cycle begins with the G_1 checkpoint, during which factors like cell size, nutrient availability, and DNA damage are assessed before allowing entry into the S phase, where DNA replication occurs. If conditions are not optimal or signals suggest that division should be delayed, cells can instead enter the G_0 phase. In G_0, cells maintain a non-dividing, quiescent state. Some cells in G_0 may remain in this state permanently, while others have the potential to re-enter the cell cycle and return to active proliferation when external conditions change, or signals dictate the need for cell division. An intra-S checkpoint monitors DNA replication integrity. Following genome duplication, the G_2 checkpoint verifies DNA integrity and completion of replication (Mahesh et al. 2022). During prophase, chromatin condenses into visible chromosomes and spindle fibres start forming. In metaphase, chromosomes align along the cell's equator. During anaphase sister chromatids are separated to opposite poles, and in telophase nuclei form around each set of chromosomes. Cytokinesis then divides the cell's cytoplasm, resulting in two daughter cells (O'Connor 2008).

Cell cycle checkpoints are also vital stages at which the cell cycle is arrested following DNA damage, to prevent the accumulation of DNA lesions before mitosis that would otherwise lead to failures including the stalling of DNA replication forks. Cancer-associated mutations that disrupt the cell cycle control can bypass checkpoints to promote continuous cell division and prevent cells from exiting the cell cycle. However, this can lead to unrepaired catastrophic DNA damage and the death of the cancer cell. As a consequence, there is some selection during oncogenesis for molecular changes that allow the survival of cells with DNA damage. In principle however, tumours will continue to grow as long as proliferation

rates exceed cell death rates in the presence of physiological levels of DNA damage. The additional damage induced by IR and by DNA-damaging drugs likely acts by 'tipping the balance' and increasing rates of damage-associated cell death present in tumours. The complexity of the tumour microenvironment and the different responses of cells to DNA damage opens a door for cell cycle-related drugs to exploit cancer-specific vulnerabilities (Shaltiel et al. 2015; Huang and Zhou 2020; Matthews et al. 2022; Hauge et al. 2023).

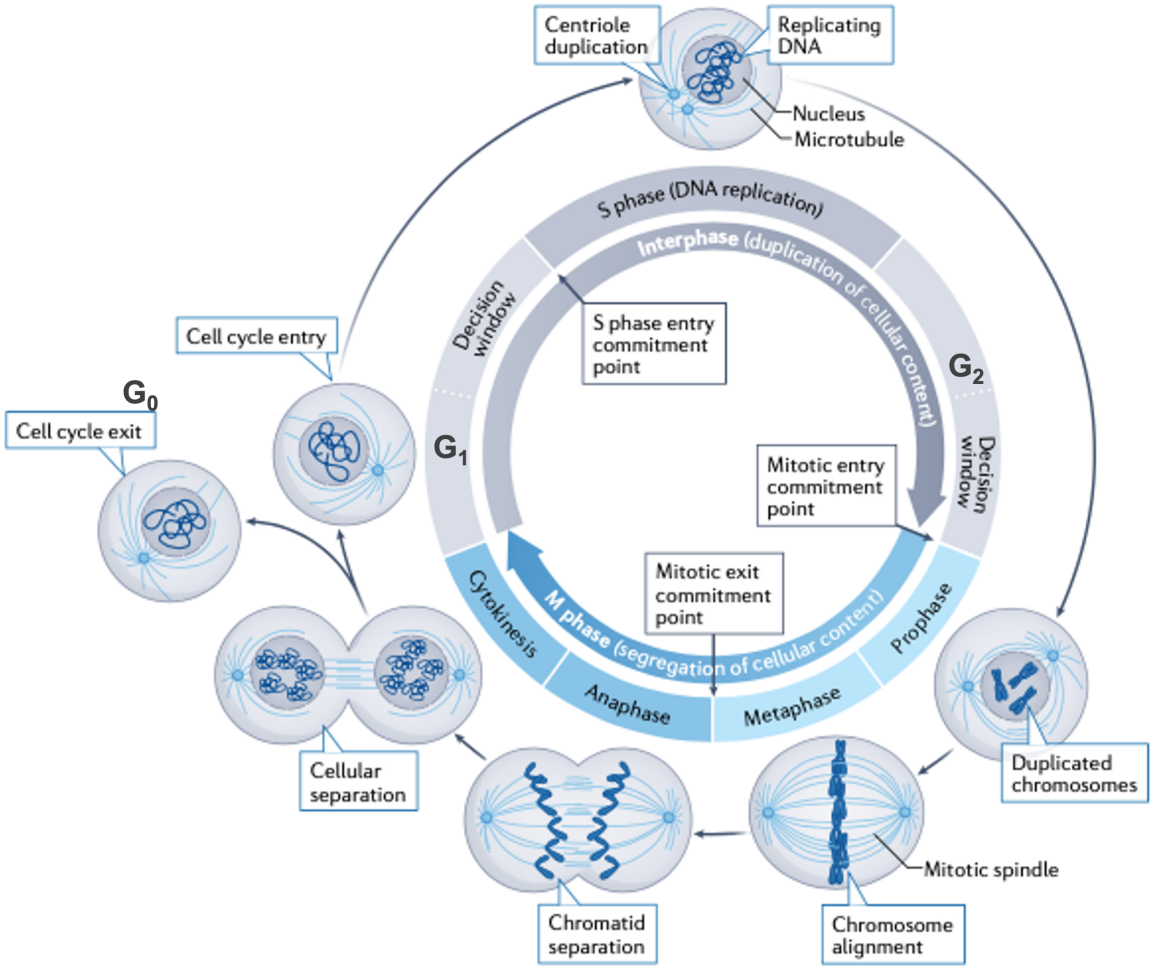

Figure 1.6. (Matthews et al. 2022) General diagram of the cell cycle. Diagram from Matthews et al. 2022 showing the different phases of the cell cycle and key processes for cell cycle progression. The cell cycle is the ordered series of events that a cell undergoes, consisting of interphase (G_1, S, G_2) and mitosis (M), during which a cell grows, replicates its DNA, and divides into two daughter cells. G_0 phase: a quiescent state where cells are not actively dividing and temporarily exit the cell cycle. G_1 phase: characterised by DNA damage and cell size checkpoints that ensure the suitability of conditions for initiating DNA synthesis. S phase: the synthesis phase where DNA replication occurs, resulting in the duplication of the genetic material. G_2 phase: characterised by DNA damage and cell replication checkpoints to confirm accurate DNA synthesis before entering mitosis. M phase: the mitotic phase during which the nucleus divides, followed by cytokinesis, resulting in the separation of replicated chromosomes into two daughter cells.

1.3.4.1. G_1 cell cycle checkpoint

The G_1 checkpoint prevents cells with unrepaired DNA damage from replicating their DNA. The primary G_1 checkpoint arrest is driven by the ATM-p53-p21 axis (Figure 1.7. – bold lines). This arrest can last for a long-time causing cell inactivation after radiation (senescence); however, many cells exhibit a transient p53-dependent G_1 delay which serves to provide time for DNA repair (Hafner et al. 2019). In response to DSBs, ATM phosphorylates Chk2 on T68 and p53 on Ser15 (Canman et al. 1998). Simultaneously, Chk2 also phosphorylates p53 on Ser20 (Chehab et al. 1999). Phosphorylation of p53 stabilises it and prevents its mouse double minute 2 homolog (MDM2)-mediated ubiquitination and degradation. In addition, ATM also directly phosphorylates MDM2, which contributes to p53 stabilisation (Khosravi et al. 1999). When accumulated in the nucleus, p53 acts as a transcription factor, controlling the cell cycle checkpoint and apoptosis (depending on the degree of DNA damage). P53 induces transcription of the cyclin dependent kinase 2 (CDK2) inhibitor p21, which binds to cyclin E-CDK2 complex in the late G_1 and to the cyclin D – CDK4/6 complex in the early G_1 to inhibit both retinoblastoma protein (Rb) phosphorylations needed to release E2F transcription factors that enable S-phase progression (EI-Deiry et al. 1994; Sladek 1997). CDK4/6, CDK2 and p21 levels thus determine G_1 primary cell cycle arrest. A secondary G_1 checkpoint arrest (Figure 1.7. – grey lines) is driven by the ATM-Chk2-CDC25A axis. CDC25A degradation is initiated directly by protein modification (phosphorylation of Ser123) (Falck et al. 2001). It has been shown that the ATR-Chk1-CDC25A axis (Figure 1.7. – grey lines) can also regulate CDK2 activity, although ATR is more active in the S phase as is directly induced following replication stress repair (Xiao et al. 2003).

.

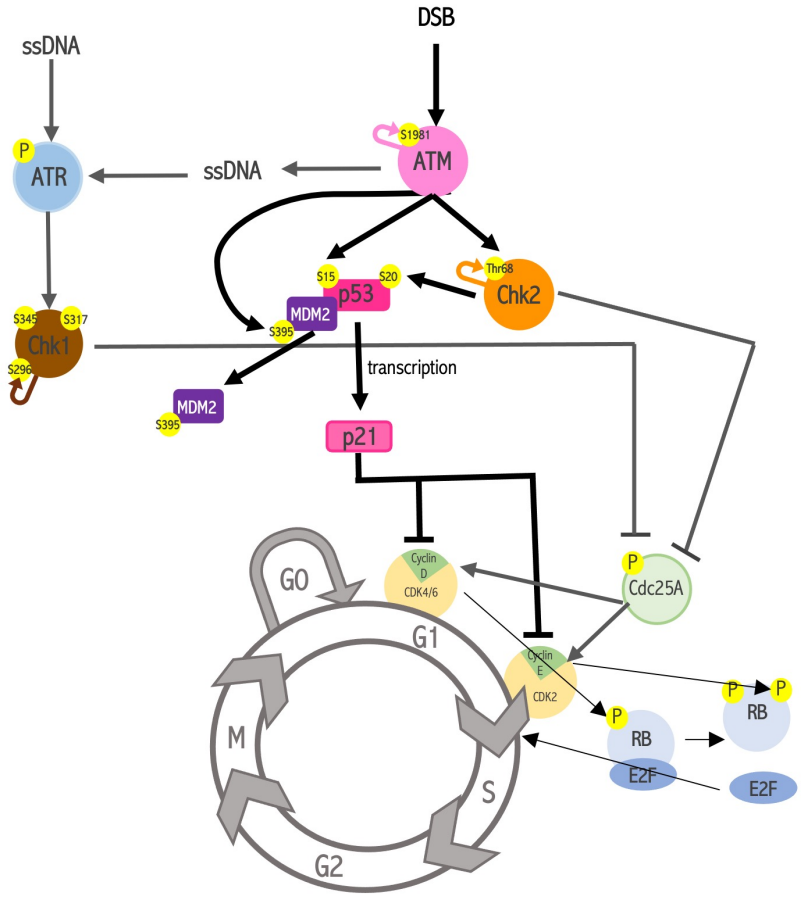

Figure 1.7. G_1 cell cycle checkpoint regulation upon DNA damage. Bold lines show primary pathway and grey lines represent other pathways for cell cycle arrest. Yellow circles with a P represent a phosphorylation and the specific phosphorylation site (e.g. S15 – serine 15 phosphorylation). Figure created in Microsoft Power Point. (El-Deiry et al. 1994; Sladek 1997; Canman et al. 1998; Chehab et al. 1999; Khosravi et al. 1999; Falck et al. 2001; Xiao et al. 2003; Shaltiel et al. 2015; Mahesh et al. 2022; Matthews et al. 2022).

1.3.4.2. Intra-S cell cycle checkpoint

Radiation-induced DNA damage slows down DNA synthesis in the S phase to allow time for DNA repair. It is mainly regulated by the ATM/ATR-Chk2/1-CDC25A pathway (Figure 1.8. – bold lines). Upon detection of DSBs, ATM or ATR phosphorylate Chk2/1. In turn, these phosphorylate CDC25A which leads to its degradation and the negative regulation of the CyclinA-CDK2 complex that results in the arrest of the cell cycle in the S phase (Falck et al. 2001; Sørensen et al. 2003; Xiao et al. 2003). An alternative, ATM-mediated, S-phase checkpoint is partly mediated through NBS1 and SMC1 phosphorylation, although the exact mechanism is not fully understood yet (Figure 1.8. – grey lines) (Lim et al. 2000; Kitagawa et al. 2004; Luo et al. 2008).

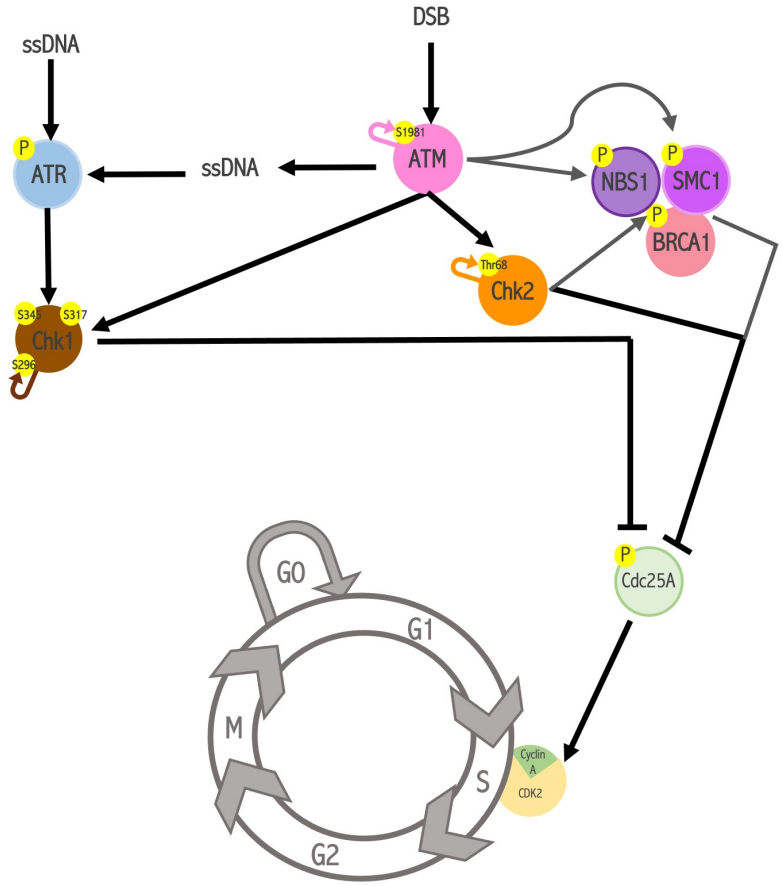

Figure 1.8. Intra-S cell cycle checkpoint regulation upon DNA damage. Bold lines show primary pathway and grey lines represent other pathways for cell cycle regulation. Yellow circles with a P represent a phosphorylation and the specific phosphorylation site (e.g. Thr68 – Threonine 68 phosphorylation). Figure created in Microsoft Power Point. (Lim et al. 2000; Falck et al. 2001; Sørensen et al. 2003; Xiao et al. 2003; Kitagawa et al. 2004; Luo et al. 2008; Shaltiel et al. 2015; Mahesh et al. 2022; Matthews et al. 2022).

1.3.4.3. G_2 cell cycle checkpoint

The G_2 checkpoint functions to delay or inhibit mitosis when DNA lesions are present following DNA replication. This helps prevent the segregation of damaged chromosomes during mitosis, which could result in loss of genetic material or other changes in the genome. The principal mechanism underlying G_2/M arrest is based on the activation of Chk1 and Wee1 via ATR. Chk1(/2) is activated by phosphorylation via ATR (/ATM) which phosphorylates CDC25 inhibiting its activity (Figure 1.9. – bold lines). CDC25C's role involves the elimination of two inhibitory phosphates from CDK1 and its inactivation preventing the cell from entering mitosis (Sanchez et al. 1997; Liu et al. 2020). Furthermore, Wee1, activated by Chk1, upon DNA damage causes G_2/M arrest by inactivating CDK1 through phosphorylation of Tyr15 (Watanabe et al. 1995). TP533 is also involved in the G_2/M checkpoint preventing G_2/M transition via p21 by decreasing the cyclin B1 levels (Figure 1.9. – grey lines). The activation of p53 can occur via ATM or Chk2. Chk2 can also directly inhibit CDC25C (Hafner et al. 2019).

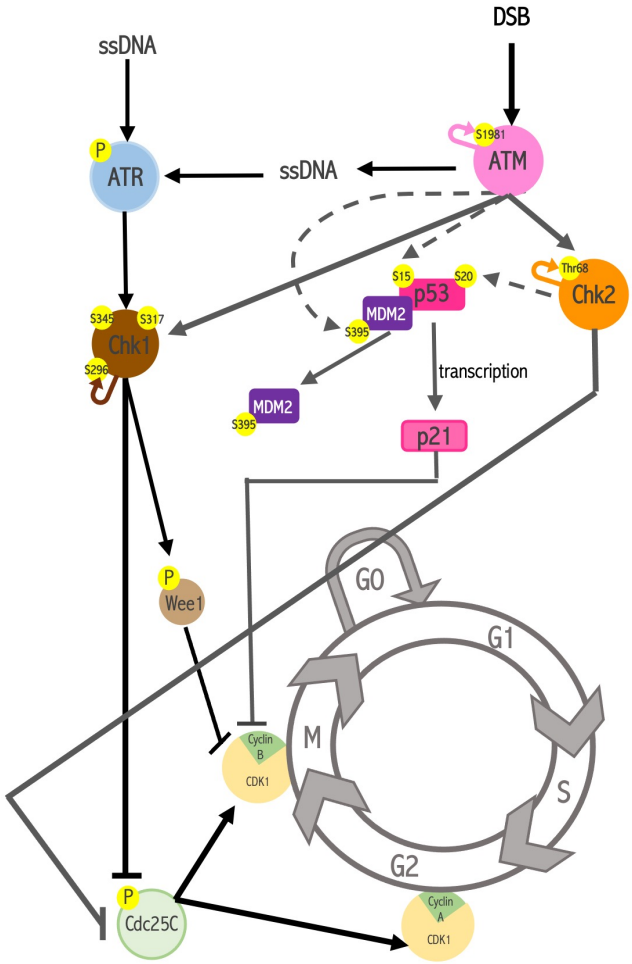

Figure 1.9. G_2 cell cycle checkpoint regulation upon DNA damage. Bold lines show primary pathway and grey lines represent other pathways for cell cycle arrest. Yellow circles with a P represent a phosphorylation and the specific phosphorylation site (e.g. S15 – serine 15 phosphorylation). Figure created in Microsoft Power Point. (Watanabe et al. 1995; Sanchez et al. 1997; Shaltiel et al. 2015; Hafner et al. 2019; Liu et al. 2020; Mahesh et al. 2022; Matthews et al. 2022).

1.3.5. Detection and repair of DSBs

There are two main pathways for post-IR DSB repair: classical non-homologous end joining (c-NHEJ) and homologous recombination (HR). Eighty percent of the damage is typically repaired via c-NHEJ. HR is an error-free repair process in most cases, but it performs recombination using the sister chromatid as a template and, therefore, it makes the process relatively slower compared to c-NEHJ repair and it is only available in S and G_2 phases of the cell cycle. c-NHEJ, on the contrary, repairs DSBs through direct ligation of the broken DNA ends, and thus requires no sister chromatic and is active in all phases of the cell cycle, but it's also an error-prone repair. The repair of residual DSBs that were unable to be repaired by the main

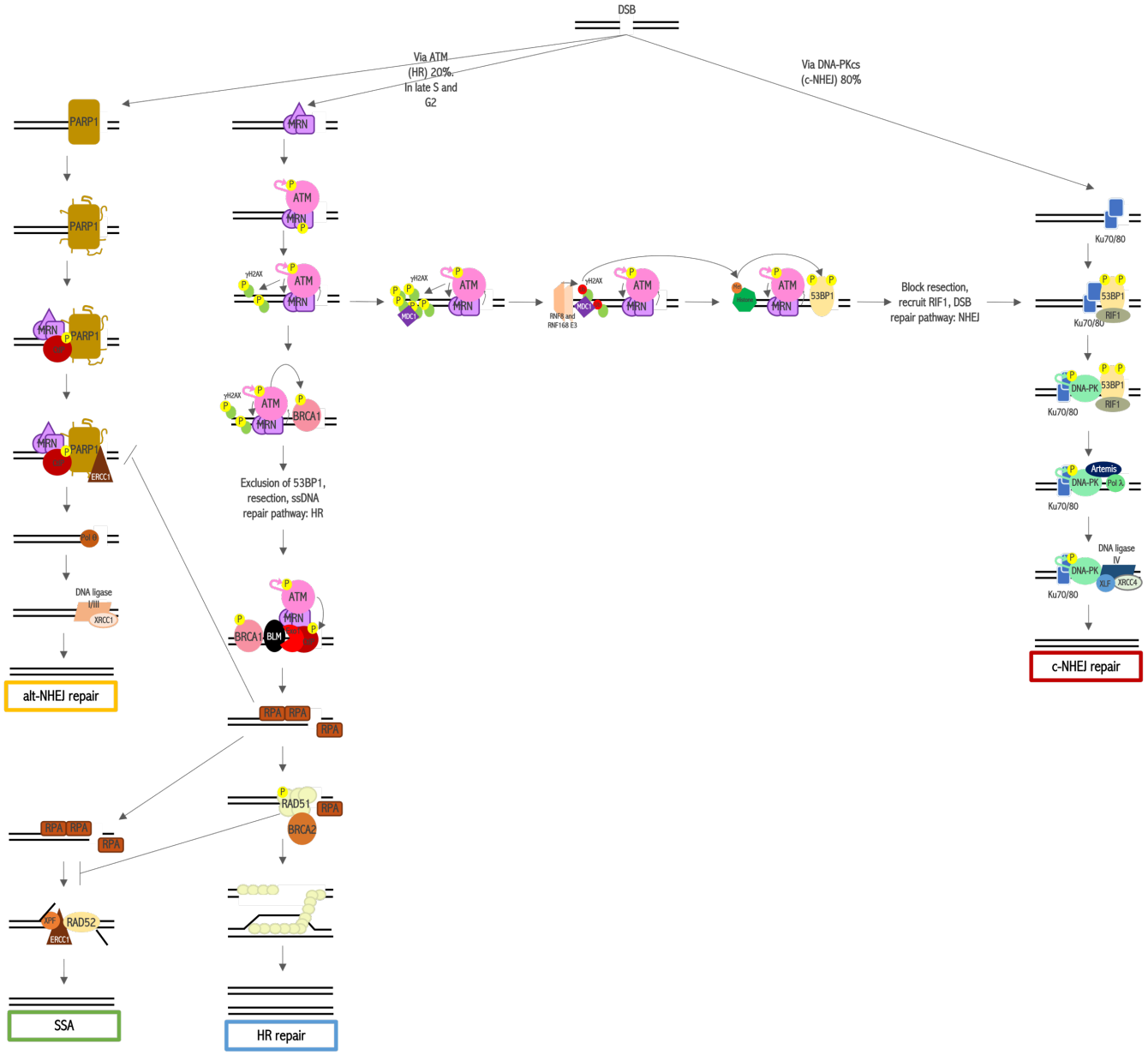

*Figure legend on the next page

Figure 1.10. Post-IR DSB detection and repair pathways. The MRN complex and Ku70/80 act as initial sensors for DSBs, facilitating the coverage of broken ends. NBS1 sequesters ATM to the DSB site, leading to its autophosphorylation and activation. This activated ATM phosphorylates NBS1, creating a positive feedback loop that amplifies the signal (Bakkenist and Kastan 2003; You et al. 2005). Additionally, ATM phosphorylates H2A histone family member (H2AX) on Serine 139, resulting in the formation of H2AX foci around DSBs, referred to as γH2AX (Rogakou et al. 1998; Burma et al. 2001). These γH2AX foci are commonly detected through immunofluorescence and used as for calculating the number of DSBs per cell. While gH2AX formation is normally ATM-mediated, it can also depend on DNA-PKcs or ATR (Ward and Chen 2001; Hammond et al. 2003; Stiff et al. 2004). Phosphorylated γH2AX foci recruit MDC1, which interacts with the MRN complex and ATM to facilitate the recruitment of RNF8 and RNF168 E3 ligases. These ligases ubiquitinate H2AX at the DSB site, influencing DSB repair mechanisms choice (Stucki et al., 2005; Mailand et al., 2007). The accumulation of 53BP1 inhibits end resection and RAD51 loading, promoting non-homologous end joining while restricting homologous recombination. Conversely, exclusion of 53BP1 favours BRCA1 recruitment and initiates HR (Daley and Sung 2014). Detection of 53BP1 though immunofluorescence is also used to identify DSBs. Details on each repair mechanism can be found in the main text in section 1.3.5. Figure created in Microsoft Power Point.

pathways, are resolved by alternative non-homologous end joining (alt-NHEJ) and single strand annealing (SSA) (Mao et al. 2008; Beucher et al. 2009). The general choice for deciding which repair pathway to use for DSB repair is based on the chromatin state, IR-induced DSB distribution, DNA-end structure, and DNA-end resection. In the first instance (Figure 1.10.), the MRN complex and Ku70-80 compete to determine the primary repair pathway to be employed, mainly based on the structure of the break ends. Ku70/80 binding would usually translate into DNA-repair via c-NHEJ; whilst MRN-binding determines repair via HR, alt-NHEJ or SSA. The regulatory mechanism of IR-induced DSB repair pathway choices are complex, beyond the scope of this introduction, and had been reviewed elsewhere (Zhao et al. 2020).

1.3.5.1. Homologous recombination (HR) repair

Following the induction of double strand breaks by ionising radiation, the homologous recombination (HR) pathway orchestrates the repair process with precision (Figure 1.10. – resolves in the blue square). Initially, as commented above, MRN complex identifies the DSB and subsequently recruits ATM kinase. This engagement prompts the phosphorylation of H2AX, resulting in the formation of γH2AX, which serves as an amplification platform for the damage signal. Breast cancer gene 1 (BRCA1) and c-terminal binding protein interacting protein (CtIP) collectively contribute to the promotion of end resection, an event facilitated by the coordinated action of Bloom syndrome RecQ like helicase (BLM) and exonuclease 1 (Exo1) enzyme (Chen et al. 2008; Nimonkar et al. 2008). This process culminates in the generation of a single-stranded DNA segment that becomes safeguarded by Replication Protein A (RPA) binding (Wold and Kelly 1988; Iftode et al. 1999).

At this juncture, the assembly of the RAD51 recombinase nucleofilament is initiated, facilitated by the involvement of BRCA2 by physically interacting with RAD51 and the

ssDNA (Davies et al. 2001; Jensen et al. 2010). The single-stranded DNA, coated with RAD51, then undergoes an intricate exploration for homologous template recognition and strand invasion, leading to DNA synthesis guided by the accurate template, ultimately achieving the restoration of the original genetic information (Baumann et al. 1996).

1.3.5.2. Classical non-homologous end joining (c-NHEJ)

Although inherently error-prone due to its template-independent nature, c-NHEJ is the principal DSB repair pathway (Figure 1.10. - resolves in the red square). Central to post-IR DSB repair via c-NHEJ is the Ku70/80 heterodimeric complex, which rapidly binds to the exposed DNA ends. Simultaneously, DNA-dependent protein kinase (DNA-PK) associates with Ku70/80, forming a high-affinity complex that further stabilizes DNA ends (Mimori et al. 1981; Gottlieb and Jackson 1993).

The c-NHEJ pathway's intricate orchestration involves additional regulatory factors such as the tumour protein p53 binding protein 1 (53BP1) and the replication regulatory timing factor 1 (RIF1). These factors contribute to the inhibition of end resection, promoting the preservation of DNA ends for direct re-joining (Feng et al. 2013). The Artemis nuclease, in collaboration with DNA-PK, functions to process and trim any damaged or protruding DNA structures, facilitating alignment in preparation for ligation (Chang and Lieber 2016). Polymerase λ engages in gap filling and extension, and its template-independent synthesis contributes to the pathway's error-prone nature (Kaminski et al. 2022). Critical to the resealing of the broken DNA strands are the X-ray repair cross complementing 4 (XRCC4) and XRCC4-like factor (XLF) complex, working in tandem with DNA ligase IV. This assembly serves as a bridge that brings the processed DNA ends together and allows for the step of ligation, completing the repair process (Grawunder et al. 1997; Ahnesorg et al. 2006).

1.3.5.3. Alternative non-homologous end joining (alt-NHEJ)

In cases where the primary repair mechanisms (HR and NHEJ) fail to repair all the remaining DSBs, these can be resolved by an alternative non-homologous end joining pathway (alt-NHEJ) (Figure 1.10. - resolves in the yellow square). Both the MRN complex and PARP1 are involved in DSB recognition for the alt-NHEJ repair pathway. ATM kinase is simultaneously activated as mentioned earlier, contributing to signal amplification (Haince et al. 2008). The CtIP protein plays a pivotal role in the initiation of end resection, a step that deviates from classical NHEJ by producing short single-stranded DNA segments. The excision repair cross complementation group 1 (ERCC1) protein processes irregular DNA

structures that arise during repair. Polymerase theta fills the DSB gap and DNA ligase I/III, along with the scaffolding X-ray repair cross complementing 1 protein (XRCC1), come into play to finalize the ligation step, ultimately re-joining the DNA ends (Audebert et al. 2004).

1.3.5.4. Single strand annealing (SSA)

Single strand annealing (SSA) is also an alternative pathway for DSB-derived 3' ssDNA repair. SSA uses homologous repeats to bridge DSB ends, causing deletion rearrangements between the repeats and, thus, it's quite mutagenic (Figure 1.11. - resolves in the green square). SSA depends on CtIP for the generation of 3' ssDNA (Symington 2016). Annealing of the flanking repeats and removal of the non-homologous 3' sequences, are mediated by RAD52 and ERCC1 and the ERCC1/XPF nuclease activity is also enhanced by RAD52 (Motycka et al. 2004; Rothenberg et al. 2008; Faridounnia et al. 2018).

1.3.6. Tumour cell outcomes after IR-induced DSBs

The type of cell response after radiation depends on several factors as radiation dose and fractioning, oxygen quantity in the environment, cell type and cell cycle phase at the time of exposure, TP53 status and DNA repair capacity, etc.

In general, upon radiation induced DNA damage, the mechanism of cell cycle arrest and DNA repair will activate (Figure 1.11.). Cell cycle arrest will cause a delayed in cell growth-rate (as these cells won't be dividing on the same rate as before) and this will translate into a decrease in general culture metabolic viability. Upon unsuccessful DNA repair, cells can maintain a long-term cell cycle arrest (senescence) or regulated cell death (apoptosis) can be activated via TP53; which will cause an initial descend on metabolic viability.

When cell cycle checkpoints are dysfunctional (e.g. cancer cells with mutations in cell cycle related genes as TP53), cells are able to re-enter mitosis with DNA damage which causes an accumulation of genetic damage and ultimately leads to mitotic catastrophe and cell death. Therefore, a dysfunctional cell cycle arrest can translate into a delayed but higher response to radiation (showing lower culture viability measurements as less cells will survive to re-populate the tumour).

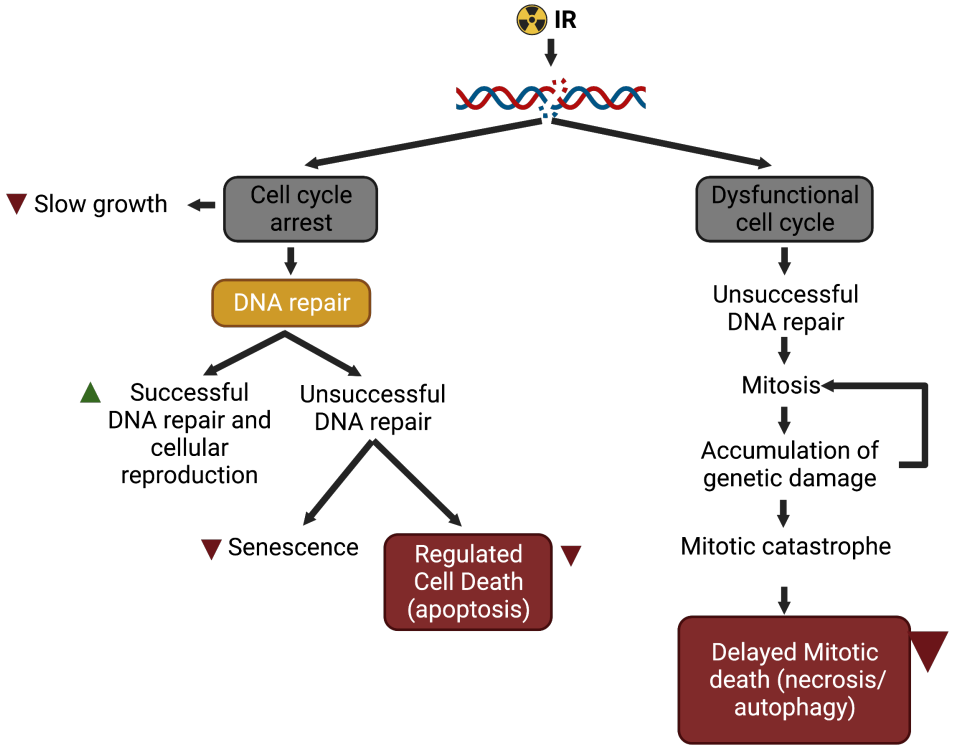

Figure 1.11. Tumour cell outcomes upon IR. Comprehensive diagram of possible outcome for tumour cells after suffering from IR, dependant on cell cycle arrest and DNA repair pathways' success. Follow figure together with main text in this section. Figure created in BioRender.

1.3.7. Targeting the DDR pathway for inducing cancer cell death

In cancer, DDR pathway is often dysregulated (e.g. TP53, ATM, ATR, BRCA1, RAD51, etc., mutations) since the genetic changes give cancer cells a selective growth advantage in the presence of background levels of DNA damage and when oncogene- and tumour-environment driven cellular stresses would normally lead to cell cycle arrest. The loss of many of the genes listed both allows cells to avoid proliferative arrest and results in increased genomic instability and a reliance on specific DDR components for survival. As explained above, there is significant redundancy amongst the cell cycle control and repair pathways such that when one pathway is compromised, cells may be able to survive by becoming reliant on alternative mechanisms of repair (see sections 1.3.4 and 1.3.5). Therefore, novel therapeutic approaches to selectively impair DDR in cancer cells have been developed. Some DNA damage repair inhibitors (DDRis) in combination with radiation, could be used in the clinic for NSCLC treatment. These exploit cancer vulnerabilities that induce synthetic lethality and impede tumour growth. Here, we focus on explaining the specific biological logic behind co-treatments with irradiation and ATR inhibitors or PARP inhibitors in TP53 or ATM mutated tumours.

1.3.7.1. ATR inhibitors (ATRi)

The logic behind using an ATRi for synthetic lethality with TP53 and/or ATM mutations relies on the relationship between ATM and ATR and is based on the mechanism of cell cycle arrest.

In normal (ATM and p53 WT) cells, exposure to IR induces cell cycle checkpoint activation via ATM (through p53, Chk2 and Chk1) and ATR (through Chk1), allowing cells to repair before entering mitosis (Figure 1.12., first panel). In the presence of an ATRi, ATM and p53 can maintain all cell cycle checkpoint functions (Figure 1.12., second panel). However, ATM or p53 tumour deficient cells are unable to activate G_1 cell cycle checkpoint in response to IR but they can maintain intraS and G_2/M cell cycle checkpoints for DNA repair before mitosis (Figure 1.12., third panel). In ATM and/or p53 deficient cells, ATR inhibition results in cells being unable to slow down the cell cycle for DNA repair, leading to accumulation of DNA damage, mitotic catastrophe, and cell death (Figure 1.12., fourth panel). Several reports have shown this mechanism in tumour cells. In TP53- or ATM-defective Chronic Lymphotic Leukemia cells, inhibition of ATR led to accumulation of unrepaired DNA damage that was not resolved pre-mitosis due to defective cell cycle checkpoints, resulting in cell death by mitotic catastrophe (Kwok et al. 2016). Similar results were reported after co-treatment with IR or cisplatin in the NCI-H23 p53 null LUAD line and in several other ATM null cancer cell lines (Reaper et al. 2011).

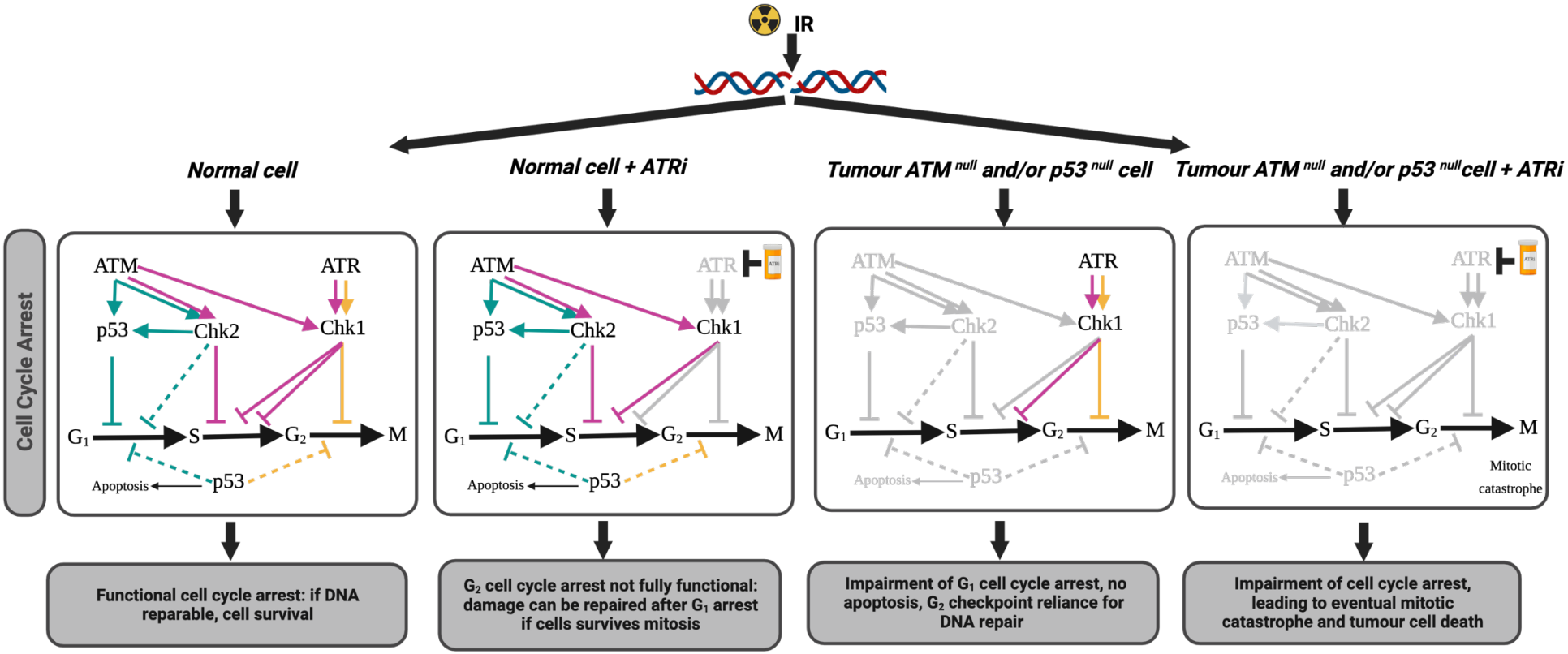

Figure 1.12. Logic behind the use of ATRi in combination with IR to exploit TP53/ATM vulnerabilities in cancer. Diagram of the expected post-irradiation double strand break (DSB) DNA damage cell cycle response in TP53 or ATM mutant cancer cells vs normal wild-type cells, both co-treated with or without an ATRi. Solid lines represent post-DSB cell cycle primary response and dashed lines represent secondary response. G_1/S arrest pathways are shown in blue, intraS in pink and G_2/M in yellow. Figure created in BioRender. (El-Deiry et al. 1994; Canman et al. 1998; Chehab et al. 1999; Falck et al. 2001; Sørensen et al. 2003; Shaltiel et al. 2015; Hafner et al. 2019; Huang and Zhou 2020; Liu et al. 2020; Matthews et al. 2022; Hauge et al. 2023).

1.3.7.2. PARP inhibitors (PARPi)

Synthetic lethality of TP53 and/or ATM mutant lines with a PARPi after treatment with IR is based on the relative redundancy amongst repair pathways such that when one pathway is compromised, cells may be able to survive by becoming reliant on alternative repair mechanisms. ATM is the central molecule for HR repair and p53 can control HR by interaction with different HR-specific proteins as RAD51 (Linke et al. 2003). PARP inhbitors have proven to be synthetically lethal with HR defective tumours, i.e. tumours with deficiencies in the Homologous Recombination repair pathway. The reason behind this is that HR defective tumours rely on SSA and alt-NHEJ for the repair of end-resected DSBs. PARP is essential for alt-NHEJ and its inhibition can be lethal to HR defective cells. In fact, PARPi are mostly used in BRCA1 deficient breast tumours (HR defective) (Ragupathi et al. 2023). In normal (ATM and p53 WT) cells (Figure 1.13., first panel), IR-induced DSBs will mainly repair via homologous recombination (via ATM-p53) and the more error-prone NHEJ. In the presence of an PARPi, ATM and p53 can maintain DNA repair via HR (Figure 1.13., second panel). ATM- or/and p53-deficient cells are impaired for HR repair, but, even if the DSB ends have already being resected, the damage can still be repaired via alt-NHEJ and SSA (Figure 1.13., third panel). Adding a PARPi to p53- and/or ATM-deficient cells results end-resected DNA repair to rely only error-prone SSA which can lead to defective-repair and ultimately cell death (Figure 1.13., fourth panel).

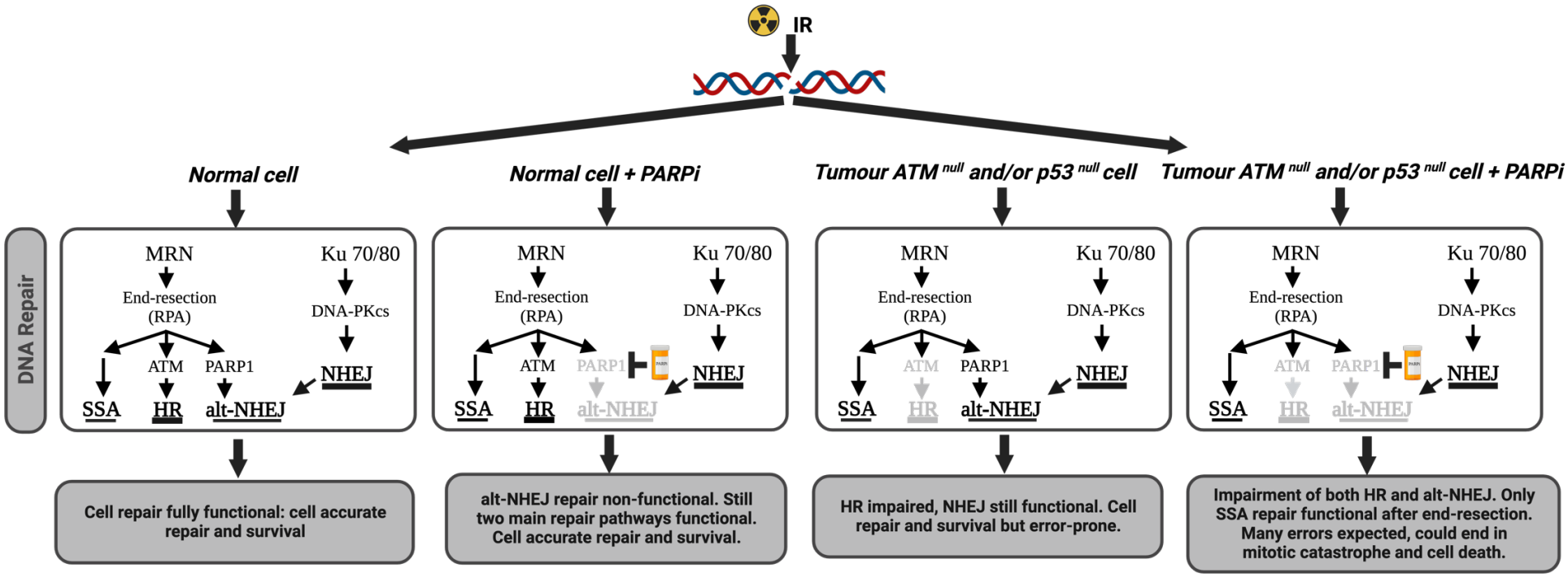

Figure 1.13. Logic behind the use of PARPi in combination with IR to exploit TP53/ATM vulnerabilities in cancer. Diagram of the expected post-irradiation double strand break (DSB) repair response in TP53 or ATM mutant cancer cells vs normal wild-type cells, both co-treated with or without an ATRi. Figure created in BioRender. (Linke et al. 2003; Mao et al. 2008; Beucher et al. 2009; Shaltiel et al. 2015; Huang and Zhou 2020; Zhao et al. 2020; Hauge et al. 2023; Ragupathi et al. 2023)

1.4. Current treatments and challenges for NSCLC

1.4.1. Surgery

Surgery is often the first-line treatment for early-stage NSCLC. It involves the removal of the tumour and possibly nearby lymph nodes. If the cancer is detected at an early stage and is localized, surgical resection can offer a curative option. However, surgical removal of a portion of the lung can lead to reduced lung function, especially if a significant amount of lung tissue is removed depending on the location of the tumour. This can result in shortness of breath, decreased exercise tolerance, and reduced overall lung capacity. Therefore, surgery might not be suitable for all patients with NSCLC and factors such as TNM stage, the patient's overall health, lung function, age, and any existing medical conditions can affect their eligibility for surgery (Mithoowani and Febbraro 2022).

1.4.2. Radiotherapy and chemotherapy

Radiotherapy is a Standard-of-care (SoC) for NSCLC where surgery is not possible in the clinic. Most interestingly, it can be focal to minimise systematic damage to non-tumour cells. In fact, certain types of radiotherapy treatments, like intensity-modulated radiotherapy (IMRT), adjust the intensity of certain beams in specific areas, enabling the delivery of high doses to particular segments of the tumour while minimising harm to neighbouring normal bodily tissues (Low et al. 2011). Radiotherapy uses high-energy beams to target and destroy cancer cells, causing DSBs. Radiation can be used in various ways, such as before surgery to shrink tumours, after surgery to kill any remaining cancer cells, or as a palliative treatment to relieve symptoms in advanced cases. Radiation can also be a definitive treatment itself (Vinod and Hau 2020). Standard-of-care for non-resectable lung cancer is chemoradiation. The PACIFIC clinical trial is a paradigm shift in treatment of lung cancer and demonstrates definitive treatment with concurrent chemoradiation and then adjuvant immunotherapy (explained later) in patients with stage III unresectable NSCLC (Spigel et al. 2022).

The most common chemotherapeutic agents used for the treatment of NSCLC include cisplatin, carboplatin, paclitaxel, docetaxel, gemcitabine, and pemetrexed. Cisplatin and carboplatin are platinum-based compounds that form DNA cross-links, disrupting DNA replication and inducing cell cycle arrest and apoptosis. Paclitaxel and docetaxel are taxanes that stabilize microtubules, crucial structures for cell division, leading to mitotic arrest and cell death. Gemcitabine interferes with DNA synthesis by inhibiting the DNA polymerase. Pemetrexed inhibits multiple enzymes involved in nucleotide and folate metabolism, hindering DNA synthesis. The mechanisms of these agents exploit the vulnerabilities of

rapidly dividing cancer cells but can also affect healthy cells, leading to the characteristic side effects associated with chemotherapy (Adjei 2004; Lee 2019) (Amjad et al. 2023).

1.4.3. Targeted and combination therapies

The treatment landscape for NSCLC has evolved with the introduction of targeted therapies and combination approaches. The National Institute for Health and Care Excellence (NICE) of the UK provides guidance to improve outcomes for patients by ensuring that the most effective treatment pathways are used, and it often stratifies patients depending on their mutations or gene alterations (https://www.nice.org.uk/guidance/ng122). Targeted therapies, such as EGFR inhibitors (erlotinib, gefitinib), ALK inhibitors (crizotinib, alectinib), ROS1 inhibitors (entrectinib), BRAF inhibitors (dabrafenib, trametinib), MET inhibitors (crizotinib, capmatinib) or RET inhibitors (selpercatinib, pralsetinib) focus on specific genetic mutations or aberrant proteins driving NSCLC growth. These drugs disrupt signalling pathways crucial for tumours that express the relevant target proteins (Guo et al. 2022).

Immune checkpoint inhibitors, such as durvalumab, pembrolizumab, nivolumab, and atezolizumab, target molecules like PD-1 or PD-L1, releasing the brakes on immune cells and enabling them to recognize and attack cancer cells. These inhibitors enhance the immune response against the tumour. Another class of immunotherapy, tumour-infiltrating lymphocyte (TIL) therapy, involves extracting immune cells from the tumour, expanding and activating them *in vitro*, and then infusing them back into the patient. Adoptive T-cell therapy augments the patient's immune response against the tumour. These immunotherapies offer durable responses and have transformed advanced NSCLC treatment by providing long-term survival benefits for certain patients (Guo et al. 2022; Mamdani et al. 2022).

Combination therapies involve utilising multiple treatments simultaneously. For instance, some patients receive immune checkpoint inhibitors (pembrolizumab, nivolumab) alongside chemotherapy or targeted therapy to enhance the immune response against cancer. Combinations like these aim to exploit synergistic effects, enhance treatment efficacy, and delay the development of resistance. These approaches mark significant advancements in tailoring NSCLC treatment to the individual molecular characteristics of the tumour, leading to improved outcomes and reduced side effects.

1.4.3.1. DNA damage response inhibitors (DDRIs) and radiation combination therapies

Defects in the DDR pathway may influence both cancer development and treatment. DNA mutations caused by DDR mechanisms' defects can lead normal cells towards becoming cancer cells, as they directly enhance the tumour growth rates and may indirectly affect the rate at which the cancers acquire additional cancer driver mutations. However, the defects in DNA repair also offer unique therapeutic opportunities since they generate cancer cell specific DNA damage repair vulnerabilities. In a DDRi-based therapy, tumour cells with specific DDR defects can accumulate DNA lesions that are not recognised or repaired, causing cytotoxity and tumour cell death. Conversely, normal cells without DDR defects will be able to repair DNA damage (see the use of ATRi/PARPi in TP53/ATM mutant tumours in section 1.3.7) (Curtin 2013).

Although DDRi inhibitors have activity in the presence of 'physiological' levels of DNA damage, the full exploitation of their potential can be enhanced by combining their delivery with drug or radiation-induced DNA damage which increase their efficacy (Chalmers 2016). The ATRi, VE-822, inhibited Chk1 phosphorylation and sensitized *in vitro* cancer (p53 and KRAS mutant) but not normal cells to radiotherapy (Fokas et al. 2012). Treating pancreatic carcinoma cells with the PARPi, ABT-888, significantly decreased PARP activity and cell viability and increased apoptosis *in vitro*. In addition, an enhancement in tumour growth inhibition (TGI) and survival was observed in orthotopic xenografts in athymic mice after treatment with both the drug and radiation (Tuli et al. 2014).

Currently, novel and exciting series of studies are aiming to determine the safety profile of multiple DDRis (ATMis, ATRis, DNA-PKis and PARPis) when used in combination with fixed-dose radical radiotherapy in patients with locally advanced NSCLC. This is a necessary step for the implementation of DDRi and radiation combination treatments as routine for patients with certain tumour vulnerabilities in the clinic. The CONCORDE study is a randomized, open-label, phase Ib, multi-institution, multi-arm clinical trial. The study aims to determine the recommended phase II dose (RP2D) of each DDRi used in combination with radical radiotherapy. The RP2D will be the dose level at which it's estimated that 25% of subjects will experience dose-limiting toxicities during a 13.5 month period from the start of radiotherapy. The results of this study are still pending. Nonetheless, it is expected to represent a major step forward in NSCLC treatment (Walls et al. 2020).

1.5. Pre-clinical models for lung and lung cancer research

1.5.1. *In vitro* 2D models

1.5.1.1. 2D cell lines

Since the HeLa cell line was derived from a cervical cancer sample taken from Henrietta Lacks in 1951; the use of 2D immortalised cell lines has been a foundational tool in scientific research, providing a consistent and reproducible model system for studying various cellular processes and diseases such as cancer. These are simple, cost-effective, easy to manipulate cultures with well-established protocols that allow for high-throughput drug screening.

Furthermore, relatively simple genetic engineering and genome editing techniques enable the manipulation of gene expression, facilitating functional focused research on individual genes. Comparison of genetically-manipulated lines with the matched control cell lines can enhance understanding of gene function (e.g. shRNA paired lines against target genes) (Boettcher and McManus 2015). However, 2D cell lines can suffer from the alteration of critical characteristics of the tumours from which they are derived as a result of their adaptation for growth on plastic. In addition, these models, because of their simplicity, struggle to recapitulate the biology present within the tumour microenvironment *in vivo*. These limitations restrict the predictive power of the cell models as analogues for the responses of tumour tissues to anti-cancer therapies, probably including responses to IR (Peng et al. 2021).

1.5.1.2. Primary cell lines

Primary cultures are isolated from living organisms and can contain populations of different cell types present in the source tissue, making them, in principle, more biologically relevant. They can be used to study cell behaviour and molecular mechanisms in a more patient-dependant native context, allowing for a better understanding of *in vivo* processes. However, they still lack the 3D microenvironment representative of the tissue of origin, including in the context of tumours, cell-cell interactions between tumour cells and between tumour cells and host cells and matrix components in the tumour microenvironment. Primary cells have not undergone significant selection as part of their culture adaptation, but as a consequence, they have a limited lifespan in culture and need to be used during very early passages before they undergo senescence. This restricts their use in repeated experiments and makes their reproducible use in long-term studies challenging (Kapalczynska et al. 2018). Finally, repeatedly obtaining primary cell lines from human tissues directly from patients raise ethical concerns and can be logistically challenging.

1.5.2. *In vitro / Ex vivo* 3D models

1.5.2.1. Spheroids

Here spheroids are defined as 3D cellular aggregates that form a spherical, self-organised, structure when cultured in culture medium (normally in the absence of additional matrix components) in low-adherence tissue-culture plates (Figure 1.14.). Spheroids are often generated from 2D immortalised cell lines that are seeded into low-adherence tissue culture plates. The cell models thus share some of the plastic adaptation-limitations described above. However, culturing cell lines in 3D does allow the study of some cell-cell interactions and for analysis of some of the effects of nutrient and oxygen gradient that may be present in tumours *in vivo* (e.g. oxygen-dependant differential response to IR). In addition, cell-line derived spheroids can highlight issues with drug penetration in therapeutic contexts, making them valuable tools for mimicking aspects of tissue-like environments *in vitro* (van Tienderen et al. 2019).

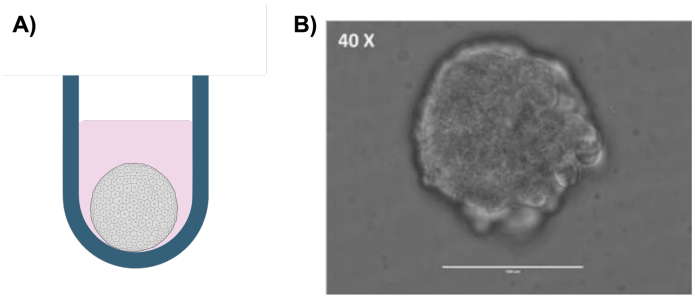

Figure 1.14. Spheroid culture (adapted from Kaushik et al. 2018). A) Diagram of a spheroid cultured in a round-bottom well. **B)** Representative image of H460 lung cancer cells growing as floating spheroids in serum-containing media. Scale bar: 100 μm.

1.5.2.2. Air-liquid interphase (ALI) cultures

Air-Liquid Interface (ALI) cultures are a specialized method for cultivating lung epithelial cells to maintain the structure of the airway epithelium. In this technique, the cells' upper surface is exposed to air, while the lower surface remains in contact with a liquid culture medium (Figure 1.15.). These cultures can consist of immortalized or primary cell lines, and co-cultures often utilise both (e.g. incorporating lung cancer-associated fibroblasts to airway epithelium A549 cultures (Horie et al. 2012)). ALI cultures are unique preclinical models that enable cells to be directly exposed to air. While this feature is essential for toxicology research and widely used in this field, it also holds significant potential for a comprehensive understanding of the relationship between NSCLC and other lung diseases such as COPD,

or the understanding of tumour initiation due to other risk factors like aerosol particles. However, these cultures are challenging to maintain and require specialized handling, and their long-term viability is limited (Berube et al. 2010; Baldassi et al. 2021).

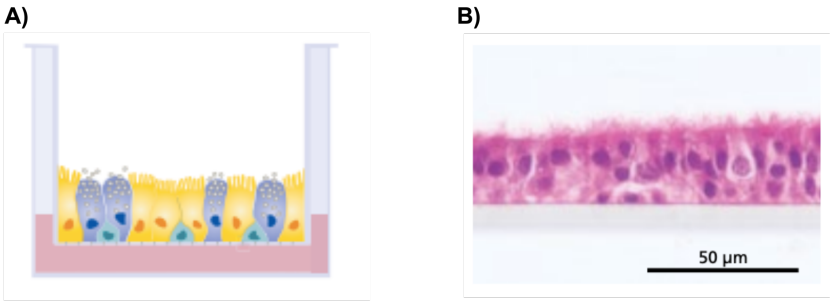

Figure 1.15. Air-Liquid Interface (ALI) culture. A) Diagram of air-liquid interface culture of bronchial epithelial cells using porous culture inserts. **B)** Haematoxylin and eosin staining of cells differentiated in the air-liquid interface in PneumaCult™-ALI that form a pseudostratified epithelium representative of the *in vivo* bronchial epithelium. Figure adapted from *https://www.stemcell.com/air-liquid-interface-culture-respiratory-research-lp.html* (STEMCELL™ Technologies).

1.5.2.3. Organ-on-a-chip cultures

Organ-on-a-chip culture systems are microfluidic platforms that mimic the structure and function of specific organs, allowing for in vitro investigation of physiological responses (Figure 1.16.). ALI cultures can be integrated into poly(dimethylsioloxane) (PDMS) microfluidic devices to construct human airway-on-a-chip cultures that contains microvascular endothelium that experiences fluid flow (Benam et al. 2016). These cultures are challenging to maintain and require specialized handling, and their long-term viability is limited. In addition, obtaining image-based data from organ-on-a-chip cultures represents a particular challenge due to their complexity. Organ-on-chips are a promising model for representing tissue-level heterogeneity *in vitro*, although more research is still needed to understand if such complicated models are strictly necessary for the recapitulation of tumour biology or if, perhaps, this can be already achieved with more simple models.

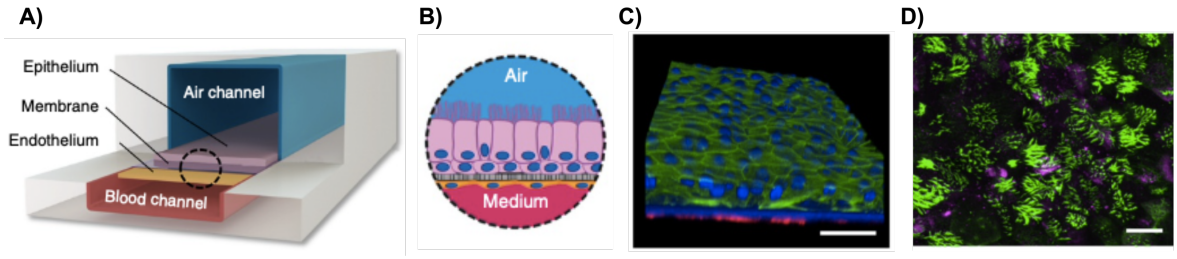

Figure 1.16. Lung organ-on-a-chip culture (adapted from Benam et al. 2016). A) Schematic diagram of a cross-section through the small airway-on-a-chip. The dashed circle highlights the area depicted in B. **B)** Diagram of the tissue-tissue interface that forms on-chip, showing differentiated airway epithelium (pink cells) cultured on top of a porous collagen-coated membrane at an air-liquid interface in the upper channel and the endothelium bellow (orange cells) with flowing medium that feeds both tissue layers. **C)** A 3D reconstruction showing fully differentiated, pseudostratified airway epithelium formed on ship by cultured hAECs (green, F-actin) with human pulmonary microvascular endothelial cells (red, F-actin) on the opposite side if the membrane. Blue denotes DAPI-stained nuclei; scale bar: 30 μm. **D)** Well-differentiated human airway epithelium formed on-chip using hAECs derived from healthy donors demonstrating the presence of high numbers of ciliated cells labelled for B-tubulin IV (green) and goblet cells stained with anti-MUC5AC (magenta). Figure and figure legend adapted from Benam et al. 2016.

1.5.2.4. Tissue explants

Tissue explants are a valuable *ex vivo* model that involves the removal of tissue from an organism and culturing it in a controlled environment. This approach maintains the tissue's architecture, cell-cell interactions, and extracellular matrix components while allowing the study of various physiological and pathological processes (Figure 1.17.). They are particularly useful for analysing the intrinsic sensitivity of the tissue/tumour 3D structure and functional studies, the immune system interaction and for penetration analysis. However, patient derived explants are in culture for a short period of time, usually up to 72 h, and the treatments are tested during this window. The conditions in culture can lead to necrosis that is not representative of the state of origin of the tissue. Therefore, effects on long-term response treatments, as radiotherapy, cannot be tested in this platform and other 3D alternatives need to be found (Powley et al. 2020; Stackhouse et al. 2021).

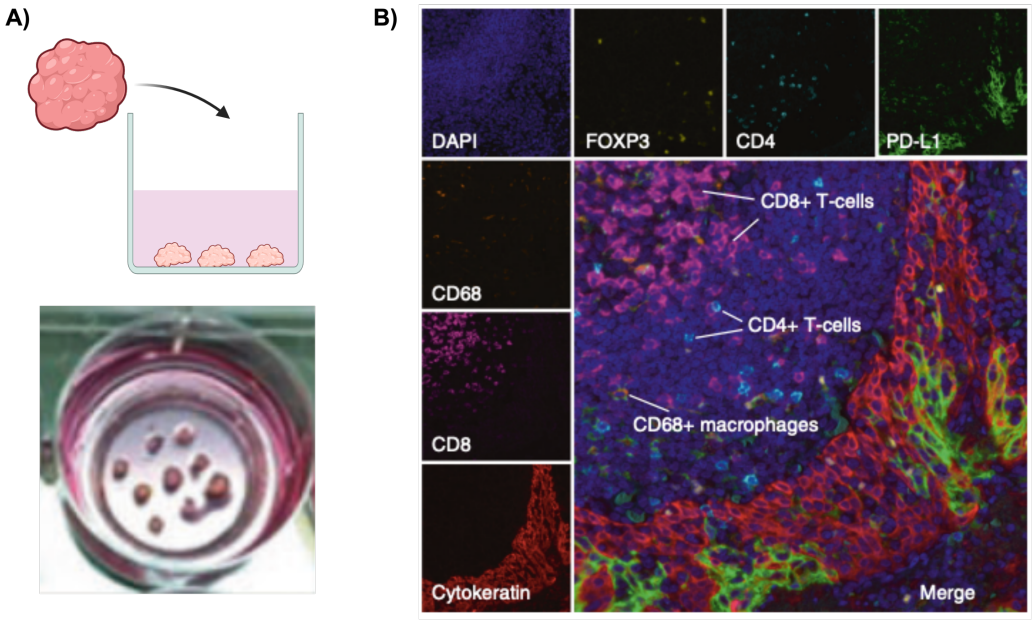

Figure 1.17. Tissue explant culture (adapted from Powley et al. 2020). A) Schematic diagram and picture of tissue explant culture, where a tumour is sectioned and cultured in a well as an explant. Diagram created in BioRender. **B)** A section of a tissue explant culture stained with DAPI as well as antibodies specific for immune cell markers (CD4, CD8, CD68 and FOXP3), PD-L1 and pan-cytokeratin followed by TSA-based fluorescent labelling is shown. This method allows for the characterisation of immune-cell subsets in the tumour microenvironment. Figure and figure legend adapted from Powley et al. 2020.

1.5.2.5. Organoids

Here 'organoids' are defined as primary tissue-derived, long-term 3D cultures that are continuously maintained in an ECM that allows the cells to self-organise into structures that mimic the tissues from which they are derived (Figure 1.18.). This applies to both normal and tumour tissues . The term 'organoid' was consistently used in connection with the long-term growth of culture in 3D pioneered by Prof. Clevers and his team with complex 'mini-organs', a 'mini-gut' organoid, derived from leucine-rich repeat-containing G-protein coupled receptor 5 positive ($Lgr5^{+}$) mouse small intestinal stem cells in 2009 (Sato et al. 2009) and the first human intestinal and human tumour organoids from colorectal cancer (CRC) in 2011 (Sato et al. 2011).

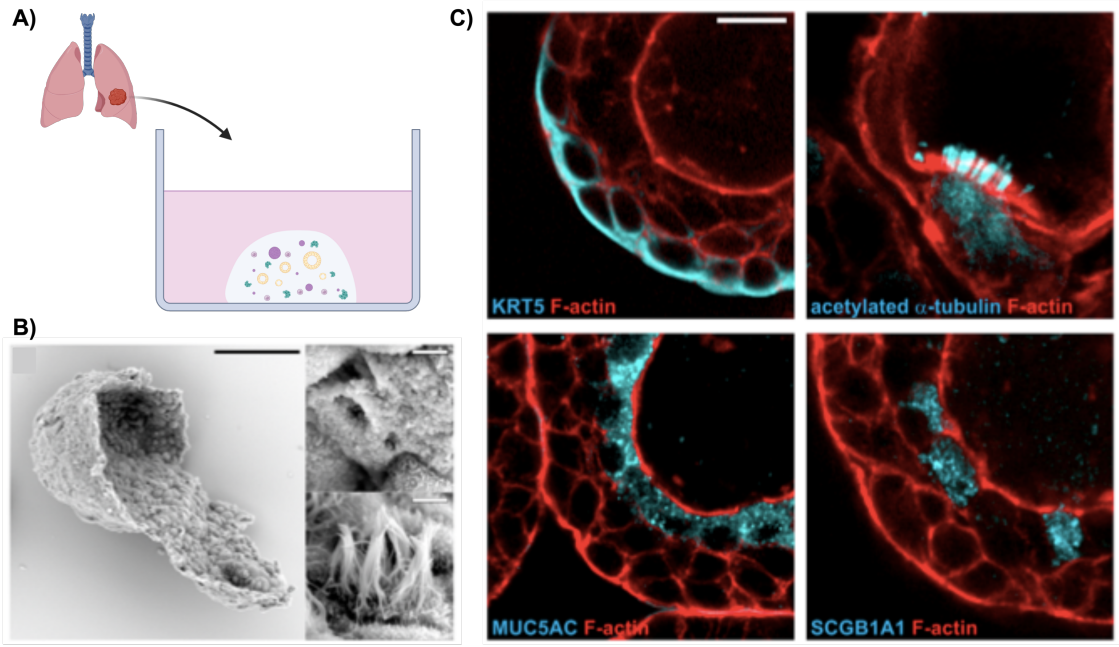

Figure 1.18. Organoid culture (adapted from Sachs et al. 2019). A) Schematic diagram of organoid cultures growth in Matrigel. Diagram created in BioRender. **B)** Scanning electron micrograph of a partially opened airway organoid visualising its 3D architecture, as well as basal and apical ultrastructure. Details display apical surfaces of secretory and multi-ciliated cells. Scale bars equal 50 μm (overview) and 2 μm (details). **C)** Immunofluorescent sections of airway organoids showing markers for basal cells (KRT5), cilia (acetylated a-tubulin), secretory cells (MUC5AC), and club cells (SCGB1A1). KRT5 is present exclusively in basally localized cells, while cilia, MUC5AC, and SCGB1A1 localise luminally. Counterstained is the actin cytoskeleton (red). Scale bar equals 10 μm. Figure and figure legend adapted from Sachs et al. 2019.

For the culture of human intestinal organoids, Sato et al. used as a base of **Advanced/DMEM F12** medium supplemented with penicillin/streptomycin **antibiotics**, **HEPES** buffer solution, glutamine supplements (**GlutaMAX**), **N2** and **B27 supplement** which increases cell survival rate, promotes the formation of tumour spheres, and prevents tumour sphere adhesion (Gu et al. 2011) and **N-Acetylcysteine**, a precursor of antioxidant glutathione (GSH) and, thus, protects the cells from reactive oxygen species (ROS) (Kerksick and Willoughby 2005). However, Clevers' innovative approach involved deciphering the critical signaling pathways (e.g. Wnt pathway) and growth factors essential for maintaining the stem cell population and tissue-specific differentiation within intestinal organoids. Therefore, in addition to the base medium a growth factor combination was added to create the human intestinal organoid medium: EGF, Noggin, R-spondin-1 (Rspo1), Wnt-3A, Gastrin, Nicotinamide, A83-01 and SB202190. Normal intestinal organoids need epidermal growth factor (**EGF**) to drive proliferation, as its removal leaded to smaller organoids due to G_1 cell cycle checkpoint arrest (Basak et al. 2017)). **Noggin** functions as a suppressor of bone morphogenic proteins (BMPs), which play a role in triggering cellular

differentiation by suppressing the transcriptional activity of Lgr5 and other genes associated with stemness (McMahon et al. 1998). The canonical Wnt/β-catenin pathway maintains stemness and promotes self-renewal of stem cells. Wnts initiate the pathway and R-spondins (as **Rspo1**) amplify it by binding to Lgr5 homologues. It has been demonstrated that **Wnt3** increases the efficiency of organoid formation. **Gastrin** has been used to promote proliferation (Colucci et al. 2005). **Nicotinamide** promotes cell survival and can facilitate human embryonic stem cell (hESC) differentiation through casein kinase 1 (CK1) inhibition (Meng et al. 2018). **A83-01** is a TGF-β/activin receptor-like kinase 5 (ALK5) and an antagonist of TGF-β signalling which inhibits proliferation as a defence against cancer growth. Therefore, A83-01 effectively prevents growth inhibition (Tojo et al. 2005). Finally, **SB202190** is a p38 mitogen-activated protein kinase (MAPK) inhibitor and protects cells form environmental stress induced apoptosis (Jiang et al. 1996). For cell sorting experiments, the team also added Y-27632. **Y-27632** is a ROCK inhibitor and, thus, is used to prevent apoptosis in culture. However, once single cells begin to grow, it can induce apoptosis by altering E-cadherin structure in hESCs and, therefore, it is only recommended to prevent anoikis during passaging in other organoids and its removal from culture medium is typical within 3 days form passaging (Koyanagi et al. 2008; Gao et al. 2019). Interestingly, the group discovered that CRC cells displayed a heterogeneous behaviour and some did not require the addition of growth factors, EGF, and/or A83-01 and/or SB202190 to the base medium to grow.

Building upon these principles, scientists adapted and tailored the medium composition to model multiple organs including normal and/or cancer brain, oesophagus, lung, breast, liver, stomach, kidney, pancreas, intestine, endometrium, cervix, prostate, and bladder organoids (Cala et al. 2023). The only long-term NSCLC organoids established at the beginning of my thesis studies were reported in 2019 by Sachs et al. (Sachs et al. 2019) at the Clevers laboratory. The medium that Sachs et al. created for the growth of normal airway and NSCLC organoids, contained all components of the original human intestinal organoid medium but N2, EGF, Wnt-3A and gastrin. However, Sachs et al. added fibroblast growth factor 7 and 10 (**FGF7** and **FGF10**) to the lung medium, which have been shown to induce organoid branching and promote differentiation towards distal lung lineages in lung epithelial stem/progenitor cells (LSPCs) (Rabata et al. 2020).

Unfortunately, Sachs et al. reported the rapid overgrowth of normal lung organoids in NSCLC organoid cultures. The authors suggested that the removal of a single component of

the medium (as in CRC organoids) could not selectively expand NSCLC organoids, due to the diversity of mutations in NSCLC (Chen et al. 2014; Jamal-Hanjani et al. 2017). Sachs et al. utilised Nutlin-3a to select for tumour organoids (success rate = 88 %, n=16). Nutlin-3a inhibits the interaction of MDM2 and p53, resulting in stabilisation and activation of p53, leading to apoptosis of wild-type normal cells. In contrast, p53 null tumour cells survive incubation with Nutlin-3a because of the lack of a functional p53 protein. TP53 is mutated in 46 % of LUADs and 91 % of LUSCs (Swanton and Govindan 2016). However, this technique for organoid-growth inevitably losses part of the NSCLC heterogeneity. They also established organoids from needle biopsies of metastatic NSCLC, technically circumventing the need for Nutlin-3a due to the absence of normal lung in this tissue of origin but the success rate is low (success rate = 28 %, n=18). At this point, better strategies for NSCLC organoid culture conditions might be needed to be able to implement this model efficiently (Sachs et al. 2019).

Nonetheless, organoids can mimic much of the 3D architecture and functionality of the organs from which they are derived, making them excellent models for studying disease mechanisms at cellular and molecular levels. In fact, H&E staining of original tumour tissue and the matched NSCLC organoid confirmed that the fundamental histological characteristics of the respective primary tumours were recapitulated in the NSCLC organoid-lines established by Sachs et al (Figure 1.19.). In addition, they also did whole genome sequencing (WGS) in some of the organoid lines and their tissue of origin revealing largely conserved mutation status further validating the models (Sachs et al. 2019).

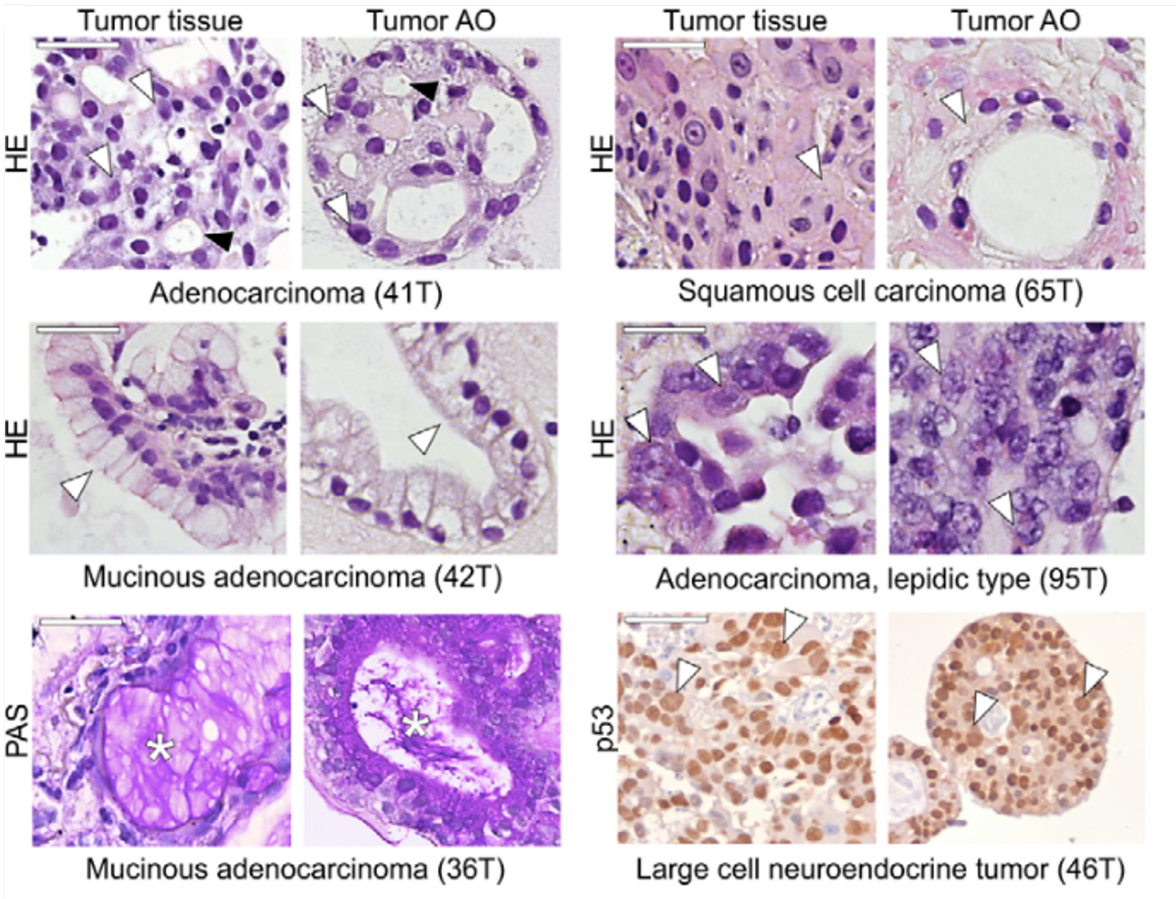

Figure 1.19. Original tumour vs. derived-organoid H&E staining (adapted from Sachs et al. 2019). Tumour airway organoids derived from different resected primary lung cancer types recapitulate their respective histopathological features. Examples include adenocarcinoma (41T, white arrowheads: multiple nucleoli, black arrowheads: tubule formation), mucinous adenocarcinoma (42T/36T, arrowheads: mucinous glands, stars: PAS-positive mucus), adenocarcinoma lepidic type (previously known as broncho-alveolar carcinoma, 95T, arrowheads: distinct large nuclei), squamous cell carcinoma (65T, arrowheads: multi-layered, keratinization), and large cell neuroendocrine tumour (46T, arrowheads: large nuclei, p53 immunolabeling). Scale bars equal 50 μm. Figure and figure legend adapted from Sachs et al. 2019.

By contrast with the organ-on-chip and ALI cultures, organoids can easily be adapted for use in high-throughput assays. In addition, techniques like the genome editing clustered regularly interspaced short palindromic repeats and CRISPR-associated protein 9 (CRIPSR-Cas9) can and have been applied to organoids to study the effects of specific genetic changes, providing insights into genetic diseases (Geurts and Clevers 2023; Lampart et al. 2023). Culturing organoids with other cell types, like pathogens, immune cells, etc. has also been tested to create a specific realistic microenvironment for certain studies (Heo et al. 2018; Hui et al. 2018; Puschhof et al. 2021; Yuan et al. 2022). Organoids have started to be used in disease modelling, personalized medicine, and drug discovery (Lancaster and Huch 2019; Nie et al. 2021). This also applied to NSCLC organoids, where Sachs et al. showed that a ERBB2 mutant line (52MET) was sensitive to both erlotinib and gefitinib (EGFR/ERBB2 inhibitors) and an ALK1 mutant line (65T) was sensitive to crizotinib (ALK/c-MET

inhibitor). Several other drug-response assays were also measured by the group, that they also showed how a TP53 mutant line (46T) was resistant to the p53-stabilising Nutlin-3a drug, the foundation for their selection method for NSCLC establishment from resection (Sachs et al. 2019). However, no radiation studies in lung cancer organoids have been reported, to our knowledge.

Overall, despite being simplified models and probably not fully recapitulating the complexity of whole organs in a living organism, organoids can help bridge the gap between *in vitro* cell cultures and *in vivo* animal models, aiding to understand human-specific aspects of organ development and heterogeneity, physiology, and disease.

1.5.3. *In vivo* mouse models

To bridge the gap between *in vitro* studies and clinical applications, *in vivo* mouse models remain an essential tool in scientific research. While *in vitro* studies provide controlled environments for studying isolated cellular processes, they may not accurately capture systemic effects and responses to therapies; even if some *in vitro* models are able to recapitulate complex tissue-level heterogeneity. Therefore, it is crucial to highlight the importance of developing systems that facilitate efficient analysis of various options *in vitro*, followed by assessment using genetically identical models *in vivo*.

Genetically Engineered Mouse Models (GEMMs) involve the manipulation of a mouse's genome to mimic specific genetic alterations found in human diseases (Kersten et al. 2017) and Cell Line-Derived Xenografts (CDXs) involve the transplantation of human tumour cell lines into immunocompromised mice (Day et al. 2015). Historically, both models have been employed to bridge the gap between findings on specific mechanisms in 2D immortalised cell lines and more realistic *in vivo* settings.

Patient-Derived Xenografts (PDXs) are created by implanting patient tumour cells directly into immunocompromised mice (Liu et al. 2023). These models have traditionally been used to translate discoveries in *in vitro* 2D primary cell cultures to *in vivo* environments. However, the development of organoids, together with the use of PDXs, has allowed for direct comparisons between *in vitro* and *in vivo* responses within the same tumour. This is achieved by using the same patient tumour tissue to create both PDXs and organoids simultaneously, resulting in a more accurate translational model. Additionally, implanting organoids into immunocompromised mice offers an opportunity to further investigate their response in an

in vivo setting and enhances the tumour growth potential compared to directly implanting patient cells (Wang et al. 2022a).

1.6. Hypothesis, aims and objectives

Cancer organoids from a range of tumours have demonstrated the ability to maintain the histological, genetical, cellular, spatial, and functional heterogeneity of their tumours of origin. In addition, they have been proven to faithfully represent clinical responses to several drug-treatments. Nevertheless, organoids are a relatively simple culture system, easy to maintain and can be adapted for high-throughput research. Their fidelity to the *in vivo* conditions of disease, positions organoids as a pivotal tool in characterising and addressing the multifaceted challenges posed by tumour heterogeneity in therapeutic contexts. At the start of this project only one description of the use of long-term organoids to study NSCLC had been published (Sachs et al. 2019). This method was suboptimal based on its tendency to allow overgrowth of normal lung tissue and the need to select for tumour cells using drug selection which led to a selective focus on only p53 negative NSCLC cultures. To our knowledge, very little work on organoid responses to radiation had been described (Hubert et al. 2016) and none on organoid responses to radiation / drug combinations, that exploit tumour vulnerabilities to combinations of radiation and DNA damage response inhibitors (DDRis). At the time this work was started, no studies had described analyses of NSCLC organoid responses to radiation.

We hypothesise that NSCLC organoids will serve as a valuable model for investigating the effects of radiation and radiation-drug combination therapies for NSCLC. The principal aim of this project was to characterise the response of NSCLC organoids to radiation and DNA Damage Response inhibitor combination therapies with a particular focus on inter-cellular differences in responses between cells within organoid cultures.

The first objective was to establish relevant radiation-response 3D assay formats. A subgoal of this work was to determine the differences between true organoids (never grown on plastic) and cellular aggregates that are grown in 3D but are derived from the transfer of 2D plastic-adapted cell lines into 3D culture in the presence of Matrigel, comparing several readouts (e.g. ATP viability levels, image-based techniques) (Chapter 3).

The second objective was to develop a NSCLC organoid biobank as a resource for subsequent organoid studies (Chapter 4).

The third objective was to assess the sensitivity of a variety of NSCLC organoids to irradiation and DDRi combinations, utilising the assays developed in the first objective. This included an analysis of the intra-organoid cellular heterogeneity in responses to irradiation (Chapter 5).

2. Materials and Methods

2.1. Tissue culture: cell lines

2.1.1. Cell lines

Cell lines with differential TP53 and ATM status were selected for this work, due to their potential synthetic lethality with DNA Damage Repair inhibitors (DDRi) and radiation (*Table 2.1*).

Table 2.1. Cell lines used in this project.

Cell line	NSCLC subtype	TP53 status	ATM status	Routine culture medium
A427 [1]	LUAD	WT	WT	ATCC recommended medium*
A549 [2]	LUAD	WT	c.4236+174A>C homozygous	ATCC recommended medium*
Calu-3 [3]	LUAD	Homozygous substitution - missense	WT	ATCC recommended medium*
NCI-H520 [3]	LUSC	Homozygous substitution - nonsense	c.1147C>G heterozygous	ATCC recommended medium*
NCI-H1299 *shATM* [4]	Not clear NSCLC	Homozygous deletion	shATM (clone #11)	Anika Weber medium†
NCI-H1299 *shGFP* [4]	Not clear NSCLC	Homozygous deletion	shGFP (clone #2)	Anika Weber medium†
COR-L105 *shATM* [4]	LUAD	WT	shATM (clone #5)	Anika Weber medium†
COR-L105 *shGFP* [4]	LUAD	WT	shGFP (clone #2)	Anika Weber medium†

Provided by 1. Prof. Trevor Dale laboratory - authenticated by STR profiling with the services of the ECACC; 2. Kindly provided by Dr. Alan Parker, School of Medicine, Cardiff University, Wales, UK - authenticated by STR profiling with the services of the ECACC; 3. Purchased from ATCC; 4. Kindly provided by Prof. Anderson Ryan laboratory, Department of Oncology, Cancer Research UK and Medical Research Council Oxford Institute for Radiation Oncology, University of Oxford, Oxford, UK. *: Specifics on Table 2.2. †: Specifics on Table 2.3. LUAD: Lung Adenocarcinoma. LUSC: Lung Squamous Cell Carcinoma. NSCLC: Non-Small Cell Lung Cancer. WT: Wild-Type.

2.1.2. Routine cell line maintenance in 2D and seeding for experiment

Cells were routinely cultured in the medium shown for each line in Table 2.2 and Table 2.3. Medium was changed every 2-3 days and lines were passaged when the cell confluence reached 70 - 85 %. For a routine passage to single-cells, growth medium was removed from the culture and cell lines were washed with prewarmed PBS (37 ^{O}C in a water bath). 0.05 % trypsin-EDTA solution was added, ensured that it washed all the cell surface and aspirated; followed by an incubation of the cells at 37 ^{O}C for approximately 7 minutes, to aid disaggregation. Complete growth medium was used to saturate the trypsin and stop the reaction. After centrifugation at 200g for 5 minutes, cells were resuspended at the densities

specified in the papers / protocols describing each cell line and in the medium specified. Cells were seeded in T-75 flasks and maintained in an incubator at 37 ^{O}C with 5 % CO_2. NCI-H1299 shGFP/shATM and COR-L105 shGFP/shATM lines were routinely cultured with 0.5 μg/mL puromycin to maintain selection of the transfected constructs within the cultures. 24 h prior to any experiment, the selection medium was removed and replaced with puromycin-free medium.

When seeding for experiments, live cells were counted in suspension prior to seeding, using Trypan Blue with Ultra-low Fluorescence Counting Slides and a Dual Fluorescence Cell Counter to count the cells and to measure viability as specified by the manufacturer (Luna, Labtech).

Table 2.2. Routine ATCC recommended culture medium for 2D cell lines.

Cell line	Media component	Final concentration	Supplier	Catalogue number
A427 and *Calu-3*	MEM	1x	Gibco	11095-080
	FBS	10 %	Gibco	10500-064
	Penicillin /Streptomycin	1x	Gibco	15070-063
	HEPES	10 mM	Invitrogen	15630-056
	Sodium pyruvate	1x	Invitrogen	11360-070
	NEAA	1x	Invitrogen	11140-035
NCI-H520	RPMI-1640	1x	PAN-Biotech	P04-18500
	FBS	10 %	Gibco	10500-064
	Penicillin /Streptomycin	1x	Gibco	15070-063
	HEPES	10 mM	Invitrogen	15630-056
	Sodium pyruvate	1x	Invitrogen	11360-070
A549	RPMI-1640	1x	PAN-Biotech	P04-18500
	FBS	10 %	Gibco	10500-064
	Penicillin /Streptomycin	1x	Gibco	15070-063
	HEPES	10 mM	Invitrogen	15630-056

Table 2.3. Routine Anika Weber culture medium for 2D cell lines from Prof. Ryan laboratory (Weber et al. 2015). These lines were also routinely cultured with 0.5 mg/mL puromycin for continuous selection of clones. 24 h prior to any experiments, the selection medium was removed and replaced with puromycin-free medium.

Cell line	Media component	Final concentration	Supplier	Catalogue number
NCI-H1299 shGFP *NCI-H1299 shATM* *COR-L105 shGFP* COR-L105 shATM	Advanced DMEM/F12	1x	Invitrogen	12634-010
	FBS	10 %	Gibco	10500-064
	Penicillin /Streptomycin	50 U / 50 μg/mL	Gibco	15070-063
	GlutaMax 100x	2 mM	Invitrogen	12634-034

2.1.3. Routine mycoplasma testing in 2D cell line cultures

To monitor for mycoplasma contamination, biochemical tests were performed on the ongoing cells culture medium using a MycoAlert PLUS Mycoplasma Detection Kit (Lonza). Briefly, the cell culture supernatant was incubated for 5 minutes with a reagent that lysed the mycoplasma cells allowing the enzymes to react with the MycoAlert PLUS substrate, catalysing the conversion of ADP to ATP. Luminescence was measured with a FLUOstar OPTIMA (BMG LABTECH) before and after (10 minutes incubation time) the addition of the substrate, creating a ratio. The kit provided a positive control and the complete medium was used as a negative control.

2.1.4. Cryopreservation and thawing of 2D cells

To freeze down cell lines, the same procedure as for a general passage was used to lift the cells from the maintenance flask (2.1.2) but, after resuspension at $1 \cdot 10^6$ cells/mL cells in 1ml of sterile ice-cold freezing medium (10 % DMSO and 50 % FBS in complete growth medium), the cryovials were placed into freezer containers at -80 ^{O}C for 24 h and then stored in liquid nitrogen long-term.

Cells from liquid nitrogen stocks were thawed rapidly in a water bath at 37 ^{O}C. The cell suspension was diluted in 9 mL of prewarmed (37 ^{O}C) complete growth medium, and cells were pelleted to remove the DMSO at 200g for 5 minutes. The supernatant was then discarded, and the cell pellet was resuspended in complete growth medium in T-75 flasks for culture.

2.1.5. Generation of 3D cultures from NSCLC 2D cell lines

2.1.5.1. Generation of 3D cultures from cell lines in Matrigel: CellAggs

For generation of 3D CellAggs, cells were lifted from the culture flasks according to the methods used for routine passage (section 2.1.2). Cells were then transported to 50 mL tubes and pelleted at 200g for 5 min, resuspended in complete growth medium and trypan blue-excluding life cells were counted. Selected seeding concentration was calculated (number of cells / mL Matrigel) and cells were concentrated by centrifugation (200g, 5 min). The pellet was resuspended in the appropriate amount of Matrigel and blobs of Matrigel-cells suspensions were seeded on the centre of pre-warmed (37 ^{O}C, 15 min) tissue-culture treated plates. Plates were turned upside down and blobs were left to solidify in an incubator at 37 ^{O}C for 20 minutes, to reduce cell attachment to the bottom of the plate. Afterwards, the appropriate culture medium (Table 2.2., Table 2.3. or Table 2.6.) was added to cover the

blobs and plates were transferred to humidified 37^{O}C / 5 % CO_2 incubators. Medium was changed every 2 – 3 days. 10 µL of Matrigel were used to generate blobs in 96 well plate format and 50 µL for 24 well plates.

2.1.5.2. Generation of 3D cultures from cell lines in Matrigel in a 'sandwich'

To allow imaging of CellAggs in ECM within a single z-plane as part of the investigation of cell culture-dynamics (section 2.6.3.2), 96 well plates were setup using a sandwich technique (see Figure 2.1. for a diagram of the 'sandwich culture'). Cells were prepared as above (2.1.5.1) until the seeding cell concentration counting step. Wells were then coated with 30 µl of Matrigel, let dry for 30 minutes at 37 ^{O}C and 100 µl of the cell suspension in culture medium, at a density that would have generated the equivalent mean volumetric cell density as for the Matrigel blobs, was seeded on top of the first cell-free Matrigel layer. The plate was returned to the incubator for 30 minutes to allow the cells to set on the Matrigel layer. After carefully removing the growth medium above the Matrigel, another layer of 20 µl of Matrigel was added on top of the first and the (cell) sandwich was allowed to dry for 20 minutes inside the incubator. Subsequently, 70 µl of growth medium was added, and the plate was placed in the IncuCyte®S3 37^{O}C / 5 % CO_2 incubator. When the first medium-change was due, no medium was removed in the *sandwich* approach, but 50 µl of new medium was added. For the subsequent medium changes 50 µL / well was carefully removed and replenished with the same quantity of fresh medium every 1-2 days.

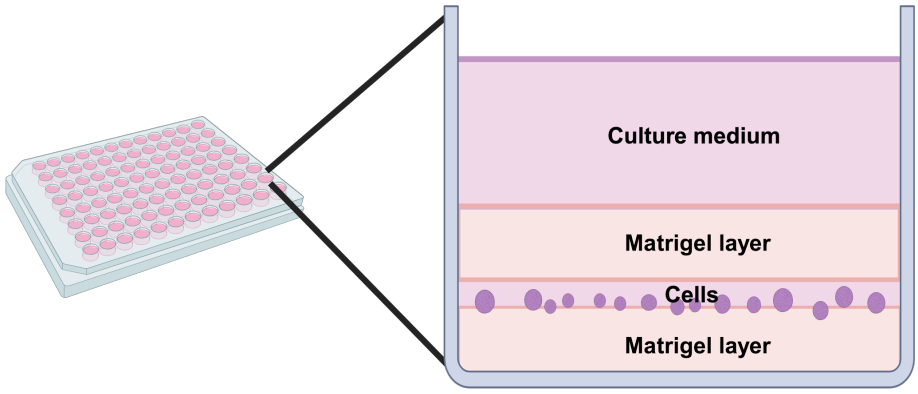

Figure 2.1. Diagram of the 'sandwich technique culture'. Final layout of the sandwich technique for seeding cells in 3D in-between two layers of Matrigel ECM topped with culture medium in a 96-well plate well. Diagram created in BioRender.

2.1.5.3. Generation of spheroids without an ECM

To generate 3D spheroids in suspension the cell disaggregation methods described above (section 2.1.2) were followed up until the point of single cell counting. However, to generate spheroids, cells were resuspended according to the numbers described in results and 150 µL of the cell suspension in complete medium was directly added into either Costar round-bottom low-adherence 96 well plates (TehermoFisher Scientific) or coated (to modify the plate surface to cell and protein repellent) faCellitate 96 well plates (BIOFLOAT^{TM}, F202003). Medium was changed by removing 100 µL of the culture medium carefully and replenishing it with the same volume every 2-3 days.

2.2. Tissue culture: organoids

2.2.1. Tissue and organoid origin

2.2.1.1. UHW patient tissue

Ethical approval for the collection and use of NSCLC and adjacent normal tissue was held by the Wales Cancer Bank (WCB). The Wales Cancer Bank had been licensed by the Human Tissue Authority to store human tissue for research under the UK Human Tissue Act (2004) (research licence 12107). WCB is accredited as a Research Tissue Bank by the Wales Research Ethics Committee (REC) 3 and operated under ISO20387:2018 Biotechnology-Biobanking-General Requirements for Biobanking. The approval allows for the release of anonymised samples to researchers conducting cancer-related activities upon successful approval of the application by the WCB External Review panel (Parry-Jones and Spary 2018).

Informed consent for collection of clinical specimens from NSCLC patients undergoing surgical resection at the UHW and specimen collection was performed by research nurses and WCB staff. Tissue sampling and histological assessment was performed by an NHS histopathologist, and anonymised relevant clinical information was obtained from the WCB. After surgical resection, a tumour and surrounding healthy sample-pair from each patient was stored and transported at 4°C in transport medium (Table 2.4.) and processed and cultured at Cardiff University immediately after sampling (within ~2h). All patient material samples were assigned a number (ISO*X*: Isolation*X*) for our records and were traceable to a WCB ID number. All human-waste generated during the isolation process was disposed of in accordance with HTA regulations.

Table 2.4. Transport medium for NSCLC tissue samples.

Media component	Final concentration	Supplier	Catalogue number
Hibernate-A medium	1x	Invitrogen	A1247501
Penicillin /Streptomycin	50 U / 50 μg/mL	Gibco	15070-063

2.2.1.2. Champions PDX tissue

An MTA/Collaboration agreement was signed between Champions Oncology and Cardiff University, drafted in accordance with the Technology Transfer Team in Research and Innovation (CU) for the use of the specific PDX-derived NSCLC tissues (Table 4.4., Chapter 4) to be used for organoid-lines set up for this project. The PDX tumours were grown by Transcure Bioservices in France and the tissue was shipped to Cardiff University in tissue transport medium (Table 2.4.) at 4ºC with a 24 h-delivery service. Some of the samples were also shipped cryopreserved when they couldn't be shipped live due to Covid restrictions. Live tumour samples were processed and cultured at Cardiff University immediately upon arrival.

2.2.1.3. Tsao laboratory Organoids (Shi et al. 2020)

A collaboration between the Dale and the Tsao Groups was established to obtain NSCLC organoids that had previously being established and characterised (Shi et al. 2020). An MTA/Collaboration agreement was signed between the Princess Margaret Living Biobank (UHN) and Cardiff University, drafted in accordance with the Technology Transfer Team in Research and Innovation (CU) for the use of the specific NSCLC organoids (Chapter 4 - Table 4.6) by the Dale group for radiation experiments for this project. Organoids were shipped in cryovials with Recovery Cell Culture Medium (Gibco, 12648010) on dry ice.

2.2.2. Organoid setup and establishment

UHW Patient-derived tissue was processed following the protocol described by Sachs *et al.*, 2019. Briefly, normal and tumour tissue pieces were first photographed for future reference to possible organoid-phenotypical relationship with tissue of origin. The tissue was then minced, washed with $AdDF^{+++}$ (Table 2.5) and digested in final culture medium: AO medium (Table 2.6) containing 1-2 mg/ml collagenase from Clostridium histolyticum (Sigma, C9407) on an orbital shaker (Kuhner ISF-1-W, set to 180 rpm) at 37^{O}C with continuous monitoring for 1-3 h until a cloudy suspension was obtained. The digested tissue suspension was sequentially mixed and sheared using 10-, 5- and 1-ml pipettes; straining the suspension after each shearing step over a 100 μm filter, which retained tissue pieces

entering a subsequent shearing step with AdDF^{+++} (Table 2.5). 2% FBS was added to the strained suspension before two rounds of centrifugation at 400g for 5 minutes and resuspension. When pellets were visibly red in colour (Iso2 and Iso3), erythrocytes were lysed using 2 ml of red blood cell lysis buffer (Sigma) for 5 min at room temperature before the addition of AdDF^{+++} medium and centrifugation at 400g for 5 minutes. Following the optional red cell lysis, the cell pellets were resuspended in AdDF^{+++} medium supplemented with 10 % FBS and the suspension was incubated for 30 minutes in contact with tissue-culture treated dishes to deplete any free fibroblasts by differential adhesion (with respect to the epithelial cells). After the 30 minutes, the unattached cell suspension was collected and centrifugated at 400g for 5 minutes. The pellet was resuspended in the appropriate amount of Matrigel (high confluency at the beginning; see Results) and 50 µl blobs were allowed to solidify on pre-warmed upside-down 24-well plates at 37^{O}C for ~20 min. Subsequently, ~500 µl of final complete medium (AO medium for UHW samples) was added to each well and plates were transferred to humidified 37^{O}C/5 % CO_2 incubators.

For PDX-derived tissue processing, apart from the procedure described above, an extra step was added, after the 'fibroblast attachment step', for mouse cell removal using a Mouse cell depletion kit (Miltenyi Biotec, 130-104-694), LS columns (Miltenyi Biotec, 130-042-4010 and MidiMACS separator (Miltenyi Biotec, 130-041-302). Briefly, 80 µl mouse depletion kit buffer and 20 µl mouse cell depletion cocktail per 2×10^6 tumour cells were added to the cell suspension and incubated for 15 minutes at 4 ^{O}C. Afterwards, 400 µl mouse depletion kit buffer per 2×10^6 tumour cells was added. Them the LS column was put in the MidiMACS magnetic separator and prepared by rinsing the column with 3 ml of mouse depletion kit buffer. The cell suspension was then added to the column and the flow through, containing the human cells, was collected. The column was rinsed twice with 1 mL of mouse depletion kit buffer. The human cell suspension was then centrifuged at 400g for 5 minutes and the pellet was resuspended in Matrigel and cultured as described above in final complete medium. However, PDX-derived samples were either cultured in Sachs medium (Table 2.6), in Sachs medium supplemented with 5 µM of Nutlin-3A (Cayman Chemicals, 1004372) or in Kim medium (Table 2.7) as indicated in the Results.

A line was considered to be established when continuous growth and multiple passages had been undertaken. For rapidly expanding lines, the time in culture was a regarded as a minimum of one month and for slower growing lines, a minimal passage number 10 was

regarded as sufficient based on previously published studies (Shi et al. 2020). Established lines also had to be robust to freezing and recovery.

Table 2.5. Tissue-processing based medium: AdDF^{+++} medium.

Media component	Final concentration	Supplier	Catalogue number
Advanced DMEM/F12	1x	Invitrogen	12634-010
GlutaMax 100x	1x	Invitrogen	12634-034
HEPES	10 mM	Invitrogen	15630-056
Penicillin /Streptomycin	50 U / 50 mg/mL	Gibco	15070-063
Primocin	50 $\mu g \cdot mL^{-1}$	Invivogen	Ant-pm-1

Table 2.6. AO medium (or Sachs medium): Airway organoid medium (Sachs et al. 2019). *Function related to cell survival. †Function related to stem cell maintenance/promotion. ‡Function related to cell differentiation.

Media component	Main function	Final concentration	Supplier	Catalogue number
R-spondin 1	†Promotes stemness (Amplifies Wnt / B-Catenin pathway)	500 $ng \cdot mL^{-1}$	Peprotech	120-38
FGF 7	‡Promotes differentiation of lung SC towards distal lineages inducing branching	25 $ng \cdot mL^{-1}$	Peprotech	100-19
FGF 10	‡Promotes differentiation of lung SC towards distal lineages inducing branching	100 $ng \cdot mL^{-1}$	Peprotech	100-26
Noggin	†Maintains stemness (Inhibitor of BMPs)	100 $ng \cdot mL^{-1}$	Peprotech	120-10C
A83-01	*Prevents growth inhibition (TGF-B / ALK5 inhibitor)	500 nM	Tocris	2939
Y-27632	*Protects cells from anoikis (Rock inhibitor)	5 μM	Abmole	M1718
SB202190	*Protects cells from environmental stress induced	1 μM	Sigma	S7067

*Table continues in the next page

	apoptosis (MAPK inhibitor)			
B27 supplement	*Increase cell survival	1x	Gibco	17504-044
N-Acetylcysteine	*Cyto-protector during oxidative and electrophilic stress (Precursor of antioxidant GSH)	1.25 mM	Sigma	A9165-5G
Nicotinamide	‡Promotes cell differentiation	5 mM	Sigma	N0636
GlutaMax 100x	Energy source, protein and nucleic acids synthesis, removing ammonia excess	1x	Invitrogen	12634-034
HEPES	Buffer	10 mM	Invitrogen	15630-056
Penicillin / Streptomycin	Antibiotics	100 $U{\cdot}mL^{-1}$ / 100 $\mu g{\cdot}mL^{-1}$	Gibco	15140-122
Primocin	Antifungal	50 $\mu g{\cdot}mL^{-1}$	Invivogen	Ant-pm-1
Advanced DMEM / F12	Base medium	1x	Invitrogen	12634-010

Table 2.7. Kim medium for organoid culture (Kim et al. 2019). *Function related to cell survival. †Function related to stem cell maintenance/promotion. ‡Function related to cell differentiation.

Media component	Main function	Final concentration	Supplier	Catalogue number
bFGF	†Maintains stemness	20 $ng{\cdot}mL^{-1}$	Thermo Fisher	13256029
EGF	*Drives proliferation	50 $ng{\cdot}mL^{-1}$	Peprotech	AF-100-15
Y-27632	*Protects cells from anoikis (Rock inhibitor)	10 μM	Abmole	M1718
B27 supplement	*Increase cell survival	1x	Gibco	17504-044
N2 supplement	‡Induces cell differentiation	1x	Gibco	17502048
HEPES	Buffer	10 mM	Invitrogen	15630-056
Penicillin / Streptomycin	Antibiotics	100 $U{\cdot}mL^{-1}$ / 100 $\mu g{\cdot}mL^{-1}$	Gibco	15140-122
Primocin	Antifungal	50 $\mu g{\cdot}mL^{-1}$	Invivogen	Ant-pm-1
DMEM / F12	Base medium	1x	Lonza	BE04687F/U1

2.2.3. Routine organoid-line maintenance in 3D and seeding for experiments

Medium was changed every 2-3 days. 7 days post-isolation an initial passage was performed, independent of any evidence of proliferation, in order to remove dying or dead cells that were present in the Matrigel suspensions. From this point, organoids were passaged every 12 days, or when several of the 'organoid' structures grew bigger than 200 μm, allowing dark cores to be observed in the larger organoids or when single cells appeared to be delaminating from larger structures. The typical split ratio was 1:4 every 10-14 days, but this was line dependent. Using the typical split ratio as a guide, the current split ratio and number of wells to seed were empirically calculated based on culture density, growth, and medium colour (indicative of metabolic activity) for each passage. In addition, a decision was made in each passage to freeze some of the material if sufficient was available.

For general passage of the organoid-lines, all tubes and pipette tips used for cell culture were pre-wet in ice-cold PBS / 10 % FBS to ensure minimal plastic-adhesion -induced sample-loss. Growth medium was removed from culture, 1 mL of TrypLE Express (Gibco, 12604013) was added and Matrigel was disrupted with a pipette. The plate was then incubated in a 37^{O}C incubator for 10-30 minutes and the suspension was mixed every 10 minutes and monitored under the microscope to observe cell dissociation within the organoids. When the majority of the culture were in single cells or 3-4 cells clumps, TrypLE was inactivated by transferring the cell suspension to a cell culture tube containing ice-cold AdDF^{+++} medium. All subsequent work was carried out at 4 ^{O}C. To remove the Matrigel, the suspension was centrifuged at 400g for 5 minutes at for the UHW and Champions organoids, and at 250g for 5 minutes at for the Tsao laboratory organoids. After discarding the supernatant, the pellet was resuspended in the appropriate amount of Matrigel (see Results) and 50 μl blobs were allowed to solidify on pre-warmed upside-down 24-well plates at 37^{O}C / 5 % CO_2 incubator for ~20 min. Afterwards, 500 μl of the corresponding complete organoid medium was added to each well and plates were transferred to humidified 37^{O}C / 5 % CO_2 incubators. Complete organoid media were Sachs or Kim medium for UHW and Champions origin organoids (Table 2.6. and Table 2.7.), and Shi medium for the Tsao laboratory organoids (Table 2.8).

Table 2.8. M26 or Shi medium for organoid culture from the Tsao laboratory (Shi et al. 2020). *Function related to cell survival. †Function related to stem cell maintenance/promotion. ‡Function related to cell differentiation.

Media component	Main function	Final concentration	Supplier	Catalogue number
CHIR 99021	†Maintains stemness (GSK-3 inhibitor, activated Wnt signalling)	250 nM	Tocris	4423
FGF 4	†Maintains stemness	100 ng·mL^{-1}	Peprotech	100-31
FGF 10	‡Promotes differentiation of lung SC towards distal lineages inducing branching	100 ng·mL^{-1}	Peprotech	100-26
Noggin	†Maintains stemness (Inhibitor of BMPs)	100 ng·mL^{-1}	Peprotech	120-10C
EGF	*Drives proliferation	50 ng·mL^{-1}	Peprotech	AF-100-15
A83-01	*Prevents growth inhibition (TGF-B / ALK5 inhibitor)	500 nM	Tocris	2939
Y-27632	*Protects cells from anoikis (Rock inhibitor)	1 μM	Abmole	M1718
SAG	‡Induces differentiation (Activated Hh signalling)	100 nM	Enzo	ALX-270-426-M001
B27 supplement	*Increase cell survival	1x	Gibco	17504-044
N-Acetylcysteine	*Cyto-protector during oxidative and electrophilic stress (Precursor of antioxidant GSH)	1.25 mM	Sigma	A9165-5G
GlutaMax 100x	Energy source, protein and nucleic acids synthesis, removing ammonia excess	1x	Invitrogen	12634-034
HEPES	Buffer	10 mM	Invitrogen	15630-056
Penicillin / Streptomycin	Antibiotics	100 U·mL^{-1} / 100 μg·mL^{-1}	Gibco	15140-122

*Table continues in the next page

Advanced DMEM / F12	Base medium	1x	Invitrogen	12634-010

When seeding for experiments, the recovered, disaggregated cell pellet was resuspended in AdDF^{+++} medium, live cells were counted and the proportion of single cells determined by Trypan Blue staining as described above. Then, total number of cells per seeding concentration was calculated and the equivalent volume was transferred to an ice-cold eppendorf. After centrifugation at 400g for 5 minutes at 4 ^{O}C for the UHW and Champions organoids, and at 250g for 5 minutes at 4 ^{O}C for the Tsao laboratory organoids; cells were resuspended in ice-cold Matrigel and seeded in appropriate plates and blob volumes depending on the experiment, as indicated in the Results.
For routine mycoplasma testing in 3D organoid cultures, the same procedures as for 2D cell lines was employed using, as the analysis was done in the culture medium.

2.2.4. Cryopreservation and thawing of organoids

All tubes and pipette tips used for cell culture were pre-wet in ice-cold PBS / 10 % FBS to ensure minimal sample-loss.

To freeze down organoids, the culture medium was removed from each well and replaced with 0.5 ml ice-cold AdDF^{+++} medium per well. The Matrigel was manually disrupted and resuspended in ice-cold tubes with AdDF^{+++} medium. This step was then repeated, and the suspension was centrifuged at 400g for 5 minutes at 4 ^{O}C for the UHW and Champions organoids, and at 250g for 5 minutes at 4 ^{O}C for the Tsao laboratory organoids. After discarding the supernatant, the pellet was resuspended in 1 mL of Recovery^{TM} Cell Culture Freezing Medium (Gibco, 12648010). The suspension was then quickly transferred to a cryovial, and these were placed into freezer containers at -80^{O}C for 24 h and stored in liquid nitrogen long-term.

Organoids from liquid nitrogen stocks were thawed rapidly in a water bath at 37 ^{O}C. The organoid suspension was diluted in 9 mL of AdDF^{+++} medium and cells were pelleted to remove the DMSO at 400g for 5 minutes at 4 ^{O}C for the UHW and Champions organoids, and at 250g for 5 minutes at 4 ^{O}C for the Tsao laboratory organoids. The supernatant was then discarded, and the organoid pellet was placed on ice and resuspended in the appropriate amount of ice-cold liquid Matrigel. Fifty µl blobs of the suspension were allowed to solidify

on pre-warmed upside-down 24-well plates at 37^{O}C / 5 % CO_2 incubator for ~20 min. Afterwards, 500 ml of the corresponding complete organoid medium was added to each well and plates were transferred to humidified 37^{O}C / 5 % CO_2 incubators. Complete organoid media were Sachs or Kim medium for UHW and Champions origin organoids (Table 2.6. and Table 2.7.), and Shi medium for the Tsao laboratory organoids (Table 2.8).

2.3. Genotyping for human NSCLC nature of established organoids

2.3.1. DNA extraction

For DNA extraction from organoids to subsequent genotyping PCR or NSCLC panel of genes target sequencing; medium culture was aspirated, organoids were washed with ice cold PBS and Matrigel was scraped and disrupted by manual trituration. Organoids were spun down at 400g for 5 mins, the supernatant was aspirated, and the pellet was resuspended in 80 µl PBS and transferred to a 1.5 mL tube. Subsequently, DNA was extracted with the QIAamp DNA Mini Kit from Qiagen using manufacturer's instructions. Briefly, ATL buffer, which contains a detergent, was added to lyse the cells and release the DNA into solution. This was then incubated with proteinase K for 1-3 h at 56 ^{O}C and the AL buffer was added, mixed by pulse vortexing and incubated for 10 minutes at 70 ^{O}C. Then, the lysate was mixed with ethanol to facilitate DNA binding to the QIAamp mini column, followed by a series of purification steps involving incubation with various buffers in the mini spin column, as instructed by the manufacturer. These steps effectively removed contaminants such as proteins and cellular debris through centrifugation processes, ensuring the purity of the isolated DNA. The purified DNA was then eluted from the QIAamp mini column by incubation with distilled water at room temperature and subsequent centrifugation at 6000g for 1 minute. Finally, the purified DNA quantity and quality was assessed using 1 µl of the sample on a NanoDrop (Labtech, ND-1000) and stored at -80^{O}C for long-term storage until its use.

2.3.2. Genotyping PCR reaction and Gel electrophoresis for visualisation of PCR products

2.3.2.1. Primer design and primer test

PCR primers for human and mouse ACTB were designed using the online primer design tool from NCBI (https://www.ncbi.nlm.nih.gov/nuccore) choosing a PCR product size of 200-1000 bp. The two primer pairs with the lowest self-complementarity were selected per species for *in silico* and *in vitro* further primer testing.

An *in silico* PCR was run per primer pair with the Genome Browser tool (https://genome.ucsc.edu) obtaining the expected product length and Tm (specified in Table 2.9.). All four primer pairs were ordered from ThermoFisher Scientific and diluted with nuclease free water to 100 µM stock. Genotyping was carried out as specified in the next section for all the primer pairs with known human and known mouse samples (positive controls) to (1) determine the specificity of the primers and (2) determine the best annealing temperature per primer pair. In the primer test, different PCRs with different annealing temperatures - 54 ^{O}C, 56 ^{O}C, 58 ^{O}C, 60 ^{O}C and 62 ^{O}C – were run and visualised by gel electrophoresis. The primer pair per species and annealing temperature chosen for genotyping after the test is indicated in Table 2.11.

Table 2.9. PCR ACTB primer pairs designed for *in vitro* testing.

Primer name	Primer sequence	Species	Expected product length (bp)	Predicted *in silico* Tm (^{O}C)
PP4 - Forward	TCGATGGGGTACTTCAGGGT	Human	478	59.96 - 61.7
PP4 - Reverse	GGCTTCCTTTCTCCCCAATCT	Human		60.27 - 63.7
PP7 h - Forward	TCTTGGGATGGGGAGTCTGT	Human	959	59.88 - 61.8
PP7 h - Reverse	GCTTCCTTTGCTCCCAATCTG	Human		59.18 - 63.1
PP2 - Forward	GCTCAGGGGACAAAGGAAGC	Mouse	814	60.96 - 63.5
PP2 - Reverse	TCGCTCTCTCGTGGCTAGTA	Mouse		59.82 - 58.9
PP7 m - Forward	CTCAGGGCAGGTGAAACTGT	Mouse	1000	59.89 - 60.3
PP7 m - Reverse	GTCTGCGCTTCCTTTGTCC	Mouse		57.89 - 60.9

2.3.2.2. qPCR reaction and gel electrophoresis

Genotyping PCR reaction was performed using the G2 Hot Start Taq (Promega, M7405) in a Thermal Cycler T3000 (Biometra) in 8 well PCR SnapStrip tubes (Anachem). The composition of the PCR reaction is specified in Table 2.10. and the PCR program conditions in Table 2.11. Negative and positive controls were included (known human and known mouse samples).

Table 2.10. PCR mix reagents and quantities.

Reagent	Quantity (µl) per PCR reaction
5x Green GoTaq Flexi Buffer	5
5x Colorless GoTaq Flexi Buffer	5
MgCl2 Solution, 25 mM	5
PCR Nucleotide Mix, 10 mM each	0.4
Forward primer	0.1
Reverse primer	0.1
GoTaq G2 Hot Start Polymerase (5u/µL)	0.2
DNA sample (25 ng/µl)	6
Nuclease-Free water	28.2

Table 2.11. Genotyping PCR program and primers.

Primer name	Primer sequence	Species	Expected product length (bp)	PCR program
PP7 h - Forward	TCTTGGGATGGGGAGTCTGT	Human	959	95°C, 5min ; (95°C, 30s; 62°C, 30s; 72°C 1min) x_{30}; 72°C, 5min; 4°C Hold
PP7 h - Reverse	GCTTCCTTTGCTCCCAATCTG	Human		
PP7 m - Forward	CTCAGGGCAGGTGAAACTGT	Mouse	1000	95°C, 5min ; (95°C, 30s; 60°C, 30s; 72°C 1min) x_{30}; 72°C, 5min; 4°C Hold
PP7 m - Reverse	GTCTGCGCTTCCTTTGTCC	Mouse		

To visualize and separate the amplified PCR fragments, agarose gel electrophoresis was performed. Agarose gels with a desired density of 2% were created by dissolving Agarose (Sigma) in 1x Tris-acetate-EDTA buffer from (Geneflow). The mixture was heated in a microwave until boiling and then allowed to cool while being swirled consistently under cold water for even cooling. 5 µL of Safe View (NBS) was added per every 100 ml of the gel solution. The prepared gel solution was poured into appropriate molds with inserted combs to create wells for loading samples. Once solidified, the gels were placed in gel electrophoresis tanks filled with TAE buffer. A gel loading dye (Promega) was added to each PCR product sample, and these were run alongside a molecular ladder (NEB) at 110V untilth desired bands were separated. The DNA bands on the gel where visualised by a GelDoc UV transilluminator (BioRad).

2.3.3. Targeted DNA sequencing for organoid-line genotyping

Targeted DNA sequencing for UHW derived organoid-lines was performed by the All Wales Medical Genetic Service by adding our organoid DNA samples to their patient sequencing pipeline. The investigated genes, analysed by next generation sequencing, are detailed in Table 2.12.

Table 2.12. Gene list of All Wales Medical Genetic Service for NSCLC mutations.

Gene list	Type of analysis	Essential regions	Reference sequence information
NRAS	Hotspots	Exons 2, 3, 4 (p.12, p.13, p.59, p.61, p.117, p.146)	NM_002524.3 (on LRG_92) - 7 exons - 189 AAs
RET	Hotspots + SV (Gene fusion)	Whole gene sequence +/- 20 bases. Hotspots Exon 11 (p.C634), Exon 16 (p.M918).	NM_020975.4 (on LRG_518) - 20 exons - 1114 AAs
KRAS	Hotspots	Exons 2, 3, 4 (p.12, p.13, p.59, p.61, p.117, p.146)	NM_033360.2 (on GRCh37) - 6 exons - 189 AAs
ERBB2	Hotspots + CNVs	Whole gene sequence +/-20bp for CNVs Hotspots in Exon 8 (p.S310), Exon 17 (p.I655, p.R678), Exon 19 (p.L755, p.I767, p.D769), Exon 20 (p.V777), Exon 21 (p.V842), Exon 22 (p.R896).	NM_004448.3 (on LRG_724) - 27 exons - 1255 AAs
PIK3CA	Hotspots + CNVs	Hotspots Exons 9, 20 (*see ref seq note) Whole gene sequence +/-20bp for CNVs.	NM_006218.2 (on LRG_310) - 21 exons - 1068 Aas. *PIK3CA exons 10 and 21 are traditionally described as exons 9 and 20 based on exon numbering starting at the ATG initiation codon which is actually in exon 2.
EGFR	Hotspots CNVs SV	Hotspots: Exons 18 (SNVs), 19 (deletions), 20 (SNVs and insertions), 21 (SNVs). Whole gene sequence +/-20bp for CNVs. EGFRvIII structural variant (in-frame deletion exons 2-7).	NM_005228.3 (on LRG_304) - 28 exons - 1210 AAs
MET	CNVs and exon 14 skipping	Whole gene sequence +/-20bp for CNVs. Exon skipping exon 13, intron 13, exon 14 and intron 14	NM_001127500.1 (on LRG_662) - 21 exons - 1408 AAs
BRAF	Hotspots	Screen exons 11 and 15 +/- 20bp	NM_004333.4 (on LRG_299) - 18 exons - 766 AAs
CDKN2A	Whole Gene Screen + CNVs	Whole gene sequence +/- 20 bases.	NM_000077.4 (on LRG_11) - 3 exons - 156 AAs
PTEN	Screen + CNVs	Whole gene sequence +/-20bp	NM_000314.4 (on LRG_311) - 9 exons - 403 AAs

2.4. Drug treatments and irradiation

Stock solutions of Olaparib (AZD2281, Ku-0059436) and VE-822 (Berzosertib, VX970, M6620) were prepared in 100 % DMSO at 1 mM, aliquoted and stored at -20^{O}C until use. Dilutions of the drugs for treatment were made with DMSO and/or culture medium.

For drug and radiation combination treatments, the medium was changed to medium with drug or DMSO control 1 h before irradiation, and 24 h post-IR cell culture medium was replaced for drug-free medium.

Irradiation was carried out using an IBL 637 irradiator containing a ^{137}Cs source. The distance from the source was continuous, therefore, the dose depended on the time of exposure (dose-rate of 0.43Gy/min). The ^{137}Cs source was regularly tested to ensure that it delivered the calculated doses (carried out by technical staff member Mark Bishop, Cardiff University). In order to establish dose-response radiation curves, a sequential irradiation

process was conducted. The plate with the highest radiation-dose (10 Gy - 1395 seconds) was initially placed in the irradiator. Once the appropriate duration had elapsed, the irradiation was halted, and a second plate was added into the machine (6 Gy - 837 seconds). This procedure was repeated for subsequent doses (4 Gy - 558 seconds and 2 Gy – 279 seconds), ensuring that all treatments concluded simultaneously.

2.5. Metabolic viability assays

2.5.1. ATP viability assays

For both 2D and 3D lines ATP viability assays were used to determine culture viability during its growth for different seeding densities or at different timepoints after irradiation (indicated per experiment) using the endpoint viability assay Cell CellTiter-Glo® 3D (Promega, G9681).

Each line was seeded at the appropriate seeding concentrations per experiment in clear bottom 96 well white plates. For 2D cell lines these ranged from 50 to 1000 live cells / well, for 3D CellsAggs these ranged between 50 – 1000 live cells / µL Matrigel and for 3D organoids concentrations of either 100, 500 or 1000 live cells / µL Matrigel were used. 10 µL Matrigel blobs were seeded per well for 3D cultures. The specific seeding densities used per experiment are detailed in the results chapters of this work. A different plate was used for each growth/radiation-dose medium condition and timepoint.

For each day in which ATP was measured, the CellTitler-Glo® 3D Cell Viability reagent was thawed at 4 ^{O}C. Both the reagent and the plate were equilibrated to room temperature for approximately 30 minutes and the CellTitler-Glo® 3D Cell Viability reagent of an equivalent volume to that of the cell culture medium present was added to each well (100 µL for 2D cultures and 50 µL for 3D cultures). The contents were mixed to induce cell lysis for 5 minutes in a R100 rotatest mixer (Luckham). The plate was allowed to incubate at room temperature for an additional 10 minutes for 2D cultures and 25 minutes for 3D cultures. Luminescence was recorded by a FLUOstar OPTIMA (BMG LABTECH) reader with an integration time of 0.5 seconds/well. Relative luminiscence of samples was normalised to medium only wells (negative controls) from samples to compensate for background signal.

2.5.2. Resazurin PrestoBlue assay

Resazurin based live-cell PrestoBlue™ Cell Viability Reagent (Invitrogen, A13261) that detects mitochondrial activity was used to measure UHW origin organoids' viability in culture over time.

100, 500 or 1000 live cells / μL Matrigel were plated in 10 μL Matrigel blobs in clear bottom 96 well black plates for up to 18 days. 90 μL of complete culture medium was added per well. As a negative control, an additional 4 wells per plate with culture medium alone were utilised. On days 3, 6, 9, 12, 15 and 18 after seeding viability was measured.

At each measuring time point, 10m μl Presto Blue Reagent was added per well and after 30 minutes of incubation at 37°C, fluorescent signal was measured in a FLUOstar OPTIMA (BMG LABTECH) reader with an excitation/emission spectrum of 560nm/610nm. Relative fluorescence of samples was calculated by by reference to medium only wells (negative controls) to account for background signal. Immediately after measuring, all medium was replenished with reagent-free complete culture medium and the plate was returned to the incubator for further continuous culture.

2.6. Brightfield image-based 3D culture analysis

2.6.1. Routine brightfield imaging for phenotype characterisation

For 3D CellAggs and organoids phenotypic characterisation, cultures were imaged at different times (usually, daily in culture – details per experiment in result chapters) with a Moticam 2000 camera attached to a Leica DMIL 090-135.001 inverted microscope. A single z-plane was taken per well. Representative examples of different morphological phenotypes of CellAggs and organoids were sampled qualitatively while observing the organoids at different timepoints. Images were post-processed in FIJI software and organoid diameters were measured by quantifying in-focus organoid's maximum diameter (the degree of eccentricity of most organoids was not too different from spherical although this was not routinely quantified).

2.6.2. GelCount™ scanning and analysis

A GelCount™ scanner (Oxford Optronix) was used for CellAgg growth assessment. CellAggs cultures were plated in 96 or 24 well plates and were scanned at different time points using the GelCount™ scanner. The acquired images were with the built-in GelCount™ scanner software (Oxford Optronix) analysed using a predefined mask or

'CHARM' to identify CellAgg structures within each well. The CHARM settings (Table 2.13.) were optimised to to allow the use of the same parameter set across the range of lines, times and treatments shown in each experiment. Superimposed images of the original scan and the applied mask were exported to manually, visually validate the accuracy of the mask. Note that the output from this technique showed an inaccurate masking and, thus, no further experiments were done with this technique (see Results).

Table 2.13. CHARM settings for mask design in GelCount™ software.

Parameter name	Parameter value
Edge detection sensitivity	50
Centre detection sensitivity	70
Circularity factor	80
Edge distance threshold	0.8
Colony diameter minimum (μm)	10
Colony diameter maximum (μm)	500
Borders from centroids	yes
Merge overlapping objects	yes
Overlap threshold	0.8
Overlap calculation	area

2.6.3. IncuCyte based live-imaging of cell line-derived 3D cultures

2.6.3.1.Live IncuCyte imaging of spheroids without an ECM

For imaging of cell lines cultured in suspension without an ECM, these were setup as described in section 2.1.5.3. Plates were then placed in the IncuCyte®S3 (Sartorius) which was placed inside a 37 ^{O}C / 5 % CO_2 incubator, and a 24 h repeat scanning was scheduled with the parameters detailed in Table 2.14. 100 μL per well was carefully removed and replenished with the same quantity of fresh medium every 2-3 days for medium change. The experiment was stopped after 7 days, and images were exported. The IncuCyte acquired images autofocussing on the biggest object. Images using a 4x objective were collected and stored.

Table 2.14. Parameters for live-imaging CellAggs cultured without an ECM in the IncuCyte®S3.

Parameter name	Parameter value
Objective	4x (96 well) 1 image per well
Channel selection	Brightfield
Scan type	Spheroid
Spheroid type	Single
Scan interval	Every 6 hours

2.6.3.2. Live IncuCyte imaging and analysis of CellAggs in a Matrigel 'sandwich'

For imaging CellAggs in an ECM in a single z-plane to investigate culture-dynamics, 96 well plates were setup using a sandwich technique as described in section 2.1.5.2. Plates were placed in the IncuCyte®S3 (Sartorius) placed inside a 37 ^{O}C / 5 % CO_2 incubator, and a 24 h repeat scanning was scheduled with the parameters detailed in Table 2.15. Fifty μL per well was carefully removed and replenished with the same quantity of fresh medium every 1-2 days for medium change. The experiment was stopped after 8.75 days. The IncuCyte acquired images autofocussing on the biggest object. Images using a 10x objective were collected and stored.

Table 2.15. Parameters for live-imaging CellAggs cultured in an ECM in the IncuCyte®S3.

Parameter name	Parameter value
Objective	10x (96 well)
Channel selection	Phase Contrast + Brightfield
Scan type	Spheroid
Spheroid type	Multi spheroid
Scan interval	Every 6 hours

For culture-dynamic analysis of the CellAggs in 3D in an ECM, two different approaches were taken: (1) creating an analysis definition for semi-automatic analysis with the Multi spheroid IncuCyte®S3 software and (2) exporting the images acquired above for post-processing via FIJI software.

(1) The semi-automated IncuCyte®S3 'multi-spheroid' mode software utilised a supervised segmentation mask that defined objects as having a set of parameters (Table 2.16). This mask was then applied to all images after manually supervising all images to ensure all the datapoints in the dataset had in-focus images and were being accurately segmented. The total area covered by cells in the field of view was automatically calculated, data was exported and plotted against time in GraphPad Prism 9.5.0.

Table 2.16. Analysis definition of mask for calculation of total area covered by cells with the Multi spheroid software analysis in the IncuCyte®S3.

	Parameter name	Parameter value
Segmentation	Sensitivity	20
	Background	80
Filters	Area min (μm^2)	100
	Area max (μm^2)	40,000
	Eccentricity min (μm^2)	0.3

(2) For the second analysis pipeline, images were exported and manually post-processed in FIJI. Videos were created by alignment of the time series of exported images. Individual CellAggs were manually tracked using the FIJI plugin MtrackJ and the following parameters were recorded to systematically compare the different CellAggs dynamics within the culture. Minimum and maximum ferret diameter over time (μm) was measured to determine if there had been 'CellAgg growth' and CellAggs were classified depending on their maximum size (40-60 μm, 60-100 μm or >100 μm). A note was made if a darker area in the CellAgg or if CellAgg dissociation was observed. The distance between the last and first location (μm) was recorded to assess the total distance migrated although this did not include the total path length the organoid had migrated since organoid paths were somewhat 'erratic'. Finally, it was noted whether any of the CellAggs merged, or if there was morphological phenotype interconversion (Based on typical ranges of behaviour, CellAggs morphology changes were classified as: start and finish solid, start and finish lumen, and start as solid and converts to lumen morphologies).

2.6.4. IncuCyte based live imaging of organoids: total area over time

For assessment of total area growth per organoid after irradiation, organoids 50 cells/ μL Matrigel were seeded in 25 μL Matrigel blobs in 24 well plate and left for 8 days to form organoids. These were then irradiated with 4 Gy of ionising radiation or sham irradiated. Plates were then placed in the3 7 ^{O}C / 5 % CO_2 IncuCyte®S3 incubator and automatic images of the wells were acquired every 6 hours for a total of 12 days post-irradiation. The 'OrganoidQC' acquiring system (Table 2.17.) in the IncuCyte acquired images from a large z-depth (~2 or 2.9mm) of multiple z-slices to result in a final image where all organoids are in focus.

Table 2.17. Parameters for imaging of organoids in IncuCyte®S3 for organoid area analysis over time.

Parameter name	Parameter value
Objective	4x (24 well)
Channel selection	Brightfield
Scan type	OrganoidQC
Scan interval	6 hours

The semi-automated IncuCyte®S3 'Organoid analysis' software utilised a supervised segmentation mask that defined objects as having a set of parameters (Table 2.18.). A mask was subsequently applied to all images, following manual supervision to ensure that all

datapoints in the dataset contained clear and accurately segmented images. The software automatically calculated the total area covered by organoids in the field of view, and this data was exported for further analysis. The results were plotted against time using GraphPad Prism 9.5.0 software.

Table 2.18. Analysis definition of mask for calculation of total area covered by organoids per well over time with the organoid analysis software in the IncuCyte®S3.

	Parameter name	Parameter value
Segmentation	Radius	Small
	Sensitivity	50
	Edge Split	On
	Edge Sensitivity	60
Cleanup	Hole Fill (μm^2)	500,000
Filters	Area min (μm^2)	No
	Area max (μm^2)	No

2.7. Organoid re-plating assay

The 'Organoid re-plating' assay was developed to assess the ability of cells isolated from organoids to form new organoids when plated as single cells (or small clusters <4 cells). 500 cells / μL Matrigel in 25 μL blobs of the organoid-lines were seeded in 24 well plates and cultured to form organoids for 7 days. These were then treated as indicated in section 2.4. Twenty-four hours post-IR organoids were dissociated with TrypLE Express, and life (trypan blue excluding) single cells were re-seeded (500 cells / μL Matrigel) and cultured to form new organoids in new 25 μL Matrigel blobs. Ten (LPTO85 and LPTO126), 14 (PDXO149) and 15 (PDXO137 and PDXO377) days after re-plating, the plates were placed inside the IncuCyte®S3 (Sartorius) imager inside a 37 ^{O}C / 5 % CO_2 incubator and an image of each well was acquired using the parameters for OrganoidQC mode detailed in Table 2.19.

Table 2.19. Parameters for imaging of organoid IncuCyte®S3 for organoid re-platting assays.

Parameter name	Parameter value
Objective	4x (24 well)
Channel selection	Brightfield
Scan type	OrganoidQC
Scan interval	Single scan

The semi-automated IncuCyte®S3 'organoid analysis' software utilised a supervised segmentation mask that defined objects as having a set of parameters (Table 2.20). The total number of organoids per radiation dose were counted and normalised as a fraction of the total number of formed organoids in the sham irradiated control for each line. For the lines and radiation-doses in which the InCucyte mask failed to accurately count organoids, images were exported and manually counted using FIJI software. Care was taken to ensure that no systematic differences in organoid counting approaches between lines or conditions were able to feed through to subsequent data analyses. All structures with a diameter > 60 μm were considered to be an organoid. When large numbers of organoids were present, a random sampling technique was employed to determine the total number of organoids. Sections of 500x500 pixels per image were captured and the count of organoids present in these sections was used to extrapolate the overall quantity.

Table 2.20. Analysis definition of mask for calculation of total number of organoids with the organoid software analysis in the IncuCyte®S3 for organoids re-platting assays.

	Parameter name	Parameter value
Segmentation	Radius	Small
	Sensitivity	50
	Edge Split	On
	Edge Sensitivity	50
Cleanup	Hole Fill (μm^2)	500,000
Filters	Area min (μm^2)	3,000
	Area max (μm^2)	200,000

2.8. Confocal immunofluorescence imaging

Organoids were either cultured in black clear bottom 96-well plates (Costar, 3803) (for cell type/general organoid-morphology stainings) or ibidi 8 well μ-Slides chambers (ibidi, 80807) (for γH2AX and/or 53BP1 stainings), fixed in the Matrigel blobs with 4% PFA for 1h at RT, washed 3 times with PBS for 10 minutes and permeabilised and blocked for 3-5 h at RT or overnight (o/n) at 4°C with 10 % donkey serum (Abcam) in IF buffer (Table 2.21). Primary antibody was incubated o/n at 4°C in IF buffer (list on primary antibodies in Table 2.22.). Afterwards, organoids were carefully washed 3 times with IF buffer for 10 minutes each and the final washed was performed o/n at 4°C. Secondary antibody was incubated for 3-5 h at RT or o/n at 4°C in IF buffer (1:200) in the dark, washed 3 times with PBS and

counterstained with 5 μg/ml DAPI in PBS for 20 min. Samples were subsequently imaged in PBS. A Zeiss 710 confocal microscope was used for image acquisition. A 40x objective was used for acquisition of cell type/general organoid-morphology and a 63x oil immersion objective was used to image γH2AX and/or 53BP1 foci. Images were acquired utilising the Zen software attached to the Zeiss 710 microscope. A z-stack covering a whole-cell area within each organoid was captured and analysed using maximum projection in FIJI software.

Table 2.21. IF buffer composition.

Buffer component	Final concentration	Supplier	Catalogue number
BSA	0.1 %	Gibco	15260-037
Triton X-100	0.1 %	Sigma Aldrich	T8787
Tween 20	0.05 %	Merck	P1379
PBS	1x	Gibco	10010-015

Table 2.22. Primary antibodies list.

Buffer component	Final concentration	Supplier	Catalogue number
γH2AX (Ser139)	1:100	Millipore	05-636
53BP1	1:100	Cell Signalling	49375
CK5	1:2000	BioLegend	905501
Acetylated-α-Tubulin	1:100	Santa Cruz Biotechnology	Sc-23950

2.9. Flow cytometry and cell cycle analysis

Twenty-four hours post-IR, organoids/CellAggs were harvested and dissociated into single cells with TrypLE, as described earlier for passaging in section 2.1.2. Cells were fixed in cold 70 % ethanol adding it drop wise to the pellet with continuous gentle vortexing to ensure fixation and minimise clumping. Fixing solution was maintained for 1 h at 4°C. Cells were then washed with PBS and 250 mg/mL RNAse A (Sigma, 10109142001) was added, DNA was stained with 10 mg/mL propidium iodide (PI – Sigma, P4170), incubated for 30 minutes at 37°C and kept overnight at 4°C. Samples were run on a LSR Fortessa flow cytometer (BD) in PBS and 10,000 single events were acquired. An unstained cell control was run.

Cell cycle analysis was performed in FlowJo 10.8.2 using its cell cycle analysis pipeline. Briefly, a dot plot of forward scatter (FSC) vs. side scatter (SSC) was created to select for the cell population and discard debris. This population was used to further gate on cells by excluding aggregates using FSC-A (area) vs. FSC-H (height); single cells typically form a diagonal shape in this graph. A histogram of PI intensity vs. cell count was plotted and the Watson pragmatic model within FlowJo for 'Cell cycle analysis' was applied, which

estimates parameters like peak position and width for each phase using mathematical distributions and assigns individual cells to specific cell cycle phases. The fit of the model was then manually inspected to ensure the proportions of cells in each cell cycle phase was correctly assigned.

2.10. scRNAseq.

2.10.1. Experiment layout and treatment

Five-hundred single cells, of the LUSC organoid lines PDXO377 ($p53^{WT}$) and PDXO149 ($p53^{null}$), were seeded per µL Matrigel in 25 µL blobs in 24 well plates and let to form organoids for 12 days (refreshing the medium every 2-3 days). The organoids were then irradiated with a single dose of 4 Gy or non-irradiated, and 4 h later, several blobs (4-6) per sample were dissociated with TrypLE into single cells and pooled together. Hereon after, all processes were carried out at 4°C. After isolation of the single cells by centrifugation (200g, 5 min), a final wash in the base culture medium with 0.04 % BSA, as recommended by 10X Genomics, was performed before the final viability was counted (Trypan Blue excluding) and cells were resuspended in the base culture medium with 0.04 % BSA in a total of 25 µl with concentrations of 700-1200 cells/µl. These concentrations were then adjusted by Angela Marchbank (CU Genome HUB) for an expected recovery of 10,000 life cell for library preparation before loading into the Chromium controller.

2.10.2. Library preparation and library construction

Library preparation was performed by Angela MarchBank following the 10x Genomics Chromium Next GEM Single Cell 3' kit. Briefly, cell suspensions were mixed with the appropriate reagents for cell capture, and the resulting emulsions were processed within the Chromium Controller to form Gel Bead-In-Emulsions (GEMs). Incubation of GEMs was carried out to ensure cell lysis and mRNA capture. Subsequently, cDNA synthesis was performed to convert captured mRNA into cDNA which was then purified with Dynabeads (magnetic bead-based purification). cDNA was then amplified to generate full-length cDNA libraries (11 cycles in a thermal cycler - Eppendorf Mastercycler X50a). To ensure purity, cDNA was subjected to cleanup with SPRIselect beads, removing any residual primers, enzymes, or contaminants. The SPRIselect beads work on the principle of selectively binding nucleic acids in the presence of a high concentration of a chaotropic salt solution.

Adapter sequences compatible with Illumina sequencing were added, and libraries were further amplified to generate adequate material for downstream sequencing. SPRIselect

beads were also used during library construction to ensure sDNA purity and to achieve the desired size range suitable for sequencing correct library size. The QC steps were carried out with a Tapestation 4200 (Agilent Technologies) to examine the size of the cDNA (D5000 tapes) and completes libraries and pools (D1000 tapes). The quantification of the cDNA, libraries and pools were carried out with a Qubit 3.0 (ThermoFisher Scientific).

2.10.3. Sequencing

An initial sequencing QC run was carried out on an Illumina Miseq sequencer with a nano 300 cycle cartridge and the main run was done on an Illumina Novaseq 6000 sequencer with a SP 200 cycle cartridge. This was carried out at the Wales Gene Park.

2.10.4. Bioinformatics analysis

Bioinformatics analysis was performed by Dr. Sarah Christofides (Genome Research HUB, CU). Raw sequencing data in the form of FASTQ files were subjected to the nf-core/scrnaseq v2.1.0 pipeline, which is part of the nf-core project that aims to provide a collection of standardised, community-driven pipelines for various bioinformatics analyses (Ewels et al. 2020) (Peltzer et al. 2023). The first step of this pipeline was the analysis of the raw data generating a standard FastQC report to assess the quality of the sequencing data. A core component of the nf-core/scrnaseq pipeline is the integrated use of CellRanger (as recommended by 10x Genomics). Briefy, CellRanger (10x Genomics) processed the raw sequencing data (adapter sequences and low-quality bases were trimmed) and reads were then aligned to the reference genome (GRCh38), finally cell barcode and UMIs were extracted from the aligned reads and barcode rank plots were generated, gene quantification was caried out and a count matrix was generated. This count matrix represents the number of RNA molecules from each gene in each single cell.

The CellRanger filtered data was then imported to R Studio and an ensemble QC using the SCTK package was performed (Wang et al. 2023). As an output we obtained metrics that included total read counts per cell, number of detected genes per cell and percentage of reads mapped to mitochondrial genes. Cells with < 20% of mitochondrial reads were then discarded. ScDblFinder doublet score was run and cell doublets were further discarded. Finally, DecontX command was used to score background RNA contamination and cells with > 0.5 % RNA contamination were further removed from subsequent analysis. The total number of cells after all filtering steps was then quantified.

2.10.6. Pseudobulk RNA analysis

Pseudobulk analysis was performed by Dr. Sarah Christofides (Genome Research HUB, CU). For the PDXO377 line, filtered data from CellRanger was imported into R, genes with less than 100 reads overall were removed and the counts per million (CPM) were calculated. An excel output for differentially expressed (DE) genes between the control and the treatment was generated, for which a DE gene was called if it showed an absolute log2FC of 0.585, equivalent to a 1.5 gene expression fold-change. I performed a separate Gene Ontology analysis with a false discovery rate < 0.05 for the top 500 upregulated genes and all downregulated genes (https://www.gsea-msigdb.org/gsea/index.jsp).

2.10.7. Post-bioinformatics single cell-RNAseq analysis

'Cell type mapping' was performed by Dr. Sarah Christofides (Genome Research HUB, CU). A tool for the unsupervised projection of scRNAseq data, scmap (Kiselev et al. 2018), was used to assign 'cell types' to our samples using as a reference the human lung cell atlas (Travaglini et al. 2020). Filtered data from CellRanger post SCTK, scDblFinder adnd DecontX filtering and reference was first re-formatted to ensure compatibility with the tool, which uses data formatted as a 'SingleCellExperiment object', and assumes by default that gene names are found in a column named 'feature_symbol' while the cell-type labels are in a column named 'cell_type1'. In addition, scmap required normalisation and log-transformation of the reference data. The 500 most informative genes from the reference data were chosen by scmap and the reference profiles were build using *scmap-cluster* for cluster-based cell-type annotation. Then *scmap-cell* was run in the reference dataset to create an index to annotate individual cells of our database. Our sample cells were then annotated to the reference using the *scmap-cluster*. For subsequent analysis *scmap-cell* assigned cells in our dataset to their 'nearest neighbours' in the reference dataset. In this case, the 'nearest neighbours' were the cells in the reference dataset most similar to the cells in the query dataset. When there was a 'tie' for commonest annotation, the cell was labelled 'ambiguous'. Then the total number of cells per group were calculated. For further visualisation of the data, I calculated the percentage of cell type per sample which was plotted using GraphpadPrism.

2.11. Data and statistical analysis

Unless otherwise stated, experiments were performed using at least three technical replicates. Raw data obtained was analysed using Microsoft Excel to calculate means and

standard deviations which were used for graphical representation of the data using GraphPad Prism 9.

2.11.1. Data normalisation for ATP and resazurin viability assays

To eliminate background signalling, the raw data obtained from the luminescence/fluorescence of samples was adjusted using readings from 'blank' wells that contained only the reagent/media mixture. Subsequently, for growth assays a plate was always measured immediately after seeding and subsequent days corrected measurement were calculated as a percentage of day 0 (100 %). For radiation/drug response assays, corrected measurements were calculated as a percentage of sham irradiated 0.05 % DMSO control. The specific days on which ATP levels were analysed are detailed per experiment in the results chapters of this work.

2.11.2. Data normalisation for organoid re-plating assays

Plating efficiency (PE) was calculated as follows:

$$\text{PE} = \frac{\text{number of organoids counted in sham irradiated control sample}}{\text{number or cells seeded}} \text{ x } 100$$

Survival fraction (SF) was calculated as follows:

$$\text{SF} = \frac{\text{number of organoids counted in a treated sample}}{(\text{number of cells seeded}) \text{ x } (\frac{\text{PE}}{100})}$$

To assess drug sensitisation effect, SF/SF ratio was calculated as follows (where ratio > 1 indicated a sensitisation to the IR-response by the drug at that specific dose), where *x* is the specific radiation-dose in which the SF ratio is calculated:

$$\frac{SF_{xGy^{DMSO}}}{SF_{xGy^{Drug}}}$$

2.11.3.Statistical analysis for IR-DDRi organoid re-platting assays

Statistical analysis for the plating efficiency was conducted in GraphPad Prism 9. Comparisons of plating efficiency between each drug and the 0.05% DMSO control at sham irradiation were done using 1-way analysis of variance (1-way ANOVA) with Dunnett's test for correction of multiple comparisons. Statistical significances were determined when p

values were less or equal to 0.5 (ns: $p>0.5$, *: $p\leq0.5$, **: $p\leq0.01$, ***: $p\leq0.001$, ****: $p\leq0.0001$).

The statistical analysis of the sensitising effect of the drugs was performed by Dr. Mark Jackson, University of Glasgow. The replicate SFs were subjected to a one-sided ratio t-test in R using the 'mratios' package (Djira et al. 2018), with ratio under the null hypothesis $p=1$. Ratios were determined across multiple radiation doses and p-values were adjusted for multiple comparison using the false discovery rate method.

3. Results - NSCLC CellAggs: cell-line derived 3D models for radiation-response

Two of the main differences between organoids and 2D cell-lines are that organoids have never been selected to grow on plastic and that they grow in 3D with the support of an ECM. Although lung cancer cell lines grown in 2D may poorly model *in vivo* responses, it's not known whether they might be able to recapitulate some aspects of the heterogeneity of tumour responses to radiation if they were to be cultured in 3D with the support of an ECM. The use of well characterised cell lines also allowed the development and standardisation of 3D assay methods to be developed in anticipation of the establishment of in-house organoid lines.

3.1. Characterisation of CellAggs

To determine whether cell-lines in 3D grown with an ECM show similar morphologies and culture-dynamics to non-plastic adapted organoids, we cultured four NSCLC cell-lines in Matrigel. These lines were selected based on the tumour type from which they were derived and their genetic background. LUAD and LUSC plastic-adapted cell-lines (see Table 3.1) were selected to represent the two most common subtypes of NSCLC. These lines have previously been cultured as spheroids (Wang et al. 2013) and / or studied for NSCLC radiation-response (Nakadate et al. 2013; Jiang et al. 2016; Boysen et al. 2019). We also chose cell-lines that differed in their TP53 status, as p53 is a key orchestrator in the DNA Damage Repair (DDR) pathway.

Table 3.1. Selected NSCLC cell lines for culture in 3D in Matrigel. NSCLC subtype and *TP53* status of NSCLC cell lines selected for growth in 3D in an ECM.

Cell line	NSCLC subtype	TP53 status
A427	LUAD	WT
A549	LUAD	WT
Calu-3	LUAD	Homozygous substitution - missense
NCI-H520	LUSC	Homozygous substitution - nonsense

3.1.1. Morphological characterisation of CellAggs

The NSCLC cell-lines (Table 3.1) were routinely maintained in 2D in ATCC recommended medium. As schematically illustrated in Figure 3.1, the selected NSCLC cell-lines were trypsinised and then cultured in 3D in Matrigel with both the ATCC recommended medium in which they were initially growing in 2D and with Airway Organoid medium (AO medium). AO medium (Sachs et al. 2019) was the first and only cell growth-factor specific lung airway patient-derived organoid medium that had been defined at the time these experiments were performed. Briefly, a suspension of 300 life cells / μL Matrigel were seeded and cultured in 10 μL Matrigel blobs in 96 well-plates with the corresponding medium. The morphology of the cell-lines in Matrigel was assessed at different timepoints (day 3, 5, 7, 10, 12, 15 and 20 post-seeding) by imaging the cells with a camera attached to an inverted microscope.

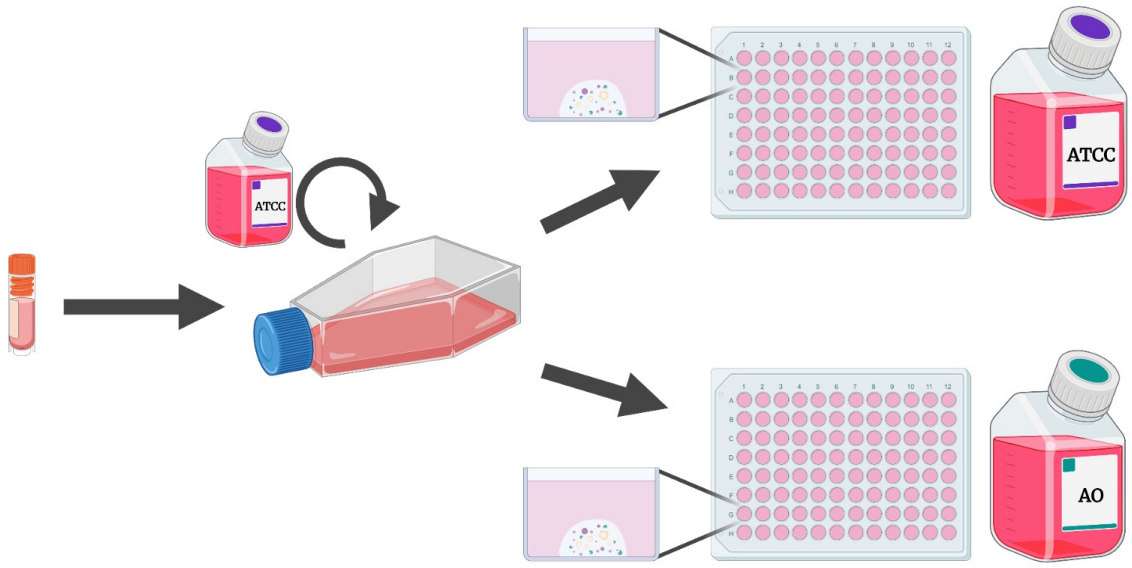

Figure 3.1. Set up of the culture of NSCLC cell-lines in Matrigel. All cell lines were thawed, grown, and maintained in their respective ATCC recommended mediums in 2D flask cultures. For each experiment, when cells reached 75 – 80 % of confluency in 2D, these were seeded from single cells in Matrigel as detailed in the Methods chapter. Importantly, these were then cultivated in 3D in Matrigel either with their correspondent ATCC recommended medium, or with AO medium from (Sachs et al. 2019).

All selected NSCLC cell-lines formed cell structures or clusters when cultured in Matrigel, both in ATCC recommended and in AO medium (see Figure 3.2). Henceforward, we will be referring to these Matrigel-embedded plastic-adapted cell-line derived clusters as *Cell Aggregates (CellAggs)*. Note that this definition does not imply that the clusters formed due to cell aggregation by comparison with cell growth (see later Figure 3.7, for time-lapse

analysis relating to this point). Despite the fact that plastic-adapted cell lines are expected to be genetically homogeneous and clonal, different CellAgg morphotypes (a distinct morphology) formed from the same plastic-adapted cell-lines when cultured in Matrigel. CellAgg morphotypes were classified in three groups (adapted from organoid-morphology classifications (Zhao et al. 2022)): solid, budding or lumen CellAggs (Figure 3.3). Solid CellAggs were mass or compact cell-clusters and generally round, especially when small in diameter. Some also had a darker core. Budding CellAggs had either budding structures or grape-like shapes and could also contain a darker centre. Lumen CellAggs formed cell-clusters with an internal lumen within round-structures. Here we found multi-layered, monolayered and cystic CellAggs (some comprising very few cells).

To further investigate the morphological inter- and intra-line differences in CellAggs and to elucidate if the different morphotypes correlated with specific medium conditions or time in culture, we quantified the percentage of each morphotype present in each cell-line (A427, NCI-H520, A549 or Calu-3), culture-condition (ATCC recommended or AO medium) and timepoint (day 3, 5, 7, 10, 12, 15 or 20 post-seeding) by reviewing the images and assessing growth (diameter-range / condition) with FIJI software (Table 3.2).

Across most of the latter timepoints, both *A427* and *A549* CellAggs were mostly solid, although lumen and budding CellAggs were also found. Representative structures for each subtype are highlighted in coloured boxes in Figure 3.2, as described in the figure legend. *NCI-H520* CellAggs, only showed solid and budding morphotypes. *Calu-3* had both solid and, in a majority of cases, lumen CellAggs, although very limited cell growth (if any) appeared to have taken place when *Calu-3* cells were cultured in AO medium.

Regardless of the culture medium used, different morphotypes were present in A427, A549 and NCI-H520 CellAggs. Moreover, the morphotype and size distribution of each line (Table 3.2) didn't substantially change when comparing CellAggs in the two media, although there appeared to be a slightly higher proportion of lumen CellAggs in A427 cells cultured in ATCC medium, while NCI-H520 CellAggs in ATCC medium reached a larger final size (200 μm) after 15 days in culture when compared with AO medium. Calu-3 CellAggs in ATCC recommended medium seemed to increase in size over time (from 30 μm to 200 μm, after 20 days in culture), whilst those cultivated in the AO medium remained static; very little growth was observed (CellAggs remained < 30 μm diameter). Taken together, the data suggest that differences in the specific media compositions used did not

affect the diverse range of morphologies that each line exhibited, if they were able to grow in 3D culture.

Imaging the cultures at different timepoints leaded to assess, in part, CellAggs culture-dynamics, which included general characteristics of the culture independent of the morphotype (size, darkness…) and morphological distribution overtime. Overall, A427 cells initially (day 3) formed CellAgg structures smaller than 30 µm (see A427 CellAggs diameter progression in Table 3.2 and red circles and dashed red arrows in panel A) in Figure 3.2), that ranged from 100 – 200 µm on day 12 and increased in size until forming a big cluster of CellAggs without clear boundaries between each other at day 20 on culture. In addition, from day 10-12 on, A427 CellAggs with darker cores arised (see orange arrow on ATCC day 12, panel A) of Figure 3.2). The presence of dark cores in organoids has been linked to hypoxia, nutrient deprivation, and increased cell death / necrosis (Hubert et al. 2016; Däster et al. 2017; Nunes et al. 2019). By the last day in culture (day 20), A427 CellAggs appeared to have lost their structural integrity and single cells were detected close to the larger structures, suggesting cells had delaminated from the initial CellAgg structure. Although no CellAgg delamination was found in A459 and NCI-H520 cultures; these had darker areas as early as day 12 in culture, as we had previously seen with A427 CellAggs (see orange arrows on Figure 3.2 – A427, A459 and NCI-H520 panel A), B) and C) respectively, on day 12). This is consistent with the expected effects of nutrient deprivation and hypoxia that may be affecting the biology of cells that were internal to the structures (and furthest from nutrients / centre of the Matrigel blob) (van Tienderen et al. 2019). Notably, some cell attachment to the underlying plastic was observed in both A549 and NCI-H520 cultures (green arrows in panel B) and C) on Figure 3.2). Cell-attachment can interfere with the results of experiments that seek to differentiate between 2D versus 3D culture outcomes.

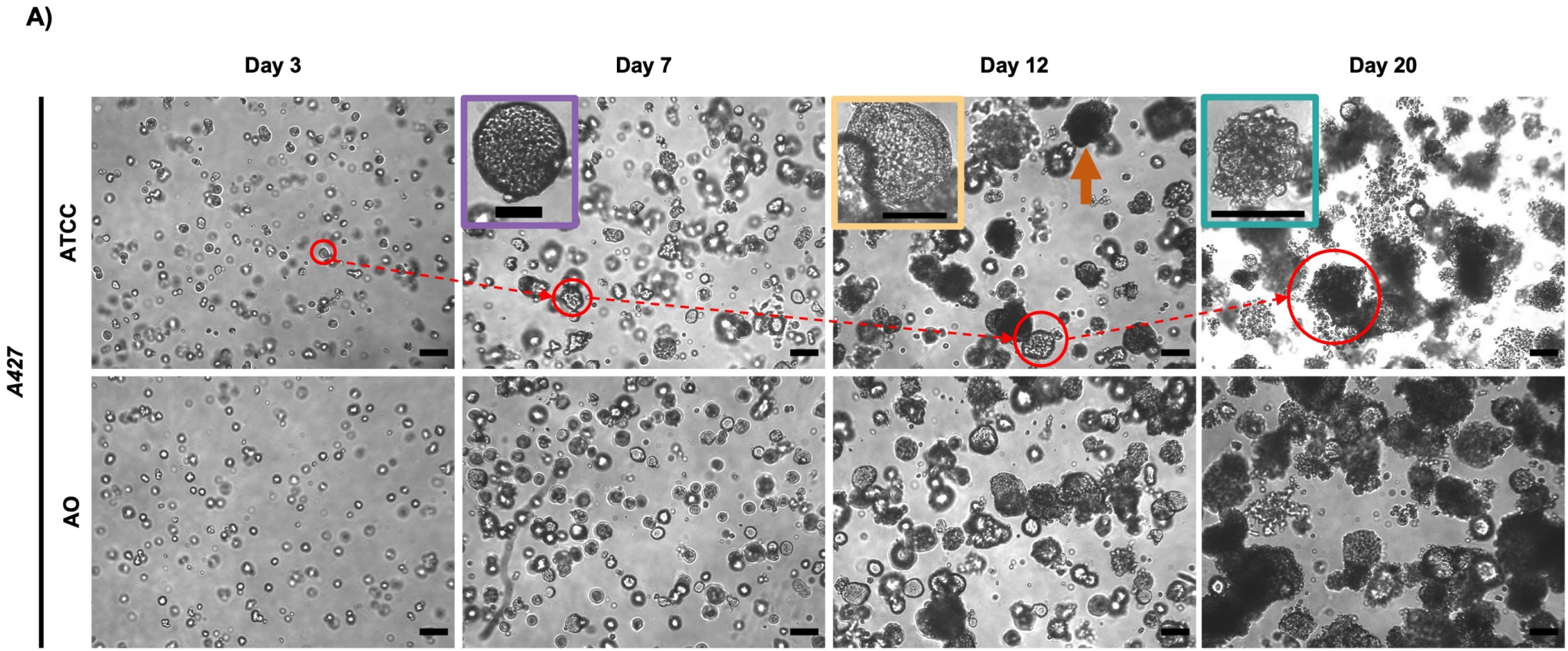

*Figure continues in the next page

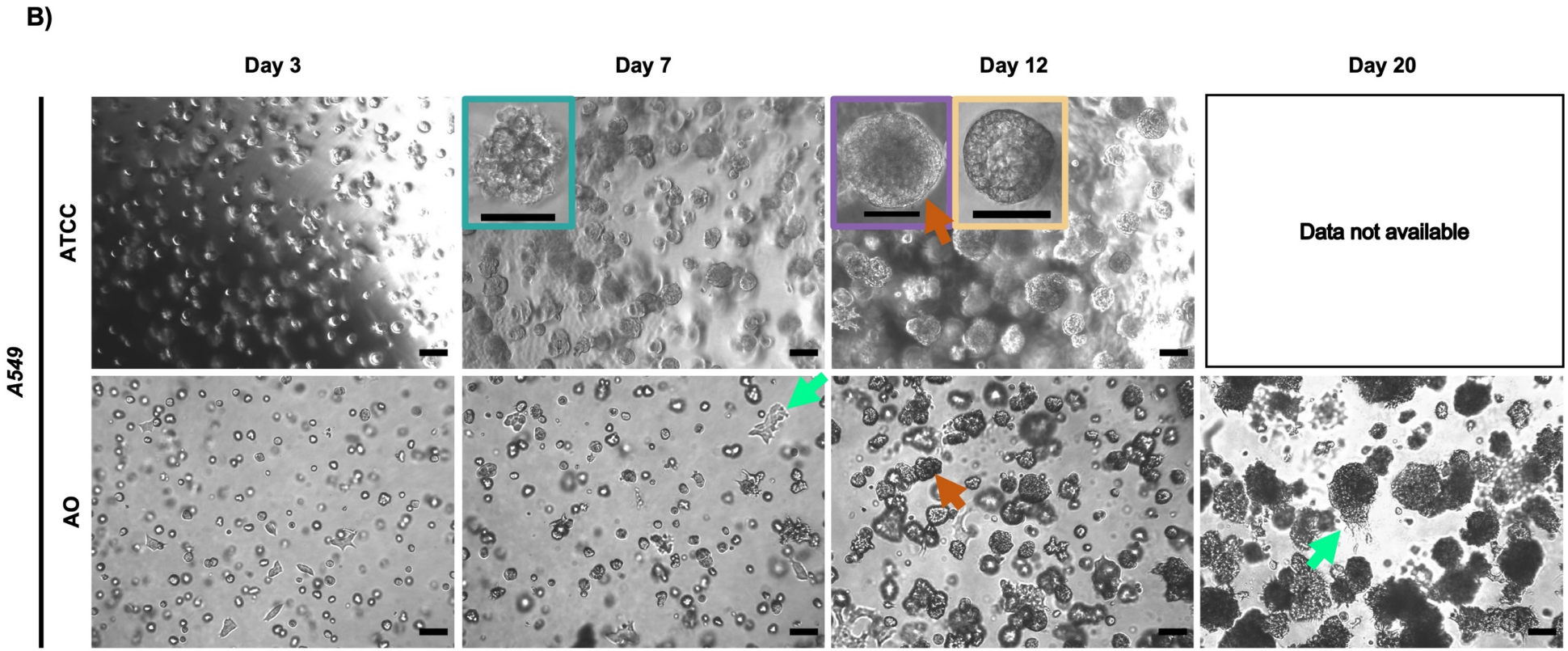

*Figure continues in the next page

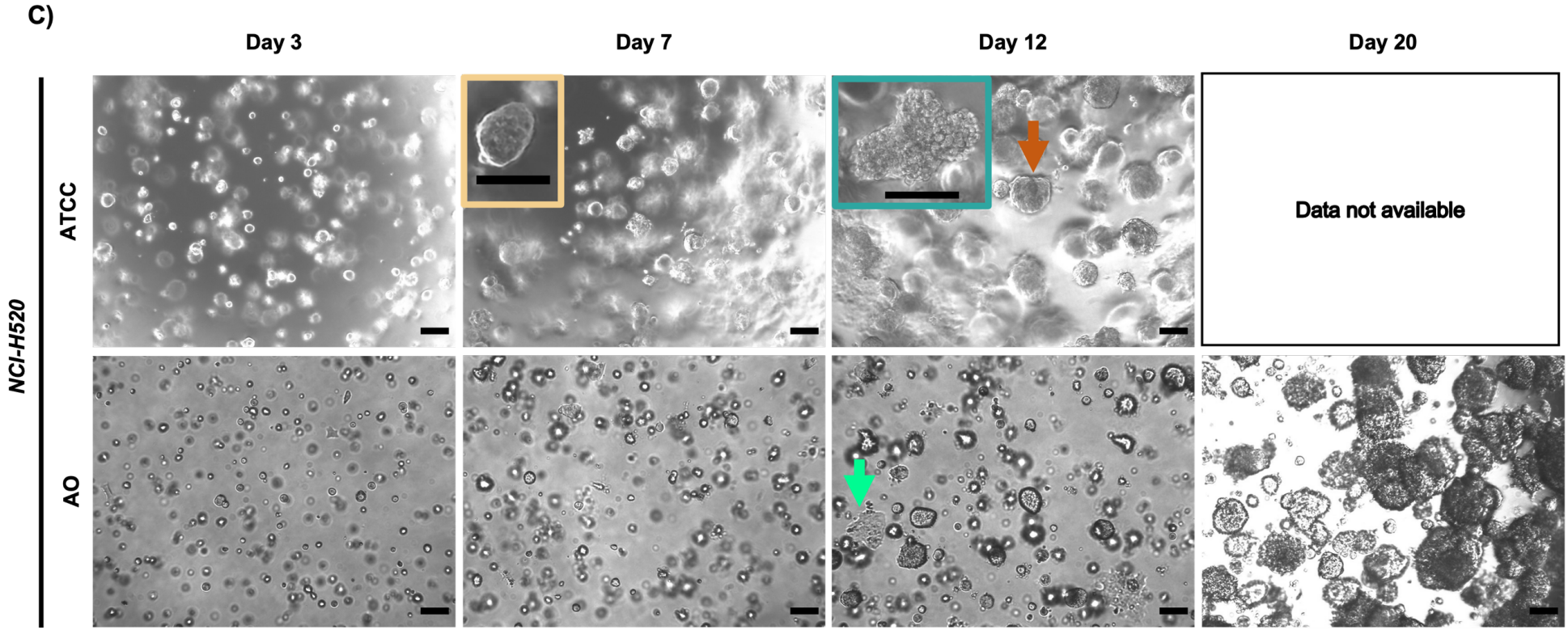

*Figure continues in the next page

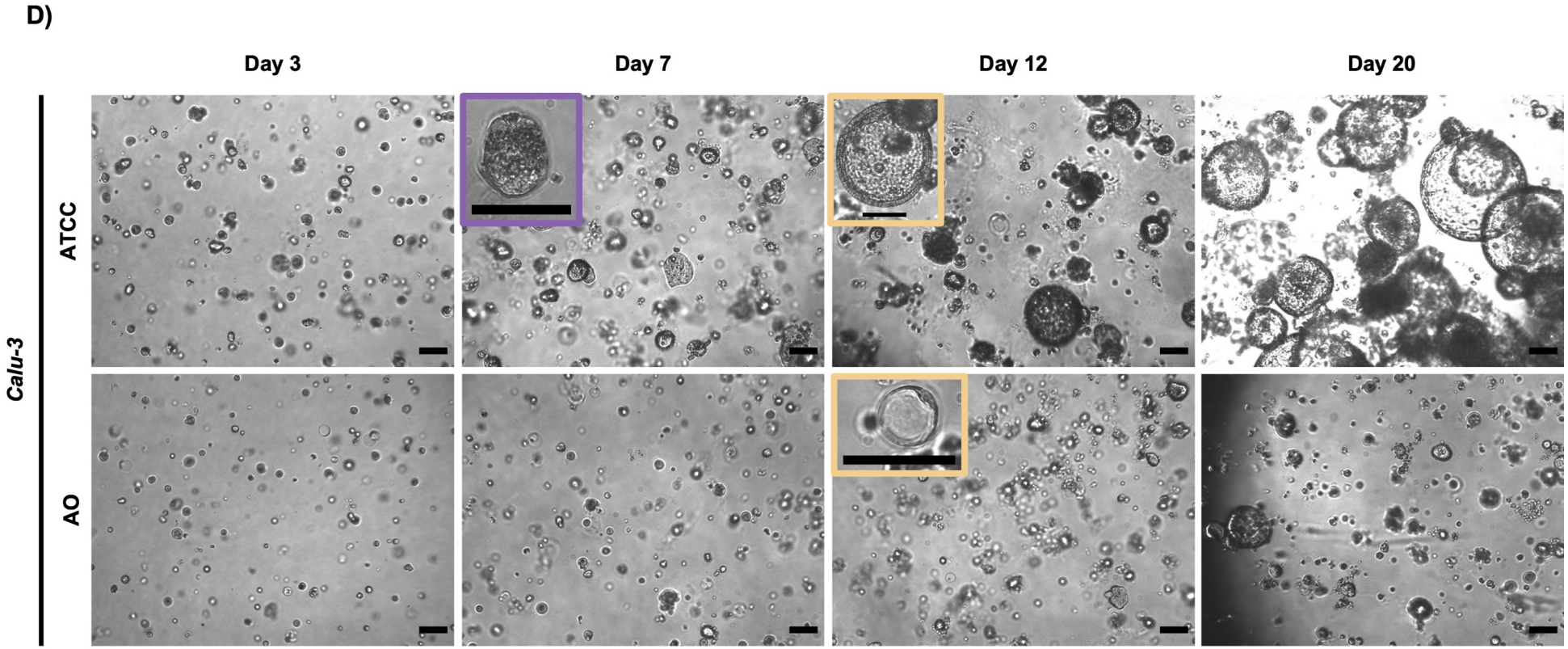

Figure 3.2. Brightfield images of NSCLC in 3D in Matrigel at different culture-stages with ATCC / AO medium. Images at different stages of the culture represented in columns (days 3, 7, 12 and 20 in culture) and NSCLC cell lines in horizontal (**A)** *A427*, **B)** *A549*, **C)** *NCI-H520* and **D)** *Calu-3*) cultured either with ATCC recommended medium or AO (Airway Organoid) medium in 3D in Matrigel. Red circles and dashed red arrows (,): Indicator of different stages of the culture: small CellAggs on day 3, darker cultures on day 12 and nearly completely black cultures and single cells on day 20. Purple outline ( ): Close-up image of solid CellAgg. Blue outline ( ): Close-up image of budding CellAgg. Yellow outline ( ): Close-up image of lumen CellAgg. Orange arrows ( ): Dark structures / cores. Green arrows ( ): cell attachment. Scale bars: 100 μm.

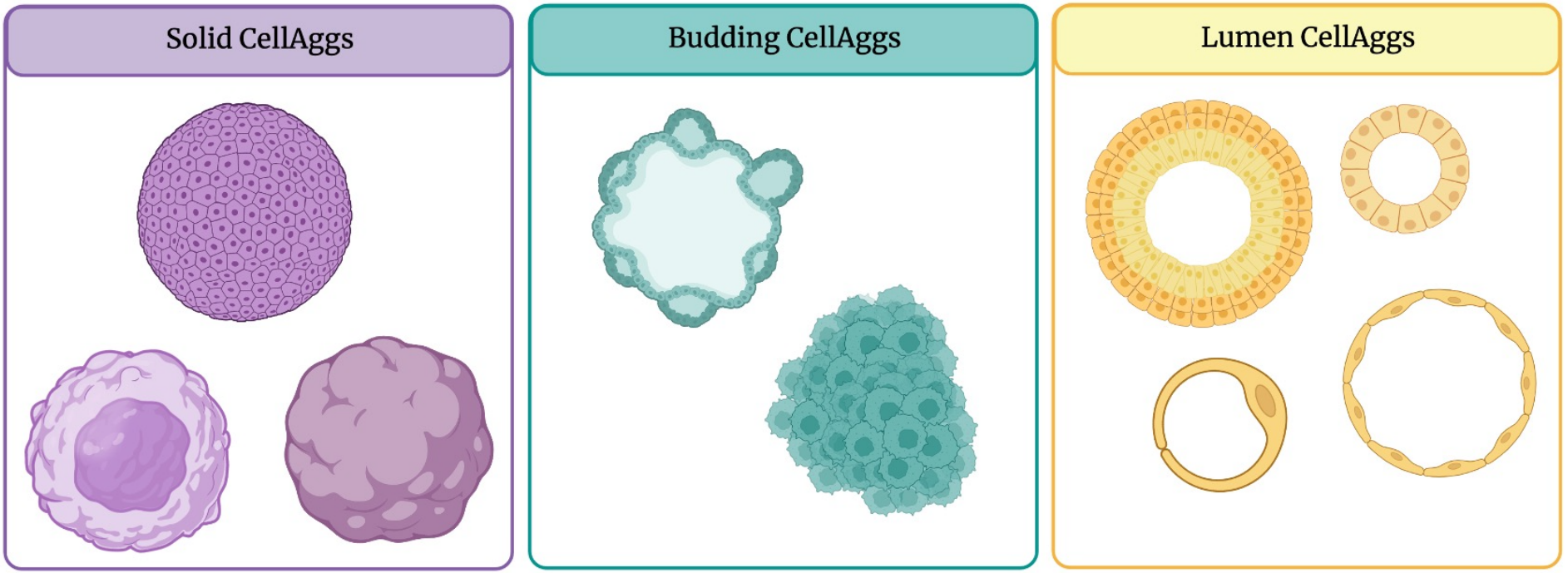

Figure 3.3. Diagram of different CellAgg morphotypes. Diagram was created via BioRender based on the morphotypes that could be observed after culturing NSCLC cell lines in 3D in Matrigel in ATCC recommended or AO (Airway Organoid) medium. Solid CellAggs: mass or compact cell-clusters, generally round, especially when small and some with a darker core. Budding CellAggs: composed of budding structures or grape-like shapes and could also contain a darker centre. Lumen CellAggs: cell-clusters with an internal lumen within round-structures that could be multi-layered, monolayered and cystic (some conformed of very few or a single cell).

Table 3.2. NSCLC cell line-derived CellAgg-morphotypes depending on the days in culture and growth medium. In this table the different percentages of morphologies that could be observed when culturing NSCLC cell line-derived CellAggs up to 20 days in ATCC recommended medium and in AO medium are displayed. The percentages and the diameter (measured in FIJI) are taken qualitatively: by observation of pictures of the cultures at different timepoints stablished in the table after seeding 300 cells / μl Matrigel.

Cell line	Days	In ATCC recommended medium				AO			
		Solid	Budding	Lumen	Diameter (μm)	Solid	Budding	Lumen	Diameter (μm)
A427	3	100	0	0	D <50, most around 30	100	0	0	D <30, most single cells.
	5	95	5	0	D <50, most around 30	100	0	0	D <50, most around 30
	7	95	5	0	D <100, most D>50	<95	5	<5	D <100, most around 50
	10	95	5	0	D <100, most D>50. Darker structures.	<95	5	<5	D <100, most D>50
	12	95	5	0	D <200, most D>100. Darker structures.	<95	5	<5	D <200, most D>100. Darker structures.
	15	80	5	15	D <250, most D>100. Darker structures.	<90	10	<5	D <250, most D>100. Darker structures.
	20	80	5	15	Big black clusters, difficult to distinguish.	<90	10	<5	Big black clusters, difficult to distinguish.
A549	3	90	10	0	D < 30	100	0	0	D < 30, some attachment.
	5	<90	10	<5	D < 50	<90	10	<5	D < 50, some attachment.
	7	<60	40	<5	D < 100	<70	30	<5	D < 100, some attachment.

Table continues in the next page

	10	<50	<50	<5	D < 150	<50	<50	<5	D < 150, some attachment.
	12	<50	<50	<5	D < 150, some attachment.	<50	<50	<5	D < 150, some attachment.
	15	-	-	-	-	<50	<50	<5	D < 150, some attachment.
	20	-	-	-	-	<50	<50	<5	D < 150, dark clusters, difficult to distinguish.
NCI-H520	**3**	90	10	0	D < 30	90	10	0	D < 30, some attachment.
	5	90	10	0	D < 30	90	10	0	D < 30, some attachment.
	7	80	20	0	D < 100, most around 50.	90	10	0	D < 50, some attachment.
	10	60	40	0	D < 150	80	20	0	D < 100, most around 50, some attachment.
	12	60	40	0	D < 150, some attachment.	80	20	0	D < 100, most around 50, some attachment.
	15	70	30	0	D < 200, dark clusters, difficult to distinguish.	70	30	0	D < 150, cell attachment.
	20	-	-	-	-	50	45	5	D < 150, dark clusters, difficult to distinguish.
Calu-3	**3**	90	0	10	D < 50, most around 30.	90	0	10	D < 30
	5	80	0	20	D < 50, most around 30	90	0	10	D < 30
	7	70	0	30	D < 100	90	0	10	D < 30
	10	60	0	40	D < 100	80	0	20	D < 60, most around 30 or single cells.

**Table continues in the next page*

	12	50	0	50	D < 200, D >100	80	0	20	D < 60, most around 30 or single cells.
	15	20	0	80	D < 200, D > 100	80	0	20	D < 60, most around 30 or single cells.
	20	10	0	90	As big as 500	80	0	20	D < 60, most around 30 or single cells.

Regarding morphotype distribution-changes over time, in *A427* culture (Table 3.2) solid CellAggs were the predominant morphotype (80 – 100 %), although budding CellAggs could also be found (5 – 10 %). Lumen CellAggs constituted less than 5 % of *A427* CellAggs cultured in AO medium, whilst they reached a 15 % from day 15 on when cultured in ATCC medium. By contrast, *A549* and *NCI-H520* CellAggs appear to initially have had a predominant solid morphotype, but by day 12 in culture develop to include both solid and budding morphotypes (nearly 50 %; Table 3.2). In Calu-3 culture in ATCC medium (Table 3.2) solid CellAggs were initially the majority, but by day 20 lumen-type CellAggs comprised 90 % of the culture. To determine if seeding density would change morphotype distribution in CellAggs, this experiment was repeated in all cell-lines with a range of different seeding concentrations (300 – 1000 life cells / µL Matrigel) but no apparent difference was found in CellAggs' size or morphotype distribution (data not shown).

Overall, we found that plastic adapted NSCLC cell lines formed CellAggs with different morphotypes when cultured in 3D with the support of an ECM, despite being expected to be genetically homogeneous and probably clonal. Moreover, this phenomenon appeared to be culture medium- and seeding density- independent. Based on their varied morphologies, CellAggs might be able to recapitulate some aspects of primary cancer biology. As has previously been described for 3D spheroids (grown in the absence of Matrigel on non-adherent plates), many of the larger 3D CellAggs had darker cores, which has been linked to cell death, but also to hypoxia and radiation resistance (Hubert et al. 2016; Nunes et al. 2019; Bouleftour et al. 2021; Menegakis et al. 2021). Importantly, the different morphotypes imply that cells positioned at different places within the CellAggs (e.g. at the edge of a CellAgg bud) may experience distinct physiological signals that might in turn be related to their radiation response.

3.1.2. Viability of NSCLC CellAggs

As we have established, different seeding concentrations did not appear to affect morphotype distribution-dynamics. However, seeding densities can affect growth rates via effects on processes aggregated under concepts such as 'growth factor conditioning effects on cell survival' and 'cell-cell contact effects on cell survival'. To test the effect of seeding density on CellAgg growth rates, suspensions of either 50, 100, 300, 500, 800 or 1000 live cells / µL Matrigel were plated with either ATCC or AO medium for up to 20 days. Relative ATP levels were measured, using the endpoint assay CellTiter-Glo® 3D.

Relative Luminescence (RLU) increased over time in all cell lines and all culture conditions (Figure 3.4), except for *Calu-3* in AO medium. This suggested the lines might be used for radiation-response assays between days 5 and 12 of culture. As expected, there was an overall increase of RLU signal when increasing the initial number of cells seeded.

With the exception of *Calu-3*, the three lines showed similar peak levels of ATP (within ~50 %) when seeded in the ATCC recommended medium for 2D growth or in AO medium (Figure 3.4). ATP levels in *A427* cells continued to increase during the time measured, implying continued cell growth, while cells from *A549* and *NCI-H520* appeared to plateau in their growth by day 12 in ATCC medium for all plating conditions, and in all but the lowest plating densities in AO medium. By contrast, ATP levels from *Calu-3* cultures did not increase in AO medium confirming the lack of increase in CellAgg number and size observed in Figure 3.2. Taken together, the similar growth and morphology of CellAggs in ATCC when compared to AO medium suggested that subsequent experiments might best be performed with the respective ATCC media, since this would also allow the cells to be maintained and then transferred to Matrigel culture without a change in culture medium.

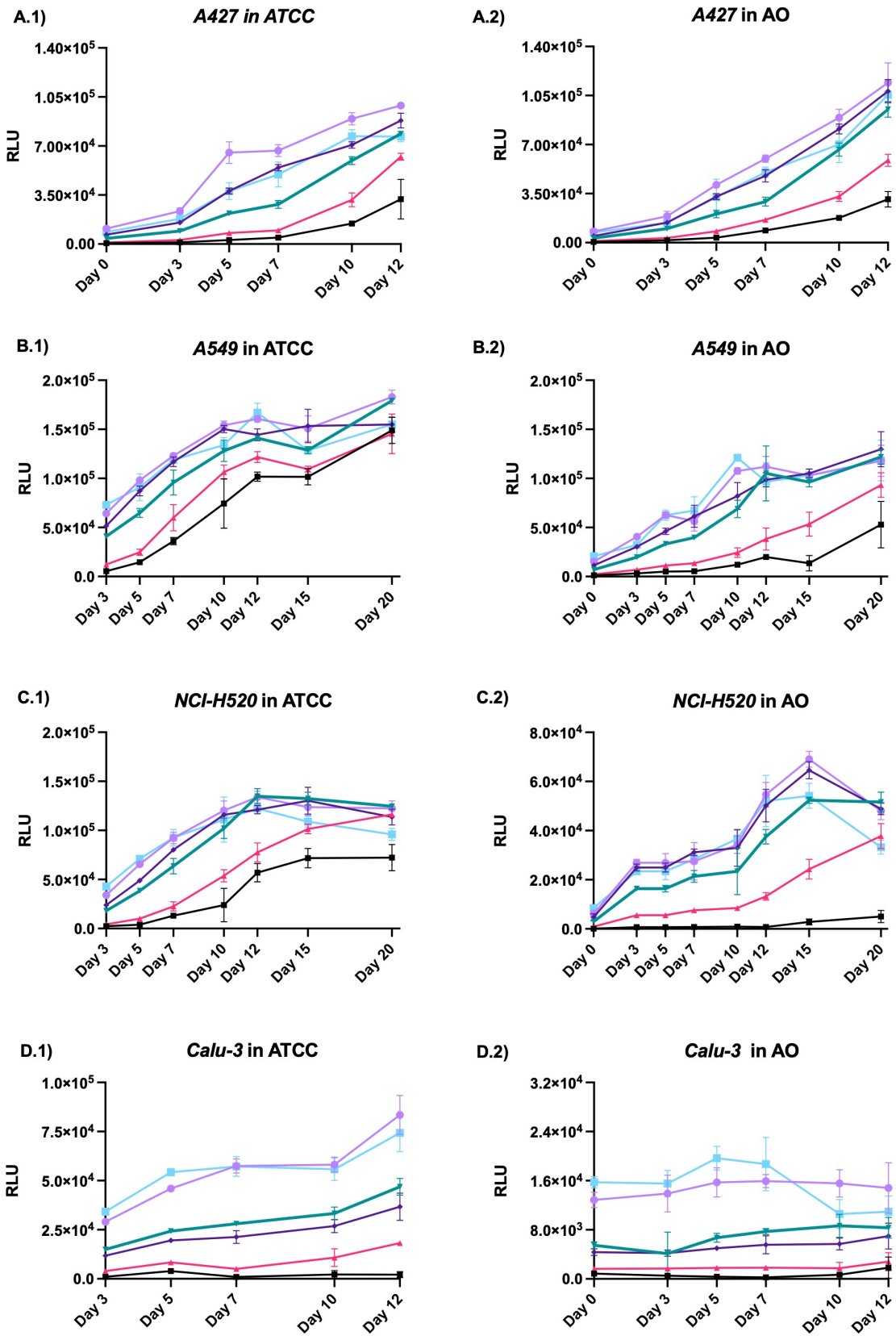

Figure 3.4. ATP RLU curves of NSCLC cell line-derived 3D CellAggs in Matrigel. Relative culture viability of **A)** *A427*, **B)** *A549*, **C)** *NCI-H520* and **D)** *Calu-3* CellAgg-lines either in **X.1)** ATCC recommended or **X.2)** AO medium at different timepoints (day 0 – 20) and with different initial seeding densities in 'life cells / mL Matrigel' (—■—: 50, —▲—: 100, —▼—: 300, —◆—: 500, —●—: 800, —■—: 1000), measured with CellTiter-Glo® 3D ATP live-cell assay and normalised over a 'medium only' well. Relative increase in RLU overtime suggests a general overall viability increase of the cultures overtime, At least 3 technical replicates were performed per experiment. RLU: Relative Luminiscence. Graphs made with GrapPad Prism 9.

To determine optimal seeding density, we next calculated the ATP-related RLU ratio (as ATP fold change) from day 3 in culture until the maximum RLU point per line in ATCC recommended medium (day 12 for A427 and Calu-3; and day 15 for A549 and NCI-H520). The fold increase is closely linked to increases in cell numbers / cell proliferation and is important to determine since proliferating cells are more sensitive to radiation-damage (Bolus 2017).

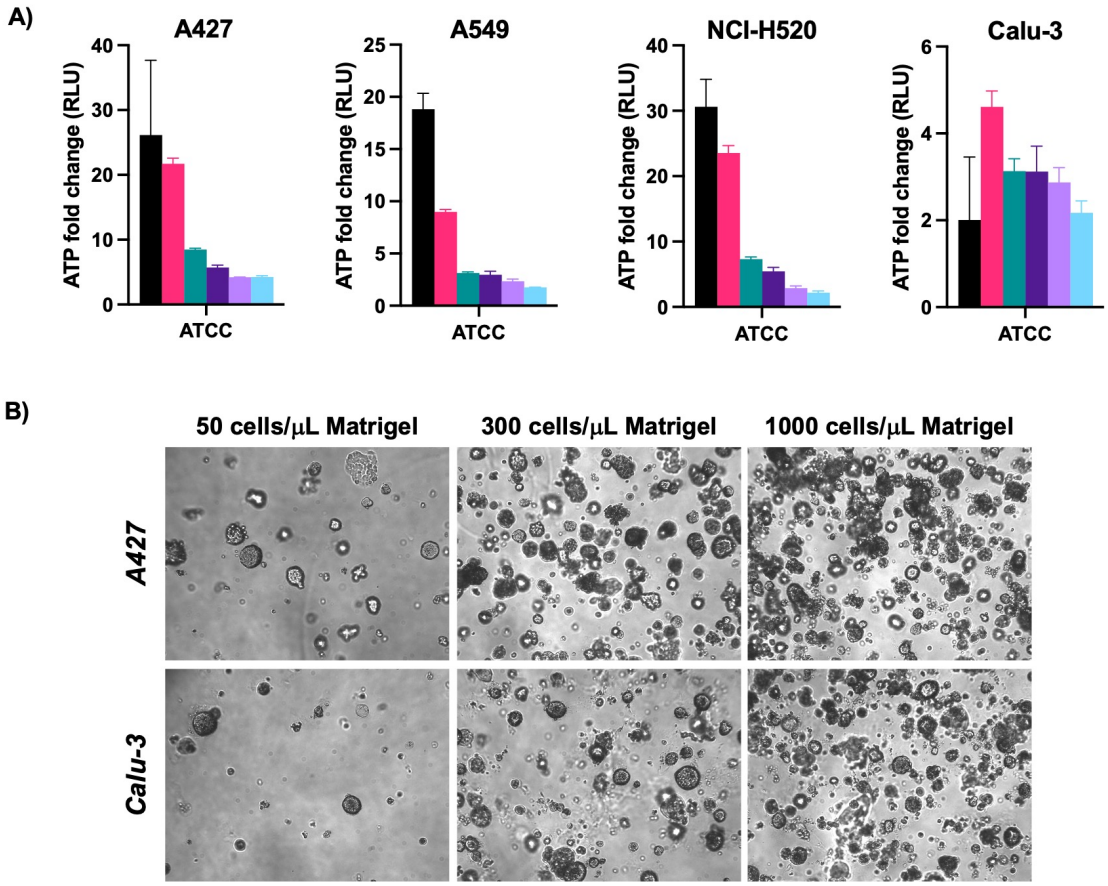

Figure 3.5. ATP ratio increment of NSCLC cell line-derived CellAggs in Matrigel. A) ATP fold change for different seeding densities in 'viable cells/ml Matrigel' (: 50, : 100, : 300, : 500, : 800, : 1000) of *A427*, *A549*, *Calu-3* and *NCI-H520* CellAggs from day 3 until maximum ATP point in culture (day 12 for *A427* and *Calu-3* cultures and day 15 for *A549* and *NCI-H520* cultures) measured with CellTiter-Glo® 3D live-cell assay in ATCC recommended medium. RLU: Relative Luminiscence. Graphs made with GrapPad Prism 9. **B)** Representative brightfield images of *A427* and *Calu-3* CellAggs cultures for different seeding densities in ATCC recommended medium at day 10 in culture.

Overall, seeding at 50 and 100 cells / µL Matrigel led to the biggest increase in RLU in all cultures (Figure 3.5, A)). 2D cell-lines often grow exponentially when seeded at low density

on plastic, but this may not occur with CellAggs as proliferation in the absence of migration will lead to high local cell densities that may locally restrict growth. In fact, low initial seeding numbers resulted in the formation of very few CellAggs (see 50 cells / μL Matrigel images of Figure 3.5, B)) and may thus increase the variance of the data, even though it apparently increased the potential 'assay window' (see bigger deviation bars with lower seeding densities in Figure 3.5, A)). Moreover, lower seeding densities might not produce enough overall cell-numbers that might be required if later re-seeding assays are needed (e.g. colony formation assays to assess culture's stem cell capability after radiation). By contrast, very high seeding densities resulted in CellAggs with poorly delineated morphological boundaries and low assay window sizes (see 1000 cells / μL Matrigel images of Figure 3.5, B)).

Overall, 300 cells / μL Matrigel was determined to be the optimal seeding concentration for CellAggs. This balanced a robust fold-increase in ATP levels whilst producing clear, separated, CellAggs that could be imaged, counted, and replated if required in later experiments.

3.1.3. Live-tracking CellAggs

To track the dynamics of CellAgg growth, two imaging systems were used. The GelCount™ (Oxford Optronix) takes low-resolution whole-well scans and can be used to image the same well over time. By contrast, the IncuCyte®S3 system from Sartorious is located inside an incubator and, when operating in the 'multiple spheroid' mode, takes images of the same exact field-of view over time.

GelCount™ analyses. A suspension of 300 life cells / μL Matrigel of *A549* was seeded and cultured in 10 μL Matrigel blobs in a 96 well-plate with ATCC recommended medium. The plate was scanned with the GelCount™ at day 3, 7 and 15 in culture. Whole-well images were processed with the semi-automated GelCount™ software. This involved the use of a supervised colony segmentation mask in which different parameters were adjusted to define objects (e.g. edge detection; centre detection; circularity factor; edge distance threshold; filtering controls for diameter maximum and minimum, complete boundaries and borders from centroids; and merging of overlapping objects). This mask was then applied to all images in a time-series (see Methods for details).

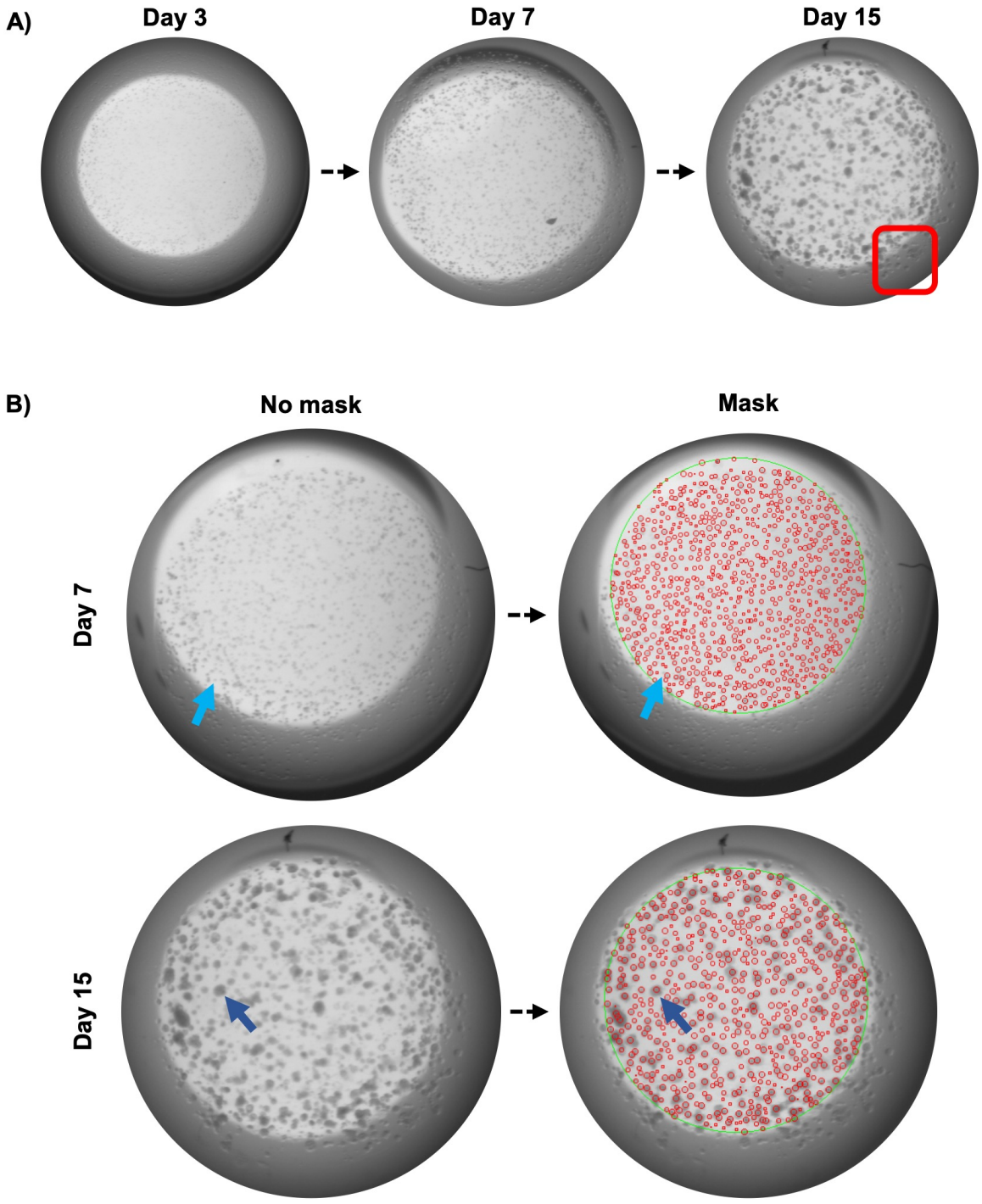

Figure 3.6. NSCLC cell line-derived CellAggs in Matrigel: image-analysis with GelCount™ . Scan images of *A549* CellAggs, at day 3, 7 and 5 as detailed in the figure confirm an increase in CellAggs number and size overtime. Cells were seeded from single cells cultured in ATCC recommended medium with a seeding density of 300 cells/ml Matrigel: **(A)** at different timepoints **(B)** at different timepoints with and without GelCount™ program's semi-automated mask. : objects not detected due to the shadow of the plate. : object not detected at day 7. : object detected as smaller, wrong diameter.

GelCount™ scans were able to confirm an increase in CellAggs-number and size over time (Figure 3.6). However, several difficulties were observed when trying to rely on the quantitative output. There was a lack of accuracy of the scan in the middle part of the well

for samples at early times in the culture (Day 3, Figure 3.6, A)). This was most likely due to the GelCount™ not being designed to image 3D Matrigel blobs and losing focus in the centre of the scans due to blob-height. Additionally, shadows were formed at the edges of the wells and as a consequence, not all CellAggs in the well could be distinguished (see **red** square, Day 15, Figure 3.6, A)). Seeding the cultures in bigger wells did not solve this problem (data not shown). Most importantly, for automating the counting of cultures, the mask that most accurately segmented CellAggs, committed errors including the lack of detection of some objects on day 7 (**light blue** arrows in Figure 3.6, B)) or under-estimating CellAggs size on day 15 (**dark blue** arrows in Figure 3.6, B)). In reality, because of the diversity of CellAgg-sizes through different timepoints, it was not possible to design a mask that would automatically and accurately segment CellAggs overtime in the GelCount™ software. The lack of an optimal imaging solution across all timepoints may in part be due to the low scan resolution. Nonetheless, with care in the use of the machine, some quantitative data could be obtained within defined ranges of parameters.

IncuCyte®S3 analyses. Live-cell imaging of CellAggs was performed using the 'multi-spheroid' software mode in the IncuCyte®S3 that was designed to follow 3D objects in suspension. We had previously seen that *Calu-3* CellAggs cultures started out as mostly solid morphology, but by day 20 in culture almost all CellAggs were lumen morphology (Table 3.2). Because of this potential culture-dynamics of *Calu-3* CellAggs, we decided to perform an IncuCyte®S3 timecourse imaging experiment on the *Calu-3* cell line. 5000 single cells were seeded in ATCC recommended medium between two layers of Matrigel, in a 'sandwich', in a 96 well-plate. Seeding the cells in a 'sandwich' maintained most CellAggs in the same z-plane and prevented the IncuCyte®S3 suffering from an automated autofocus problem when handling CellAggs in different z-planes (see Figure 3.7, A)). The IncuCyte®S3 was maintained inside an incubator and automatic images of the same specific field of view per well were acquired every 6 hours for a total of 8.75 days. Images were processed via 2 different pipelines. The first one involved using the semi-automated IncuCyte®S3 'multi-spheroid' mode software analysis. This software utilised a supervised segmentation mask that defined objects as having a set of parameters (e.g. area and eccentricity minimum and maximum and background / cells contrast). This mask was then applied to all images and the total area covered by cells in the field of view was automatically calculated. For the second analysis pipeline, images were exported and manually post-processed to create videos of the culture and to track individual CellAggs using a manual

FIJI plugin MtrackJ (Meijering et al. 2012). Several dynamical parameters were manually measured over time (e.g. minimum and maximum ferret diameter over time (μm), straight distance between last and first location (μm), etc.). A more detailed explanation of the set of image-acquiring and data-processing methods is described in the Methods chapter.

In focus, high resolution brightfield (Figure 3.7, C)), and phase (data not shown) images of the *Calu-3* line were acquired in the IncuCyte. Analysis with the automatic IncuCyte®S3 'multi-spheroid' mode software showed an increase in the total area covered by segmented objects in the field of view over time, quantitatively confirming CellAgg growth (Figure 3.7, B)). The data suggests that this automated technique might be used for future high throughput, whole-culture, radiation-response assays. However, it is important to consider that the 'sandwich' seeding technique depended on a specific Matrigel-stiffness (that varied with temperature and protein concentration) and was therefore difficult to replicate and was not always successful. This complication was later addressed by using the IncuCyte®S3's 'organoid' mode, instead of the 'multi-spheroid' mode. However, this software / imaging mode was not available at the time these initial experiments were performed (see Chapter 5).

A wide range of interesting biology was observed in the videos generated by the manual analysis pipeline (Video 3.1, Appendix - *https://youtu.be/AX72NXL1PqU*). CellAgg growth, migration, fusion and even morphotype conversion appeared to be happening. To monitor these phenomena more closely, 20 individual cells were manually tracked from t=0 to t=8.75 days. The tracks created on the MTrackJ FIJI plugin were displayed in different colours (Video 3.1, Appendix - *https://youtu.be/AX72NXL1PqU*).

We measured the minimum and maximum diameter of each CellAggs over time. Almost 100 % of CellAggs (19/20) showed significant growth over the time analysed (8.75 days). Fourty percent (8/20) of the CellAggs reached 40-60 μm in size, 45 % (9/20) reached 60 and 100 μm, and 15 % (3/20) reached sizes greater than 100 μm by 8.75 days. These data were consistent with our previous assessment of the culture by brightfield microscopy (Table 3.2) where most *Calu-3* CellAggs were smaller than 100 μm between days 7 and 10 in culture.

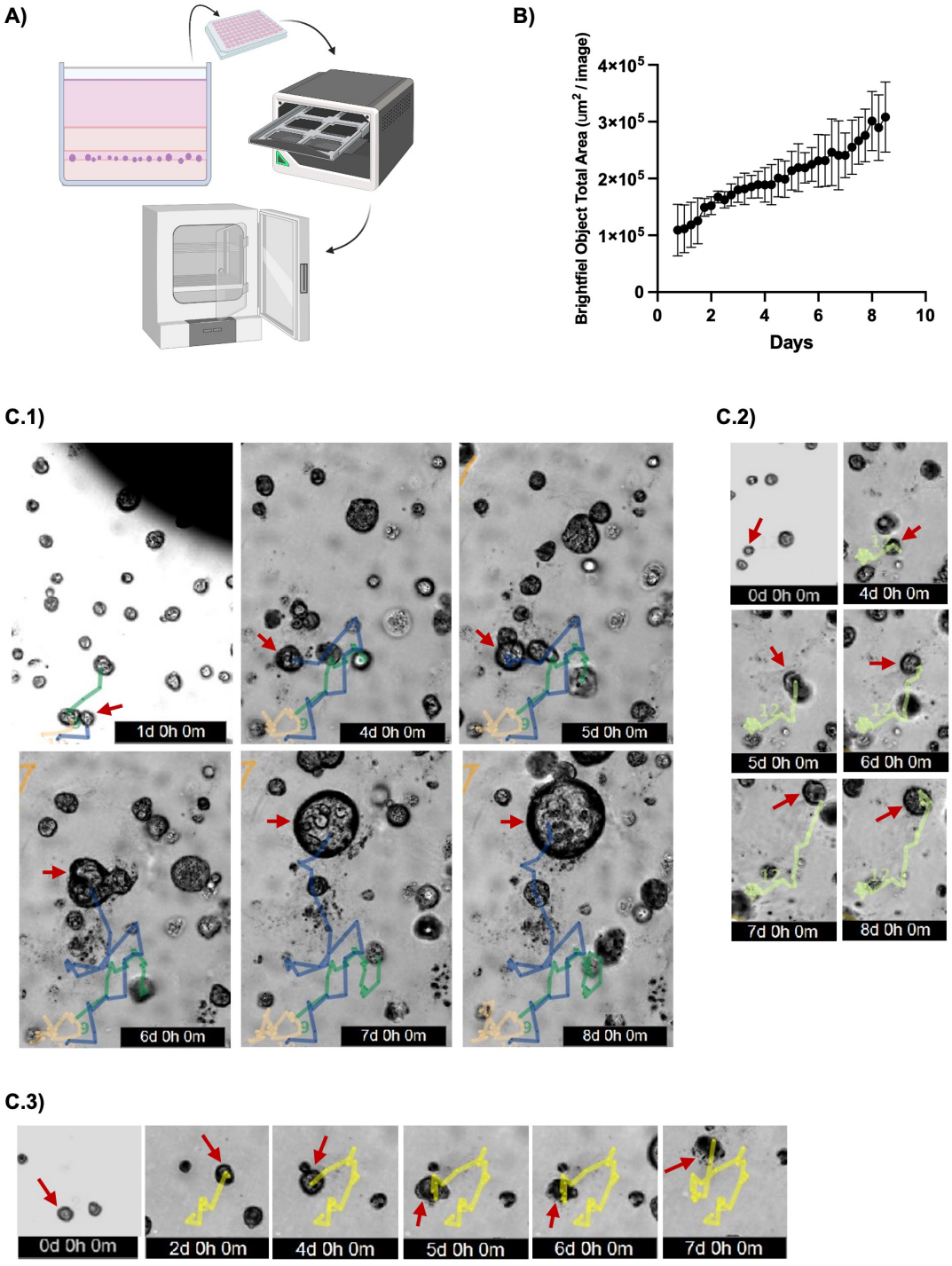

Figure 3.7 NSCLC cell line-derived CellAggs in Matrigel: live-cell analysis with IncuCyte®S3. Analysis of *Calu-3* line at different timepoints in the IncuCyte®S3 'multi-spheroid' mode, with 5000 live cells seeded in a Matrigel 'sandwich' in ATCC recommended medium, enabled tracking individual CellAggs overtime. **A)** Diagram of set-up of 'sandwich' wells and IncuCyte®S3 machine. **B)** Brightfield object total area (μm^2 / image) overtime graph from semi-automatic masking on IncuCyte®S3. n=3. **C)** Selected images from different timepoints (as in the image) from *Video 3.1* showing Calu-3 CellAgg dynamics. Differentially coloured lines represent the track done by the CellAgg until that particular time point. Red arrows pointing the tracked CellAgg at each timepoint. **C.1)** Dark blue track showing a high-motile CellAgg that merges with others overtime. **C.2)** Green track showing CellAgg growth from single cell and CellAgg-CellAgg interactions without fusion. **C.3)** Yellow track showing delamination of a CellAgg overtime.

We then checked frame-by-frame dynamics to see if the changes in CellAgg diameter was due to CellAgg growth and/or CellAgg-CellAgg fusions. Although larger CellAggs usually resulted from fusion of multiple CellAggs with all CellAggs larger than 70 µm merging at least once (7/20) (Figure 3.7, C.1)), CellAggs from single cells also grew (40 % of the total tracked CellAggs grew from single cells without merging). Interestingly, most CellAggs that did not fuse appeared to briefly contact each other (Figure 3.7, C.2)). These dynamics are of importance for the future interpretation of CellAgg's radiation-response assays, as colony formation assays (CFAs) should not be used to infer a clonal origin unless the cell or organoid line has been continuously imaged.

Some of the CellAggs in culture (25 % - 5/20) became darker over time or delaminated basally into single cells, a structure that likely included dead cells and cellular debris. Whether cells that lose connection with their neighbours die or whether dying cells are ejected from the larger CellAggs (Figure 3.7, C.3)), no corelation was found between cell delamination and any other culture-dynamic assessed.

It was evident by watching the videos that most CellAggs migrated over time (Video 3.1., Appendix - *https://youtu.be/AX72NXL1PqU*). To track this more accurately, we measured the distance from frame 1 (t=0h) to frame 35 (t=8.75 days) in a straight line per CellAgg and we found that all analysed CellAggs migrated at least 50 µm and around 60% migrated more than 200 µm in a single direction. Although the migration sometimes appeared to be more directional, some CellAggs moved in 'circular' tracks where the CellAggs did not appear to migrate in any particular direction (see tracks-patterns in Video 3.1., Appendix - *https://youtu.be/AX72NXL1PqU*). Enhanced cell migration has previously been associated with tumour cell plasticity, Epithelial-Mesenchymal Transition (EMT) and tumour metastasis and has been extensively studied in 2D. More recently, studies on the effect of the ECM environment on motility found that novel migration mechanisms (e.g. single cell, streaming and collective invasion) better represent *in vivo* tumour biology and are often neglected in 2D studies (Friedl et al. 2012).

Frame-by-frame tracking of the 20 CellAggs offered an opportunity to better understand the morphotype-dynamics previously seen in section 3.1.1. Interestingly, 60 % (12/20) of the *Calu-3* CellAggs appeared to undergo conversion from small solid to large lumen CellAggs. The remaining 40 % of the culture was divided into 30 % (6/20) CellAggs that remain solid

and 10 % (2/20) CellAggs showing lumen-morphology as early as day 2 of culture. Together with the previous data that showed a 90 % of lumen *Calu-3* CellAggs by day 20 in culture; the results indicate that there is a conversion from solid to lumen morphology over time of *Calu-3* CellAggs. These morphologies somewhat resemble published lung airway organoids that displayed different lung cell types and 3D cell-cell interactions (Kim et al. 2019; Sachs et al. 2019; Shi et al. 2020).

Overall, results suggest the need for a systematic study of all these dynamic events in different lines and with multiple replicates and media compositions in a 3D ECM controlled environment, in order to fully understand the complexity of 3D culture biology. Complex imaging techniques, sophisticated analysis methods and computational processes will ultimately be required to allow the complete interpretation of 3D CellAgg and organoid biology.

3.2. Effects of ATM/p53 status on radiation and drug response in 2D NSCLC cell lines

The complex dynamics and morphological variety exhibited by CellAggs prompted the initiation of a series of experiments to compare radiation responses in cells grown in 2D and 3D. Through a collaboration with Prof. Anderson Ryan's laboratory (Oxford University), we were able to access two matched pairs of cell lines that differ in the expression of the radiation response regulator ATM. These lines were NCI-H1299 (TP53 homozygous deletion) and *COR-L105* (TP53 WT) each line constitutively expresses either an shRNA against ATM or against a control target (GFP) (Table 3.3). As discussed in the Introduction, the combination of TP53 and/or ATM status should alter cell responses to radiation treatments (section 1.3.7. of the Introduction chapter). Moreover, synthetic lethal approaches based on tumour-specific mutations have been proposed to chemically enhance tumour cells' radiosensitivity. One such approach is the use of DNA Damage Response inhibitors (DDRi) in combination with ionising radiation (IR). Treatment with an ATR (Ataxia Telangiectasia and Rad-3 related) inhibitor has been proven to enhance radiosensitivity by preventing G_2/M cell cycle checkpoint arrest, especially when the G_1 checkpoint is deficient, as in the case of p53/ATM deficient tumours (Weber et al. 2015). The availability of matched cellular pairs differing in ATM expression offered the potential for examining interactions between genetic status and radiation and drug response in 3D by comparison with 2D assays.

Table 3.3. Matched pairs of NSCLC cell lines for drug-radiation treatments. NSCLC subtype and *TP53* and *ATM* status of NSCLC cell lines selected drug-radiation assays from the Ryan laboratory (Weber et al. 2015)

Cell line	NSCLC subtype	TP53 status	ATM status
NCI-H1299 *shATM*	Non clear NSCLC	Homozygous deletion	Stable knockdown
NCI-H1299 *shGFP*	Non clear NSCLC	Homozygous deletion	control
COR-L105 *shATM*	LUAD	WT	Stable knockdown
COR-L105 *shGFP*	LUAD	WT	control

3.2.1. Effects of seeding densities on ATM knockdown vs WT on growth-rate on TP53 WT vs mutated NSCLC cell lines in 2D

To first determine optimal seeding densities in our hands for 2D comparator studies, 50, 100, and 500 live cells / well of the *NCI-H1299* lines and 100, 500, and 1000 live cells / well of the *COR-L105* lines were seeded in 2D in 96 well plates and grown for up to 8 days. ATP levels were measured in endpoint assays each day with CellTiter-Glo® 3D.

Seeding densities of 100 and 500 live cells / well resulted in the highest relative increase in ATP levels for NCI-H1299 and COR-L105 lines respectively relative to levels immediately post-seeding, regardless of their ATM status (red arrows in Figure 3.8, A)). Interestingly, whilst in the TP53 WT line (COR-L105) shATM showed a slower rate of increase in RLU compared to the shGFP control (Figure 3.7, B.2)); the opposite was observed in the TP53-deleted line (NCI-H1299), where shATM had a faster RLU increase compared to its shGFP (Figure 3.7, B.1)). Although this might initially have suggested that different lines responded differently to the loss of ATM in terms of cell-growth; it was not possible to exclude the possibility that differences in the apparent growth-rates may be due to clonal variation unrelated to ATM function. Interestingly, ATM knockout prostate cancer cells have previously been reported to increase cell proliferation and xenograft tumour growth by altering metabolism and enhancing the Warburg effect (Xu et al. 2019). Growth-rate is nonetheless a relevant parameter to consider when interpreting radiation-responses since more rapidly proliferating cells are expected to be more sensitive to radiation-damage.

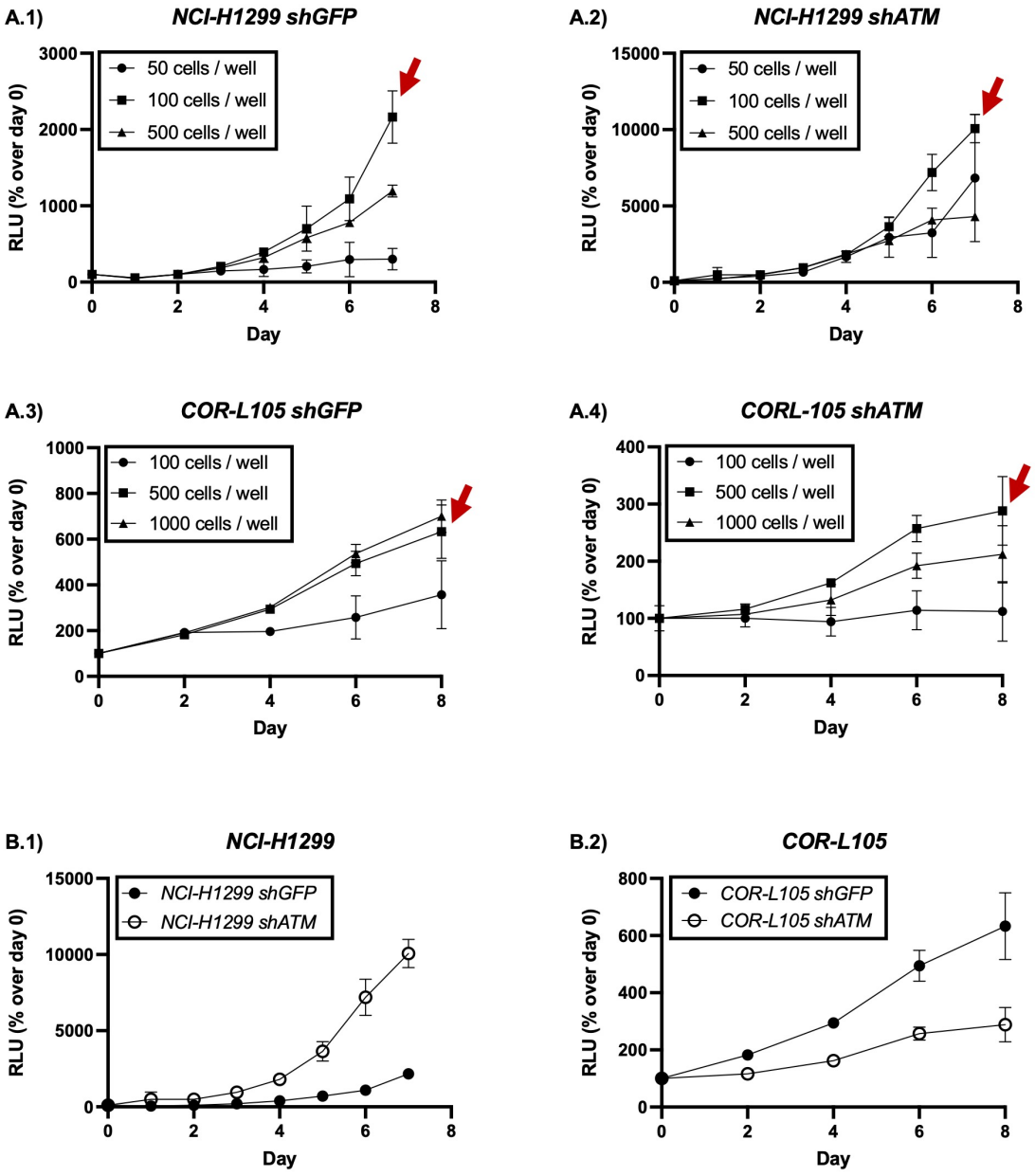

Figure 3.8. Effects of seeding density on growth rates of NSCLC shATM/shGFP paired lines. Viability, measured with CellTitler-Glo® 3D ATP live-cell assay, of NCI-H1299 (**A.1**) and COR-L105 (**A.3**) stable ATM knockdown 2D cell lines (shATM), or the respective shGFP controls (**A.2** and **A.4**, respectively) at different cell seeding concentrations (50, 100, 500 or 1000 cells / well) overtime. Red arrows signalling highest relative ATP increment curve. **B)** Comparison of growth rates *shATM* versus *shGFP* lines seeded at 500 cells/well. NCI-H1299 (**B.1**) and COR-L105 (**B.2**). n=3.

3.2.2. Effects of ATM knockdown on radiation-response on TP53 WT vs mutated NSCLC cell lines in 2D

Clonogenicity or Colony formation assays (CFA) are the current gold-standard method for determining reproductive cell death after radiation (Puck and Marcus 1956; Franken et al. 2006). Previous studies by Prof. Ryan's laboratory using CFAs showed that ATM knockdown increased the radiosensitivity of both the COR-L105 ($TP53^{WT}$) and the NCI-H1299 ($TP53^{null}$) lines (Weber et al. 2015). Nonetheless, we were keen to study radiation responses in simpler 2D ATP assays in anticipation of the potential complexity of setting up colony formation assays in 3D. In addition, it was noted that cell-replating assays are hard to perform at the higher throughput required to carry out drug and radiation dose-titrations. It was expected that radiation-response cell viability (ATP) assays in the four cell lines might mirror responses previously observed in CFA assays and that responses might be rationalised by reference to both ATM and p53 status.

Briefly, 100 cells / well of NCI-H1299 shATM / shGFP and 500 cells / well of COR-L105 shATM / shGFP were seeded in 96 well plates and irradiated with a single dose of 2, 4, 6 or 10 Gy of ionising radiation (IR). Culture medium was replaced with fresh medium 24 h post-IR to wash off death floating cells. Relative ATP levels were measured 3 and 5 days post-IR for NCI-H1299 and COR-L105 respectively.

Previous work by Dr. Anika Webber (Ryan's laboratory) using colony formation assays showed ATM knockdown reduced cell numbers in the shATM/shGFP line pairs after IR (Figure 3.9, B) and C)). We hypothesised that we would be able to reproduce this phenomenon using ATP readout assays.

In previous CFA assays with the shATM/shGFP line pairs, it was observed that p53 WT cells were more radiosensitive compared to p53 null cells, while ATM positive cells were more resistant to radiation. However, predicting the observed radiation responses from first principles based on mechanism is not straightforward, in part due to the relative effects of cell death versus repair and survival together with the differential effects of senescence versus apoptosis on ATP levels. These processes and outcomes that were predicted based on a combination of mechanism and prior CFA assay data are illustrated in Figure 3.9, A). Prior CFA data is shown in , Figure 3.9, B) and C) and our end point ATP data in Figure 3.9 , D) and E).

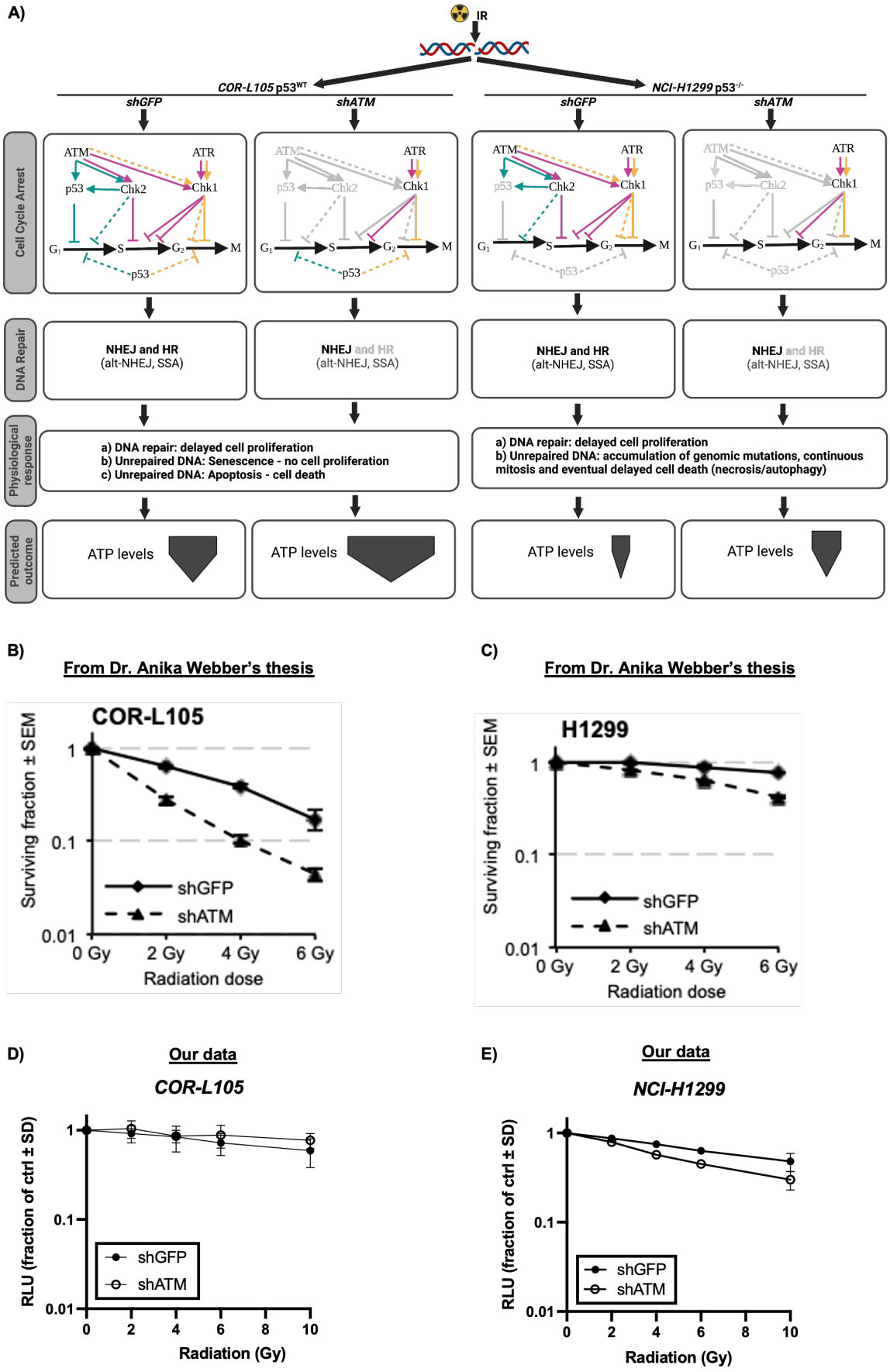

Figure 3.9. ATM and p53 status-dependant radiation response of NSCLC cell lines. A) Diagram of the expected post-irradiation double strand break (DSB) DNA damage response of a p53 WT (*COR-L105*) and p53

*Figure legend continues in the next page

null (*NCI-H1299*) NSCLC cell lines, each with ATM knockdown (*shATM*) and control (*shGFP*). Each column represents a cell line and each row a DNA damage response: cell cycle arrest, DNA arrest, physiological response, and predicted outcome (ATP level measurements post-ionising radiation, based in part of previously published data in these lines presented in B) and C) in this figure). In the cell cycle arrest diagram, solid lines represent post-DSB cell cycle primary response and dashed lines represent secondary response. G_1/S arrest pathways are shown in blue, intraS in pink and G_2/M in yellow. In the predicted outcomes the width of the arrows represents the relative drop in ATP levels after IR, the wider the arrow the lower the ATP levels. **B)** Clonogenic survival (CFA) of COR-L105 and **C)** NCI-H1299 *shATM* and *shGFP* lines following exposure of the indicated doses of IR. N=3, n=3. *This graph is published in Dr. Anika Webber thesis, Prof. Anderson Ryan laboratory, Oxford University.* **D)** Relative culture viability (CellTiter-Glo® 3D ATP live-cell assay) of COR-L105 and **E)** NCI-H1299 *shATM* and *shGFP* following exposure of the indicated doses of IR, measured 3 days (for NCI-H1299 lines) or 5 days (for COR-L105 lines) post-irradiation. N=3, n=3. Graphs made with GrapPad Prism 9.

As expected, RLU, indicative of ATP levels in all cultures, decreased with higher radiation dosages. shATM knockdown in the NCI-H1299 p53 null line resulted in a greater reduction in ATP levels than in the control line (Figure 3.9, E)). This was similar to that observed in the CFA assays (Figure 3.9, C)). By contrast no ATM status-dependent difference in relative ATP levels post-IR was detected in the TP53 WT line (COR-L105) (Figure 3.9, D). The smaller effect size in our NCI-H1299 data suggested that ATP assays generate less robust data than that produced by the CFA format.

3.2.3. Effects of ATM knockdown on cell-cycle state after irradiation of a TP53 mutated NSCLC cell line in 2D

We next wanted to assess in our hands the effects of irradiation on the cell cycle status. We chose to focus on the *NCI-H129* line in which we were able to reproduce the previously-described radiation responses. This line is p53 null and should have a defective G_1/S cell cycle arrest (although the ATM-Chk2 pathway should still be active) leaving the cells to accumulate in the G_2/M phase of the cell cycle. Previous data demonstrated that ATM knockdown further enhanced G_2/M arrest post-IR (Anika Weber thesis; Figure 3.10, A)).

Briefly, we irradiated (10 Gy) or sham-irradiated NCI-H1299 shGFP/shATM 2D cells. 24 h post irradiation, these were harvested, fixed in suspension and analysed by flow cytometry following Propidium Iodide staining. FlowJo software (Cell cycle assessment: Watson Model) was used to analyse 10,000 single cells per data point (see Methods for details; Figure 3.10, C).

Irradiation of NCI-H1299 cultures increased the number of cells in the G_2/M phase of the cell cycle (Figure 3.10, B) and C)). Moreover, the change in % (comparing Ctrl to IR) of cells in G_2/M was considerably higher in the ATM knockdown line compared to its shGFP

counterpart. These results and the differences with non-irradiated cells were consistent with what had previously been reported (Figure 3.10, A)) and suggested that the 2D NCI-H1299 shATM/shGFP cell response could be recapitulated in our hands.

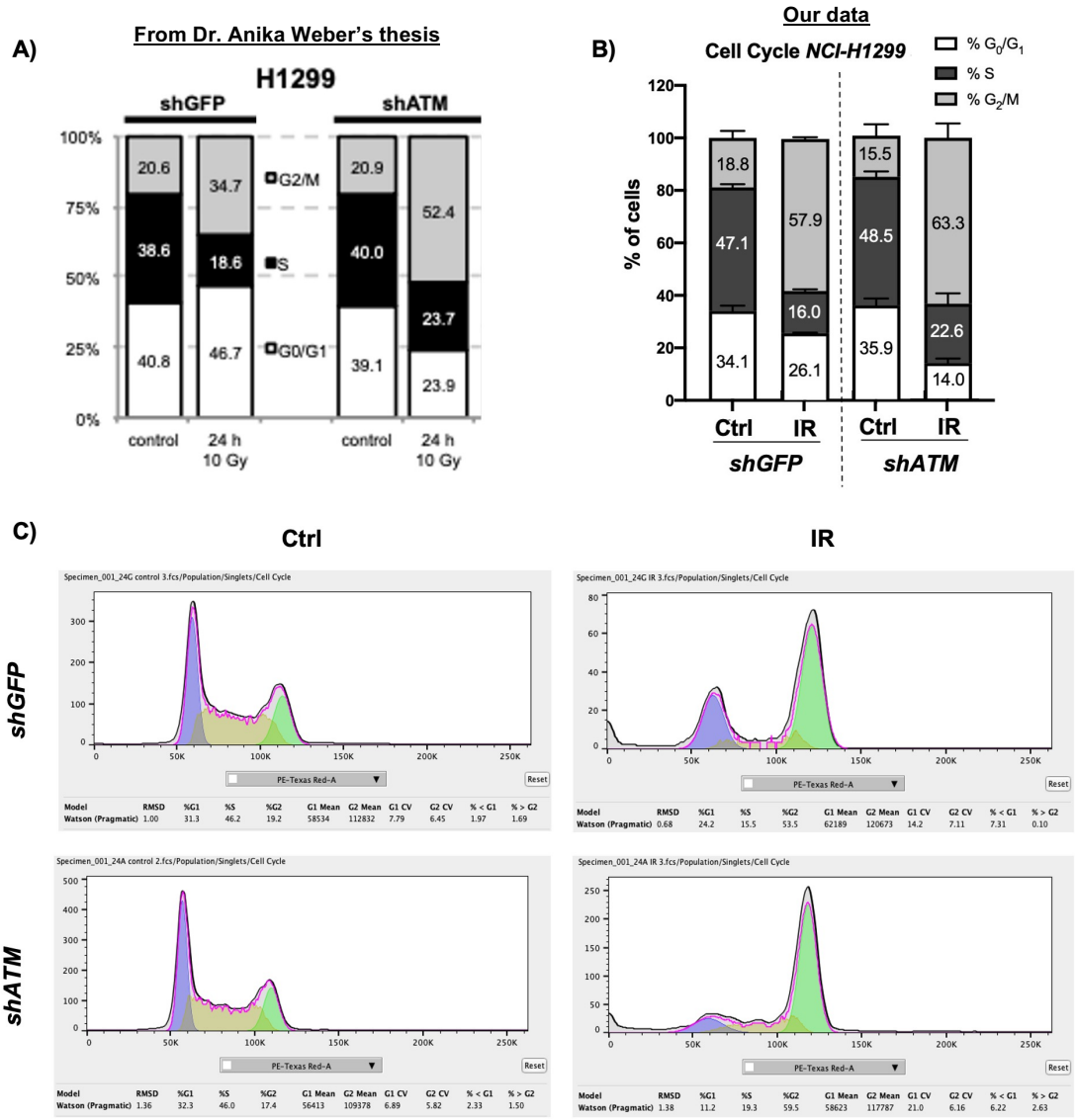

Figure 3.10. Post-irradiation cell cycle response of *NCI-H1299* 2D line. Cell cycle analysis (PI staining and flow cytometry) of *NCI-H1299* stable ATM knockdown cell line (*shATM*) or the respective control (*shGFP*), 24 h after 10 Gy of a single-dose irradiation showing increase of G_2/M after IR. **A**) Cell cycle analysis data carried out by Dr. Anika Webber. N=3. This is published in Dr. Anika Webber thesis, Prof. Anderson Ryan laboratory, Oxford University. **B)** Cell cycle analysis data. n=3. C) Representative histogram of cell cycle. Data was analysed in FlowJo 10.8.2. Graphs made with GrapPad Prism 9. **C)** Representative histogram of cell cycle Data was analysed in FlowJo 10.8.2.

3.2.4. Effects of ATM knockdown on radiation and DDRi combination treatment - response on TP53 mutated NSCLC cell lines in 2D

A synthetic lethal approach using a combination of radiation and an ATR (Ataxia Telangiectasia and Rad-3 related) inhibitor should radiosensitise G_1 checkpoint arrest-deficient tumours (Figure 3.11, A)). Dr. Anika Weber (Ryan's laboratory) previously showed that the use of an ATRi in combination with the loss of ATM resulted in premature entry into mitosis, chromosome fragmentation, mitotic catastrophe and cell death following irradiation of NCI-H1299 cells (Weber et al. 2015). They also showed that co-treatment with IR and ATRi in an ATM competent line (Figure 3.11, B)) yielded a similar colony formation response compared to just IR treatment in the NCI-H1299 ATM knockdown line. We set out to determine whether we were able to reproduce these data with ATP readouts.

100 cells / well of NCI-H1299 shATM / shGFP were seeded in 96 well plates and allowed to attach for 24 h. They were then treated with a 0.1 μM of the ATRi (VE-822) for 1 h before irradiation to ensure the inhibition of the molecules at the irradiation time with a single dose of 2, 4, 6 or 10 Gy. Twenty-four hours post-IR the DDRi was removed and replaced with fresh culture medium lacking the DDRi. Three days post-IR, ATP levels were measured.

With increasing dosages of ionising radiation, a decrease in RLU was observed (Figure 3.11, C)). This was enhanced by the addition of the ATRi in each line. IR-treated shGFP line was the most radioresistant, whilst IR and ATRi co-treated shATM line resulted in the most radiosensitive line. Interestingly, both IR-only treated shATM line and IR and ATRi co-treated shGFP line showed similar decreases in ATP levels. This trend was consistent, with what was mechanistically expected (Figure 3.11, A)) and with what had previously been shown by Prof. Ryan's laboratory in their CFAs (Figure 3.11, B)). We also showed that radiosensitivity to the ATRi was dose-dependent and could also be applied to co-treatment with a Poly (ADP-ribose) Polymerase (PARP) inhibitor (Supplemental Figure 3.1, Appendix).

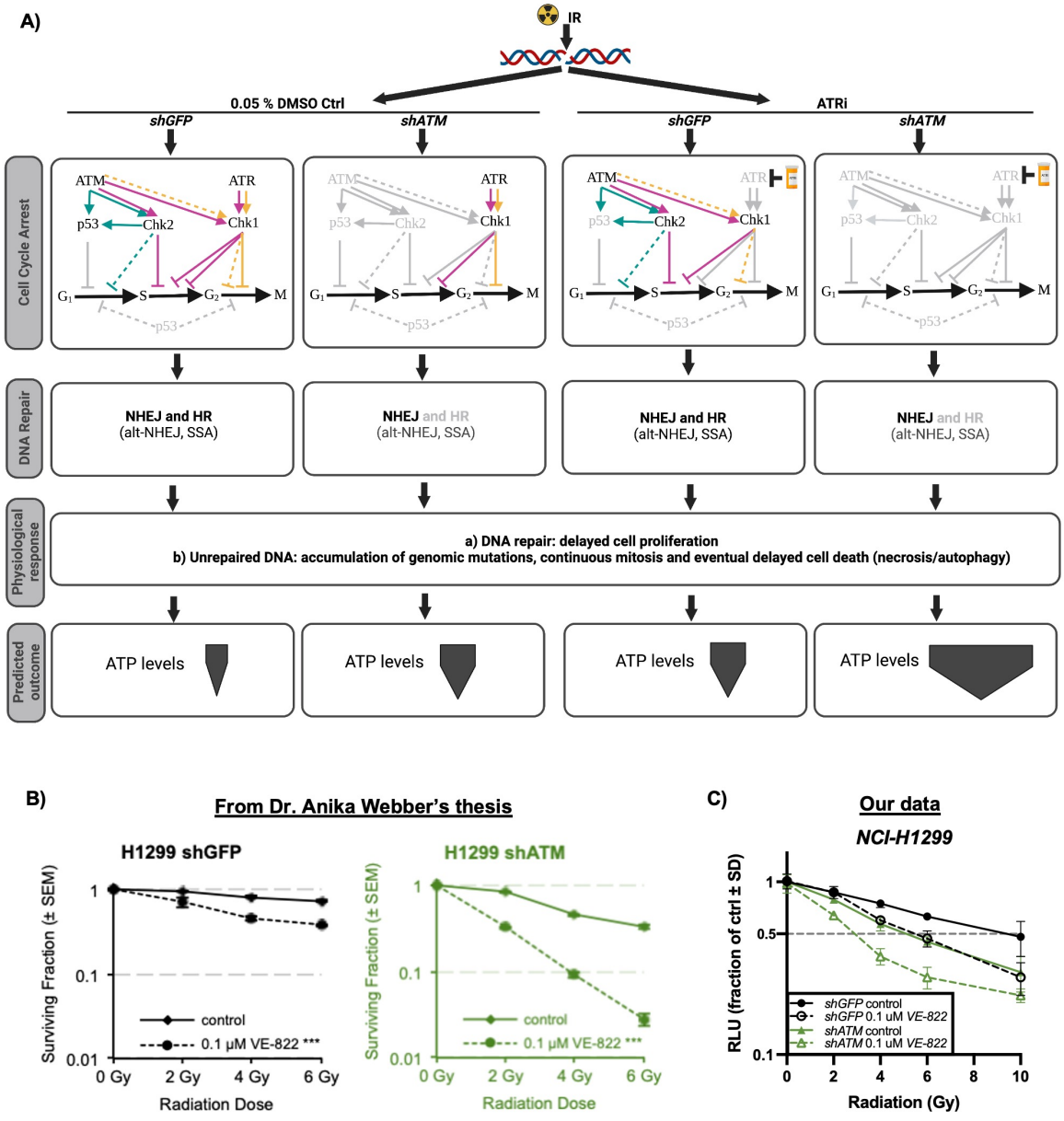

Figure 3.11. ATM and p53 status-dependant radiation and ATR inhibition combination response of NSCLC cell lines. A) Diagram of the expected post-irradiation double strand break (DSB) DNA damage response of the p53 null (*NCI-H1299*) NSCLC cell lines, each with ATM knockdown (*shATM*) and control (*shGFP*), either treated with 0.1 µM *VE-822* ATR inhibitor (ATRi) or a 0.05 % DMSO control. For details of the structure of the diagram, see Figure 3.10, A).. **B)** Clonogenic survival (CFA) of stable ATM knockdown cell lines and corresponding *shGFP* controls derived from *NCI-H1299* cells following combined treatment with IR and ATRi. Cells were irradiated after pre-treatment with 0.1 µM *VE-822* for 1 h. *VE-822* exposure was continued for 23 h after irradiation. Surviving fractions were normalised to DMSO treated or inhibitor treated mock-irradiated controls, respectively. N=3, n=3. Error bars = SEM. This is published in Dr. Anika Webber thesis, Prof. Anderson Ryan laboratory, Oxford University. **C)** Relative culture viability (CellTitler-Glo® 3D ATP live-cell assay) of stable ATM knockdown cell lines and corresponding *shGFP* controls derived from *NCI-H1299* cells following combined treatment with IR and ATRi. Cells were irradiated after pre-treatment with 0.1 µM *VE-822* for 1 h. *VE-822* exposure was continued for 23 h after irradiation. RLU were normalised to DMSO treated or inhibitor treated mock-irradiated controls, respectively. N=3, n=3. Error bars = SD. Graphs made with GrapPad Prism 9.

Overall, in this section we have confirmed the usefulness of the TP53 mutated NCI-H1299 ATM knockdown (shATM) and control (shGFP) lines to assess the ATM-TP53 status-dependant radiation and DDRi combination-therapies' response with a high-throughput technique using ATP levels. In the next section, we aimed to explore this further, in a 3D Matrigel-embedded context.

3.3. Effects of ATM/p53 status on radiation and drug response in 3D NSCLC CellAggs

3.3.1. Effects of seeding densities on ATM knockdown vs WT on growth-rate on TP53 WT vs mutated NSCLC cell lines in 3D

To first determine optimal seeding densities of NCI-H1299 shATM and the control shGFP (Table 3.3.) lines in 3D, different cell concentrations were seeded in Matrigel ECM to create CellAggs. The line was maintained in 2D and seeded in 3D for each experiment, utilising culture methods used for the CellAggs described in Figure 3.1. NCI-H1299 maintenance culture medium was used for all formats. One hundred, 500 and 1000 live cells / μL Matrigel were seeded and cultured in 10 μL Matrigel blobs in 96 well-plates and grown for up to 15 days. ATP levels were measured in endpoint assays on days 0, 3, 5, 7, 10, 12 and 15 with CellTiter-Glo® 3D.

All seeding densities resulted in the formation of CellAggs. However, 100 cells / μL Matrigel showed the highest fold increase in ATP levels for both the shATM and the shGFP NCI-H1299 CellAggs after 3-5 days culture (red arrows in Figure 3.12, A)). As a consequence, this initial cell concentration was used for subsequent assays. Interestingly, the increase in cell numbers (ATP levels) observed in 3D-seeded NCI-H1299 CellAggs, was greater in shGFP than shATM cells; the opposite of what was observed in 2D (Figure 3.8, B.)). Of particular importance, it was observed that 3D embedded CellAggs were accompanied by 2D cells which had, it was assumed, migrated to contact the underlying plastic in both shATM and shGFP NCI-H1299 lines (Figure 3.12, C)).

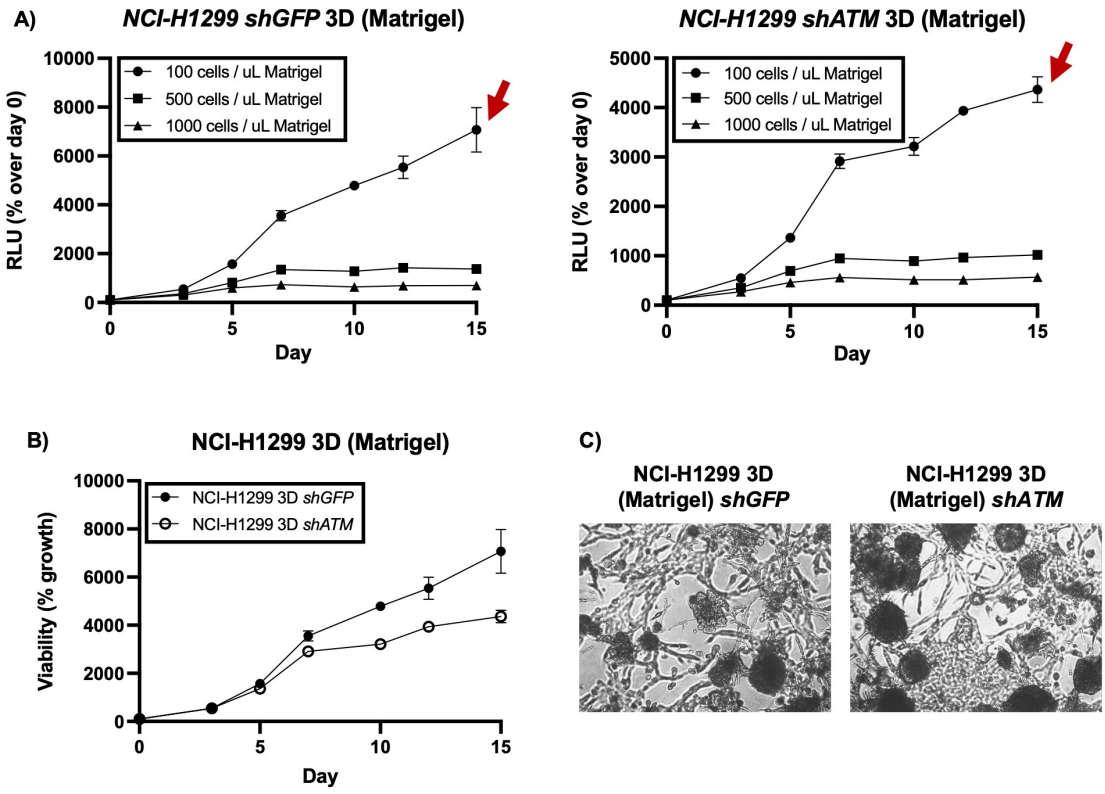

Figure 3.12. Initial seeding density and ATM status affects viability and window of assay in NSCLC spheroids in Matrigel. A) Viability, measured with CellTitler-Glo® 3D ATP live-cell assay, of NCI-H1299 stable ATM knockdown CellAggs in Matrigel (shATM), or the respective shGFP controls at different cell seeding concentrations (100, 500 or 1000 cells / μL Matrigel) overtime. **B)** Direct comparison of stable ATM knockdown effect on viability overtime with optimal seeding density (100 cells / μL Matrigel) on NCI-H1299 CellAggs. **C)** Representative images of NCI-H1299 shGFP/shATM CellAgss grown in Matrigel. n=3. Graphs made with GrapPad Prism 9.

3.3.2. Effects of ATM knockdown on radiation and DDRi combination treatment - response on TP53 WT NSCLC CellAggs in 3D

Ultimately, the propensity of the *NCI-H1299 shGFP / shATM* lines to migrate and contact the plastic meant that we were unable to distinguish between 2D and 3D responses to radiation using bulk ATP responses as readouts. Nonetheless, we were able to image 3D CellAgg responses to radiation. Following IR, an increase in γH2AX and 53BP1 foci, indicative of DSB locations, was observed in NCI-H1299 CellAggs compared to their non-irradiated control (Supplemental Figure 3.2., Appendix). Maximum signal for both markers was achieved 1 h post-IR, and by 24 h after treatment no γH2AX or 53BP1 foci were locatable, suggesting that most of the DNA of the 3D structures was repaired by 24 h post-IR (Supplemental Figure 3.3., Appendix).

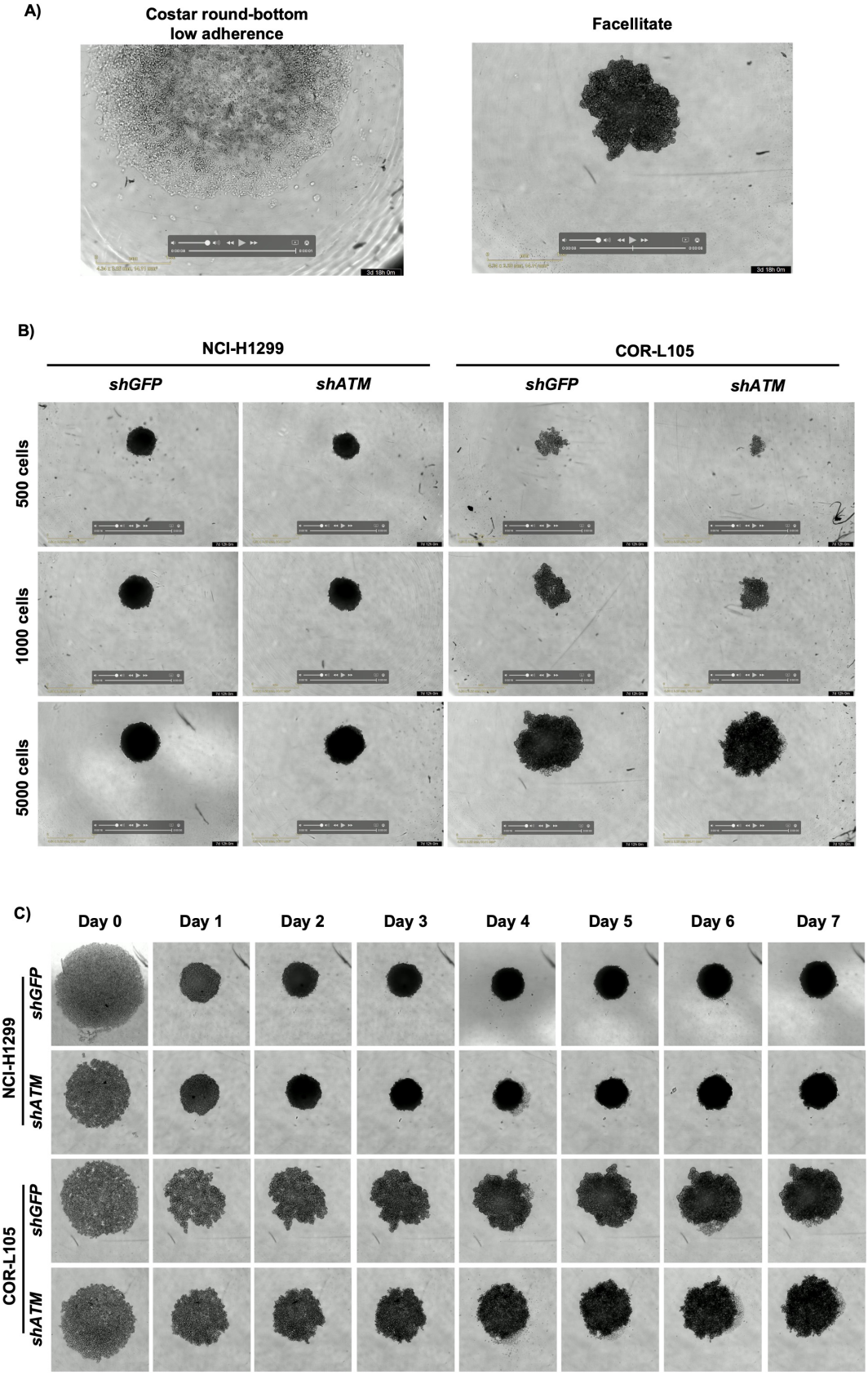

Figure 3.13. NSCLC spheroids growing without an ECM. A) COR-L105 *shGFP* line can only grow in 3D in specially coated FaCellitate, as they adhere even in low adherence round bottom plates. **B)** COR-L105 and NCI-H1299 stable ATM knockdown (shATM), or the respective shGFP controls spheroids in Facellitate plates at different cell seeding concentrations (500, 1000 or 5000 cells /well) on day 7 in culture or **C)** with a concentration of 5000 cells / well overtime. All mages were taken with the single spheroid mode on the IncuCyte®S3.

Some effort was put in to attempts to reduce 2D attachment in the presence of Matrigel. One solution that was explored was to culture the cells in coated FaCellitate plates (Figure 3.13). When cultured in suspension with no ECM we were able to grow cells in 3D. However, this format generates single spheroids per well and, perhaps due to the lack of Matrigel, the structures did not show the diverse phenotypic heterogeneity observed in CellAggs (Figure 3.2). Unfortunately, Matrigel could not be added to these plates as it lifted off the plastic within seconds of plating, due to the ultra-low adherence nature of the surface.

3.4. Key summary

In this chapter we wanted to explore whether NSCLC immortalised cell lines could recapitulate some of the intra-tumour heterogeneity responses to radiation if cultured in 3D with the support of the ECM. We showed that even though plastic-adapted cell lines are expected to be genetically homogeneous and probably clonal, different CellAgg morphotypes (Solid, Budding, Lumen) formed from the same lines. This was promising as different morphotypes imply that cells positioned at different places within the CellAggs may experience distinct physiological signals that might in turn modulate their radiation response in physiologically relevant ways. Moreover, we were able to individually track 3D CellAggs growing in Matrigel overtime and follow some of the morphotype-dynamics of the culture. This should in turn allow the quantification of different structures' morphological responses to radiation.

We verified in our hands that ATM / p53 deficient NSCLC lines rely on the G_2/M checkpoint for cell cycle arrest and DNA repair after radiation-treatment; but that loss of function of all ATM, p53 and ATR were necessary for a strong radio-sensitisation. Specifically, we showed that this response could be seen in a high-throughput system measuring viability (ATP), rather than just the gold-standard CFA, but that the effect size (assay window) needs to be assessed on a line-to-line basis.

We also learned that growing CellAggs in an ECM in 3D is a line-dependant phenomenon, as some lines have such a high propensity to bind to plastic that it was not possible to compare 2D with 3D data. As cell lines, by definition, are selected for growth on plastic, we chose to focus subsequently on primary organoid lines which had never been optimised for growth on plastic.

4. Results – Establishment and characterisation of human-derived NSCLC organoids

At the outset of the PhD, the goal was to establish a small bank of NSCLC organoids and methods that could be used to characterise their radiation responses. This chapter describes the approaches taken to generate NSCLC organoids and their use for DDRi and radiation combination assays.

At the time this project was initiated, no long-term patient-derived NSCLC organoids had been described in the literature. Four months into the project and while the Cardiff clinical tissue pipeline was being established, the first paper describing 'Human airway disease' organoid-models was published (Sachs et al. 2019). Since that report, several other protocols have been published by different groups (Kim et al. 2019; Chen et al. 2020; Dijkstra et al. 2020; Li et al. 2020; Shi et al. 2020; Werner et al. 2021; Ma et al. 2022). As will be described, our goal of establishing a biobank of NSCLC organoids that was large enough for the intended studies was unsuccessful and the radiation response work was eventually undertaken utilising organoids from a biobank established by Prof. Ming-Sound Tsao's group at the Princess Margaret Cancer Centre, Toronto, Canada. Nonetheless, a small number of organoid lines were established at Cardiff University.

4.1. Establishment of UHW patient-derived NSCLC organoids

To create a patient-derived NSCLC and normal lung organoids biobank, we worked with the University Hospital Wales (UHW) and the Wales Cancer Bank (WCB) to establish a NSCLC tissue pipeline based on what was previously produced for Colorectal Cancer (CRC) organoids (Badder et al. 2020). Ethical approvals, consent forms and critical working relationships with clinical personnel were established and the pipeline started producing biopsies that were processed for culture. Prior to the Covid-19 outbreak, 9 lung biopsies were processed in experiments that were initially aimed at defining optimal culture conditions. The samples comprised 1 NSCLC and 4 matched NSCLC and normal adjacent tissue pairs (4+4 samples), from 21/05/2019 to 24/09/2019. Unfortunately, the pipeline was suspended with the onset of Covid-19. Initially, it was anticipated that the pipeline would be reopened at a later date. However, this did not happen and lung sampling and the associated clinical and technical support for the project was withdrawn for the duration of this project.

4.1.1. Clinical information on specimens that were received from UHW

Clinical information on the specimens and histopathological diagnosis can be seen on Table 4.1. All resected tumour material, except for the small pieces used for this project, was routinely fixed and analysed by UHW histopathologists as part of the diagnostical pipeline. Specimens were classified based on H&E histopathology. When the visual regularities of cell shapes and tissue distributions were not clear enough to classify the tissue, NSCLC subtype-specific marker stainings were used for further classification. CK7, TTF-1, and Napsin-A were used to identify LUAD whilst p63 and CK5/6 identified LUSCs (Osmani et al. 2018; Nicholson et al. 2022). Additional markers were used to classify the Iso2 specimen (as specified in Table 4.1) as it was found to be positive for both LUAD and LUSC markers (CK7, TTF-1, Napsin-A and p63). A KRAS mutation was identified in the Iso3 sample. Mutated KRAS is common in LUAD and can be used for targeted therapy (Jamal-Hanjani et al. 2017). Stage T2 and T3 specimens were received (T1 tumours were too small to have enough tissue usable for research, as all tissue is fixed for diagnostical sampling). Cancer was found in the lymph nodes in two of the patients (relating to samples Iso2 and Iso3) although metastasis wasn't confirmed for any of the specimens. Overall, we received one Lung Squamous Cell Carcinoma (LUSC – Iso1) and 4 Lung Adenocarcinomas (LUAD – Iso2-5).

Table 4.1. Histopathological information of specimens received from the UHW. LUAD markers: CK7: Cytokeratin 7; TTF-1: Transcription Termination Factor 1; Napsin-A; CK20: Cytokeratin 20; CDX2: Caudal Type Homeobox 2; GDCFP-15: Gross Cystic Disease Fluid Protein 15. LUSC markers: p63; CK5/6: Cytokeratin 5/6; GATA3. S100: prognostic marker involved in cell invasion and metastasis. KRAS: Kristen Rat Sarcoma Virus. N/A: not available. Histopathological assessment on samples was carried out by NHS pathologists and anonymised data was procured to us via WCB.

Sample ID	Diagnosis	TNM staging	Sex	Age	CK7	TTF1	Napsin-A	P63	CK5/6	CK20	GATA3	S100	CDX2	GDCFP-15	KRAS
Iso1	LUSC	T3 N0 MX	M	68	N/A	N/A	N/A	N/A	N/A	N/A	N/A	N/A	N/A	N/A	N/A
Iso2	Poorly differentiated LUAD	T2b N2 M0	F	77	+	+	+	+	-	-	-	-	-	-	N/A
Iso3	LUAD	T2b N2 MX	F	47	N/A	+	+	-	-	N/A	N/A	N/A	N/A	N/A	c.35G>C p.(Gly12Ala)
Iso4	LUAD	T2b N0 MX	F	72	N/A	N/A	N/A	N/A	N/A	N/A	N/A	N/A	N/A	N/A	N/A
Iso5	LUAD	T3 N0 MX	F	61	+	+	+	N/A	N/A	N/A	N/A	N/A	N/A	N/A	N/A

4.1.2. Pipeline and establishment of UHW patient-derived NSCLC organoids

From the NSCLC tissue specimens, we were able to establish 3/5 organoid-lines (Iso1LT, Iso3LT and Iso5LT). Note that our definition of establishment encompasses long-term culture, freezing and successful recovery of the lines. Iso2LT and Iso4LT were slowly lost during passages over the first 1-2 months post isolation (data not shown). The same applied to all adjacent normal samples which unfortunately did not achieve long-term organoid - formation. In fact, one of the now widely recognised problems of NSCLC organoids was the low success rate of long-term expansion, which was only 28 % from needle biopsies in Sachs et al. (Sachs et al. 2019).

Samples were received on ice in transport medium (see methods) and were immediately processed based on the Sachs et al. (Sachs et al. 2019) procedure (detailed in methods) (Figure 4.1, A)). Most of the specimens received consisted of a layer of tissue 0.3 x 1x1 cm (Figure 4.1, B)). Several alterations to the published protocol were carried out for the following reasons. It was observed that normal tissue dissociated faster than tumour when incubated with collagenase at 37 ^{O}C, so an extended digestion was found to be required together with careful monitoring of the time required to obtain a cloudy suspension (never exceeding 3 h of incubation). In addition, whenever blood was observed in the sample, incubation with an erythrocyte lysis buffer was performed. To avoid fibroblast contamination, we implemented a fibroblast-adherence step in which the cells were incubated on tissue culture plastic in a medium with 10 % FBS for half an hour (see methods). This step was additionally applied in between passages for some of the lines when fibroblast-like structures in 3D were observed under the microscope.

A mixture of single cells and cell clusters were seen immediately after plating the isolated cell suspensions in matrigel with growth factor-rich Sachs medium (*Figure 4.1, **C**)*). Due to the mix of single cells and clusters, we were not able to calculate a precise seeding isolation cell density. However, we observed that a high density was necessary for the formation of compact, organoid-like structures. Samples that had lower initial densities did not form organoid-like clusters until they were down-passaged into a smaller volume. The need for initial high-densities for organoid-formation during line-establishment had previously been reported for other organoid-lines (Shi et al. 2020).

By the third day in culture, organoid-like structures had formed and about a week after isolation the samples were passaged with manual trituration (without breaking the already

formed small structures) to remove dead cells that were 'trapped' in the Matrigel and to allow the surviving structures to better grow *(Figure 4.1, **C**))*. At this stage, these structures were quite small (~ 30 µm). For expansion of the samples, cultures were passaged every 10-15 days, when structures grew bigger than 200 µm, when dark cores were observed or when single cells appeared to be delaminating from larger structures. For passaging, larger structures were broken into single cells or cell clusters with TryPLe – see methods.

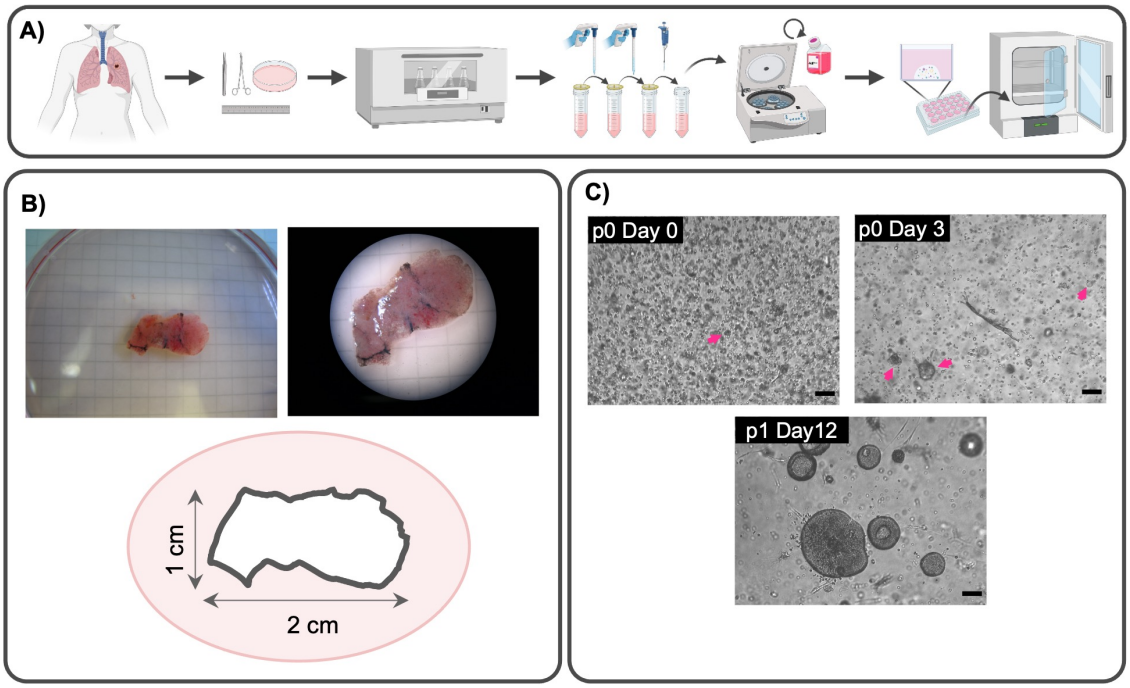

Figure 4.1 Isolation of Lung/NSCLC organoids from patients in UHW. A) Diagram of tissue-processing and organoid isolation (based on (Sachs et al. 2019)). **B)** Example pictures and diagram of received specimens for organoid-isolation. Each square in the background is 0.5 x 0.5 cm, for reference. **C)** Pictures of Iso1LT sample at Day 0 and 3 (immediately after isolation) and 12 days after the first passage. Pink arrows point formed organoids in early cultures. Scale bar: 50 µm.

4.1.3. Characterisation of UHW patient-derived NSCLC organoids

The Sachs paper reported that normal tissue organoids overgrew tumour organoids and described organoids with lumens as having a 'normal phenotype' similar to that generated by normal lung epithelium (Sachs et al. 2019). Sachs et al. added Nutlin-3A to their medium to select for p53-mutant cultures as a method to select for tumour versus normal organoids since Nutlin induces apoptosis in cells (normal and tumour) that are wild type for p53. However, whilst p53 is mutated in 91 % of LUSC, only 46 % of LUAD have a TP53 mutation (Jamal-Hanjani et al. 2017). Unfortunately, the p53-status or histopathology was not known in advance and it was therefore decided to avoid using Nutlin-3A initially. Our

specimens came from the core of the tumour and, therefore, it was expected to be mainly comprised of tumour cells. However, no prior cell-type specific curation was done at the time of isolation and establishment (with the aim of maintaining intratumour heterogeneity) and thus, we could not control for 'normal' cell contamination. The samples needed to be expanded to a sufficient level to allow an analysis of their genomic background to check their tumour status. In the meantime, some characterisation was done on the samples while expanding sufficient material for freezing down.

As we were expanding the cultures, budding, solid and cystic organoid-like morphotype structures were observed (Figure 4.2). These morphotypes have previously been described for 3D CellAggs (Figure 3.2/3, Chapter 3). To further analyse this phenomenon, we quantified the percentage of each morphotype by reviewing microscopic images of each organoid-line (Iso1LT, Iso3LT, and Iso5LT) at different time points (day 3 – 20 post-passaging in single cells) (Table 4.2).

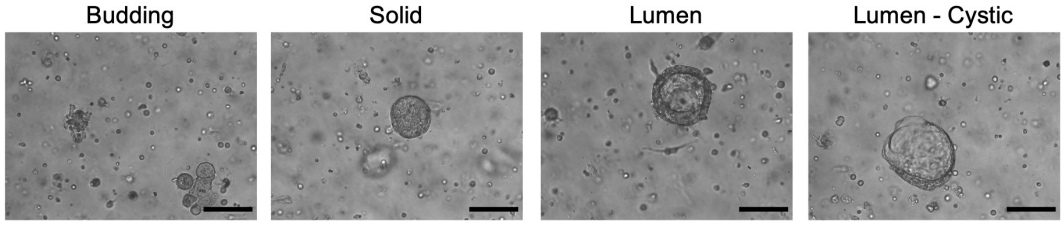

Figure 4.2. Representative brightfield images of UHW patient-derived organoids' morphotypes. Scale bars: 100 μm.

Table 4.2. UHW patient-derived organoids' morphotypes quantification depending on the days in culture. In this table the different percentages of morphologies that could be observed when culturing NSCLC patient-derived organoids from single cells up to 20 days in culture are displayed. The percentages are taken qualitatively: by observation of pictures of the cultures at different timepoints stablished in the.

NSCLC organoid-line	Days in culture	Morphotype		
		Solid	Budding	Lumen
Iso1LT p2	**3**	85	5	10
	5	85	5	10
	7	80	5	15
	10	70	5	25
	12	70	5	25
Iso3LT p2	**3**	60	>1	50
	5	55	>1	55
	7	55	>1	55

Table continues in the next page

	10	55	>1	55
	12	55	>1	55
	15	55	>1	55
Iso5LT p9	**3**	80	>1	20
	5	80	>1	20
	10	70	>1	30
	12	70	>1	30
	16	60	>1	40
	20	50	>1	50

The most common morphotype for NSCLC organoids was solid, comprising up to 85 %, 60 % and 80 % in Iso1LT, Iso3LT and Iso5LT respectively (Table 4.2). The lumen morphotype was also common in these lines, reaching up to 55 % of the culture in Iso3LT organoids. It was also noted that more lumen morphotypes appeared in all lines over time (e.g lumen morphotype comprised 10 % on day 3 to 25 % on day 12, in the case of Iso1LT) coinciding with larger organoids. Lumen organoids have previously been related to the overgrowth or normal organoids in culture, as previously mentioned (Sachs et al. 2019). The fact that this morphotype appeared to increase over time demonstrated the importance of continuously checking the tumour status of the samples at later timepoints. Although some budding organoids were seen, this was not a very common morphotype in the analysed lines.

We also aimed to study the effect of seeding concentration on organoids' viability. In the previous chapter we used ATP measurement (CellTitter-Glo 3D, Promega) to assess viability in culture with effective results in NSCLC cell lines. However, this is an endpoint assay. Patient-derived organoids were very precious samples (particularly line expansion, freezing and banking). Therefore, a cell-permeant resazurin based method was used (PrestoBlue, Thermo Fisher Scientific), this measured the reducing environment of viable cells as a culture-viability readout and did not require cell lysis. Suspensions of either 100, 500 or 1000 live cells / µL Matrigel were plated in 10 µL Matrigel blobs for up to 18 days. On days 3, 6, 9, 12, 15 and 18 after seeding, the organoids were incubated with PrestoBlue, fluorescence was measured, and clean culture medium was replenished after each measurement.

Relative Luminescence (RLU) increased continuously up to day 9 in culture in all seeding densities for both Iso1LT (LUSC) and Iso5LT (LUAD) organoid-lines, suggesting continuous cell growth (Figure 4.3). However, growth at all seeding concentrations in

Iso5LT and the lowest seeding concentration in Iso1LT appeared to plateau by day 9. Notably, the percentage of growth for Iso5LT (nearly 3000 % of seeding day) line was considerably higher than those for Iso1LT (~1000 %), suggesting that the proliferation-rate of the organoids from the LUAD sample could be three times that of the LUSC sample. It was noticed however, that repeated exposure to PrestoBlue reagent eventually stained the Matrigel blue, making imaging of organoids difficult. Furthermore, although the reagent was classified as non-toxic, repetitive exposure might have indirectly affected culture viability and the structural integrity of the ECM. Therefore, it was concluded that the use of the reagent wasn't optimal in combination with Matrigel for long-term measurements (>5 days). As an alternative, parameters such as organoid number, average and maximum diameter and cell-covered area might be used to measure culture-growth during the early establishment of organoid-cultures (Supplemental Figure 4.1., Appendix).

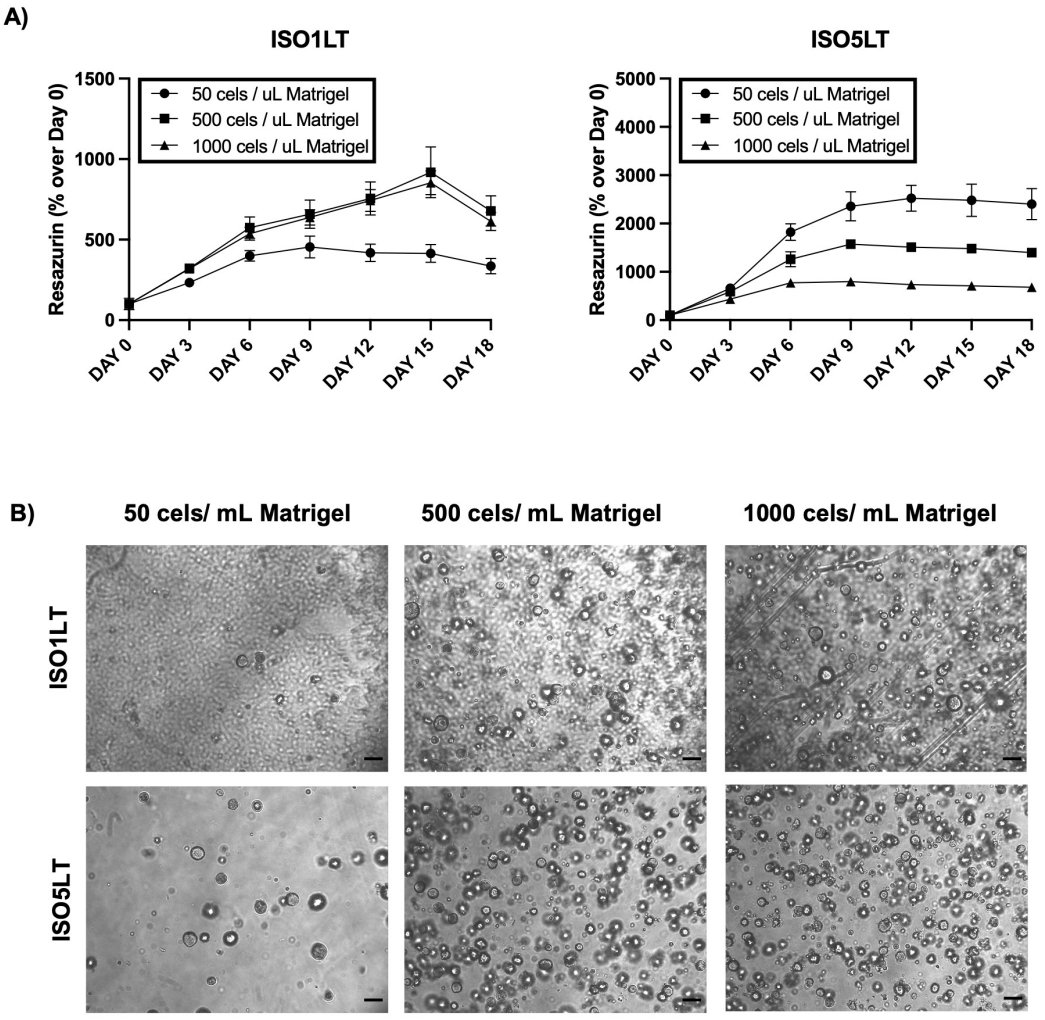

Figure 4.3. Effect of initial seeding concentration to viability of UHW patient-derived organoids. A) Viability, measured with PrestoBlue live-cell assay of Iso1LT and Iso5LT lines at different cell seeding concentrations (50, 500 or 1000 cells / μL Matrigel, in 10 μL Matrigel blobs) overtime. **B)** Representative pictures of cultures from (A) on day 9 of culture. Pictures taken with a camera atta inverted microscope. 3 technical replicates were performed per experiment. Graphs made with GrapPad Prism 9. Scale bar: 100 μm.

To determine whether the patient-derived NSCLC organoid-lines were primarily comprised of tumour cells, DNA from the cultures was characterised by sequencing for commonly mutated NSCLC genes (performed routinely by the All Wales Medical Genetics Service) (see Methods). Hotspots mutations in NRAS, RET, KRAS, ERBB2, PIK3CA, EGFR, MET, BRAF, CDKN2A and PTEN were analysed by next generation sequencing in the lines that had been established: Iso1LT (p8), Iso3LT (p13) and Iso5LT (p6). As shown in Table 4.3, the only variant calls found were just known polymorphisms. It was extremely unlikely that none of the mutations within the screen would be identified in DNA that was definitively derived from tumour, strongly suggesting that the majority of the DNA from the lines at the time of sequencing (passages 6-13) was from normal cells (Jamal-Hanjani et al. 2017). To further check this conclusion, culture of the three lines was attempted in a growth factor-restricted medium that was later shown to support the growth of tumour but not normal cells (Kim et al. 2019). Unfortunately, no organoids grew suggesting that by this point, tumour organoids had been lost from the cultures (Supplemental Figure 4.2., Appendix).

Table 4.3. UHW patient-derived organoids' NSCLC hotspot mutations. Variant calls after NGS on NSCLC organoids carried by NSH experts as detailed in Methods.

Organoid-line	Gene	Exon	Variant	HGVS c.	HGVS p.	Allele freq.	Conclusion
ISO1LT P8	RET	2|20	10:43595968A>G	c.135A>G	c.135A>G (p.=)	0.961	**WT**
	RET	7|20	10:43606687A>G	c.1296A>G	c.1296A>G (p.=)	0.484	**polymorphism**
	RET	13|20	10:43613843G>T	c.2307G>T	c.2307G>T (p.=)	0.972	**WT**
	ERBB2	17|27	17:37879588A>G	c.1963A>G	p.Ile655Val	0.487	**Known Poly**
ISO3LT P13	RET	13|20	10:43613843G>T	c.2307G>T	c.2307G>T (p.=)	0.474	**Poly**
	RET	14|20	10:43615094C>T	c.2508C>T	c.2508C>T (p.=)	0.495	**polymorphism**
	ERBB2	17|27	17:37879588A>G	c.1963A>G	p.Ile655Val	0.495	**Known Poly**
	RET	7|20	10:43606687A>G	c.1296A>G	c.1296A>G (p.=)	0.48	**polymorphism**
	RET	2|20	10:43595968A>G	c.135A>G	c.135A>G (p.=)	0.956	**WT**
	EGFR	20|28	7:55249063G>A	c.2361G>A	c.2361G>A (p.=)	0.492	**Known Poly**
ISO5LT P6	RET	13|20	10:43613843G>T	c.2307G>T	c.2307G>T (p.=)	0.969	**WT**
	ERBB2	17|27	17:37879588A>G	c.1963A>G	p.Ile655Val	0.462	**Known Poly**
	RET	2|20	10:43595968A>G	c.135A>G	c.135A>G (p.=)	0.964	**Poly**
	RET	2|20	10:43596085C>A	c.252C>A	p.Asn84Lys	0.048	**Genuine**
	RET	7|20	10:43606687A>G	c.1296A>G	c.1296A>G (p.=)	0.976	**polymorphism**

Following the Covid-19 shutdown, an alternative PDX-based approach was explored via collaboration with Champions Oncology in collaboration with Cellesce Ltd.

4.2. Establishment of PDX-derived NSCLC organoids

As primary human tissue was no longer available for organoid generation, a decision was taken to purchase PDX tumours from Champions Oncology. As discussed in the introduction, PDX tumours have never been grown on plastic and have been shown to perform better that CDX models for drug discovery applications. Champions Oncology agreed to ship freshly isolated tumours from a subset of their lung cancer NSCLC lines. Isolation and initial setup of these lines to establish NSCLC organoids was done by Mr. Matthew Zverev due to restricted access to Cardiff University labs as a result of the Covid-19 outbreak.

4.2.1. Sample criteria and tumour characteristics

Champions Oncology Ltd offered a wide range of PDXs with both whole exome and RNA sequencing data available, useful for linking to treatment-response. A systematic search of the Champion's database was performed using the following criteria: tumours from primary sites were selected to ensure tumour origin in the lung; both LUSC and LUAD tumours were chosen to represent the two major subtypes of NSCLC; treatment-naïve tumours were chosen to better represent unselected, primary, *in vivo* tumour heterogeneity; we also opted for both TP53 and ATM mutant, and WT tumours. The status of other key regulators of the DNA Damage Repair pathway were selected, such as ATR, PARP1 and DNA-PKcs to ensure they were not mutated. The subset of lines selected for organoid-formation and their properties are shown in Table 4.4. Importantly, the PDX lines promised to allow repeated attempts at exploring different culture conditions against the same genetic material based on the shipping of non-frozen tumour material at defined intervals.

Table 4.4. Characteristic of selected PDX lines for organoid formation. WT: Wild-Type. SNV: Single Nucleotide Variation.

Model	Tumour site	Histology	Treatment history	TP53 status	ATM status	ATR status	PARP1 status	DNA-PKcs status	Age	Gender	Ethnicity	Smoking history
CTG-1878	Primary	**LUAD**	Naive	**SNV splice site donor**	**SNV splice site region**	WT	WT	WT	69	Male	Caucasian	Former smoker
CTG-1885	Primary	**LUAD**	Naive	**WT**	**WT**	WT	WT	WT	72	Male	Black or African American	Smoker
CTG-1955	Primary	**LUSC**	Naive	**pR158fs del**	**pL2482R SNV**	WT	WT	WT	75	Female	Caucasian	Former smoker
CTG-2557	Primary	**LUSC**	Naive	**WT**	**WT**	WT	WT	WT	N/A	Male	Asian	Smoker

4.2.2. Establishment of PDX-derived NSCLC organoids

The PDX tumours were grown for Champions Oncology by Transcure Bioservices in France. Tumours were continuously monitored and when reaching ~1000 mm^3, mice were sacrificed, and the resected tumours were shipped in transport medium (Table 2.4, Methods) at 4°C with a 24 h-delivery service to Cardiff (details on some tumour-measurements on Supplemental Table 4.1., Appendix). Samples were processed immediately upon arrival at Cardiff University.

Initially a series of three sequential implantation sessions were agreed with Champions, in collaboration with Cellesce LTd. The goal of the studies was to allow a small subset of tumours to be analysed across an extended period of time, such that learning from initial work could be used to optimise later organoid establishment methodology. However, Champions changed their decision to supply fresh material at late notice (due to alterations in shipping route availability due to Covid-19). Therefore, the 2nd and 3rd implantations of PDXs CTG-1878, CTG-1885 and CTG-1955 were cancelled and tumours from CTG-2557 that had already been implanted with fragments were frozen and shipped on dry ice.

The isolation and establishment of organoids from PDXs was performed using the same protocol described in the for patient-derived UHW tumours. However, due to the nature of the host for tumour-growth, a mouse cell depletion step was added, as PDX tumours can contain mouse fibroblasts. The cells were passed through a LS column in a MidiMacs separator after a mouse cell depletion cocktail was added to the cell suspension. Briefly, monoclonal antibodies conjugated with MACS® MicroBeads were used to label the mouse cells. The cell suspension was then loaded onto the specialized column within the magnetic field of the separator. This resulted in retaining the magnetically labelled mouse cells within the column while allowing the unlabelled human cells to pass through. Only human cells were further cultured.

Once the cells were collected and plated in Matrigel blobs, the culture was split into two and cultured with growth-factor rich Sachs medium (Sachs et al. 2019) and with the more growth-factor restricted, newly published, Kim medium (Kim et al. 2019). Additionally, line CTG-1955 was also cultured in Sachs medium with Nutlin-3A as it was p53 negative. These different strategies for tumour organoid formation aimed to increase our success-rate and overcome normal tissue overgrowth. Kim medium is a less rich medium for NSCLC organoids with a 70 % success-rate (n=39) in forming tumour organoid lines (Kim et al.

2019) (Kim medium – Table 2.7, Methods). In addition, culturing line CTG-1955, which was a TP53 mutant, in Sachs medium supplemented with Nutlin-3A should select the cultured for TP53 mutant tumour cells as described by Sachs et al. (Sachs et al. 2019).

Organoids from two of the three PDX models were established. Organoids from the line CTG-2557 were established in both Sachs and Kim media, while organoids from CTG-1955 only grew in Sachs media. Surprisingly, the TP53 mutant line did not grow in Sachs medium with Nutllin-3A despite the suggestion that this should be allowed for cells in a TP53 null background. However, this was only tested for one concentration of Nutlin-3A (5 μM). For an overview of PDX-derived line-fate see Table 4.5.

Table 4.5. Overview of PDX-derived organoid lines. Yes / No: Organoids grew/ didn't grow. N/A: Not Applicable as not tested.*Only grew from fresh sample, not frozen, in these medium conditions.

Model	Grew on mice?	Shipped fresh/frozen	Grew in culture in Cardiff		
			Kim medium	Sachs medium	Sachs medium + Nutlin-3A
CTG-1878	No	N/A	N/A	N/A	N/A
CTG-1885	Yes	Fresh	No	No	N/A
CTG-1955	Yes	Fresh	No	Yes	No
CTG-2557	Yes	1 Fresh and 1 frozen	Yes	Yes*	N/A

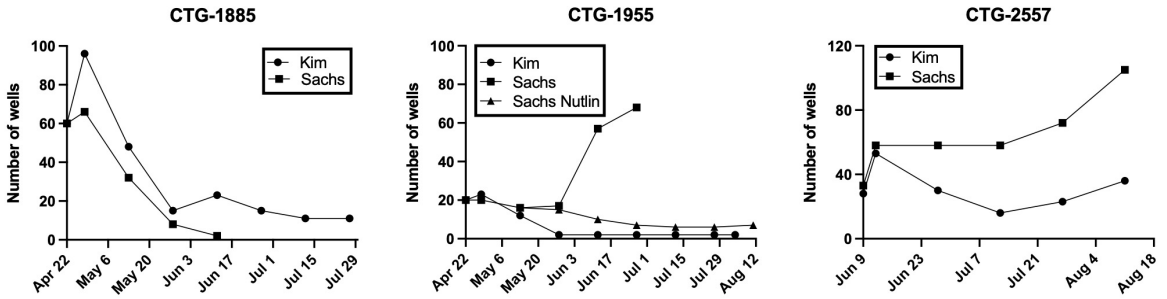

Figure 4.4. Establishment of PDX derived NSCLC organoids. Number of wells expanded over time. Graphs made with GrapPad Prism 9. Isolation and initial setup of these lines was done by Mr. Matthew Zverev due to restricted access to Cardiff University labs as a result of the Covid-19 outbreak.

An organoid-line could not be established from the CTG-1885 (LUAD, TP53 WT) tumour even though a good number of wells were seeded following isolation (60) as the organoids failed to expand in culture. The CTG-2557 (LUSC, TP53 WT) line started growing into culture 1 month post seeding (Figure 4.4.) and was then successfully established (expanded

in culture, frozen and recovered) in both Sachs (2557SLT) and Kim (2557KLT) medium. In addition, this line also grew in Kim medium when later directly established from frozen tissue (CRYO 2557KLT) (data not shown).

To confirm that the established organoid lines 2557SLT, 2557KLT and CRYO 2557KLT contained NSCLC cancer cells, a genotyping experiment was performed to confirm they contained human and not mouse DNA. PCR using human-specific and mouse-specific primers (for ACTB, actin beta – Primer test in Supplemental Figure 4.3., Appendix -) detected a expected band around 1000 bp in the 2557SLT sample with the human primers but not in the mouse ones (green rectangles, Figure 4.5). By contrast, the opposite was observed for the 2557KLT and CRYO2557KLT lines, suggesting that the material expanded in the Kim medium was of mouse origin, possibly mouse fibroblasts. Positive control human DNA was obtained from the previously described human organoids (Iso5LT). Positive control mouse DNA came from mouse tail (Dale laboratory). As a routine, it was determined that regular genotyping would be required during the passage of organoid lines.

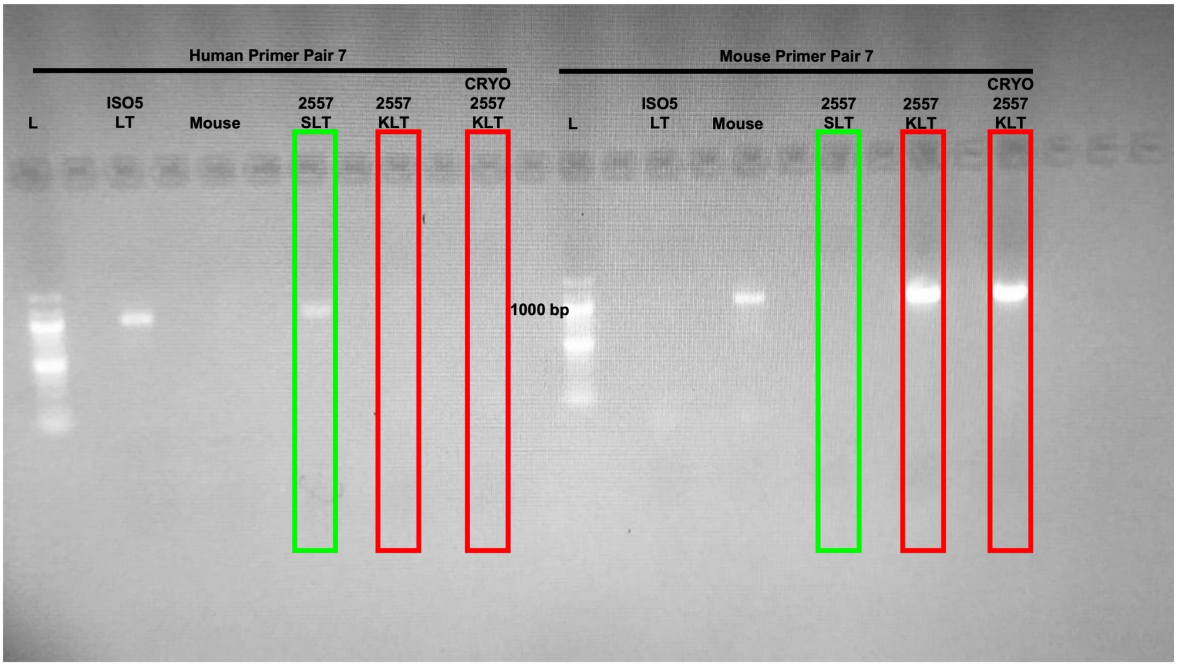

Figure 4.5. Genotyping of PDX-derived organoids. Gel electrophoresis of PCR products for either human or mouse actin showing the human nature of the 2557SLT line. Samples: 2557SLT, 2557KLT and CRYO 2557KLT organoid-samples. ISO5LT: human organoid sample. Mouse: mouse sample from Dale laboratory. L: Ladder. Green rectangle: human samples. Red rectangle: mouse samples.

4.2.3. Characterisation of PDX-derived NSCLC organoids

To test the effect of seeding density on 2557SLT NSCLC organoid growth rates, 100, 500 or 1000 live cells / μL Matrigel were plated in 10 μL Matrigel blobs in 96-well plates for up to 10 days. Relative ATP levels were measured at various timepoints, using the endpoint assay CellTitler-Glo® 3D.

Relative Luminescence (RLU) increased over time in all seeding concentrations (Figure 4.6, A)). This suggested that the line might be used for radiation-response assays at least up to day 10 in culture, regardless of the seeding concentration. Therefore, we then decided to test the radiation-response of this line. Briefly, 500 cells / μL Matrigel of 2557SLT were seeded in 10 μL Matrigel blobs in 96 well plates, allowed to formed organoids for 7 days and irradiated with a single dose of 2, 4, 6 or 10 Gy of ionising radiation (IR) or sham-irradiated with gamma irradiation. Relative ATP levels were measured 3 days post-IR using CellTitler-Glo® 3D.

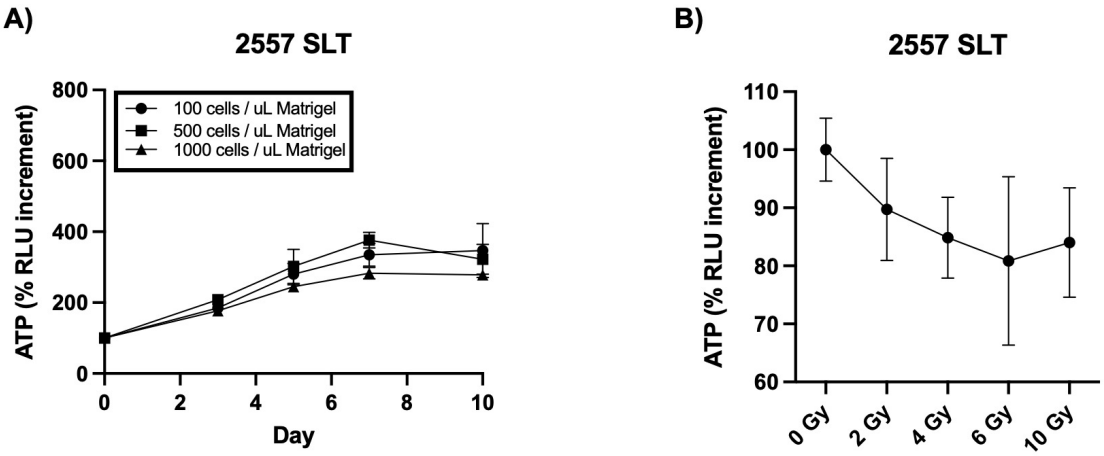

Figure 4.6. Characterisation of 2557SLT NSCLC organoid-line. Viability, measured with CellTitler-Glo® 3D ATP assay of 2557SLT organoid-line **A)** at different cell seeding concentrations (100, 500 or 1000 cells / mL Matrigel) overtime or **B)** 3 days after treatment with radiation n=3. Graphs made with GrapPad Prism 9.

As expected, the RLU value, which indicates the relative ATP levels in the culture, decreased with increasing radiation dosages. Although no significance was noted, there was a clear trend correlating culture viability and IR-dosage. Assay-optimisation may be required to reduce sample error data.

However, at this point we only had a single NSCLC confirmed organoid-line and this was felt to be insufficient as a starting point for a study of NSCLC organoids' response to drug-radiation treatments. To address this challenge, it was decided to establish a collaboration

with Prof. Ming-Sound Tsao (Princess Margaret Cancer Centre, Toronto, Canada) to obtain NSCLC organoids they had previously established and characterised.

4.3. NSCLC organoids from the Ming Tsao laboratory

The Tsao group used 30 surgically resected primary NSCLC patient tissues and 35 PDXs for NSCLC organoid culture establishment using their own M26 medium (Shi medium – Table 2.8, Methods). This medium had been modified from one used to derive normal lung organoids from pluripotent stem cells. This medium lacks some of the components present in Sachs medium for promoting self-renewal of stem cells and that were shown to be necessary for normal cell growth such as R-spondin1 or Noggin (Sachs et al. 2019). It does, however, contain CHIR99021, a GSK-3 inhibitor that acts as a Wnt activator and has demonstrated to be required for initial formation and differentiation of normal lung alveolar organoids (Hu et al. 2020; Hoffmann et al. 2022). The exact component of each of the organoid mediums used in this chapter can be found in (Sachs/AO medium – Table 2.6 -, Kim medium – Table 2.7 -, Shi/Tsao medium – Table2.8 - Methods).

The Tsao group achieved a 15 % success rate in long-term organoid establishment (> 3 months, > 10 passages). The percentage of tumour cells in the organoids was assessed by histology (H&E original tumour and organoid) and lineage markers (TTF-1, p63, CK5/6, CK7). To determine the percentage of human vs. mouse cells in the PDXOs, $EpCAM^+$ cells (human epithelial cells) and $H2K^+$ cells (mouse cells) were characterised by flow cytometry. In addition, all long-term organoid line's somatic mutations and copy number aberrations were assessed by WES and RNA-seq and results were consistent between the organoids and their matched patient tumour and/or PDX tissue (Shi et al. 2020).

Similar to our rationale for selecting NSCLC 2D cell lines in Chapter 3; we decided to grow both LUAD and LUSC organoids to represent the most common subtypes of NSCLC, as well as p53 mutant and wild-type lines, since p53 is a key regulator of the DNA Damage Repair pathway and its status should affect tumour-response to radiation and radiation-DDRi combination therapies. All organoid-lines were ATM wild type and, thus, ATM mutations could not be explored in this instance. The lines selected as part of the collaboration and some of their characteristics are presented in Table 4.6. Frozen vials were shipped to Cardiff University where they were cultured and expanded as published (Shi et al. 2020). Briefly, organoids were cultured in Matrigel blobs covered with M26/Shi medium (Table 2.8, Methods) and passaged every 7-15 days.

Table 4.6. Characteristic of NSCLC organoid-lines from Tsao Group. Diff: differentiated. KT: keratinising. P-X-O: Patient, xenograft, and organoid (Shi et al. 2020).

Model	Passage number received at Cardiff University	NSCLC subtype	TP53 status	H&E and markers, both tumour and organoid	% Of tumour cells in organoids	Gene correlation Patient/PDX vs organoid	Organoid split ratio (for Shi et al.) (wells)
LPTO126	p9	LUAD, solid	WT	H&E. $TTF1^-$, $p63^-$	85% (histology and IHC)	0.661	1 to 4
PDXO137	p9	LUAD, acinar and papillary	Nonsense (P-X-O)	H&E. $TTF1^+$, $p63^-$	6.9% EpCAM, 0% H2K (flow)	0.845	1 to 6
LPTO85	p15	LUAD, mucinous	Missense (O)	H&E. $TTF1^-$, $p63^-$	95% (histology and IHC)	0.666	1 to 4
PDXO377	p9	LUSC, moderately diff. and non-KT	WT	H&E. $TTF1^-$, $p63^+$	87% human EpCAM, 0.1% H2K (flow)	-	1 to 4
PDXO149	p11	LUSC, moderately diff. and KT	Missense (P-X-O)	H&E. $CK5^+$, $p63^+$	96% human EpCAM, 3.2% H2K (flow)	0.779	1 to 3

While expanding the organoid-lines, we realised that LUSC lines displayed a more solid morphotype whilst LUAD lines typically exhibited more budding or lumen-like morphologies, although different morphologies could be seen within the same organoid-line. To further explore these representative morphologies, we fixed the organoids in Matrigel to retain their 3D structure and imaged them following staining with DAPI and for expression of acetyl-alpha-tubulin to stain the cytoskeleton. Additionally, we stained the organoids with the CK5 antibody, a basal cell lung marker usually positive in LUSC. PDXO149 and PDXO377 lines were positive for the CK5 marker, at least in the cells on the outside layer of the organoids, consistent with them being LUSC organoids since LUSC mainly originates in the bronchi (Figure 4.7). The Tsao laboratory also had showed that both PDXO149 tumour and organoid lines were positive for CK5 staining (Shi et al. 2020). The PDXO149 and PDXO377 were mainly round, solid cell masses. Cells within PDXO377 organoids appeared to be more compact, forming more dense 3D structures compared to PDXO149 organoids. This suggests that organoid diameter cannot be used as a directly proportional measure of the number of cells within an organoid. In contrast, all three LUAD lines showed mainly budding or lumen organoids (defined previously in Chapter 3 – Figures 3.2/3). LPT085 organoids were round or oval, big structures with a large single lumen in the centre and a single layer of cells delimiting it. LPT0126 and PDXO137 were lumen or budding organoids. These typically consisted of multiple inner lumens bounded by a single or two layers of cells. These may better represent alveolar-like morphologies, from which LUAD are thought to arise (Hoareau et al. 2021).

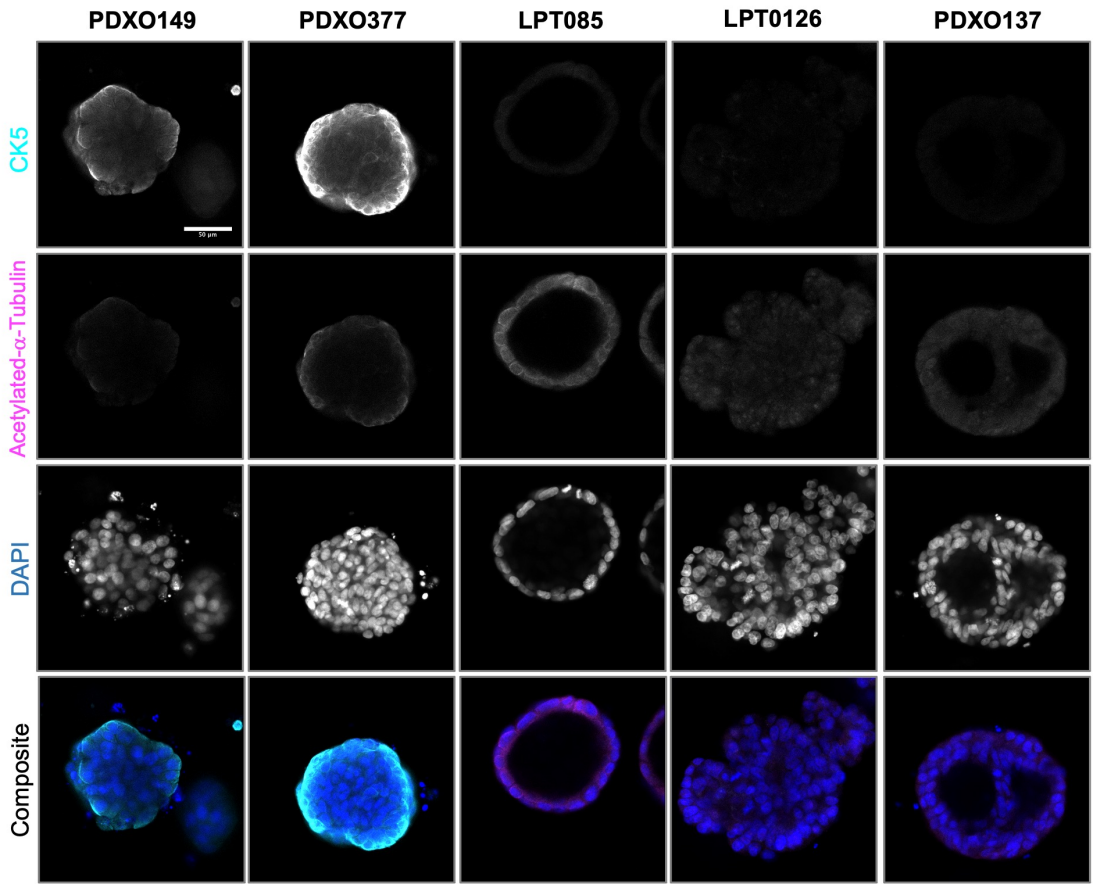

Figure 4.7. Representative morphologies of Tsao's laboratory NSCLC organoids. Confocal microscopy of NSCLC organoids with lung cell markers. CK5: Cytokeratin 5, basal airway cell marker.

4.3.1. Characterisation of Tsao's laboratory NSCLC organoids

General recommendations from the Tsao laboratory were to seed lines with high-confluency to achieve greater organoid-formation. However, we wanted to test the effects of seeding density ourselves, in part to define a consistent seeding density for our later radiation and radiation-DDRi combination assays in all lines. A hundred, 500 or 1000 cells / µL Matrigel were plated in 10 µL Matrigel blobs in 96 well plates for up to 15 days and relative ATP levels were measured, using the endpoint assay CellTitler-Glo® 3D as a measurement of organoid-viability.

Viability (measured as % of growth, based of RLU being 100 % at seeding day) increased over time in all NSCLC organoid-lines and at all seeding densities (Figure 4.8, A)). All lines seemed to increase their percentage of growth between day 7 and 12 in culture, at least with the 2 lowest seeding concentrations, suggesting that the lines might be used for treatment-response assays in between these days. The lower seeding densities (100 cells / µL Matrigel) resulted in very few organoids; and the highest seeding densities (100 cells / µL Matrigel)

resulted in organoids with poorly delineated boundaries and a small assay window (Figure 4.8., A)). These results were consistent with what we had previously determined with the CellAggs for 3D ECM cultures where low seeding densities; whilst resulting in the biggest increase of RLU, also increased the variance of the data (Figure 3.4/5, Chapter 3). Therefore, we decided to use 500 cells / μL matrigel for our future organoid-treatment assays.

The Tsao laboratory used organoid split ratio as an indicator of organoid-lines' growth. This ratio was based on the number of wells that were seeded from a single well when passaging. However, this was not a very accurate method to measure growth-rate as initial seeding density was not controlled; no specific cell number was seeded, the culture was a mixture of single and clusters of cells and the number of days the cells remained in culture was not consistent. To have a more accurate idea on the inter-line relative growth differences, we plotted the percentage of growth of all the different lines (with the selected seeding concentration of 500 cells / μL Matrigel) and the doubling time of each organoid-line was calculated between defined time points (day 7 to 12 in culture) (Figure 4.8, B) and C)). The LUAD mucinous line (LPTO085) was the line with highest percentage growth, followed by the LUAD p53 WT line (LPTO126). The remaining lines had notably higher doubling times, although the LUSC p53 WT line's (PDXO377) doubling time was less than the LUSC p53 mutant line's (PDXO149) (83 vs. 111 h). Finally, the LUAD p53 mutant line (PDXO377) was the one with the lowest percentage of growth and, thus, the highest doubling time among the analysed lines. No correlation was noted between known organoid-characteristics (NSCLC subtype, p53 status, patient or xenograft origin…) and organoid doubling time.

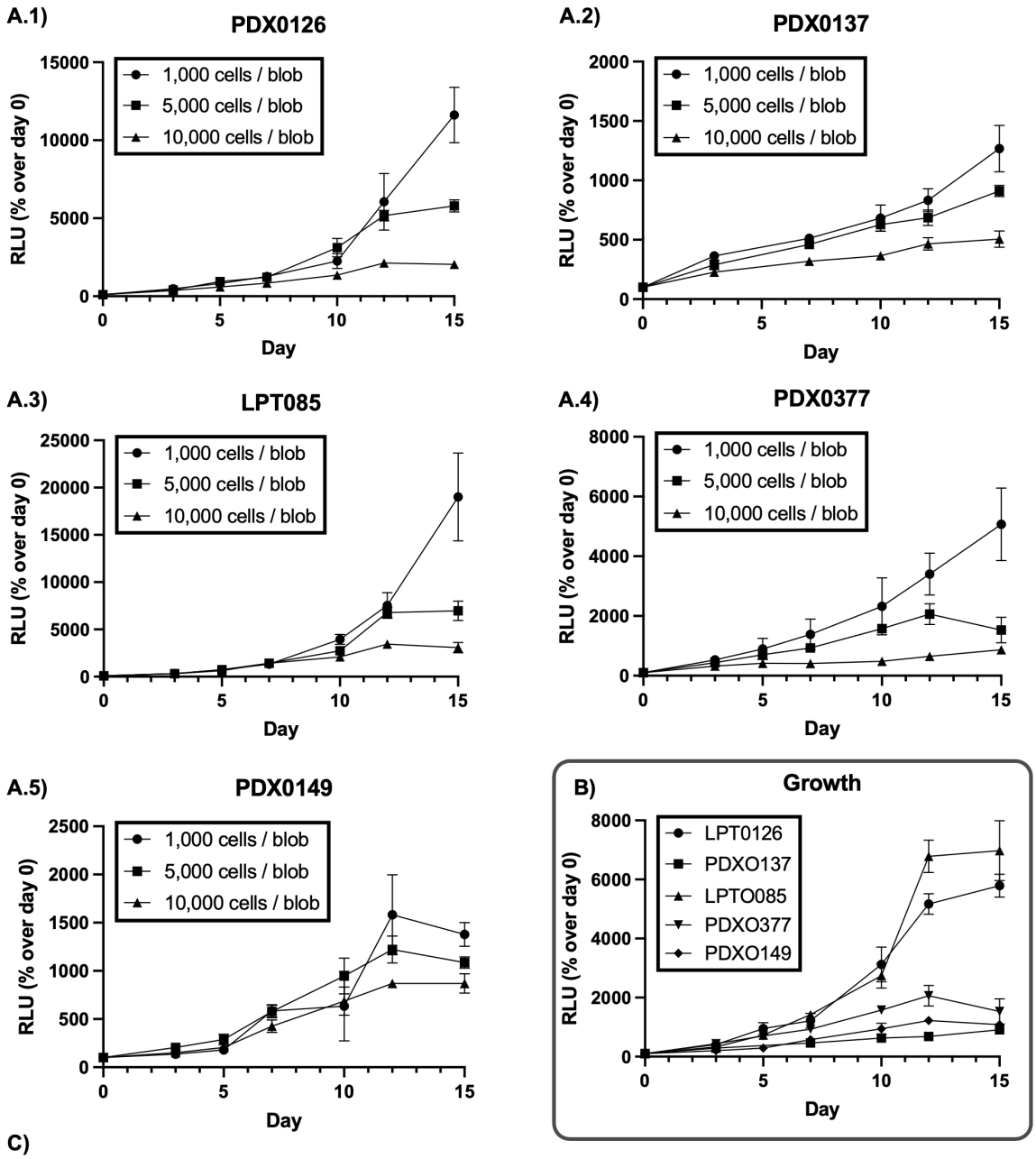

C)

	LPT0126	PDXO137	LPTO85	PDXO377	PDXO149
500 cells / uL Matrigel	57.55	209.67	53.32	83.55	111.15

Figure 4.8. Tsao laboratory NSCLC organoids' growth. Viability, measured with CellTitler-Glo® 3D ATP live-cell assay, of NSCLC organoid lines showed an increase overtime **A)** at different cell seeding concentrations (100, 500 or 1000 cells / μL matrigel), **B)** at 500 cells / μL matrigel. **C)** Doubling time NSCLC organoids measured from day 7 to 12 in culture based on (B). n=3. Graphs made with GraphPad Prism 9.

Overall, the studies had established robust NSCLC growth parameters for the organoid-lines ready for DDRi and radiation combination assays. The selected lines included both LUAD and LUSC lines that differed in their TP53 status (Table 4.6).

4.4. Key summary

In this Chapter we aimed to create a patient-derived NSCLC organoid biobank in Cardiff. Unfortunately, we were not able to establish lines from patient material. However, we were able to establish a NSCLC organoid line from a single PDX model. The expertise in handling lung cancer organoids was, however, useful in supporting the rapid establishment and characterisation of NSCLC organoids from the Tsao laboratory.

High cell confluency was found to be initially required for NSCLC organoid-formation. The passage after isolation or thawing of cryopreserved vials proved crucial for expanding the organoid-lines. We observed that gentle manual trituration was required to ensure that already-formed small organoids do not break. By contrast, for later passages, breaking of organoids into single cells or small cell clusters was an effective method for organoid-line expansion. In addition, we saw that culturing the cells for half an hour in a 10 % FBS supplemented medium could be used to reduce fibroblast numbers from lung tumour samples. In the case of PDX-derived organoids, passing the cell suspension through a mouse/human selective column might be a good step to enrich tumour cells, although it is important to ensure beforehand that the suspension contains primarily single cells. In any case, when establishing NSCLC organoids, it is imperative to assess the tumour percentage (via histology, flow, cytometry, genotyping for a housekeeping gene…) over several passages.

Finally, through a collaboration with Tsao laboratory, we were able to acquire a small group of NSCLC organoids, expand and freeze them down. These lines included both LUAD and LUSC differing in TP53 status.

5. Results – Effects of radiation and DDRi combination therapies on NSCLC organoids

The work in this chapter aimed to study the response of patient-derived NSCLC organoids to radiation and radiation-DNA damage repair inhibitors combination novel therapies by developing and applying methods for the analysis of radiation-responses using NSCLC organoids.

5.1. Measuring NSCLC organoid responses to radiation based on changes in organoid area

Two of the most widely investigated responses of tumours to radiation are growth delay and clonogenicity reduction. To investigate NSCLC organoids' responses to radiation their growth was measured using an assay that quantified a 2D projection of the total area covered by organoids within the 3D Matrigel blob using the IncuCyte®S3 microscope that allows cultures to be imaged continuously within an incubator.

Briefly, NSCLC organoids were digested with TrypLE Express into a single cell suspension and 50 cells/ μL Matrigel were seeded in 25 μL Matrigel blobs in 24 well plates. Although the best seeding density for continuous increase of ATP viability in NSCLC organoids was previously found to be 500 cells/μL Matrigel (Figure 4.8, Chapter 4), a lower seeding density was used for this particular experiment to overcome the difficulties in measuring the total area covered by organoids in a confluent 3D environment. Cells were cultured for 8 days to form organoids with a range diameter size of 30-100 μm. Organoids were irradiated with 4 Gy of ionising radiation or sham irradiated. Plates were then placed in the IncuCyte®S3 incubator and automatic images of the wells were acquired every 6 hours for a total of 12 days post-irradiation (Figure 5.1., A)). A manually supervised mask was created with the recently available 'Organoid Analysis Software' that is linked to the 'OrganoidQC' image acquiring system of the IncuCyte which facilitates issues linked to focal plane: images are acquired from a large z-depth (~2 or 2.9mm) of multiple z-slices to result in a final image where all organoids are in focus.

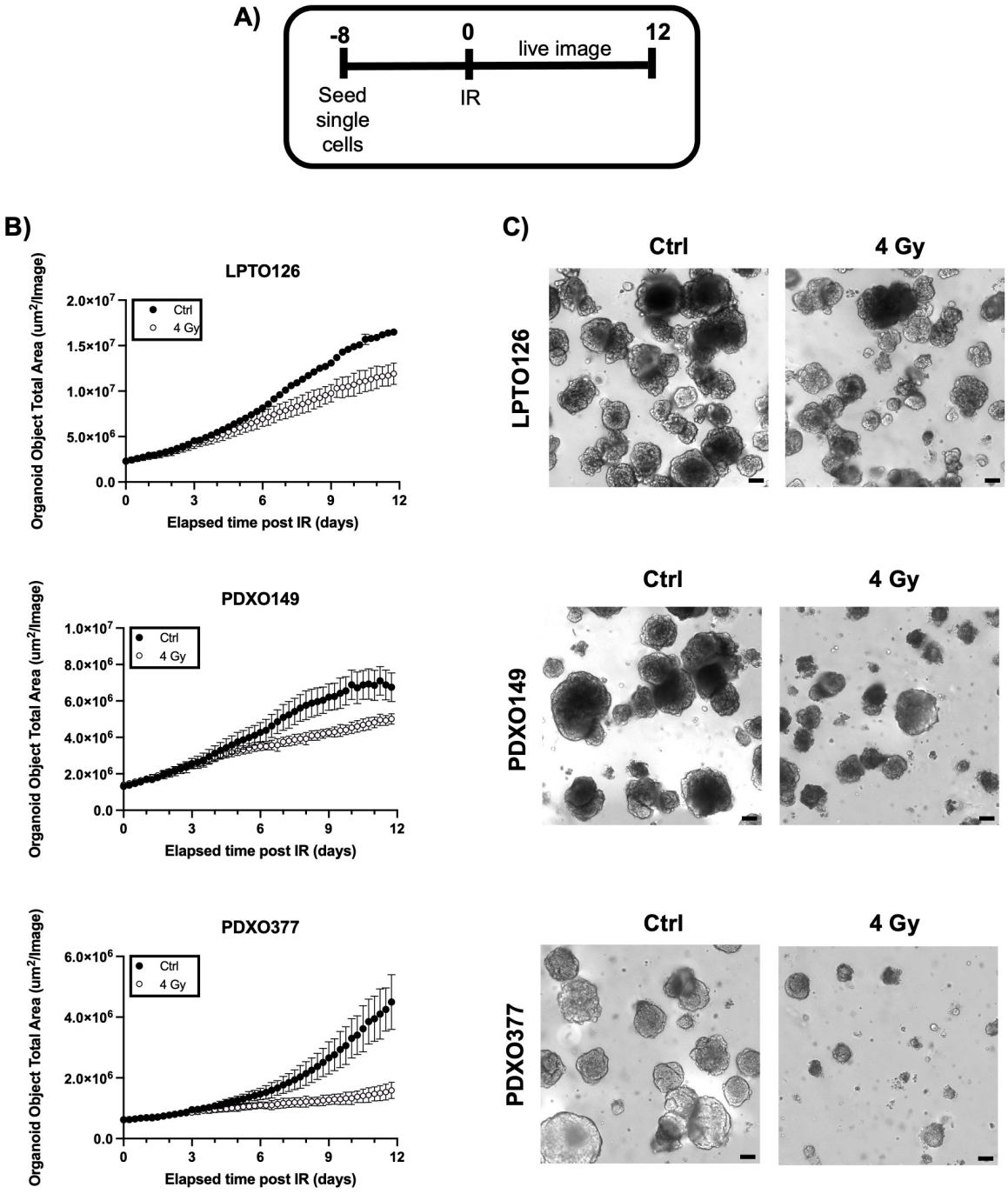

Figure 5.1. Organoid cultures cover less well-area after irradiation. Live imaging of NSCLC organoid-lines (LPTO126, PDXO149 and PDXO377) taken by the IncuCyte®S3 'organoid mode' over time (day 0-12) after 4 Gy of irradiation or sham irradiated. **A)** Diagram of assay. The numbers at the top of the bars indicate the day in which the action at the bottom of the bar was taken. **B)** Analysis of images taken by the IncuCyte®S3 showing the total area covered by NSCLC organoid cultures (μm²/image) after IR. n=3. Graphs made with GrapPad Prism 9. **C)** Representative cuts of images analysed in 'B' at day 10 post IR. Scale bar: 100 μm.

Clear differences in the total area covered by organoids between the control and treated cultures were observed from day 6 post-irradiation for all three lines studied (Figure 5.1, B)). LPTO126 and PDXO149 (Figure 5.1., B) and C)) displayed a similar pattern of growth and radiation response, with both the irradiated and treatment culture-areas continuing to

increase after irradiation, although the growth-rate of the irradiated samples was substantially slowed. The total area covered by organoids in the non-IR control started to plateau from day 10 for both LPTO126 and PDXO149. By contrast, the PDXO377 line showed no plateau in growth and also showed the biggest differences between the IR and sham-IR samples following irradiation (Figure 5.1., B) and C)).

5.2. Measuring radiation responses using metabolic (ATP) assays

To identify the optimal response time for ATP assays using NSCLC organoids, 500 single cells were seeded per μL Matrigel in 10 μL blobs in 96 well plates and cultured to form organoids for 7 days (Figure 5.2., A)). The organoids were then irradiated with a single dose of 2, 4, 6, or 10 Gy or sham irradiated, and ATP levels were measured in endpoint assays on days 0, 3, 5 and 7 post-IR. All ATP measurements were plotted relative to the control 0 Gy on day 0.

Relative Luminescence (RLU) levels from the LUAD lines (LPTO126 and PDXO137) continued to increase for, at least, 5 to 7 days after irradiation (Figure 5.2., B)). Regardless of the radiation-dose, no difference was found between treated and irradiated samples in these lines. By contrast, the RLU from LUSC lines (PDXO149 and PDXO377) was lowered following irradiation in a dose-dependent manner. Day 5 post-IR was selected as the optimal time point for a metabolic end point assay based on the fact that differences in some lines (radiation dose-dependent decrease of ATP levels) were already being observed and that ATP levels were previously shown to plateaued by day 12 post-seeding (equivalent to day 5 post-IR) in prior characterisation experiments (Figure 4.8., Chapter 4).

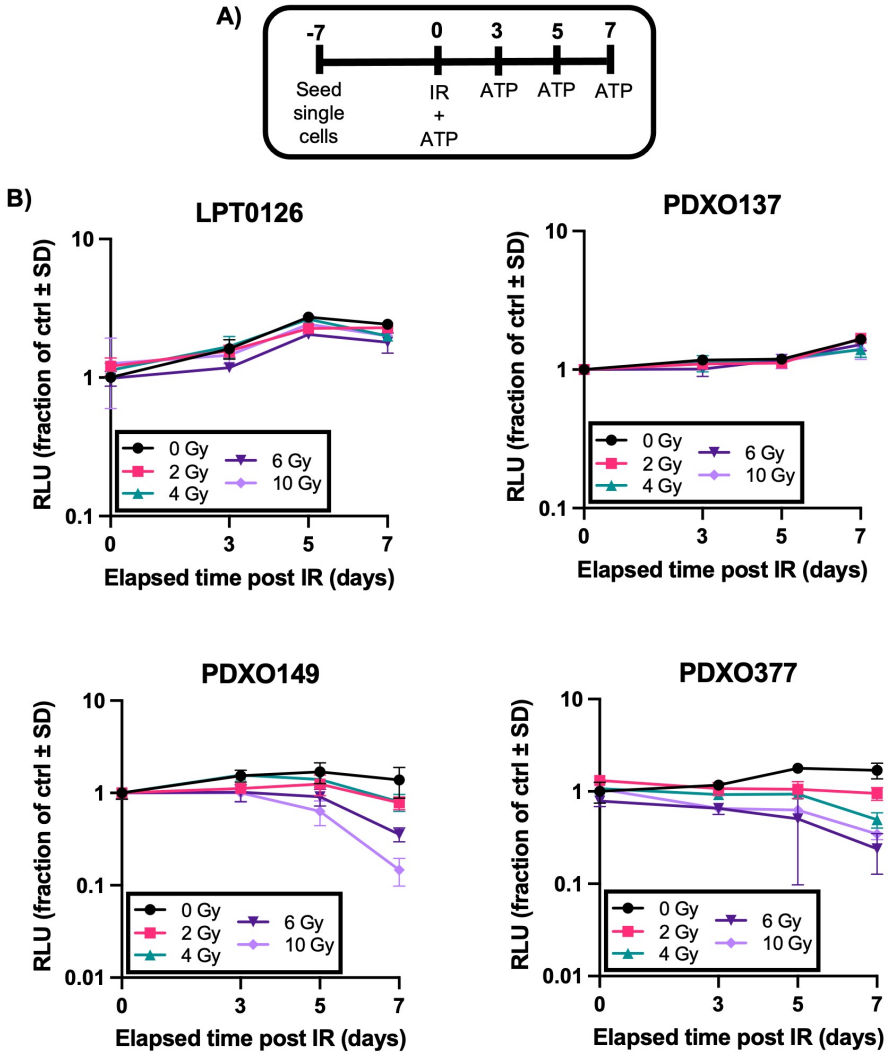

Figure 5.2. Radiation effect in organoid culture viability over time. Relative ATP levels as Relative Luminescence (RLU), measured with endpoint CellTitler-Glo® 3D ATP live-cell assay, of NSCLC organoid-lines (as per graph titles) treated with 2-10Gy of single dose ionising radiation or sham irradiated. ATP measured 0, 3, 5 and 7 days post-IR. **A)** Diagram of assay. The numbers at the top of the bars indicate the day in which the action at the bottom of the bar was taken. 'ATP' is used for indicating when culture relative ATP levels were measured. **B)** Graphs of post-IR response made with Graphpad Prism 9. n=3.

To allow simultaneous line-to-line comparison of the NSCLC organoids, a day 5 experiment was repeated for all of the NSCLC organoid-lines. Relative radiosensitivity at day 5 post-IR was plotted as RLU vs radiation dose for each of the lines (Figure 5.3., A)).

A)

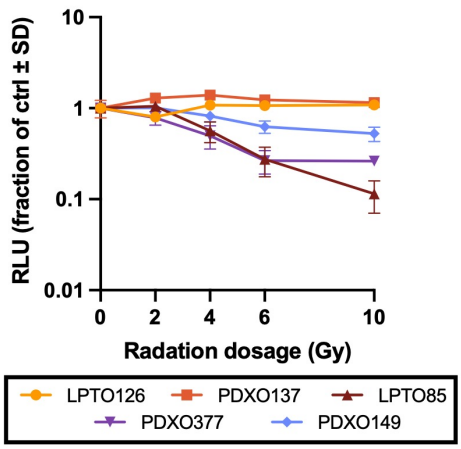

B)

Model	NSCLC subtype	TP53 status
LPTO126	LUAD	WT
PDXO137	LUAD	Nonsense (P-X-O)
LPTO85	LUAD	Missense (O)
PDXO149	LUSC	Missense (P-X-O)
PDXO377	LUSC	WT

Figure 5.3. LUSC and LUAD organoid line responses to irradiation. A) Relative ATP levels as Relative Luminescence (RLU), measured with endpoint CellTitler-Glo® 3D ATP live-cell assay, of NSCLC organoid-lines (as per graph legend) treated with 2-10Gy of single dose ionising radiation or sham irradiated. ATP measured 5 days post-IR. Graphs made with Graphpad Prism 9. n=3. **B)** NSCLC subtype and TP53 status of NSCLC organoid lines from Tsao Group used in this assay (Shi et al. 2020). More detailed description of the lines can be found in Chapter 4, Table 4.6 of this thesis.

LPTO85, PDXO149 and PDXO377 lines showed a clear dose-dependent response to radiation (Figure 5.3., A)). PDXO149, the TP53 mutant line, showed lower responses to radiation than the other LUSC line, PDXO377 (TP53 wild-type), suggesting that the PDXO377 line was more radiosensitive. No radiation responses were observed in the LPTO126 and PDXO137 LUAD lines. The biggest relative decrease in ATP levels was observed in the LUAD line LPTO85. Interestingly, this was the only line in which most organoids exhibited a lumen phenotype (tumour of origin was determined to be mucinous subtype – Table 4.6, Chapter 4 -). Intestinal colorectal cancer organoids that contain lumens have been shown to collapse and loose their budding structures after irradiation, which has been associated with a reduction in organoid formation capacity (Yao et al. 2020).

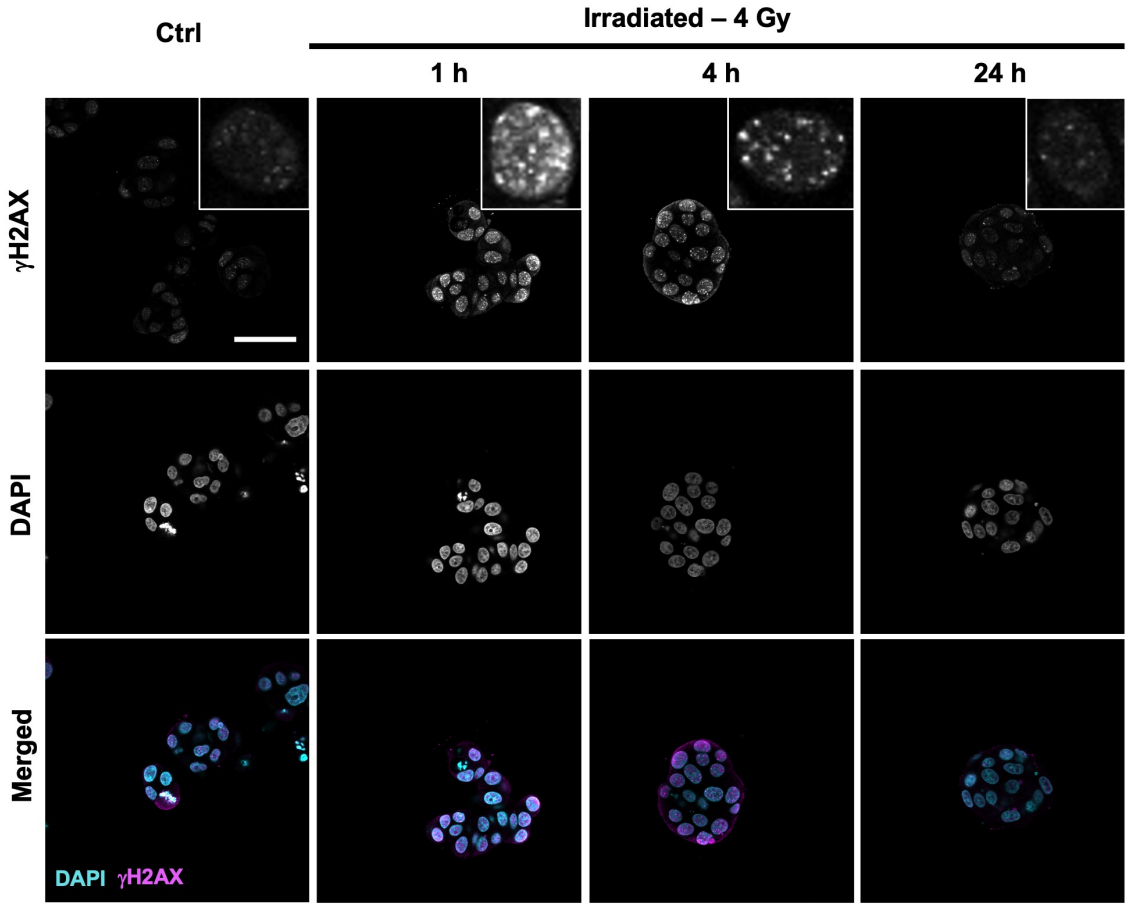

Figure 5.4. DNA damage over time response of PDXO149 organoids after irradiation. Maximum projection of z-stacks on fluorescence confocal microscopy on PDXO149 NSCLC organoids in Matrigel 1 h, 4 h and 24 h after 4 Gy of irradiation and a non-irradiated control. Immunostaining was performed with a gH2AX antibody and DAPI for nuclear staining. Scale bar: 100 μm.

To look for the presence of radiation response biomarkers, the irradiated PDX0149 organoids were analysed by immunocytochemistry for γH2AX expression, as was previously described for the CellAggs (Supplemental Figure 3.2/3, Appendix). Irradiation increased the numbers of γH2AX foci, indicative of DSB sites (Figure 5.4.). Maximum signal was reached 1 h after IR and no γH2AX foci were localizable 24 h after treatment, indicating that most of the DNA of the surviving organoids was repaired by 24 h after irradiation.

To investigate whether pre-treatment with a DDRi would enhance radiation responses in NSCLC organoids, 500 cells / μL Matrigel in 10 μL blobs of all available NSCLC organoid-lines were seeded in 96 well plates and cultured to form organoids for 7 days. One hour before irradiation, organoids were treated either with a titration of 0.03-1 μM of *VE-822* (ATRi) or 0.3-10 μM of *Olaparib* (PARPi) and then irradiated with a single dose of 2, 4, 6,

or 10 Gy or sham irradiated. 24 h post irradiation cell culture medium was replaced for drug-free medium. 5 days post irradiation ATP levels were measured and normalised over the sham irradiation, 0.05 % DMSO control.

RLU data from each drug concentration, radiation dose and line is shown in Supplemental Figure 5.1. (Appendix). This dataset showed that high concentrations of both drugs (10 μM *Olaparib* PARPi and 1 μM *VE-822* ATRi) had radiation-independent effects on organoid growth. A subset of this data is presented in Figure 5.5 for two particular drug concentrations: 0.1 μM *VE-822* and 3 μM Olaparib. These drug concentrations were selected as the focus for Figure 5.5 and for later experiments based on the observation that they did not reduce organoid RLU in the absence of radiation.

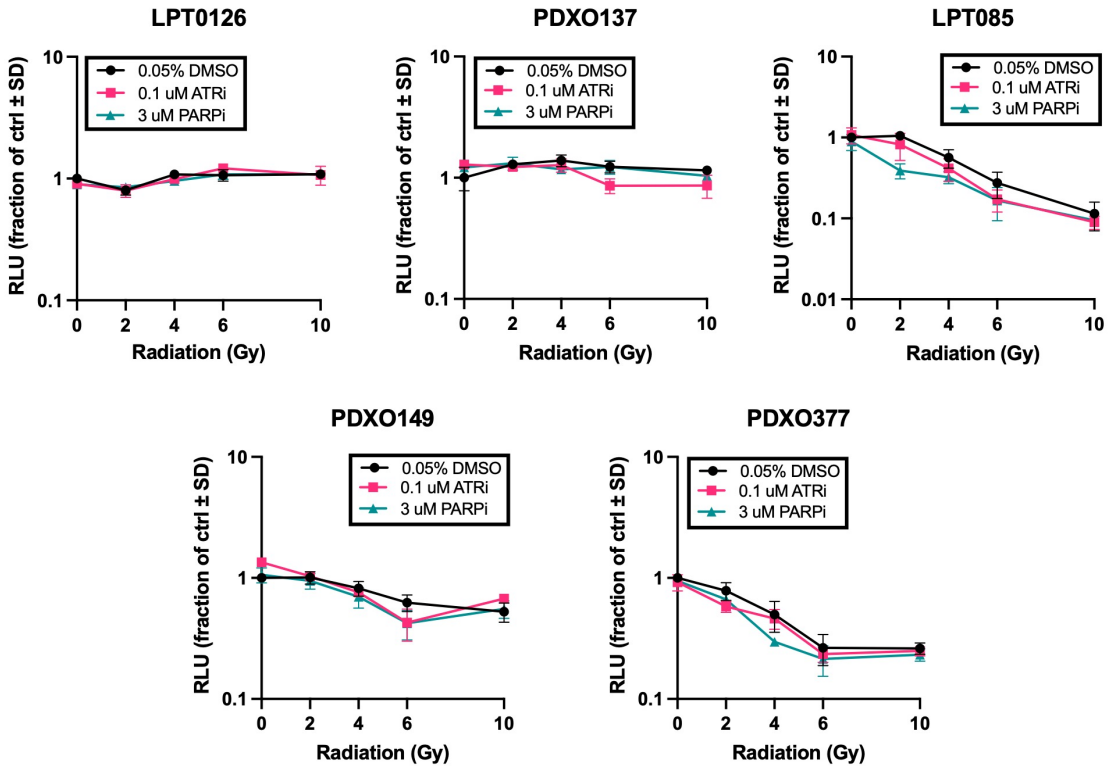

Figure 5.5. NSCLC organoid lines' viability after treatment with ionising radiation and/or DNA Damage Repair inhibitor. Relative ATP levels as Relative Luminescence (RLU), measured with endpoint CellTitler-Glo® 3D ATP live-cell assay, of organoids (as per graph titles) treated with 2-10 Gy of single dose ionising radiation or sham irradiation and 0.05 % DMSO control or a titration of and ATRi (0.1 μM) or an PARPi (3 μM). ATP measured 5 days post-IR. Drug was added 1 h pre-IR and culture medium was replaced 24 h post-IR with drug-free medium. n=3. ATRi: Ataxia Telangiectasia and Rad3-related inhibitor, *VE-822*. PARPi: Poly (ADP) Polymerase inhibitor, *Olaparib*. Graphs made with GrapPad Prism 9.

At concentrations of DDR inhibitors that did not alter RLU alone, irradiation had limited effects on ATP levels although some decrease in viability was observed with PARPi treatment compared to 0.05 % DMSO in lines LPTO85 and PDXO0377 at 2 Gy and 4 Gy, respectively (Figure 5.5.). Only very high doses of the ATRi or the PARPi seemed to induce sensitivity to radiation in some of the NSCLC lines (Supplemental Figure 5.1., Appendix). The drug- but radiation-independent effects on viability likely increased the variance of combinatorial data due to the low absolute numbers of cells analysed in some combinations. Although synergy between therapeutics can be analysed using systematic Dose-Effect approaches (e.g. determination of the Combination Index (CI) (Chou 2010; Duarte and Vale 2022)), a pragmatic approach was taken in subsequent studies. This involved using DDRi inhibitors at concentrations (0.1μM VE-822 and 3 μM Olaparib) previously proven effective by our collaborators in the Anderson Ryan group in NSCLC cell lines (colony formation assays).

The lack of a strong readout from the ATP-based assay prompted the development of an assay of organoid clonogenicity since this assay format in 2D cell lines has previously been shown to be more effective in measuring reductions in reproductive potential.

5.3. Development of an organoid re-plating assay to measure radiation responses

A replating assay was designed to assess the potential of single cells that had been isolated from irradiated organoids to form new organoids. Briefly, 500 cells / μL Matrigel in 25 μL blobs of LPT0126, PDXO137, LPTO85, PDXO149 and PDXO377 NSCLC organoid-lines were seeded in 24 well plates and cultured to form organoids for 7 days (Figure 5.6., A)). These were then irradiated with a single dose of 2, 4 or 6 Gy or sham irradiated. Twenty-four hours post-IR organoids were dissociated with TrypLE Express, and life (trypan blue excluding) single cells were re-seeded (500 cells / μL Matrigel) and cultured to form new organoids in new 25 μL Matrigel blobs (n=3). Ten (LPTO85 and LPTO126), 14 (PDXO149) and 15 (PDXO137 and PDXO377) days after re-seeding image of each well was acquired with the IncuCyte®S3 system, organoid mode, that acquires images from a large z-depth (~2 or 2.9mm) of multiple z-slices to result in a final image where all organoids are in focus.

The total number of organoids per radiation dose were counted and normalised as a fraction of the total number of formed organoids in the sham irradiated control per line (taking into account the plating efficiency, as described in the methods section). The specific details of the organoid counting method varied according to the line and in some cases the dose

delivered due to a number of practical issues. Some lines and conditions generated high density cultures of organoids whilst others had very few organoids per well. An image analysis mask was used to count organoids with an area >3000 μm^2. However, this standard method was suboptimal at counting very dense organoids and did not perform well separating organoids in confluent cultures in the IncuCyte®S3 'Organoid Analysis Software'. Where automated approaches failed, manual methods were substituted with care taken to ensure that manually acquired and automated approaches registered equivalent numbers. This manual supervision ensured that every well was manually supervised. When low numbers of organoids were present, every organoid was individually counted. When large numbers of organoids were present, random 500x500 pixel images from the whole-well were counted and the total numbers of organoids were extrapolated.

By contrast with the ATP metabolic readout, the organoid replating assay showed strong evidence of radiation responses for all lines examined (Figure 5.6., B)). Representative images of organoid-growth used for data quantification can be found in Figure 5.6., D). Two LUAD lines (LPTO126 and PDXO137) showed no response at 2 Gy but radiation decreased the surviving fraction to 0.5 after 4 Gy of radiation. Among the two LUSC lines, the PDXO377 TP53 wild-type line was the most responsive, showing a 0.001 fraction of surviving organoids after 6 Gy of IR (Figure 5.6., B)), suggesting that PDXO377 line was most radiosensitive than the other LUSC line PDXO149 (TP53 WT) (0.1 fraction of surviving organoids after 6 Gy of IR). LPTO85 lumen line resulted in the most apparent loss of reproductive capability, specially at higher radiation doses. In fact, no growth was observed at all after 6 Gy of radiation, thus the missing datapoint. Importantly, the relative order of radiation sensitivity for the different lines was consistent with the ATP-dependent assays as shown in Figure 5.3. The biggest difference between the two assay formats might be the greater 'assay window' present in the replating assays.

Interestingly, although the LPTO126 line did not lose much of its reproductive capability after irradiation compared to the other lines, a clear diameter shift with increasing doses of irradiation was observed in the organoids that did grow after irradiation. Most organoids were 60 – 90 μm in the control whilst smaller organoids grew after irradiation (increase in 30 – 60 μm organoid population, with increasing radiation doses, and decrease in bigger organoids) (Figure 5.6., C)). This delay in growth, which is a typical response to radiation, was observed in all the studied lines (data not shown).

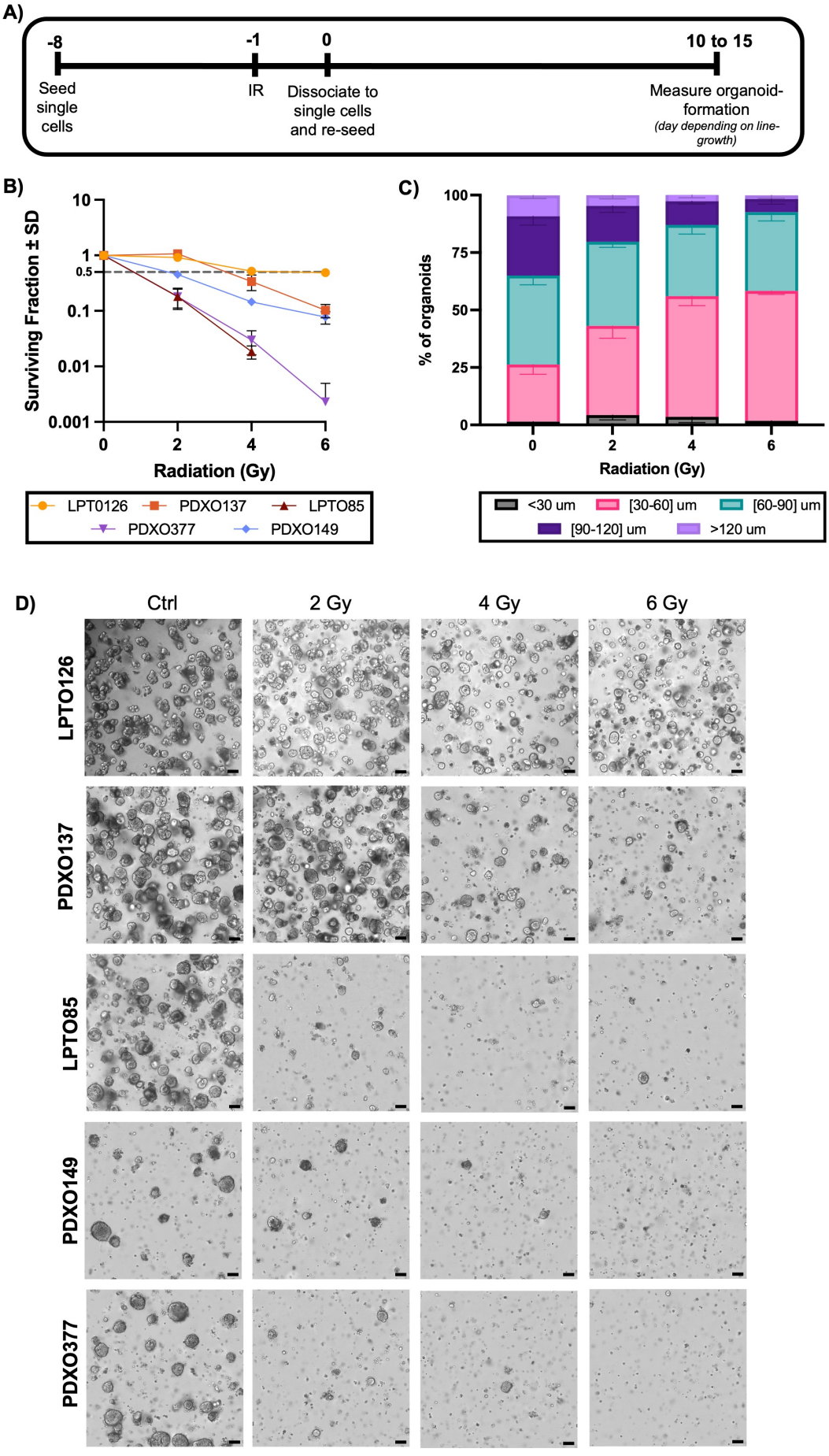

Figure 5.6. Organoid formation capcity of NSCLC organoids after irradiation and re-plating. Organoid formation assays of NSCLC organoids post-irradiation. Number of organoids formed were measured and

*Figure legend continues in the next page

surviving fraction was calculated at day 10 (for LPTO126, PDXO137 and LPTO85), day 14 (PDXO149) or day 15 (PDXO137) after re-seeding the cultures into single cells post-IR. **A)** Diagram of assay. The numbers at the top of the bars indicate the day in which the action at the bottom of the bar was taken. **B)** Post-IR surviving fraction graphs of NSCLC organoids (as per legend in the figure) treated with a single dose of 0-6 Gy of irradiation. **C)** Diameter distribution graph of post-IR surviving formed LPTO126 organoids. **D)** Representative pictures of organoids in 'B'. Scale: 100 μm. Graphs made with Graphpad Prism 9. n ≥ 3.

5.4. Analysing radiation-DDRi interactions using organoid-replating assays

To investigate DDRi – radiation interactions in a replating assay format, the NSCLC organoids were pre-treated with an ATRi or a PARPi for 1h prior to irradiation (0.1 μM of VE-822 (ATRi) or 3 μM of Olaparib (PARPi)). Twenty-four hours post-IR organoids were dissociated into single cells and live (trypan blue excluding) single cells were re-seeded (500 cells / μL Matrigel) to form new organoids in drug-free medium. Ten (LPTO85 and LPTO126), 14 (PDXO149) and 15 (PDXO137 and PDXO377) days afterwards, each well was imaged with the IncuCyte®S3 system in organoid mode.

Plating efficiency (PE) was assessed for DMSO control, ATRi, and PARPi drugs (Figure 5.7, Supplemental Table 5.1). The addition of either an ATRi or a PARPi to the LPTO85, PDXO149 and PDXO377 lines led to a substantial reduction in plating efficiency (Figure 5.7, **C)**, **D)** and **E)**). Notably, and as an example, a pronounced effect was observed with the exclusive impact of 3 μM of the PARPi on the LPTO85 line, where PE_{DMSO}=7.53% compared to PE_{PARPi}=0.95% (a statistically significant difference with a p-value < 0.0001). These findings indicate significant single-agent activity for both ATRi and PARPi in LPTO85, PDXO149 and PDXO377 lines. Conversely, no significant PE difference was recorded in the PDXO137 line (Figure 5.7., **B)**), suggesting that neither ATRi nor PARPi had an effect on this line as single-agents. The LPTO126 line exhibited and increase in plating efficiency following treatment with the ATRi or the the PARPi (Figure 5.7., **A)**), suggesting that the addition of the drug in this line promoted organoid forming or growth in the absence of irradiation.

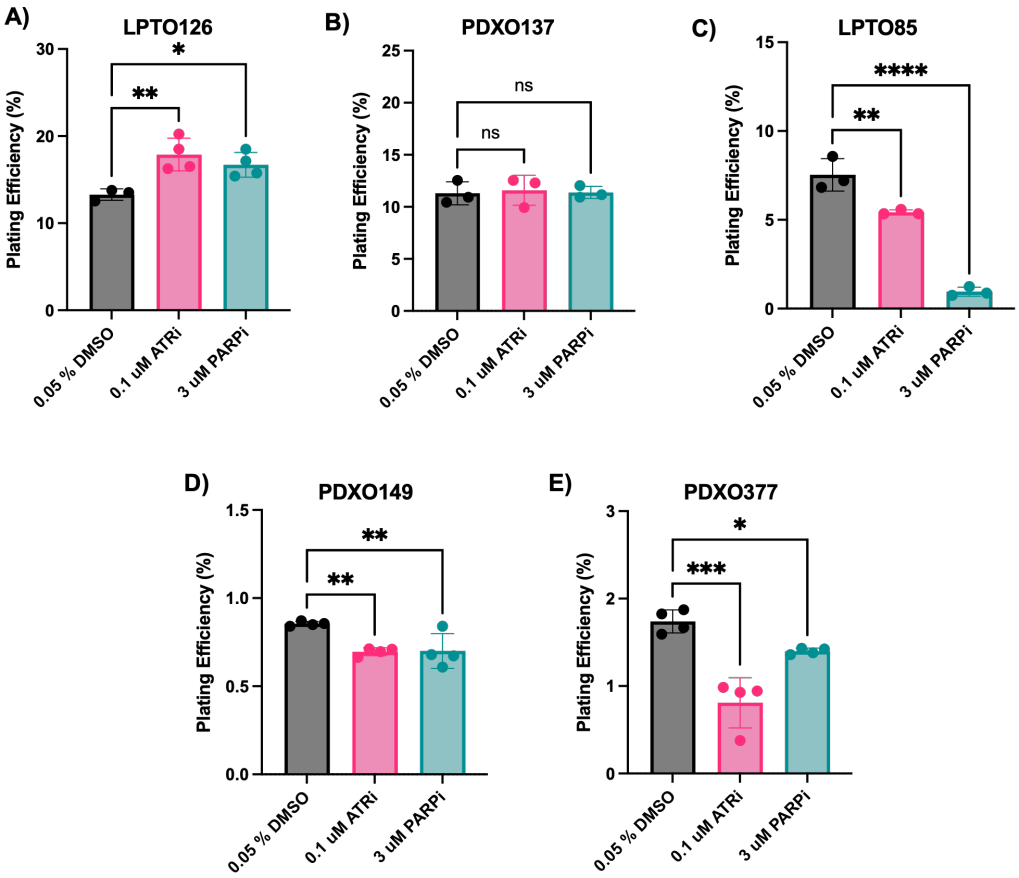

Figure 5.7. Plating efficiency of NSCLC organoids after treatment with DDRis. Organoid formation assays of NSCLC organoids with 0.05 % DMSO ctrl or 0.1 μM of an ATRi or 3 μM of a PARPi. Organoids were cultured with either an ATRi or a PARPi 1 h prior to irradiation. Number of organoids formed were measured plating efficieny was calculated at day 10 (for **A)** LPTO126, **B)** PDXO137 and **C)** LPTO85), day 14 (**D)** PDXO149) or day 15 (**E)** PDXO137) after re-seeding the cultures into single cells in a DDRi-free medium 24h post-treatment. Statistical significance of data was calculated in comparison to the 0.05% DMSO ctrl using 1-way ANOVA with Dunnett's test for correction of multiple comparisons. Statistical significances were determined when p values were less or equal to 0.5 (ns: p>0.5, *: p≤0.5, **: p≤0.01, ***: p≤0.001, ****: p≤0.0001). Statistical analysis and graphs made with Graphpad Prism 9. Specific PE numbers used for this are displayed in Table S5.1. n ≥ 3. ATRi: Ataxia Telangiectasia and Rad3-related inhibitor, *VE-822*. PARPi: Poly (ADP) Polymerase inhibitor, *Olaparib*.

To evaluate the impact of combining a drug with varying doses of irradiation, surviving fractions (SFs) were computed in both presence and absence of the drug (i.e. 0.05% DMSO control, 0.1 μm ATRi sample and 3 μm PARP sample). The SFs were normalised to the plating efficiencies per drug, as detailed in the methods section, ensuring accurate assessment of sensitising drug responses at different irradiation doses and preventing misinterpretation arising from the drug-only single effect in each organoid line. The SF ratio ($SF_{xGy}^{DMSO}/SF_{xGy}^{Drug}$) was calculated, and the ratio t-test statistical analysis was performed (Figure 5.7., tables). The ratio is presented across multiple radiation doses, recognising that the radiation response is non-linear, and thus, the ratio is anticipated to vary across different doses.

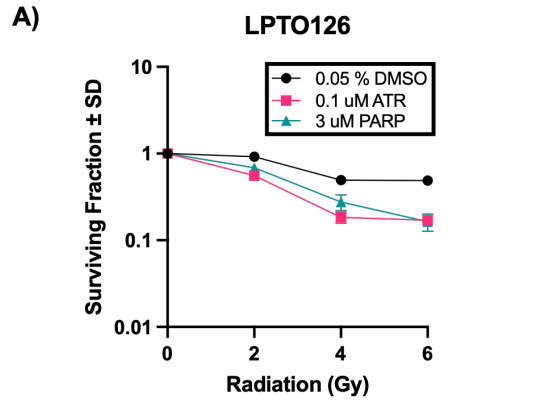

LPTO126	2 Gy	4 Gy	6 Gy
$SF_{xGy}^{DMSO}/SF_{xGy}^{ATRi}$	1.621, (*) P=0.0126	2.559, (**) P=0.007755	2.86, (***) P=0.0002582
$SF_{xGy}^{DMSO}/SF_{xGy}^{PARPi}$	1.294, (*) P=0.03511	1.69, (*) P=0.01326	3.036, (***) P=0.0002582

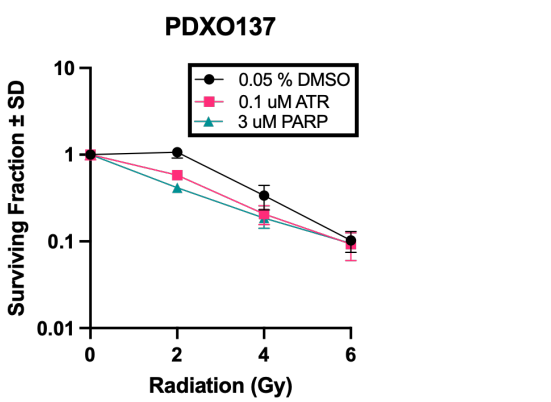

PDXO137	2 Gy	4 Gy	6 Gy
$SF_{xGy}^{DMSO}/SF_{xGy}^{ATRi}$	1.841, (ns)	1.651, (ns)	1.107, (ns)
$SF_{xGy}^{DMSO}/SF_{xGy}^{PARPi}$	2.613, (*) P=0.04029	1.891, (ns)	1.107, (ns)

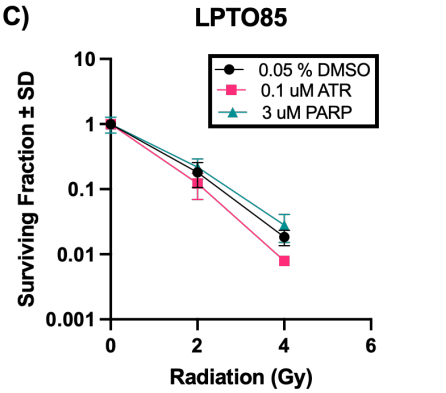

LPTO85	2 Gy	4 Gy
$SF_{xGy}^{DMSO}/SF_{xGy}^{ATRi}$	1.432, (ns)	0.625, (ns)
$SF_{xGy}^{DMSO}/SF_{xGy}^{PARPi}$	0.803, (ns)	N/A

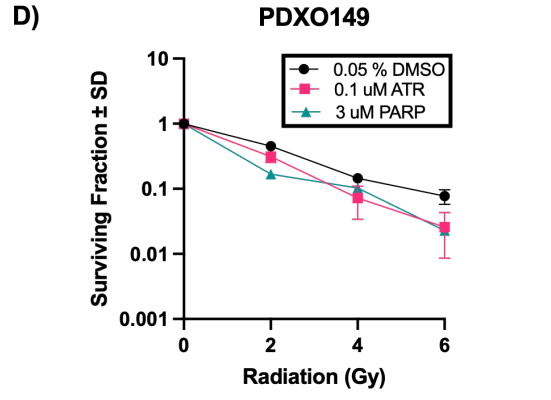

PDXO149	2 Gy	4 Gy	6 Gy
$SF_{xGy}^{DMSO}/SF_{xGy}^{ATRi}$	1.44, (*) P=0.03511	2, (*) P=0.03351	3.1, (*) P=0.01185
$SF_{xGy}^{DMSO}/SF_{xGy}^{PARPi}$	2.687, (**) P=0.007755	1.381, (*) P=0.04052	3.444, (**) P=0.007755

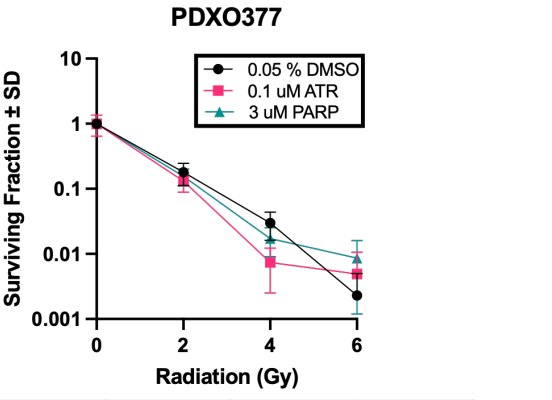

PDXO377	2 Gy	4 Gy	6 Gy
$SF_{xGy}^{DMSO}/SF_{xGy}^{ATRi}$	1.127, (ns)	3, (*) P=0.03511	N/A
$SF_{xGy}^{DMSO}/SF_{xGy}^{PARPi}$	1.145, (ns)	1.714, (ns)	N/A

Figure 5.8. Radiosensitisation of NSCLC organoids after treatment with DDRis. Organoid formation assays of NSCLC organoids post-irradiation and DDRi combinations. Organoids were cultured with either an ATRi or a

Figure legend continues in the next page

PARPi 1 h prior to irradiation. Number of organoids formed were measured and surviving fraction was calculated at day 10 (for **A)** LPTO126, **B)** PDXO137 and **C)** LPTO85), day 14 (**D)** PDXO149) or day 15 (**E)** PDXO137) after re-seeding the cultures into single cells in a DDRi-free medium 24h post-treatment. Post-IR surviving fraction graphs of NSCLC organoids treated with a single dose of 0-6 Gy of irradiation and/or 0.1 μM of and ATRi or 3 μM of a PARPi SF ratios and statistical significance of data in tables bellow each graph. The SF ratio ($SF_{xGy}^{DMSO}/SF_{xGy}^{Drug}$) for each IR dose is compared a value of 1, in R with the 'mratio' test (Dr. Mark Jackson). Graphs made with Graphpad Prism 9. n ≥ 3. ATRi: Ataxia Telangiectasia and Rad3-related inhibitor, *VE-822*. PARPi: Poly (ADP) Polymerase inhibitor, *Olaparib.*

In general, the surviving fraction of NSCLC organoids was consistently lower in the drug-treated samples compared to the DMSO drug-free control indicating a trend of radiosensitisation by DDRis (Figure 5.8.). LPTO126 LUAD ($p53^{WT}$) and PDXO149 LUSC ($p53^{null}$) lines exhibited statistically significant SF ratios across all investigated irradiation-doses (Figure 5.8., **A)** and **D)**), with SF ratio values exceeding for the PARPi at 6 Gy (LPTO126 $SF_{6Gy}^{DMSO}/SF_{6Gy}^{PARPi}$=3.036, p=0.0002582; PDXO149 $SF_{6Gy}^{DMSO}/SF_{6Gy}^{PARPi}$=3.444, p=0.007755). These indicate clear radiosensitising activity for both the ATRi and the PARPi in these lines across different radiation doses. Contrastingly, the SF ratio differences computed for the LPTO85 line are not statistically significant (Figure 5.8., **C)**). Interestingly, this line is also the most radiosensitive one amongst the evaluated lines (Figure 5.6., B)) and both the ATRi and the PARPi have demonstrate robust single-agent activity in this context (Figure 5.8., **C)**). Altogether this suggests that both the ATRi and the PARPi exhibit single agent activity against the LPTO85 organoids but do not display radiosensitising activity. However, it should be considered the possibility that the assay window may be too narrow in this line to accurately assess the combined effects of drug and radiation responses, potentially influenced by strong SF decrease after irradiation in the DMSO control. Both PDXO137 and PDXO377 lines exhibited SF ratios greater than 1, suggesting radiosensitisation by a drug in a certain irradiation-dose. However, in the case of PDXO137 (Figure 5.8., **B)**), only the addition of the PARPi at 2Gy of radiation was proven significant (i.e. $SF_{2Gy}^{DMSO}/SF_{2Gy}^{PARPi}$=2.613, p=0.04029) and in the case of PDXO377 (Figure 5.8., **E)**), significance was observed only with the addition of the ATRi at 4Gy of radiation (i.e. $SF_{4Gy}^{DMSO}/SF_{4Gy}^{ATRi}$=3, p=0.03511).

Taken together, the data suggest that NSCLC organoids can be sensitised to radiation using DDRis, but that the concentrations of DDRis and radiation dose that maximise synergy may need to be optimised for each assay format and line.

5.5. Effects of DDRi combined with radiation in NSCLC organoids' cell cycle

Part of the DNA damage response to radiation-damage involves arrest or alterations to the cell cycle due to radiation-specific checkpoints that arrest cells until DNA has been repaired or until cells activate apoptotic or autophagy pathways. To explore the effects of adding an ATRi or PARPi and radiation treatment on the cell cycle, treated cells were stained with Propidium Iodide and analysed by flow cytometry.

Briefly, 500 cells / µL Matrigel in 25 µL blobs of LPT0126, PDXO137, LPTO85, PDXO149 and PDXO377 NSCLC organoid-lines were seeded in 24 well plates and cultured to form organoids for 7 days. These were then pre-treated 1 h before irradiation with a DDRi (4 Gy, 0.1 µM ATRi or 3 µM PARPi), irradiated (4 Gy, 0.05 % DMSO) or sham-irradiated (0.05 % DMSO). Twenty-four hours post irradiation, organoids were harvested, dissociated into single cells with TrypLE Express, fixed in suspension, and analysed by flow cytometry following Propidium Iodide staining. FlowJo analysis software (Cell cycle assessment: Watson Model) was used to analyse 10,000 single cell events per data point (see Methods for details).

Irradiation of the TP53 wild-type lines LPTO126 and PDXO377 increased the number of cells in the G_2/M phase of the cell cycle, from 10.5% ± 2.8 to 35.2% ± 3.6 for LPTO126 and from 16.9% ± 6.9 to 38.2% ± 10.5 for PDXO377 (Figure 5.9., A) and B)). G_2/M cell cycle arrest is a widely known radiation response that allows cells to stop and repair DNA damage. When treated with an ATRi the G_2/M arrest was mostly inhibited (% 16.9 ± 5 G_2/M for LPTO126 (from 35.2 %) and 24% ± 4 G_2/M for PDO377 lines (from 38.2 %). This response was expected from the mechanistic point of view, as ATR is one of the central molecules controlling G_2/M cell cycle arrest following DNA damage. By contrast, incubation with the PARPi slightly increased G_2/M arrest effect compared with IR alone in these two TP53 WT lines. This phenomenon had previously been shown in healthy fibroblasts and in HR defective melanoma cells (Weigert et al. 2020).

TP53 mutated PDXO149 organoids did not show a large increase in cell numbers in G_2/M after radiation, increasing only from 11.5% ± 1.9% to 14.9% ± 0.2 (Figure 5.9., **D)**). Although p53 mainly controls G_1 cell cycle arrest, it is also involved in post-IR G_2/M cell cycle checkpoint arrest. In fact, TP53 mutated glioblastoma cells have been shown to evade G_2/M checkpoint after treatment with 'extremely low- frequency electromagnetic fields',

compared to a TP53 WT line (Mehdizadeh et al. 2023). Similar pattern as the PDXO149 line could be noted in the other TP53 mutated line PDXO137. LPTO85 (TP53 mutated) did seem to arrest cells in G_2 upon irradiation. However, cell cycle data in lines PDO137 and LPTO85 shouldn't be strongly interpreted as only a single replicate could be done.

Co-treatment of PDXO149 line organoids with an ATRi and IR (Figure 5.9., D)) did not seem to have an effect on the cell cycle progression (similar response was seen in the PDXO137 line), suggesting that TP53 mutation was sufficient to avoid a G_2/M cycle checkpoint arrest. As with the previously studied TP53 WT lines, incubation with a PARPi did increase G_2/M cell cycle checkpoint arrest 24 h after irradiation in the TP53 mutated lines (Figure 5.9., C), D), E)).

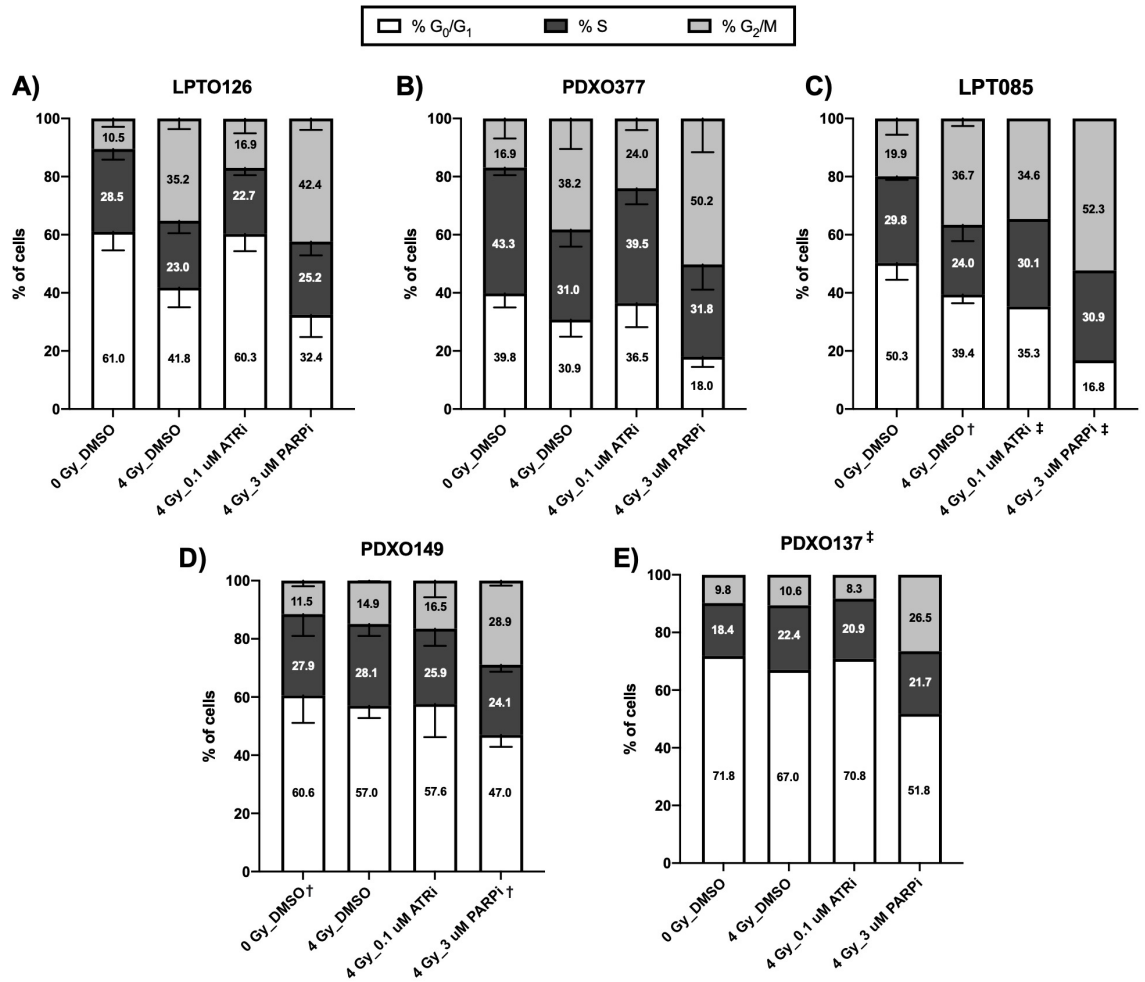

Figure 5.9. Cell cycle response of NSCLC organoids to irradiation and DDRI combination. Cell cycle analysis (PI staining and flow cytometry) of NSCLC organoids (as per graph titles) 24 h after 0 / 4 Gy of a single-dose irradiation with / without a DDRi. DDRi added 1 h before irradiation. ATRi: VE-822. PARPi: Olaparib. Data was analysed in FlowJo 10.8.2 cell cycle, Watson model. Graphs made with GrapPad Prism 9. n≥3. †: n=2. ‡: n=1.

Taken together, the cell cycle data suggests that organoid cell responses to irradiation are consistent with the mutational background of the line and the expected mechanism of action of the DDRi used in the studies.

5.6. Transcriptional response of NSCLC organoids to IR

Immunohistochemical studies of NSCLC organoids showed heterogeneity in the expression of cell type markers including TP63 and TTF-1, suggesting that cells within NSCLC organoids may exist in markedly different differentiative state to each other (Shi et al. 2020). Similar observations have been made in colorectal cancer (CRC) organoids. Some CRC tumour subtypes have been observed to contain mucin-secreting goblet cells suggesting that cells within organoids (and cells within tumours) are able to partially differentiate. Systematic studies of primary tumours and organoids by scRNAseq revealed that organoids displayed similar transcriptional patterns, cell clustering, as the original tumour (Wang et al. 2022b). In addition to cellular heterogeneity, organoids also show spatial heterogeneity with respect to oxygen and nutrient gradients (Stadler et al. 2015; Hubert et al. 2016; Nunes et al. 2019). Consequently, it is reasonable to anticipate intra-organoid cell heterogeneity in NSCLC organoids too. It can be hypothesised that individual cells within a NSCLC organoid will be differentially sensitive to radiation based on their physiological and differentiative status. Similar differences in radiosensitivity *in vivo* may help explain radioresistance in some tumour types and could be important in helping to understand tumour re-growth following radiotherapy. To better understand differences in radio-responses between cells in organoid culture, scRNAseq was used to analyse NSCLC responses.

The 10x Chromium 3' scRNAseq was used for the studies conducted. At the core of the system is the Chromium Controller, which partitions cells into nanoliter-sized gel beads in emulsions (GEMs). Each successful GEM contains a single cell, a single barcoded gel bead and reverse transcription reagents (Figure 5.10., A)). During reverse transcription, the cellular mRNA is converted into complementary DNA (cDNA) which incorporates a unique barcode per bead. Importantly, the technique relies on mRNAs from individual cells being labelled with unique barcode identifiers (UMIs) since the only primers for reverse-transcription are provided by the bead that has been captured with the cell in the same emulsion droplet. These barcoded cDNAs are then pooled together and subjected to library preparation and sequencing, allowing for the simultaneous analysis of thousands of individual cells.

For the experimental layout, 500 single cells of the LUSC organoid lines PDXO377 ($p53^{WT}$) and PDXO149 ($p53^{null}$) were seeded per µL Matrigel in 25 µL blobs in 24 well plates and cultured to form organoids for 12 days (Figure 5.10., A)). 12 days of growth was expected to create big enough organoids in order to ensure differential hypoxia and nutrient deprivation gradients within each organoid (Stadler et al. 2015; Hubert et al. 2016; Nunes et al. 2019). The organoids were then irradiated with a single dose of 4 Gy or non-irradiated and returned to the a 37 ^{O}C 5% CO_2 incubator. Four hours later, several blobs (4-6) per sample were pulled together to make for sufficient material, and organoids were dissociated with TryPLe into single cells. The decision to use the 4-hour post-irradiation timepoint was based on capturing immediate radiation responses before cell death or changes in apparent 'cell type' occurred. This aimed to allow for the correlation of cellular identity both before and after irradiation, facilitating inference regarding radio-responses in individual cells present prior to radiation therapy (Borras-Fresneda et al. 2016). After isolation of the single cells, a final wash in the base culture medium with 0.04 % BSA, as recommended by 10X Genomics, was performed before the final viability was counted (Trypan Blue excluding) for loading in the Chromium Controller (Figure 5.10., B)). All library preparation was done by Angela Marchbank at the CU Genome HUB and sequencing was carried out in the Wales Gene Park (details in methods).

A)

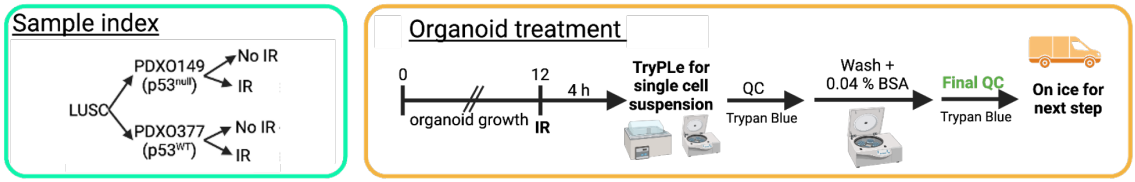

B)

	Total cells/mL	Viability (%)	% of single cells	Average cell size (µm)
PDXO377, 0 Gy	$1.02 \cdot 10^6$	82.7	94	11.9
PDXO377, 4 Gy	$1.17 \cdot 10^6$	90.8	93.9	11.9
PDXO149, 0 Gy	$9.47 \cdot 10^5$	90	71.4	15.9
PDXO149, 4 Gy	$8.56 \cdot 10^5$	91.6	78.2	15.7

Figure 5.10. Sample workflow for single-cell RNAseq experiment. A) Sample index and organoid treatments before library preparation for single-cell RNAseq sequencing. **B)** Trypan Blue excluding life cell final count before library preparation per sample.

The output data of the sequencing was run through the 'CellRanger' standard pipeline for 10X Genomics 3' scRNAseq pipeline by the CU Genome HUB's Bioinformatic specialist Dr. Sarah Christofides. This pipeline aligned the scRNAseq data to the human genome and sorted transcripts by barcode (individual bead) and UMI (individual initial mRNA) counting to generate a matrix containing unique transcripts that were linked to individual 'cells' based on their barcodes. The pipeline also involved filtering out 'cells' with low numbers of transcripts depending on a barcode rank plots (Figure 5.11., C)). The total number of cells per sample called by CellRanger are indicated in the second column of Table 5.1.). Cells with < 20 % of mitochondrial reads, doublets (scTK package) and cells with > 0.5 % RNA contamination (decontX) were further removed, as standard. Details of the bioinformatics analysis can be found in the methods. The final number of cells used for subsequent analysis are indicated in the last column of Table 5.1.

Table 5.1. Total number of cells per sample 'assigned' by the bioinformatics pipeline after scRNAseq.

Sample	N of cells out of CellRanger	N of cells after removing cells with < 20% mitochondrial reads	N of cells after removing doublets	N of cells after removing cells with > 0.5 % RNA contamination
PDXO377, Ctrl	389	375	329	368
PDXO377, IR	719	719	653	562
PDXO149, Ctrl	368	368	355	302
PDXO149, IR	324	324	316	131

Unfortunately, the data generated pointed to a major problem with the batch of manufacturer-supplied beads. This problem was acknowledged by the manufacturer and likely involved the 'lysis' of beads at some point prior to their delivery. Although this reagent failure dramatically affected the data that was generated, it still allowed some useful information to be ascertained from the experiments.

The failure observed in the scRNAseq experiment using the 10X Genomics kit was due to the release of components from the beads, which had the effect of generating more than one 'cell' (called by each specific bead barcode) from an individual GEM. This was likely

because (see Figure 5.11., B)) low levels of unique 'cell' primers in solution contaminated GEMs containing an intact bead (with high levels of bead-specific primers) and an intact cell. The contaminating primers from the lysed beads primed cDNA synthesis in the GEM, resulting in the generation of multiple PCR products from the same cell that would be labelled as if they were from distinct cells in the subsequent data analysis. The low level of the contaminating primers by comparison with the intended cell primers present in intact beads generated multiple unique 'cell' signatures that each contained only a few transcripts. This was observed in the barcode rank plots (Figure 5.11., C)) where ~8.9 million 'cells' with less than 500 UMI counts each (individual original mRNA transcripts) were detected, even when 'only' around 10,000 original cells were actually loaded into the Chromium Controller. Conversely, around 10,000 cells with at least 1000 UMI counts each are usually detected in a functional 10X Genomics Chromium 3' single-cell RNAseq experiment. Unfortunately, we only obtained around 300-500 real cells (with > 500 UMI counts each) in our experiment (last column Table 5.1). This low number of 'cells' in the analysis pipeline restricted the number of analyses that could be performed with statistical confidence. Two of the approaches that did provide useful information came from single cell identity annotation and *pseudobulk*-RNAseq analyses (see Discussion for consideration of additional analyses that would have usefully informed the study of radiation responses).

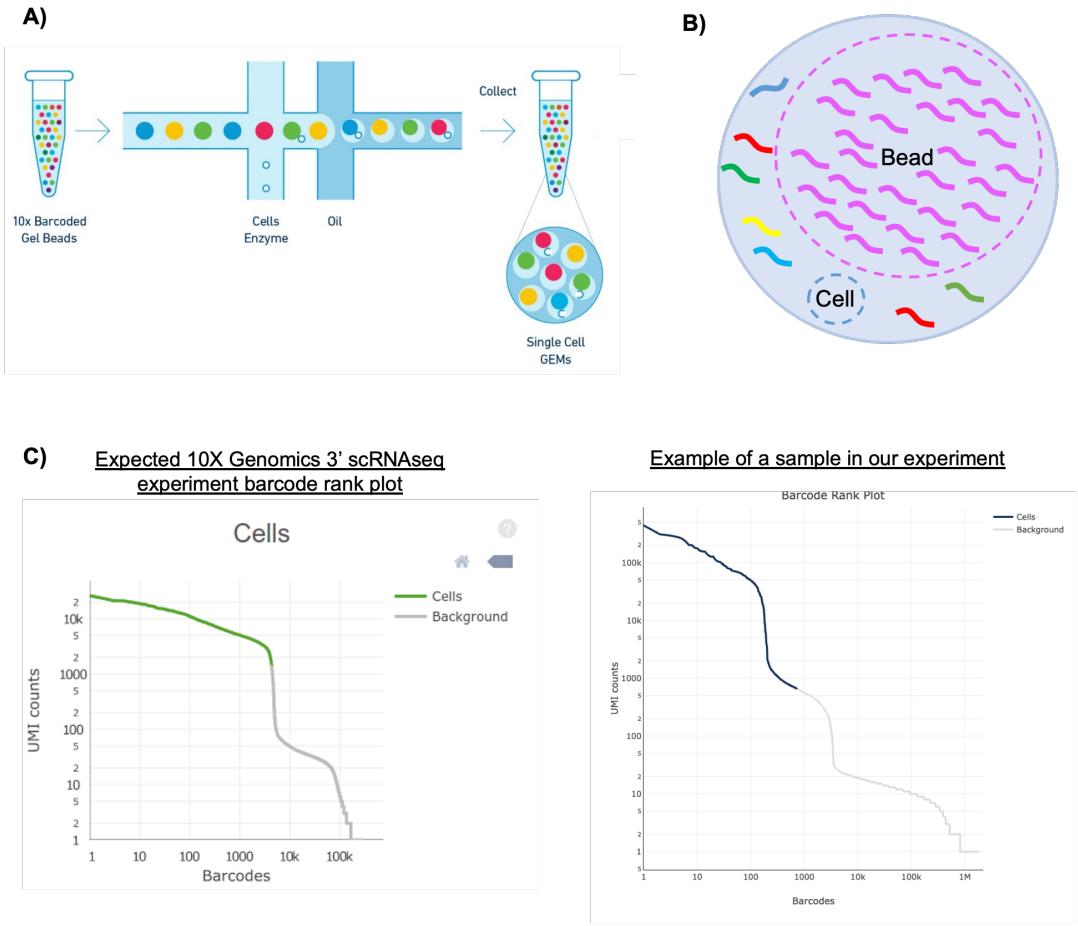

Figure 5.11. 10X Genomics Chromium 3' single-cell RNAseq experiment failure. A) Diagram for Chromium Controller function from 10X Genomics. **B)** Diagram of a representative GEM obtained in our experiment containing and intact cell, an intact bead and extra material internalised from disrupted beads. **C)** Barcode Rank Plots ranking each barcode (individual bead) from most UMI (original mRNA transcript) counts to least. The left diagram represents an expected plot in a scRNAseq experiment and the right diagram is a representative example of one of our sample's barcode rank plot.

To evaluate the heterogeneity of the NSCLC organoids in terms of 'cell-type' the filtered data from PDXO377 control and PDXO149 control samples (non-irradiated) were mapped onto the recently published molecular cell atlas of the human lung (Travaglini et al. 2020) using scmap-cell, a tool for the unsupervised projection of scRNAseq data. Scmap finds the 10 nearest neighbours to each cell (i.e. the 10 most similar cells to each query cell) and then picks the annotation that is most common among the neighbours; if there is a 'tie' for commonest annotation, the cell is labelled 'ambiguous'.

The reference data from Travaglini et al. was obtained by scRNAseq from 3 patients, sequencing approximately 75,000 cells across all lung tissue compartments and circulating blood and annotation of clusters was based on enriched expression of canonical cell identity markers. It is worth clarifying, before further points can be made, that the reference data

subclassified basal cells into different basal-states. Basal cells were, thus, $CK5^+$ cells that didn't fall in any of the following descriptions: proliferating basal cells that were enriched in cell cycle genes; differentiating basal cells that exhibited CK5 decrease expression and increase expression of HES1, CK7 and SCGB3A2, indicating active differentiation towards other epithelial fates; and proximal basal cells that had been resected from the bronchus (also $CK5^+$).

Analysis using the scmap-cell tool identified several lung airway epithelium cell types (Figure 5.12.) in LUSC cultures, suggesting that LUSC organoid cultures display significant cellular heterogeneity. Interestingly, we also saw inter-line differences in cell type percentages per organoid-line. In PDXO377 line, most detected cells were basal (total of 76 %, divided into 12 % basal, 4 % differentiating basal, 19 % proliferating basal and 40 % proximal basal) although especially some mucous and goblet cells were also detected. In PDXO149 line, the highest percentage of annotated cells were goblet cells (39 %), followed by differentiated basal (17 %), proximal basal (13 %) and proliferating basal (7 %). Club and ciliated cells were also detected here. Basal transformed cells are considered the CSCs of LUSC, therefore, the fact many of the annotated cells in the LUSC organoids were basal suggest a good representation of *in vivo* LUSC tumours. Nonetheless, a direct single-cell level comparison between the organoid-line and its tumour tissue of origin would be needed to demonstrate the direct representation at the cell-type level.

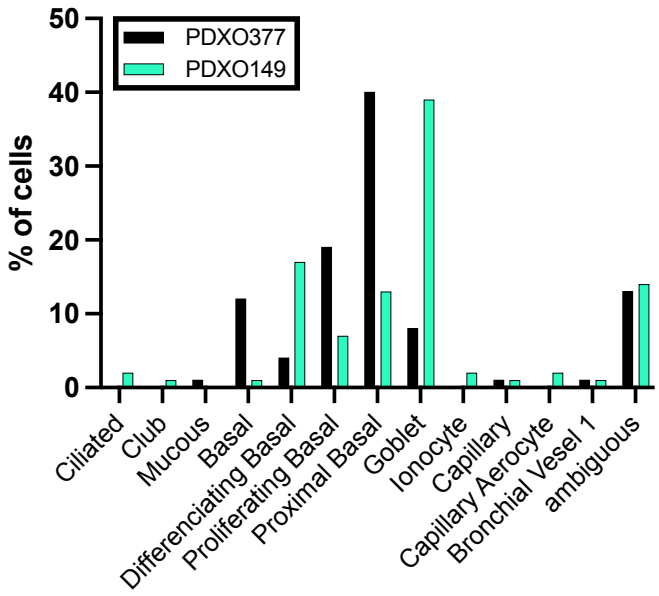

Figure 5.12. NSCLC cell-heterogeneity. Cell annotation of PDXO377 (total of 368 cells) and PDXO149 (total of 302 cells) cells based on Travaglini et al.

We then investigated the potential impact of radiation on the proportions of different cell types within the PDXO377 line. To achieve this, the same annotation technique as previously described for the PSCO377 and PDXO149 control samples was perform on the PDXO377 IR sample (Figure 5.13.). However, we refrained from conducting further analysis on the PDXO149 line due to insufficient cell count (only 131 cells in the IR sample).

The major difference between the control and the IR PDXO377 organoids was the % of proliferating basal cells (Figure 5.13., red arrow). This was reduced by almost half (19 % on ctrl vs 11 % on IR), suggesting some level of cell cycle arrest in the TP53 wild-type PDXO377 line post-IR, that coincides with our previous cell cycle data in which G_2 arrest was observed after IR (see Figure 5.9., B)).

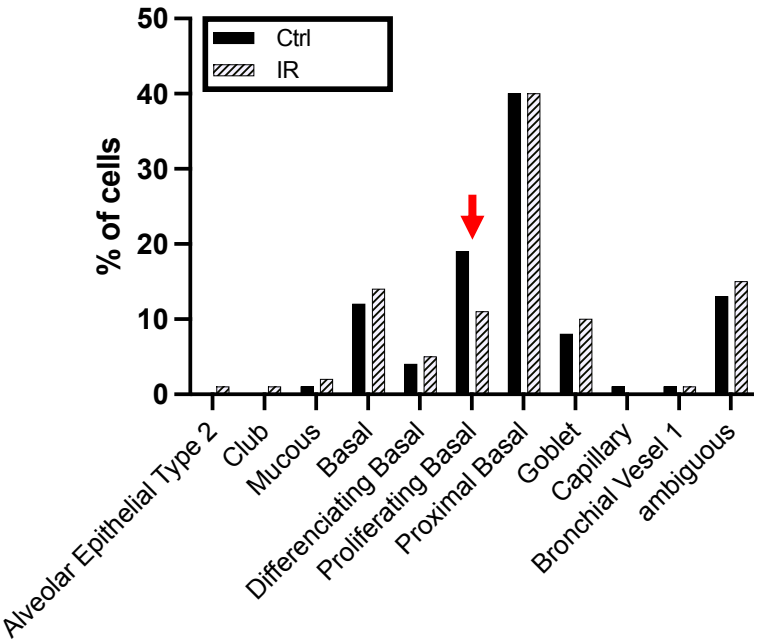

Figure 5.13. Impact of irradiation on cell type heterogeneity in the LUSC PDXO377 organoid-line. Cell annotation of PDXO377 Ctrl (total of 368 cells) and PDXO377 IR (total of 562 cells) cells based on Travaglini et al. Red arrow pointing at the major difference between IR and non-IR sample.

To further explore the overall effect of irradiation in PDXO377 organoids, the samples were analysed as a *pseudobulk*-RNA experiment. This analysis was formed using data from the filtered cells dataset from CellRanger as previously described. Genes with less than 100 reads overall were removed, the expression data was transformed into counts per million and the Ctrl and IR samples were compared in R Studio. As only a single replicate per sample was available, differentially expressed (DE) genes could not be called by statistical p-value,

and thus DE genes were called if they showed a log2FC of 0.585, equivalent to a 1.5 gene expression fold-change. Two thousand and fifty-three genes were DE in the irradiated sample compared to the control, 1661 genes were upregulated and 392 downregulated. The 500 most upregulated genes and all the downregulated genes were separately analysed for Gene Ontology (GO) analysis with a false discovery rate (FDR) < 0.05 (see details in methods).

As it can be seen in Figure 5.14. 'Regulation of cell differentiation' and 'Cell-cell signalling' were upregulated in the irradiated sample. In addition, downregulation of signatures like 'Regulation of cell population proliferation', 'cell division' and 'mitotic cell cycle progress' and downregulation of 'regulation of cell death' and 'apoptotic process' were detected, suggesting that irradiated PDXO377 cells may slow down cell proliferation and arrest cells for DNA repair downregulating apoptosis.

A) Upregulated

Gene Set Name	p-value
GOBP_CELL_MORPHOGENESIS	4.42E-15
GOMF_PURINE_NUCLEOTIDE_BINDING	2.22E-12
GOBP_RESPONSE_TO_CYTOKINE	7.83E-12
GOBP_POSITIVE_REGULATION_OF_MOLECULAR_FUNCTION	7.93E-12
GOBP_CELL_MOTILITY	9.35E-12
GOBP_REGULATION_OF_CELL_DIFFERENTIATION ←	2.32E-11
GOBP_CELL_CELL_SIGNALING ←	4.60E-11
GOBP_REGULATION_OF_CATALYTIC_ACTIVITY	1.24E-10
GOMF_MOLECULAR_FUNCTION_REGULATOR_ACTIVITY	1.48E-10
GOBP_REGULATION_OF_TRANSPORT	1.49E-10

B) Downregulated

Gene Set Name	p-value
GOBP_REGULATION_OF_CELL_POPULATION_PROLIFERATION ←	2.10E-11
GOBP_REGULATION_OF_CELL_DEATH ←	5.40E-11
GOCC_EXTERNAL_ENCAPSULATING_STRUCTURE	2.33E-10
GOBP_APOPTOTIC_PROCESS ←	4.11E-10
GOBP_EPITHELIUM_DEVELOPMENT	1.35E-09
GOBP_POSITIVE_REGULATION_OF_CELL_POPULATION_PROLIFERATION	5.07E-09
GOBP_NEGATIVE_REGULATION_OF_CELL_DEATH	1.41E-08
GOBP_CELL_DIVISION ←	1.50E-08
GOBP_MITOTIC_CELL_CYCLE_PROCESS ←	3.54E-08
GOBP_ENZYME_LINKED_RECEPTOR_PROTEIN_SIGNALING_PATHWAY	3.98E-08

Figure 5.14. GO terms of upregulated and downregulated genes in PDXO377 IR vs Ctrl. Gene Ontology terms of differentially expressed genes, **A)** Upregulated and **B)** Downregulated and their p-values which counts for the 'hypergeometric distribution of overlapping genes over all genes in the gene universe'. Red arrow points to the most interesting signals in relation to radiation-response.

Overall, despite the encountered experimental problems, we were able to show cellular intracultural heterogeneity within NSCLC organoids and a clear reduction of markers of cell proliferation after irradiation together with downregulation of cell division, cell cycle progress and apoptosis.

5.7. Key summary

In this chapter we aimed to develop and implement different analysis methods for studying the response of NSCLC organoids to radiation and radiation-DNA damage repair inhibitors.

Differences in the total area covered by NSCLC organoids between control and treated cultures were observed from day 6 post-irradiation on using an assay that live-imaged and automatically quantified organoids within a 3D Matrigel blob (IncuCyte). In addition, a clear dose-dependent response to radiation was detected in some of the NSCLC lines using a metabolic ATP assay. However, it was found that each line needed to be optimised for the assay, as there was data scattering observed, particularly at high doses of irradiation or with particularly 'resistant' organoid-lines. To overcome these difficulties, we successfully developed a new organoid re-plating assay that was highly sensitive and able to detect significant radiation dose-dependent response differences in NSCLC organoids. This assay revealed important information that was previously overlooked by ATP assays. Additionally, we observed an enhancement of radiation sensitivity in NSCLC organoids lines after pre-treatment with a PARPi or an ATRi, as demonstrated by the results from our organoid re-plating assay. These findings will be further discussed in the Discussion chapter.

Our study also demonstrated that radiation exposure led to an increase in the number of γH2AX foci, which serve as markers for DNA double-strand breaks in the investigated PDXO149 organoids. The maximum signal was observed at 1 hour after irradiation, and by 24 hours post-treatment, no detectable γH2AX foci were present. This suggested that the majority of DNA damage in the surviving organoids was repaired within 24 hours following radiation exposure. Moreover, cell cycle assays revealed that NSCLC organoids exhibited the anticipated mechanistic response following irradiation (and also with pre-treatment with an ATRi or a PARPi) depending on their TP53 status.

Although we were unable to conduct a single-cell transcriptomics analysis on the IR response of the NSCLC organoids; our findings demonstrated that LUSC organoids

exhibited distinct 'cell types' within each culture, which may reflect the *in vivo* conditions of LUSC. Additionally, irradiation treatment resulted in reduced cell proliferation and apoptosis in PDXO377 organoids (as observed through pseudobulk RNAseq), consistent with our previous report of G_2 cell cycle arrest following radiation in this organoid line.

Overall, we performed and design several successful assays to analyse organoids' response to radiation. Our results revealed varying responses among different NSCLC organoid lines, suggesting inter-line differences in their radiation sensitivity. We also observed potential intra-line variations in terms of differential 'cell types' within the organoids. These might contribute to differences in NSCLC organoids intra-line response to radiation, although this is yet to be investigated and will be further discussed in the Discussion chapter.

6. General discussion

In recent years, there has been growing interest in utilising organoids as a tool for cancer research. Many organoids have been established from multiple tissue types, but at the start of this project, the establishment of long-term NSCLC organoid cultures was in its infancy. Only one research paper on NSCLC organoids had been published and, from resection samples, it described only TP53 mutant cancer organoids since it relied upon the use of a drug to select for TP53 mutant tumour cells (Sachs et al. 2019). During this project, additional reports of the generation of NSCLC organoid lines were published (Kim et al. 2019; Chen et al. 2020; Dijkstra et al. 2020; Li et al. 2020; Shi et al. 2020; Werner et al. 2021; Ma et al. 2022). Access to NSCLC organoid lines from Shi et al. was particularly important for the key studies described in this thesis (Shi et al. 2020).

Although radiation is a standard treatment in many tumour types, there have been a very limited number of studies of radiation responses using organoids (Nagle and Coppes 2020; Yao et al. 2020; Lucky et al. 2021). In particular, at the time of writing, no reports had described the use of NSCLC organoids for analysing radiation responses. One reason for this gap in knowledge is likely to be the generic challenges associated with studying radiation-responses in 3D and a second reason is the fact that NSCLC organoid banks have only recently been described. One of the key results described in this thesis was the development of sensitive methods that can be used to study NSCLC organoid responses to radiation.

6.1. Development of a sensitive assay for radiation-response in 3D organoids

The gold standard for assessing the radiation response of 2D cell lines is the clonogenicity assay or colony formation assay (CFA), a classic and widely utilised technique in radiation biology and cancer research. The assay assesses the ability of individual cells to form colonies (of at least 50 cells) after exposure to ionising radiation, providing valuable information about cell survival and reproductive death. As an example, a general start point for a tumour cell line with 25-40 % plating efficiency (PE) in 6 well plates, consists of platting 200 cells for the sham-irradiated and 2 Gy doses, 400 cells for 4 Gy, 1000 cells for 6 Gy and 5000 cells for 8 Gy. The PE refers to the ratio of the number of colonies formed in an untreated line, to the number of cells seeded. After seeding, cells are allowed to attach and are treated with IR before the first division has happened. 24 h post-IR

(potentially lethal damage is already repaired) death cells are washed out with a medium change and remaining cells are subsequently incubated until cells in control dishes have formed sufficiently large colonies (typically 10-20 days, line-dependant). Subsequent wash, fixation, staining, and manual or automated colony counting yield data (number of colonies with >50 cells) form the basis for constructing dose-dependent survival curves (the number of colonies that arise after treatment of cells, expressed in terms of PE, is called the surviving fraction). The CFA offers critical insights into a cell line's post-IR long-term proliferation potential (Puck and Marcus 1956).

By contrast with the simple 2D assay format described above, the implementation of 'organoid formation assays' in 3D was a more complex challenge. Key features that distinguish 2D and 3D assay formats include the fact that dead cells are not 'washed away' in 3D assays. Both 2D and 3D formats allow non-proliferating cells to contribute to metabolic readouts, such as readouts of ATP, while 3D organoid assays can access readouts that explore the greater diversity of phenotypes seen in 3D (e.g. 3D morphological changes).

Although a range of NSCLC organoid assay formats were explored in this thesis, the most sensitive assay format identified was an organoid re-plating assay in which organoids were re-plated following irradiation. This was achieved by dissociation of the organoids with TrypLE, 24 h post-irradiation of fully formed organoids (after 7 days in culture from initial single cells), and re-plating from single cells to form new organoids. The total number of organoids per treatment were counted when the non-irradiated control had reached big-enough organoid-sizes. The quantified number of organoids ($d > 60$ μm) was used to create radiation dose-dependent survival curves. This assay format provided all surviving single cells (or small doublets / clusters) from the organoid culture with a fresh environment that directly assessed organoids' reproductive capability after irradiation (instead of assessing whether existing organoids grew larger than an initial size). The replating assay is probably the closest 3D assay format to that of the gold standard 2D CFA since both rely on the growth of colonies/organoids from single cells. Moreover, the ability to grow from single cells, compared to the ability to grow further when in the presence of surrounding cells (as in an already formed organoid), puts greater pressure on cells' ability to survive thereby more efficiently revealing the consequences of the radiation damage on individual cells.

Using the NSCLC organoid re-plating assay, inter-line differences in radiosensitivity, that were partially obscured in the simpler ATP metabolic assays, were uncovered although the exact time frames were not the same. In general, smaller organoids in size were formed after high irradiation doses and, in some very sensitive lines, very little organoid-growth could be seen from single cells (i.e. very few cells gave rise to an organoid). Moreover, I was able to detect line-dependant radiation sensitivity enhancement on the NSCLC organoids lines upon pre-treatment with a PARPi or an ATRi utilising the organoid re-seeding assay (These results and their significance will be further discussed in detail later, along with the basis of inter-line heterogeneity – see section 6.2).

A study has examined the response of fully formed CRC organoids to radiation. This will be later discussed in-depth in relationship with organoids' vs patients' responses to radiation and drug treatments. However, the methodology used for assessing organoid treatment-response is worth discussing in this section. Yao et al. conducted what they called 'organoid formation assays' to evaluate radiation response by visually determining if an organoid was considered a 'living organoid' post-irradiation, without re-plating. This assessment involved counting darkened or altered phenotype organoids, such as those lacking their main structure in the case of lumen-based organoids (the majority of CRC organoids), as indicators of cell death. This technique was validated by neutral red assay, which relies on the ability of live cells to incorporate neutral red to their lysosomes whilst dead cells lose this capacity (Yao et al. 2020). NSCLC organoids, however, mostly displayed solid phenotypes and, therefore, it was not possible to rely on structural integrity to determine the viability/cellular status of the NSCLC organoids. In contrast, the re-plating assay described here directly evaluated the proliferative potential of irradiated cells within the organoid.

Although the replating assay was sensitive, the format might be further optimised to reduce error and the effective size of the assay window particularly at higher radiation doses. To address this issue, which is due to decreasing clonogenicity at high IR-doses, in 2D assay formats a dose-dependent increase in the initial seeding is used for CFAs, as explained at the beginning of this section. However, this approach was not directly applicable to organoids. I showed that initial seeding cell concentrations can affect organoid forming capacity itself and general culture dynamics (due to local vs. global cell dynamics). In addition, dead or dying cells in a 2D environment usually lose their attachment to the plate and are washed away with a medium change, while in the 3D

environment remain trapped in the Matrigel. As a consequence, some kind of separation of dead and living cells would be required before an equivalent format might be implemented in 3D. However, this might be complicated as cells can die at different points during the colony/organoid formation assay and, although in 2D they would be washed away with a final medium wash before counting, this might be very complicated to implement in 3D at any timepoint after re-plating. Alternatively, future experiments at higher doses might simply seed more total number of wells for higher radiation doses (maintaining the same seeding density and, thus, not altering the radiation-independent organoid formation capacity). Nevertheless, with the current re-platting assay methodology, I was able to detect post-IR surviving fractions bellow 0.01 and still observe significant changes in combined treatments even at fraction levels as low as 0.1 (Figures 5.6/7, Chapter 5). These values, although highly line-dependant, are in the range of those usually observed in NSCLC 2D formats (Weber et al. 2016).

In the thesis, a range of other assay formats were also explored. Some of these offered complementary data while others may have utility in particular contexts such as high throughput contexts when used with particular organoid lines.

The use of image-based readouts can in principle provide an organoid-by-organoid readout of radiation responses. However, in this thesis, a majority of image-based assays that were used integrated organoid image parameters. The IncuCyteS3 platform and Organoid Analysis IncuCyte software could be used to continuously image 24-well plates within an incubator over multiple closely-spaced time points. The automatic data generated by this platform produced tight quantitative data and was able to accurately track subtle changes in total organoid population area with precision. When three NSCLC organoid lines were exposed to 4 Gy of radiation, the IncuCyte platform in combination with the Organoid Analysis IncuCyte software showed clear radiation-dependent changes in total area of well covered by organoids with low levels of apparent variance. Therefore, it would be anticipated that this image-based assay format would offer data with an assay window / sensitivity that would complement the functional organoid re-plating assay data (Figure 5.1., Chapter 5).

Although high quality data was generated using the imaging modalities and software described, the long-term potential of imaging-based assays likely remains under-exploited. More might be done to explore radiation response by exploiting changes in

organoid morphology changes. Recent work showed that CRC organoids demonstrated clear morphological changes to small molecule inhibitors of the Wnt pathway even while changes in metabolic responses (ATP levels) were variable or inconsistent (Badder et al. 2020). The full quantification of 3D organoid morphology requires sophisticated microscope imaging platforms and it often requires the fixation of the samples (preventing easy longitudinal time-course studies), but may ultimately be a highly valuable platform that can take advantage of the complex biology that is present within the organoid context.

Recent advances in imaging techniques may actually allow the integration of both metabolic and imaging data. One approach to do this might be a combination of light microscopy and optical metabolic imaging (OMI). OMI utilises optical techniques, such as multiphoton imaging, to measure changes in cellular metabolism and redox states. By monitoring autofluorescent molecules like NADH (nicotinamide adenine dinucleotide) and FAD (flavin adenine dinucleotide), OMI can provide real-time, label-free insights into cellular metabolic activity and mitochondrial function. This non-invasive and high-resolution imaging approach might enable researchers to assess early metabolic responses to radiation exposure in individual cells and multicellular organoid structures. As with the IncuCyte system, OMI offers the advantage of dynamic, continuous monitoring over time, capturing subtle metabolic changes that may precede cellular phenotypic alterations. Additionally, it eliminates the need for exogenous probes or labels, minimising potential interference with cellular processes. Using OMI, Pasch et al. showed a strong correlation between changes in CRC organoid diameter and metabolic activity (as measured by NAD(P)H / FAD ratio) when assessing organoids responses to radiation and fluoracil (5-FU, antimetabolite); 82 % of treatments were categorised as effective, intermediate, or non-effective by both methods (Pasch et al. 2019). Similar positive correlations were reported in breast cancer and pancreatic cancer organoids using OMI to assess sensitivity of known drugs (Sharick et al. 2020).

A further advantage of imaging-based approaches is that they can be combined with the imaging of physiological or differentiative markers (Lukonin et al. 2021). Assays for live/dead cell dyes (e.g. amine-reactive fixable dyes) that are / are not excluded by an intact plasma membrane offer a straightforward means of distinguishing between viable and non-viable cells, facilitating the quantification of radiation-induced cytotoxicity (Perfetto et al. 2010; Lekshmi et al. 2017). Additionally, specific radiation marker

staining enables the visualization of targeted cellular components or processes, shedding light on radiation-induced changes in specific pathways and in a cell-by-cell basis. Immunofluorescence staining of γH2AX is commonly used as a radiation-response readout based on its well-established role as a marker of DNA double-strand breaks (DSBs). Punctate staining for γH2AX is highly sensitive since even a few DSBs can result in the formation of visible foci, making it a valuable tool for detecting radiation-induced DNA damage at low doses. Furthermore, the persistence of γH2AX foci over time provides insights into the kinetics of DSB repair, helping to delineate cellular responses to radiation exposure, including DNA damage recognition and repair processes (Raavi et al. 2021). I demonstrated that 4 Gy of irradiation increased the numbers of γH2AX foci, both in a NSCLC organoid line and in NSCLC CellAggs. The maximum signal was observed 1 hour after irradiation, while no visible γH2AX foci were present after 24 hours, suggesting efficient DNA repair within surviving cultures by this time point (CellAggs: Supplemental Figures 3.2/3, Appendix and organoids: Figure 5.4., Chapter 5). However, measuring γH2AX foci in organoids resulted in a very low throughput, tedious, experimental work. These imaging methodologies collectively provide a comprehensive framework for the assessment of radiation response *in vitro*, enabling the elucidation of cellular dynamics, and molecular mechanisms, thereby advancing our understanding of the effects of ionising radiation on diverse cell types and experimental contexts. Additional imaging based assays (e.g. 53BP1 staining) might in the future also be used to study localised radiation responses in NSCLC organoids. Ultimately, it would be useful to be able to correlate individual cell responses to radiation within an organoid, based on their expression of radiation response biomarkers, to their ability to functionally generate new organoids in a re-plating assay. This type of combined assay would require the development of a live-cell readout for intra-cellular DNA damage responses.

In the short-term, practical image-based assays that can be used for routine radiation response assays will likely focus on the use simple outputs that ‘integrate parameters’ such as the total area of well occupied by organoid in both fixed end point and live-cell assay formats. However, even with these existing formats, there are a number of practical issues that confront the experimentalist. These practical issues-convert many or even most ‘automated’ assays into manually supervised assays that require careful optimisation and curation. Assays need to be optimised line-by-line, via the specification of imaging acquisition parameters, software ‘mask’ parameters and quantification parameter ‘thresholds’. Each organoid, based on its subtly different properties was found

to need careful optimisation of seeding density to optimally match the pipeline's analysis parameters. Taken together, the approaches above can be very time consuming for assays that require comparisons of multiple lines. As a consequence, simple metabolic readouts will continue to be an experimental mainstay.

Metabolic readouts (such as the measurement of relative ATP levels as a marker of cell viability) are the most utilised readout in 3D treatment-response assays. The ATP assay measures the relative cellular ATP content. This usually correlates with the number of viable cells, although it is in principle possible that a reduction in ATP may result from a reduction in ATP per cell or a reduction in the total number of viable cells. ATP assays in the 3D format are largely routine through the use of the optimised CellTiter-Glo 3D luciferase-based readout. The ATP assay is an easy, rapid, and high-throughput technique, although it may lack the detailed mechanistic insights and long-term survival information provided by re-plating organoid formation assays. My findings indicate that the sensitivity of ATP readouts to detect radiation-response differences is dependent on the specific cell line and experimental conditions. My study in 2D cell lines demonstrated that ATP assays displayed similar responses as CFAs in some cases but not in others. In fact, I observed that while ATP viability assays were unable to measure a difference between control and treatment in radiosensitive lines (COR-L105, as determined by CFAs by the Anderson Ryan laboratory), ATP assays were able to report differences, aligned with CFA patterns, in quite radioresistant lines (NCI-H1299, as determined by CFAs by the Anderson Ryan laboratory) (Figures 3.9. and 3.11., Chapter 3) (Weber et al. 2016). In my experiments with NSCLC organoids, the effect of radiation on more radioresistant lines (as seen by re-platting organoid formation assays) or the effects of adding a PARPi or an ATRi to radiation treatment were not detected using ATP assays but were very apparent in re-plating assays (compare Figure 5.3., A) to Figure 5.6., B) and compare Figure 5.5. to Figure 5.8., Chapter 5). However, a study made by Lucky et al. where they assessed the viability of nasopharyngeal cancer organoids after irradiation in organoids grown either under normoxic or hypoxic conditions, demonstrated that organoids cultivated in hypoxic conditions exhibited greater levels of radioresistance compared to their counterparts grown under normoxic conditions and these differences were detectable using an ATP readout (CellTiter-Glo 3D) (Lucky et al. 2021). Overall, it appears that the sensitivity of ATP assays for detecting radiation response depends on factors such as cell/organoid line and experimental conditions. A possible strategy for future high-throughput radiation experiments in organoids could involve initially

evaluating the relationship between ATP assays and CFAs using a limited range of radiation and drug doses/concentrations per organoid line. If a positive correlation was then observed, subsequent high throughput testing in those lines could be conducted primarily using ATP assays.

Overall, in order to accurately assess the response of organoids to radiation, a combination of techniques may be necessary. However, my study has shown that direct evaluation of post-IR reproductive cell death in 3D re-plating assays is crucial and should not be replaced by indirect, less sensitive methods such as routine ATP assays unless key results are frequently checked using both formats in parallel.

6.2. Inter-tumour and inter-organoid line heterogeneity

Currently, patients are stratified for targeted therapies depending on the genetic characteristics of their tumours. Shi et al. demonstrated that their NSCLC organoids recapitulated the somatic mutations and gene expression profiles that characterised the tumour from which they were derived as measured by WES, RNAseq and histology (H&E) comparisons (Shi et al. 2020).

Inter-line differences in radiation responses of organoid lines generated by Shi et al., (LPTO85, PDXO137, LPTO85, PDXO149 and PDXO377) were observed in radiation dose-response assays. Analysis in the organoid re-platting assay format showed that two of the LUAD lines were more radioresistant than the two LUSC lines (Figure 5.6., Chapter 5). Clinically, LUSC has been shown to be more radiosensitive than LUAD (Nomori et al. 2021). Although the number of samples in the study here were very low, the rank-order of sensitivity based on histopathology is what might have been expected. The only exception to this is the LUAD line LPTO85, which was the most radiosensitive line amongst all analysed. The reasons for this difference remain unclear without extensive further study. However, it is worthwhile noting that this was the most rapidly proliferating line (Figure 4.8., B), Chapter 4) and the only line with mostly lumen morphology organoids (with a single layer of cells surrounding the lumen) instead of solid or budding (Figure 4.7., Chapter 4). Low levels of hypoxia and rapid proliferation are both expected to cause radiosensitivity.

When assessing the radiosensitivity in terms of the TP53 mutational status, I found that the TP53 mutant LUSC line was more radioresistant than the TP53 WT line; whilst the

contrary was observed in the LUAD lines, where the TP53 mutant lines seem to be more radioresistant than the WT one (Figure 5.6., B), Chapter 5). However, the prediction of the overall radiosensitivity of a line based on the TP53 status is very complicated, as p53 is differentially and simultaneously involved in many radiation-response pathways (DNA damage response and repair, cell cycle control, apoptosis etc.) and cancer-metabolism related responses (Fei and El-Deiry 2003; Deben et al. 2016; Mantovani et al. 2019; Kong et al. 2021). Higher number of samples would be needed to investigate this.

Despite the number of lines involved in the analysis being suboptimal, the functional response of the organoids to radiation treatment as assessed by their pot-IR G_2 arrest (or lack of it) closely matched what was expected based on the lack or presence of p53 (Figure 5.9., Chapter 5). Moreover, detailed consideration of cell cycle parameters when radiation was combined with DNA damage inhibitors (ATRi/PARPi) showed that organoid responses to inhibitor-radiation combinations made mechanistic sense in terms of the cells predicted response based on the genetics of the line and the drug treatment. For example, line LPTO126 that was TP53 WT and was arrested in G_2 after IR, progressed into G_2 in the presence of the ATRi as might have been predicted (see Figure 5.9. and accompanying text in Chapter 5).

In addition, when analysing pseudobulk RNAseq data from the TP53 wild-type LUSC organoid line (PDXO377) after 0/4 Gy of irradiation, I found an upregulation of pathways involved in ‘Regulation of cell differentiation’ and ‘Cell-cell signaling’ in the irradiated sample. Conversely, there was a downregulation of pathways related to ‘Regulation of cell population proliferation,’ ‘Cell division,’ ‘Mitotic cell cycle progression,’ as well as processes associated with regulation of cell death and apoptosis.

Taken together, all of these results demonstrate for the first time that NSCLC organoids could serve as valuable and promising tool for studying inter-line radiation responses *in vitro*.

6.3. Intra-tumour and intra-organoid heterogeneity: inter-cellular heterogeneity

In addition to inter-line (inter-patient) heterogeneity, intra-line (inter-cellular) heterogeneity is likely to play a crucial role in determining the individual cellular responses of NSCLC cells to radiation. For example, it has widely been acknowledged that cancer stem cells may be selectively resistant to various therapies, including

radiation, based on differences in their proliferation rate, intrinsic radiation resistance, drug export capabilities and molecular pathways (Singh et al. 2015; Vlashi and Pajonk 2015; Perez-Gonzalez et al. 2023). In addition to 'cancer stem cells' (which are sometimes poorly defined), other differentiative or metabolic features within NSCLC *in vivo* will lead to differential responses to radiation (e.g. hypoxic cells tend to be more radioresistant (Bouleftour et al. 2021; Menegakis et al. 2021)) (Stadler et al. 2015; Hubert et al. 2016; Nunes et al. 2019). One of the main challenges faced in the clinic for treatment of NSCLC is that the intra-tumour heterogeneity makes it challenging to develop effective, targeted therapies. Together with the fact that NSCLC has a high recurrence rate (from cells that have been able to re-populate the tumour due to their treatment-resistance nature); an important goal of a useful *in vitro* system is the ability to act as a model for the inter-cellular heterogeneity of patient's tumours *in vivo*. When used for radiation-response research it should be focussed on investigating the nature of NSCLC heterogeneity and specifically the inter-cellular heterogeneity of the treatment-response, and finding radiation-resistance and heterogeneity representative markers to be able to predict NSCLC recurrence, to find new therapeutic targets.

Interestingly, some *in vivo* tumour characteristics have already been investigated in 3D in simple large spheroid models. Note that these models are derived from cell lines and typically have a diameter of 400-500 μm which are significantly larger than typical organoids as described here. Spheroids are cultured without an ECM and have been shown to generate nutrient, oxygen, pH and growth factor gradients which lead to nested necrotic, hypoxic, quiescent and proliferative zones from the core to the surface of the spheroid that mimics aspects of tumours *in vivo* (Swietach et al. 2012; Stadler et al. 2015; Lazzari et al. 2017; Nunes et al. 2019). The differential penetration of nutrients in spheroid models likely extends to drug penetration. However, Karolak et al. suggested that drug penetration constraints are not solely determined by organoid size but also by other tumour characteristics, such as morphology and cellular packing density, features that organoids closely recapitulate in culture (Karolak et al. 2019).

To determine whether simpler cell line systems could mimic some of the morphological and functional heterogeneity observed in organoid cultures, a number of cell lines were cultures as 3D 'CellAggs' by culturing 2D cell lines in 3D in Matrigel. Dark cores, indicative of hypoxic areas, were observed in the CellAggs after 10 days in culture (d = 100-200 μm) suggesting that culture of cell lines in an ECM may generate the growth-

altering gradients as previously reported in spheroids. Most interestingly, when cultured as CellAggs in Matrigel, NSCLC cell lines showed some phenotypic differences reminiscent of organoids (e.g mixtures of solid, budding, lumen-containing structures) (Figure 3.2. and 3.3., Chapter 3). These morphologies were also seen in NSCLC organoid-cultures (Figure 4.2. and 4.7., Chapter 4). Interestingly, the CellAggs morphologies were not dependent on specific growth factors in the medium, as no difference was detected in phenotype distribution (morphotype and size) when the CellAggs were cultured in growth factor-rich medium or defined media (Table 3.2, Chapter 3). However, the biggest problem in using cell lines as CellAggs models was their propensity to migrate out of the Matrigel matrix and to attach to the bottom of the culture plate (Figure 3.12., C), Chapter 3). Nonetheless, inter-conversion from one morphotype to another was observed in one of the CellAggs lines, from solid to lumen morphology (Figure 3.7, Chapter 3 and Video 3.1., Appendix - https://youtu.be/AX72NXL1PqU). This phenomenon points in the direction of some underlying heterogeneity in CellAggss, compared to classical spheroids (Beck et al. 2022). Research into the impact of the ECM environment on cellular motility has revealed emerging migration mechanisms (e.g., single cell migration, streaming and collective invasion) previously neglected that more accurately reflect *in vivo* tumour biology; suggesting that CellAggs should be further investigated in relation to tumour motility (Friedl et al. 2012).

Overall, my research suggests that CellAggs could be useful as an intermediary model in between spheroids and organoids, possibly offering insights on drug penetration dynamics and cell motility and polarity.

To investigate the intra-organoid heterogeneity in more detail, two of the Shi et al. LUSC organoid lines (PDXO149 and PDXO377) were studied by scRNAseq. Both proliferating and non-proliferating cell subgroups were found, which could translate into more radiosensitive/radioresistant cell groups (Santos-de-Frutos and Djouder 2021). Most interestingly, by mapping the cells into a previously published scRNAseq lung reference dataset (Travaglini et al. 2020), I confirmed that the composition of the LUSC organoids was mainly basal (different stages of basal: proliferating, differentiating, etc.) and goblet cells, although some ciliated, club, mucous and ionocyte cells were also detected (Figure 5.12., Chapter 5). These results are representative of *in vivo* cell heterogeneity from airway epithelium origin which is the proposed origin for LUSCs. Follow up studies may

be able to take these studies further allowing a close mapping of cell types present in organoids to those present in tumours and to those present in the normal lung under different physiological conditions.

Recently, both colorectal cancer (CRC) and pancreatic ductal adenocarcinoma (PDAC) organoids were characterised by single cell RNAseq and were shown to display intra-organoid heterogeneity. Seven CRC organoids were sequenced by scRNAseq and both differentiated cell clusters (goblet, intermediate and enterocytes) and stem-like cell clusters (including $Lgr5^{+}$ cells) were found, representative of *in vivo* epithelial tumour tissue (Wang et al. 2022b). PDAC organoids were derived from 18 primary tumours and sequenced by scRNAseq. Here different cellular states that were shared across different tumours were identified. The different clusters displayed cycling, non-cycling and differentiated cells (in line with our preliminary results in NSCLC organoids), they expressed migration, secretion, adhesion, or digestion activity which were functional characteristics that reflected their pancreatic lineage and demonstrated the intra-organoid heterogeneity (Krieger et al. 2021). Interestingly, as both cycling and differentiated cell clusters were detected in PDAC organoids, Krieger et al. went on to define a 'differentiation trajectory' of PDAC organoid cells applying the new concept of RNA velocity. RNA velocity is a computational technique applied to scRNAseq data to infer the direction and speed of gene expression change within individual cells, thereby providing insights into their trajectories of origin. This is accomplished by examining the ratio of unspliced to spliced RNA reads for specific genes, which serves as an indicator of transcriptional activity and enables predictions about the future state of a cell (La Manno et al. 2018). Integrating this with pseudotime analysis, that orders individual cells along a developmental trajectory based on their gene expression; Krieger et al. were able to create a 'pseudotime axis' that represented progression through different cellular states within an organoid and included the speed and direction of these transitions (Van den Berge et al. 2020). Across all patients, trajectory startpoints correlated with clusters of cycling cells, leading to a convergence onto a specific cycling cell cluster as the origin of a cell population. Conversely, trajectory endpoints were mainly situated in a distant non-cycling cell cluster. A distinct bifurcation point was identified during the G_1 phase where cells either re-entered the cell cycle or underwent differentiation towards a secretory state. The pseudotime analysis approach identified potential drivers of cellular fate, such as GGCT (gamma-glutamylcyclotransferase) and RANBP1 (Ran-binding protein 1), which showed increased expression soon after the bifurcation point in cells re-entering the cell

cycle. On the other hand, CEACAM6, a cell adhesion gene, and S100A6, encoding a calcium-binding protein, were found to be upregulated in differentiating cells (Krieger et al. 2021).

By analogy with the Krieger study, it is possible to imagine how the effects of radiation treatment might be followed in 'pseudotime' in a number of NSCLC organoids to determine both how different cellular subpopulations respond to radiation (differences would be expected), but also analyse how radiation may dynamically alter the developmental trajectories of organoid cells in culture. To take this one step further, the responses of the organoids might be compared to that of cells isolated directly from patients, particularly if this is possible from patient tumour biopsies during treatment. However, it is anticipated that this would present many logistical challenges, both to access the relevant patient samples and to acquire sufficiently large sample sizes. Where side by side organoid / patient tumour response comparisons have been carried out, they have shown that organoids have significant predictive power. For example, Vlachogiannis et al. showed using CRC organoids that organoid responses accurately predicted the response to targeted agents or chemotherapy in patients, with a sensitivity of 100 %, specificity of 93 %, positive predictive value of 88 % and negative predictive value of 100 %; demonstrating the potential usefulness of organoids in drug treatment (Vlachogiannis et al. 2018).

Recently, Yao et al. demonstrated that patient-derived organoids could be used to predict patient chemoradiation responses in locally advanced rectal cancer (LARC) (Yao et al. 2020). Organoids were derived from rectal cancer biopsies from treatment-naïve LARC patients in a phase III clinical trial. Yao et al. irradiated the LARC organoids with 8 Gy, treated them with 5-FU (10 μM; antimetabolite) or irinotecan (10 μM; topoisomerase I inhibitor) and used the organoid size, together with Cell Titer-Glo 3D ATP assays, to measure organoid survival. The vital stain neutral red staining was also used to identify living cells within cultures (Ates et al. 2017). A great diversity in radiosensitivity amongst the different lines was observed. In the clinical trial, pathological tumour regression grade (TRG) after total mesorectal excision was used as a readout to assess the response of 80 patients with LARC after neoadjuvant chemoradiation (NACR). Patients received a combination of radiation and oral administration of 5-FU, with or without irinotecan. Six patients experienced a clinical complete response (cCR) and declined surgical intervention, after which they remained recurrence-free for over one year. The study

demonstrated that patients who exhibited positive clinical responses also had organoids that displayed sensitivity to at least one of the three treatment components. Moreover, combinatorial therapies in the patients yielded results that were consistent with responses by 22 out of 23 LARC organoid lines. Out of the total sample size, 34 patients experienced favourable clinical responses while their organoids were responsive to either irradiation, 5-Fu or irinotecan; conversely, another group of 34 patients had a poor response and resistance towards irradiation and drugs in their corresponding organoids. Henceforth, data on sensitivity derived from testing the LARC organoids matched well with the actual clinical outcomes for the majority of cases (68 out of 80), yielding an overall match ratio of approximately 85%. The aggregated organoid data thus strongly correlated with patient's clinical outcomes accuracy being estimated at 84.43% alongside a sensitivity rate reaching 78%, and specificity of 91.97% (Yao et al. 2020). The authors suggested that organoid responses might, in future, be used by clinicians to predict the optimal combination of standard of care (SoC) therapies that are offered to patients. Clearly this approach would require the development of methods that would allow the rapid and efficient establishment of organoid lines such that *in vitro* responses can be assessed in a timely manner for patient benefit. Whether similar approaches might be useful for the treatment and staging of patients with NSCLC is currently unknown.

An alternative or complementary approach to the use of live organoids as predictive models, might be the identification of biomarkers that better predict patient responses. As argued earlier, the identification of intra-organoid cellular heterogeneity using scRNAseq should identify markers whose expression positively or negatively correlates with radiation responses. These markers might be further developed as response-predictive biomarkers by correlating their expression with patient responses. This might be carried out retrospectively in stored biopsies from prior clinical studies.

The initial scRNAseq study described in Chapter 5 (Figures 5.10/11) suggests an optimal approach to identify radiation-response biomarkers would include the following steps:

- Experimental layout of NSCLC organoids radiation scRNAseq study

Several NSCLC organoids lines with different genetical and histopathological backgrounds should be seeded from single cells and treated with 4 Gy of irradiation or sham irradiated after 12 days in culture. Four to six hours post-irradiation organoids should be dissociated into single cells with TrypLE and 10,000 cells per condition should be loaded through the standard pipeline for 10X Genomics 3’ scRNAseq pipeline for a

scrRNAseq experiment. This would allow big enough organoids to represent the cell heterogeneity present in tumour patients, as well as hypoxia and nutrient deprivation gradients.

- Bioinformatics analysis of scRNAseq

After sequencing, data should be mapped to the human genome, cell numbers should be adjusted depending on barcode rank plots and meaningless data discarded (such as cells with < 20 % of mitochondrial reads, doublets (scTK package) and cells with > 0.5 % RNA contamination (decontX)) and normalised to obtain comparable RNA per gene, per cell counts using standard packages as Sctransform in the software Seurat (Satija et al. 2015).

- Analysis of scRNAseq study: finding biomarkers of inter-cellular heterogeneous radiation-response

For the subsequent data-analysis, a key integrative analysis that compares and combines each treatment and control sample should be used with the Seurat pipeline (Stuart et al. 2019). First, a canonical correlation analysis (CCA) should be run in R with the software Seurat. Instead of components (as with the classical 'principal components analysis'), CCA captures common sources of variation (anchors) between two datasets and aligns the two samples. Then, a graph-based clustering should be performed identifying pairs of mutual nearest neighbours (Lovain algorithm – Seurat software), which would further be visualised with the non-linear dimension reduction uniform manifold approximation and projection (UMAP). Conserved and differentially expressed genes between clusters can then be analysed (using Wilcoxon rank sum test: log2 scale of 0.25 and p-value cut-off of 0.05). These could then be mapped into the recently published 'integrated cell atlas of the lung in health and disease', discussed in the introduction, to elucidate the identity of each cell cluster (Sikkema et al. 2023). Finally, selected genes can be visualised in UMAPs to find either 'cell type' or 'radiation-response' markers. These will provide several outputs of interest for patients' intra-tumour differential responses to radiation:

(1) The identification of genes exhibiting similar expression patterns across samples (control vs. treatment) may serve as indicators of conserved cell types, potentially representing intra-organoids and intra-tumour patient cell heterogeneity.

(2) The identification of genes that undergo consistent changes in all clusters can be regarded as markers independent of cell type for assessing radiation-response, potentially representing global, cell type independent, organoid/tumour responses to irradiation.

(3) Most interestingly, the identification of genes that display altered expression patterns in specific clusters but not all could potentially function as organoid radiation-response markers contingent on cell type, potentially representing patients' intra-tumour inter-cellular heterogeneity of the response to radiation. This could be further linked to radiosensitive/radioresistant cell subtypes.

- Further validation of identified biomarkers in the organoid platform

Immunofluorescence staining for spatial visualisation of clusters within an organoid would provide further information on the cell-type distribution pattern within each organoid and co-staining with cluster specific radiation-response biomarker (after IR) would further validate the signature seen in the scRNAseq with a separate technique. Moreover, functional assays, like FACS for specific surface marker and the organoid re-plating assay, would functionally confirm each markers' utility to detect radiation-sensitivity inter-cellular heterogeneity-related markers.

- Patient correlation studies

A panel of putative radiation-response biomarkers would be developed to allow their use with archived patient material. Individual mRNAs or their encoded proteins from the candidate biomarker could be studied in paraffin-embedded histological sections, often available in cancer biobanks. After validation of the biomarker specificity, they would be utilised to study clinical samples in collaboration with clinicians who have developed or are studying NSCLC radiation responses.

Altogether, this approach would identify markers of NSCLC organoid phenotypic heterogeneity and radiation response that could ultimately translate into new therapeutic approaches for NSCLC recurrence and would increase the scientific knowledge on radiation response heterogeneity patterns in NSCLC.

6.4. Further development of *in vitro* NSCLC models for radiation response research

As described above, NSCLC organoids can be used to model radiation and drug responses *in vitro*. There are two distinct potential application areas for NSCLC organoids. Firstly, organoids can be used to predict the efficacy of novel therapies including treatments involving irradiation. Secondly, organoids might be used to predict the efficacy of existing therapeutic combinations (including radiation) as part of personalised medicine approaches. Each of these distinct applications will require different approaches to the development of NSCLC organoids. For the development of novel therapeutics, it will be important that the full range of genetic and phenotypic models is well-represented by a

large bank of organoid models, such that efficacy can be correlated with genotype and phenotype. By contrast, the use of organoids in personalised medicine would require the efficient and rapid establishment of organoids such that their availability would be assured and timely in relation to their use in a clinical context. However, both approaches will require significant improvements in the rate and efficiency of NSCLC organoid establishment.

6.4.1. Recommendations for the design of NSCLC organoid culture medium

Although my studies of organoid establishment conditions were limited by tumour availability, a NSCLC organoid line was established (Figures 4.4. and 4.5., Chapter 4). The growth factor cocktails currently used for tumour organoid cultures are based on those used for colorectal cancer (CRC) organoids (Sato et al. 2009; Sato et al. 2011). The base medium usually consists of Advanced DMEM/F-12, buffer solutions, glutamine supplements and antibiotics (some also added antimycotics) and is complemented with several small molecules and ligands. Due to the reported overgrowth of normal tissue in lung tumour organoid cultures, two main medium-design approaches had been used to address the issue:

(1) Using Nutlin-3a for selective growth of TP53 mutant tumour tissue. TP53 is mutated in 91 % of LUSCs and 46 % of LUADs (Swanton and Govindan 2016). Sachs et al. first utilised Nutlin-3a in 2019 to successfully select for NSCLC organoid growth in a rich growth-factor medium (Table 6.1.). They also successfully generated lung tumour organoids from metastatic NSCLC needle biopsies, eliminating the requirement for Nutlin-3a due to the absence of normal lung tissue in this specific sample origin. This approach achieved a success rate of 28% with a total of 18 cases. Since then, other groups have used the same medium composition (with slightly different molecule concentrations – see Table 6.1., without Nutlin-3a) to generate NSCLC organoids with reported varying success rates of 80 % (n=12) (Li et al. 2020) and 17 % (n=30) (Dijkstra et al. 2020).

(2) Kim et al. used a different approach to overcome normal tissue overgrowth in NSCLC organoid cultures. They developed a protocol to assess the quality of the tissue itself before culturing the organoids. After dissociating the tissues using collagenase, they prepared slides with cell suspension H&E stained to evaluate the proportion of viable epithelial-like cells. They categorised the samples into primarily epithelial cell-predominant, fibroblast-predominant or acellular samples. Then, only samples that were

predominantly composed of epithelial cells were used as starting material for generating NSCLC organoids. After this they reported that the minimum basal medium they used (that did not contain Wnts, Noggin, SB202190 or Nicotinamide – Table 6.1. -, which have been reported to be essential for lung normal organoid growth and will be discussed later in this section) was enough to overcome the normal tissue overgrowth (success rate = 70 %, n=39) (Kim et al. 2019). In 2020 Chen et al. used the same medium to grow a smaller cohort of patient-derived NSCLC organoids (success rate: 86%, n=6 – Table 6.1.) (Chen et al. 2020). I also attempted to grow PDX-derived NSCLC organoids in Kim et al. medium but only 1 out of 3 samples grew long-term in culture and it was shown to be heavily contaminated with what were likely to be mouse-derived fibroblasts.

Finally, an 'in-between' culture medium containing elements of both of Sachs et al. and Kim et al. media (Table 6.1.) was described. This medium (Shi et al. 2020) achieved a 15 % (n=10) success rate in long-term NSCLC organoid establishment and 71 % success rate (n=47) in short-term cultures. The term 'long-term cultures' refers to organoid lines that have been successfully maintained for more than 10 passaged and could be preserved through freezing and recovery. The loss of culture lines during the transition from short-term cultures to long-term lines was also noted within the limited sample numbers that were established during the work for this thesis. Similar short-term versus long-term differences in culture potential were initially observed during the establishment of colonic organoids within this laboratory and the issue was only resolved when the levels of active Wnt ligand were increased above a threshold during the time in culture (T. Dale; personal communication). These observations suggest that changes to the media composition and concentrations need to be systematically explored to optimise long-term culture.

There are some essential signalling pathways that have been suggested for consideration for the establishment of NSCLC organoid as described by Ma et al. in Figure 6.1 (Ma et al. 2022). The general approach for the future design of NSCLC organoid mediums could be to utilise tumour's inherent mutations to add/remove key molecules involving these pathways. Here I propose possible future opportunities depending on the signalling pathway:

(1) Wnt pathway maintains stemness. Wnt ligands initiate the pathway and R-spondins amplify it by binding to Lgr5 homologues (Figure 6.1., A)). It has been demonstrated that Wnt3 increases the efficiency of lung organoid formation (Rabata et al. 2020). R-spondin-

1 is used to promote stemness in NSCLC organoids. In addition, CHIR99021 directly inhibits the stabilisation of β-catenin by inhibition of GSK-3 and has also been used in NSCLC organoids to maintain a 'Wnt active' environment without the need of using the less stable ligands. While the frequency of mutations in pivotal genes associated with the Wnt pathway, such as β-catenin or APC is infrequent in NSCLC; aberrant signal transduction within the Wnt pathway remains somehow related to tumour progression (Xue et al. 2023). Removing R-spondin-1 or CHIR99021 form the culture medium could help select for these tumours that already have a constant 'Wnt on' phenotype. However, the simultaneous culture of new organoids in both pro-Wnt medium and mediums with no Wnt might be needed to achieve maximum establishment success rates.

(2) TGF-β/BMP pathway promotes differentiation of stem cells. TGF/BMP ligands bind to the two receptors: type I for BMP ligands (which can be inhibited by Noggin (McMahon et al. 1998)) and type II for ALKALs (which can be inhibited by A83-01 (Tojo et al. 2005)) (Figure 6.1., B)). Upon activation, the receptor complex phosphorylates the receptor-regulated Smad proteins (R-Smads), these associate with the common partner Smad1 and accumulates within the nucleus where directly binds to the DNA regulating target gene expression. Inhibiting this pathway promotes stem cell maintenance. It should be further investigated if the use of both Noggin and A83-01 is strictly necessary for NSCLC organoids' growth or if withdrawing one of these two could give tumours an advantage in growth compared with normal tissues.

There seem to be a fine line between utilising the Wnt and TGF-β/BMP pathways to select for tumour organoids, and successfully growing organoids in the first place. Kim et al. (Kim et al. 2019) showed that the addition of Wnt3a, Noggin and A83-01 to their restrictive growth medium enabled the growth of organoids in normal bronchial sample tissues. Therefore, systematic culture of different combinations of factors related to these pathways from the same, well-characterised, tumour tissue origin and in a variety of NSCLC tumour tissues is required to elucidate the precise combination needed for NSCLC organoid selective growth.

Table 6.1. Differences in-between several NSCLC organoid establishments.

Publication	Success rate	Selecting agent?	Concentration of small molecules / ligands													
			NAC	SAG	R-spondin-1	CHIR99021	A83-01	Noggin	SB202190	Y-27632	Nicotinamide	EGF	FGF7	FGF10	bFGF	FGF4
Sachs et al. 2019	n/a with Nutlin-3a and 28 % (18) from needle biopsies	Nutlin-3a (5 μM)	1.25 mM	-	500 ng/mL	-	500 nM	100 ng/mL	50 μM	500 μM	5 mM	-	25 ng/mL	100 ng/mL	-	-
Li et al. 2020	80 % (12)	-	1.25 mM	-	500 ng/mL	-	500 nM	100 ng/mL	10 mM	10 mM	10 mM	-	25 ng/mL	20 ng/mL	-	-
Dijkstra et al. 2019	17 % (30)	-	1.25 mM	-	10% conditioned medium	-	500 nM	10% conditioned medium	1 μM	5 μM	10 mM	-	25 ng/mL	100 ng/mL	-	-
Shi et al. 2020	15 % (10) + 71 % (47) extra only for short-term	-	1.25 mM	100 nM	-	250 nM	500 nM	100 ng/mL	-	10 μM	-	50 ng/mL	-	100 ng/mL	-	100 ng/mL
Kim et al. 2019	70 % (39)	Pre-assessment of tissue purity	-	-	-	-	-	-	-	10 μM	-	50 ng/mL	-	-	20 ng/mL	-
Chen et al. 2020	86 % (6)	-	-	-	-	-	-	-	-	10 μM	-	50 ng/mL	-	-	20 ng/mL	-

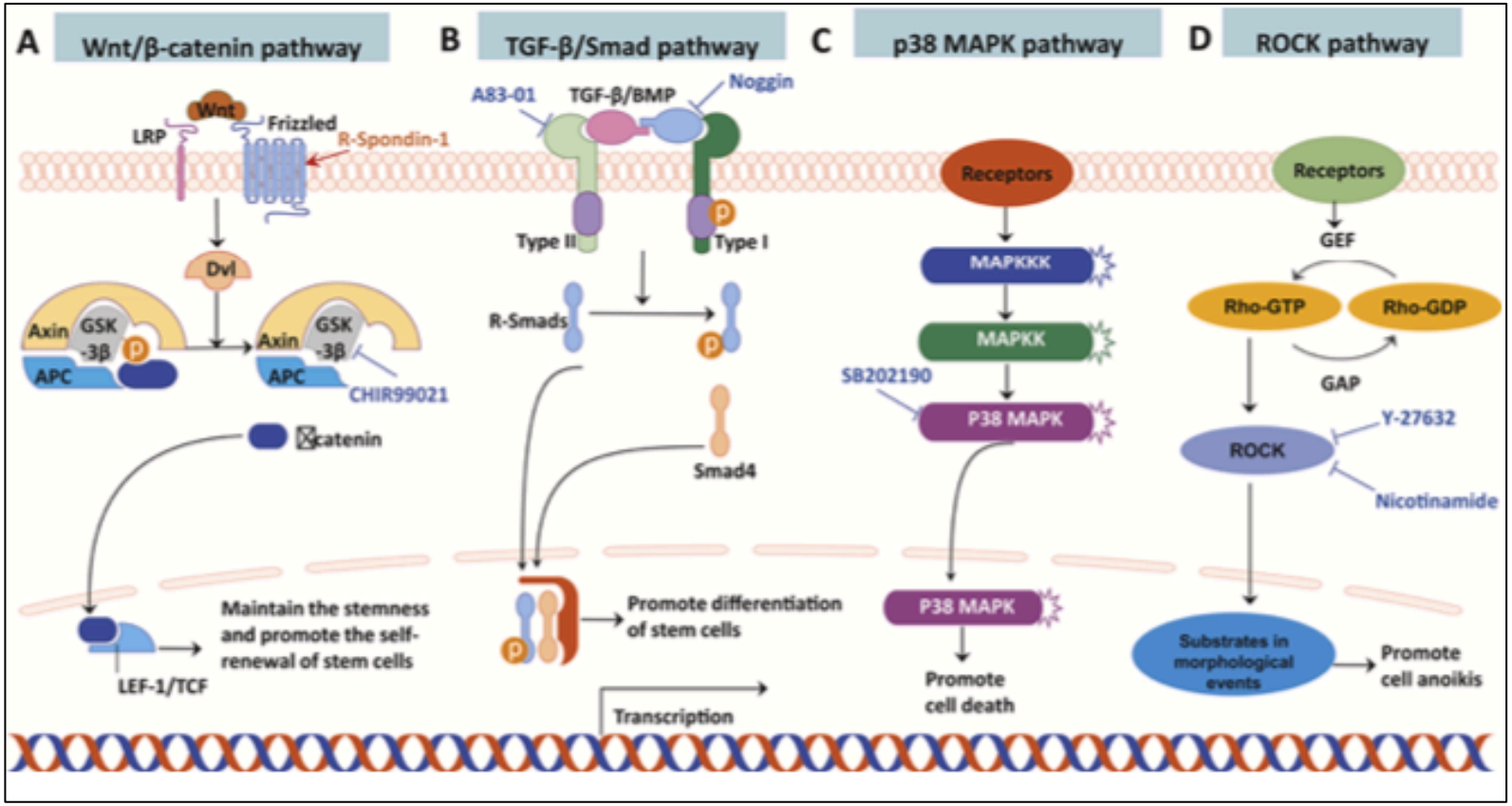

Figure 6.1. (Ma et al. 2022). Signalling pathways related to NSCLC organoids medium components. Essential signalling pathways needed to be considered during the establishment of lung cancer organoids. Key molecules acting on these pathways are labelled with orange (agonists) or blue (antagonists). **2A.** Activation of Wnt/β-catenin pathway maintains stemness of stem cells. Wnt3A initiates and RSPO1 then enhances the Wnt/β-catenin pathway, by binding to Lgr5 homologues. CHIR99021 also activates the pathway, by inhibiting GSK-3, and subsequently decreasing phosphorylation and keeping stabilisation of β-catenin. **2B.** Activation of TGF-β/Smad pathway promotes stem cell differentiation. Noggin inhibits the type I TGF-β receptor, also known as bone morphogenetic proteins (BMPs), while A83-01 is an inhibitor of Type II TGF-β receptor, also known as activin receptor-like kinase 5 (ALK5). **2C.** The p38 mitogen-activated protein kinase (MAPK) pathway promotes cell death, and SB202190 protects cells from apoptosis by inhibiting this pathway. **2D.** Activated by guanine nucleotide exchange factors (GEFs), GTP-bound Rho subsequently activates rho-associated protein kinases (ROCKs) to phosphorylate several substrates leading to morphological events, including cell contraction, dynamic membrane blebbing, nuclear disintegration, and the fragmentation of apoptotic cells into apoptotic bodies. Nicotinamide and Y-27632 protect cells from apoptosis by inhibiting ROCK.

(3) The p38 MAPK pathway promotes cell death upon stress stimuli. Upon activation, p38 MAPK, a serine/threonine kinase, phosphorylates a wide array of downstream effector molecules, including transcription factors and kinases (Figure 6.1., C)). This phosphorylation event leads to the modulation of gene expression and protein activity. SB99021 evades apoptosis by inhibiting this pathway. However, highly varying concentrations of SB99021 have been used for growth of NSCLC organoids (ranging 1 μM to 10 mM – Table 6.1.) and systematic dose-dependent growth assays might be needed to further address this point. Interestingly, Kim et al. did not use SB99021 in their cultures, including for growth of normal organoids from normal tissue. In addition, TGF-β receptor can activate the MAPK pathway in a Smad-independent pathway. Thus the use of A83-01 might be sufficient to evade cell death without the need of SB99021, due to the crosstalk of pathways (Yu et al. 2002) and should be investigated in NSCLC organoids.

(4) ROCK pathway enables cell anoikis. Upon activation of the GTPase RhoA, it activates ROCK kinases which, in turn, phosphorylate several downstream targets leading to cytoskeletal reorganisation and actin filament dynamics (Figure 6.1, D).). Consequently, the ROCK pathway is implicated in numerous morphological events including cell anoikis, as mentioned. Both Y-26732 and Nicotinamide are used as ROCK inhibitors to prevent this. Interestingly Y-27632 is continuously used in NSCLC organoid culture mediums, but only for the first 3 days after digestion and passaging in CRC organoids (Sato et al. 2011). In fact, Y-27632 has been reported to induce cytoplasmatic collapse in attached growing hESCs by actin filament de-polymerisation and microfilament condensation (Gao et al. 2019). If this is also applied for NSCLC organoids is yet to be investigated. Nicotinamide, however, is also a precursor of NAD and essential in energy metabolism, thus it might be more challenging for cultures to survive without this factor (Mehmel et al. 2020).

In addition, removal of EGF, which has been reported to cause cell sinking (losing their 3D organisation) in breast cancer organoids (Sachs et al. 2018) but is a key component of the Kim et al. medium (Table 6.1.), and sequential addition of 7 day culture of FGF2 followed by FGF10, which has been reported to induce the best lung organoid formation (Rabata et al. 2020), are some other medium components worth exploring in NSCLC organoids.

Shi et al. introduced the addition of smoothened agonist (SAG) to their culture medium. SAG is a cell permeable ligand that modulates the coupling of Smo with its downstream effector, it induces sonic hedgehog (Shh) pathway activation and counteracts inhibition of Smo. SAG has previously been added to hPSC organoids for lung cell differentiation towards distal fate (TTF-1 upregulation) (Dye et al. 2015) and the Shh pathway is important for the evolution of radioresistance of many tumours (Carballo et al. 2018). Canonical activation of the Shh pathway in NSCLC has also been found, and a specific Shh+ cell population was show to overexpress (microarray) CSC genes and Wnt pathway targets (Leprieur et al. 2017; Giroux-Leprieur et al. 2018). The role of SAG in NSCLC organoids needs to be further investigated.

I showed that lines that had been established in a growth-factor rich medium (Sachs et al. medium) did not survive when transferred to a restrictive medium (Kim et al. medium) (Supplemental Figure 4.2., Appendix). However, the challenge of establishing a line that has not already been established (a catch-22 problem) is that alternative conditions can only be explored in relation to the volume of the tumour available. This bottleneck and the possibility that large tumour resection samples contain multiple genetically distinct clones are problems for this overall. Therefore, here I suggest two parallel strategies for identifying better medium composition for particular NSCLC samples:

(1) There is a need to develop a systematic viability assay (that is not endpoint) that allows researchers to monitor cultures early and make decisions about medium component changes to maintain maximum culture growth at early times of NSCLC organoid establishment. Two-photon fluorescence imaging of NADH has previously been used in several cell lines and tumour spheroids to live-quantify the metabolic state of the cultures (Vergen et al. 2012). This technique could be adapted to organoids to measure metabolic state at early stages of the culture. Most excitingly, a new DNA-based ATP nanosensor (quenching system excited by ATP) has just been developed and shown to register real-time ATP monitoring in NSCLC organoids for up to 26 days (both for growth-monitoring and drug-response assays) measured by fluorescence (Zhang et al. 2023). The design of the ATP nanosensor consists of tFNA (tetrahedral framework nucleic acid) and four AS (ATP-targeted aptamer strands). The tFNA serves as the base structure of the ATP nanosensor and is extensively used in various biomedical applications due to its excellent biocompatibility, cell permeability and low cytotoxicity (Chen et al. 2021). The AS serve as the sensing components in the quenched state within the ATP nanosensor structure.

When cultivated with living cells, TDF-AS enters the cellular through endocytosis. The fluorescence resonance energy transfer (FRET) between Cy3 fluorophore and BHQ2 quencher results in a low fluorescence signal background before sensing starts. Once intracellular ATP is present, ATP molecules recognise and bind to the Cy3-modified aptamer strand, leading to separation of the BHQ2-modified strand from AS and an increase in fluorescence signal on organoids. To determine ATP concentration, Zhang et al. incubated different concentrations of ATP solutions with these DNA constructs and their fluorescence intensities were measured using specific excitation/emission wavelengths. This demonstrated a mechanism where changes in fluorescence intensity indicated presence and concentration of ATP (Zhang et al. 2023). Using this new technique to rapidly adapt culture conditions upon NSCLC organoid establishment (depending on culture ATP levels) might be a useful next step to ensure NSCLC organoid successful establishments.

(2) Efforts have been made to establish a consensus single medium for NSCLC organoids. A different strategy would be adapting medium cultures to each specific tumour itself, trying to maintain the heterogeneity intrinsic of the tumour without selecting for a specific feature and thus, better recapitulating the *in vivo* conditions of each specific tumour. This approach is particularly interesting for the use of organoids in personalised medicine. However, an important challenge in designing a medium for NSCLC organoids is the limited knowledge researchers have about the tissue's histopathology and genetic background at the time of establishment. To preserve maximum amount of cell viability, the original tissue is usually processed for organoid establishment as soon as possible following surgical removal. Interestingly, Llamazares-Prada et al. developed and validated a simplified, efficient, and versatile workflow that allowed for long-term storage of lung tissue samples (normal and tumour) without compromising cell viability. Cell viability was assessed using flow cytometry by staining with SyTOX, a non-permeable DNA binding dye. No significant difference in cell viability was observed between the fresh and cryopreserved samples. To ensure successful recovery of the diverse material, the sample was initially separated through manual macroscopic dissection into three distinct populations: (1) airway and vessel enriched; (2) airway-free, tumour-free parenchyma; and (3) tumour. Each population was then cryopreserved individually. Llamazares-Prada et al. conducted an RNAseq analysis on cryopreserved normal lung samples and found that the gene expression patterns were retained after cryopreservation. Additionally, they isolated airway basal cells from the cryopreserved

samples and observed their ability to form basal cell spheres capable of differentiating into ciliated and goblet cells, confirming the maintenance of the progenitor estate of basal cells even after cryopreservation (Llamazares-Prada et al. 2021). Therefore, the establishment of NSCLC organoids from cryopreserved tissues seems plausible and an alternative worth exploring. Surgically removed tumour sample could be separated into 2, one used for WGS (and possibly even RNAseq) and the other one cryopreserved. Only once WGS, RNAseq and histopathology (from the clinic information) has been determined, the frozen sample should be used to establish organoids depending on the specific tumour's characteristics.

To fully exploit NSCLC organoid medium selection and translate this to wider NSCLC organoid culture studies, I propose that an initial study (with a significantly large sample numbers) should be conducted to classify different genomic, transcriptional and histological 'types' or 'states' and determine ideal culture conditions for each 'type'. This can be done utilising previous knowledge of ligands, small molecules and signalling pathways for the establishment of NSCLC organoids as recommended above, WES information on the tumour tissue of origin and incorporating the use of DNA-based ATP nanosensors discussed above. Ultimately, the goal would be to create a systematic pipeline in which *X* 'tumour type' would be cultured in *Y* medium; and researchers would have all the necessary information about the tumour before starting organoid-establishment, leading to an informed decision on the medium conditions. This approach would, also, potentially help maintain the heterogeneity of cultures and better recapitulate the *in vivo* microenvironment; potentially increasing, at the same time, the % of NSCLC organoid establishment success rate, with potentially requiring less tissue to produce organoids (allowing growth from smaller tissue samples such as biopsies, making comparisons between patient tumour tissue and organoids at different stages of treatment possible).

In addition to exploring the growth characteristics of cancer organoids as using the approaches described above, it would also be worthwhile exploring and comparing how normal lung organoids respond to the same conditions, since tumour cells may phenotypically be close to subpopulations of genetically normal lung epithelial cells in particular physiological contexts.

6.4.2. Co-culture models for immunotherapies and radiation treatment

In the longer-term, cancer organoids as models might themselves be replaced by better *in vitro* models. Incorporating different cell types, such as stromal cells, immune cells, vasculature-like structures, or pathogens, in co-culture with cancer organoids has been shown to be useful for studying the complex interactions that drive cancer development and response to treatment. Particularly interesting for NSCLC organoids is co-culture with immune cells. Immune checkpoint inhibitors (ICIs) are currently used as first-line and second-line treatments for NSCLC. One such checkpoint is the programmed cell death protein 1 (PD-1) receptor and its ligand, PD-L1. PD-1 is a receptor on the surface of T cells, while PD-L1 is a protein frequently expressed on some cancer cells. When PD-L1 on cancer cells binds to PD-1 on T cells, it can suppress T cell activity, enabling cancer cells to evade immune surveillance. Exploiting this pathway involves using immune checkpoint inhibitors (e.g., pembrolizumab, nivolumab) to block the PD-1/PD-L1 interaction, 'releasing the brakes' on T cells and enhancing their ability to target and destroy cancer cells (Borghaei et al. 2015; Brahmer et al. 2015; Herbst et al. 2016; Rittmeyer et al. 2017).

Dijkstra et al. obtained NSCLC organoids and tumour-reactive T cell populations from the same 6 patients' peripheral blood. Following *in vitro* exposure of PBMC (Peripheral Blood Mononuclear Cells) to these autologous tumour organoids, they found an expansion of tumour-reactive $CD8^+$ (a subtype of T cells) populations in two of the patients after two weeks of co-culture. This method demonstrated the feasibility of inducing patient-specific tumour-reactive T cell responses by co-culturing PBMC and autologous tumour organoids (Dijkstra et al. 2018). Recently, in a study conducted by Takahashi et al., the effectiveness of PD-1 inhibitors Nivolumab and Pembrolizumab in lung cancer patient-derived organoids was examined using xCELLigence, a non-invasive, label-free method for real-time cell impedance monitoring (Cerignoli et al. 2018). The system allowed over time continuous monitoring of the '% of cytolisis' (the percentage of target cells that were killed by effector cells, checkpoint inhibitors, or both when compared to cells alone control). The findings revealed that when used alone, these inhibitors did not show significant impact on the organoids due to the absence of immune cells present in the original tumour tissue. However, in a co-culture system involving PBMC and lung cancer organoids, PD-1 inhibition resulted in notable destruction of tumour cells (Takahashi et al. 2019). This highlights the relevance of utilising co-culturing techniques for evaluating immunotherapy treatments in NSCLC organoids.

Interestingly, several clinical trials have indicated that incorporating radiation with immune checkpoint inhibitors (ICIs) yields better results for patients with metastatic lung cancer compared to the use of ICIs alone (Azghadi and Daly 2021). In fact, the administration of durvalumab (a monoclonal antibody that blocked PD-L1/PD-1 interaction) is now considered a standard treatment for unresectable stage III NSCLC after chemoradiation, based on findings from the PACIFIC trial (Hui et al. 2019). Hence, the co-cultivation of NSCLC organoids and immune cells holds immense potential as a research platform for exploring the synergistic effects of radiation therapy and immune checkpoint inhibitors in treating NSCLC, that are arising in the clinical setting, and to study this should be a priority for the future of NSCLC organoids and radiation investigation.

In the longer-term, it is possible that cells from NSCLC organoids may be incorporated into models such as organ-on-a-chip systems to allow the tumour cell compartment to be studied in the presence of other cell types that are present within primary patient tumours including endothelial cells, tumour fibroblasts and normal lung cells. It would be predicted that these more complex models would have greater predictive power although they would likely require the greater understanding of NSCLC biology when grown in culture to allow their effective use in the assessment of treatments including radiotherapy.

Appendix

Video 3.1. Calu-3 CellAgg culture live-imaging tracking. *(https://youtu.be/AX72NXL1PqU)*

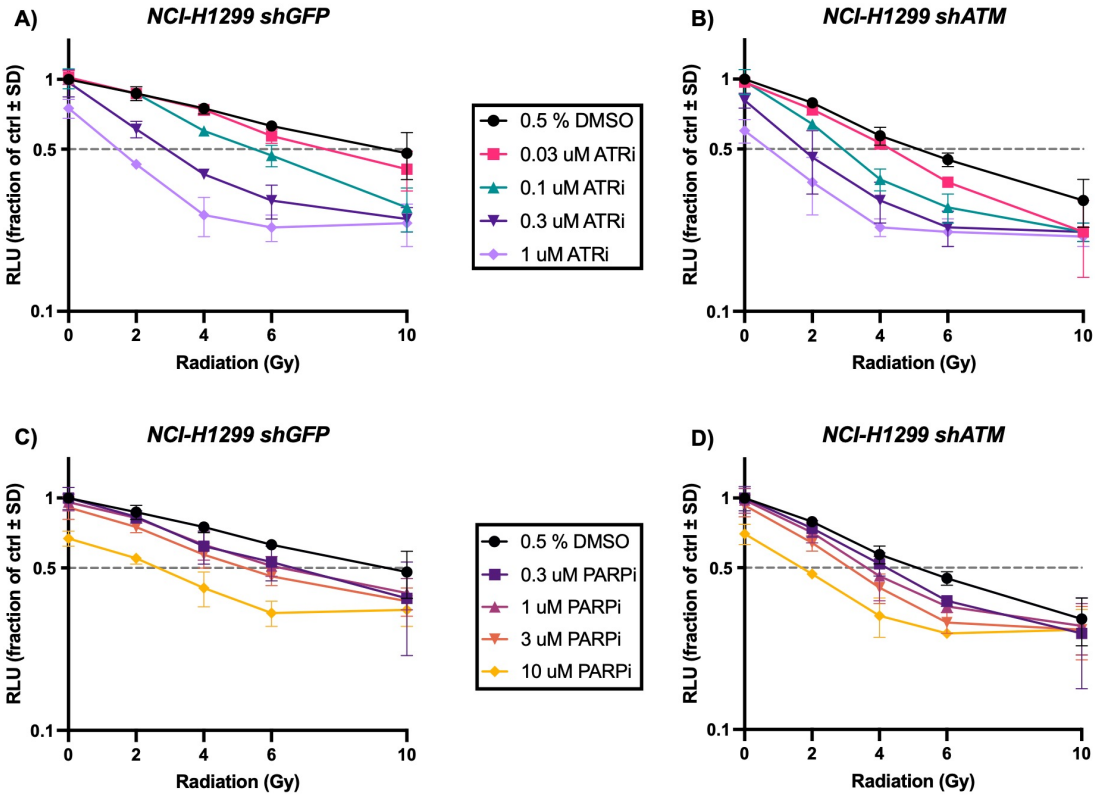

Figure S3.1. NSCLC cell lines' viability after treatment with ionising radiation and/or DNA Damage Repair inhibitor. Relative ATP levels as Relative Luminescence (RLU), measured with endpoint CellTitler-Glo® 3D ATP live-cell assay, of cells (as per graph titles) treated with 2-10Gy of single dose ionising radiation or sham irradiation and 0.5 % DMSO control or a titration of and ATRi (VE-822) or an PARPi (Olaparib) as per the legends in the figure. ATP measured 3 days post-IR. Drug was added 1 h pre-IR and culture medium was replace 24 h post-IR with drug-free medium. shGFP: line constitutively expressing an shRNA against GFP control target (GFP). shATM: line constitutively expressing an shRNA against ATM. n=3. ATRi: ATR inhibitor, VE-822. PARPi: Poly (ADP) Polymerase inhibitor, Olaparib. Graphs made with GrapPad Prism 9.

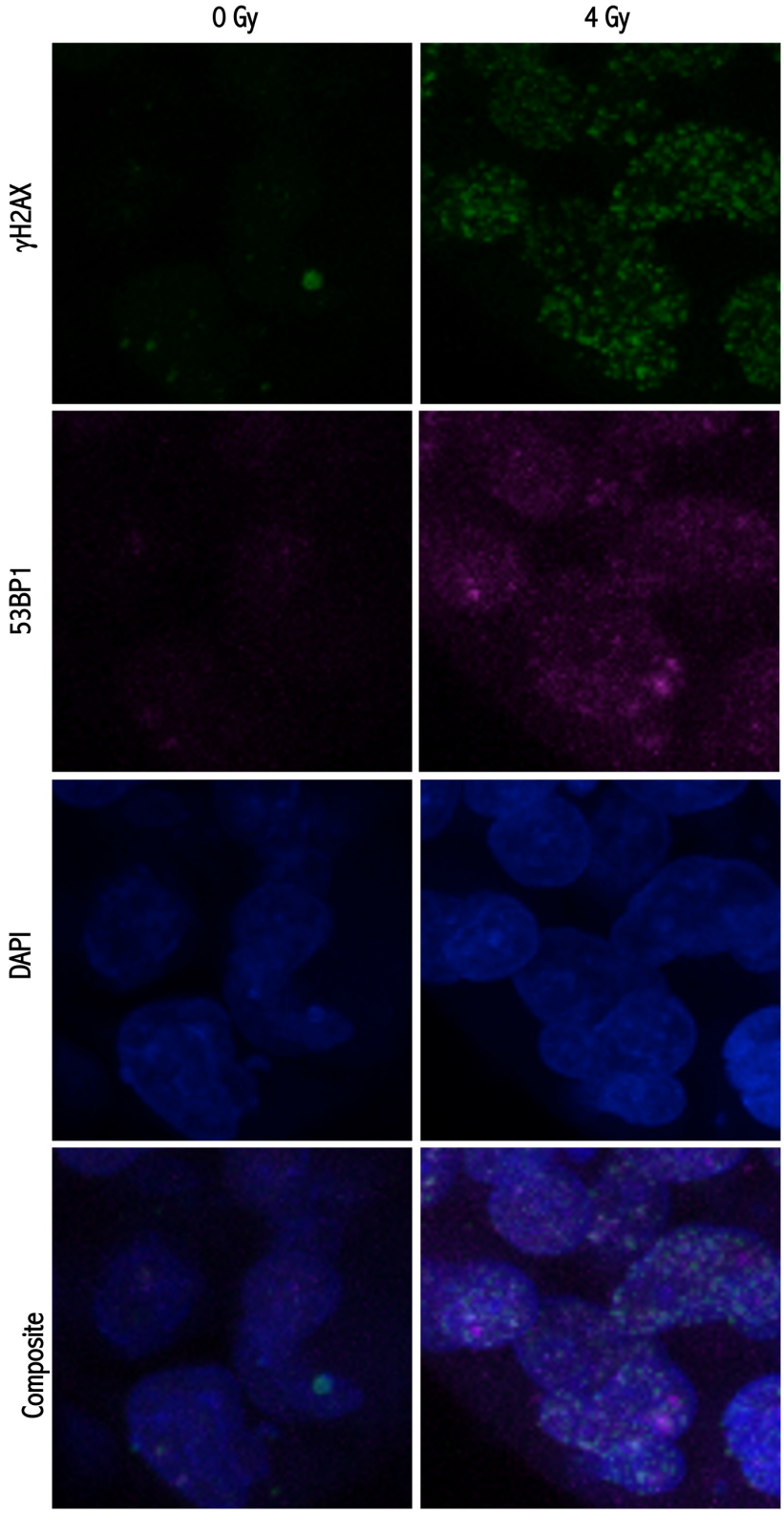

Figure S3.2. DNA damage response of NSCLC spheroids in Matrigel at 1 h after irradiation. Close-up of Maximum projection of z-stacks on fluorescence confocal microscopy of NCI-H1299 *shGFP* NSCLC CellAggs in Matrigel 1h after either 4 Gy of irradiation or non-irradiated controls. Inmunostaining was performed with γH2AX and 53 BP1 antibodies and DAPI for nuclear staining.

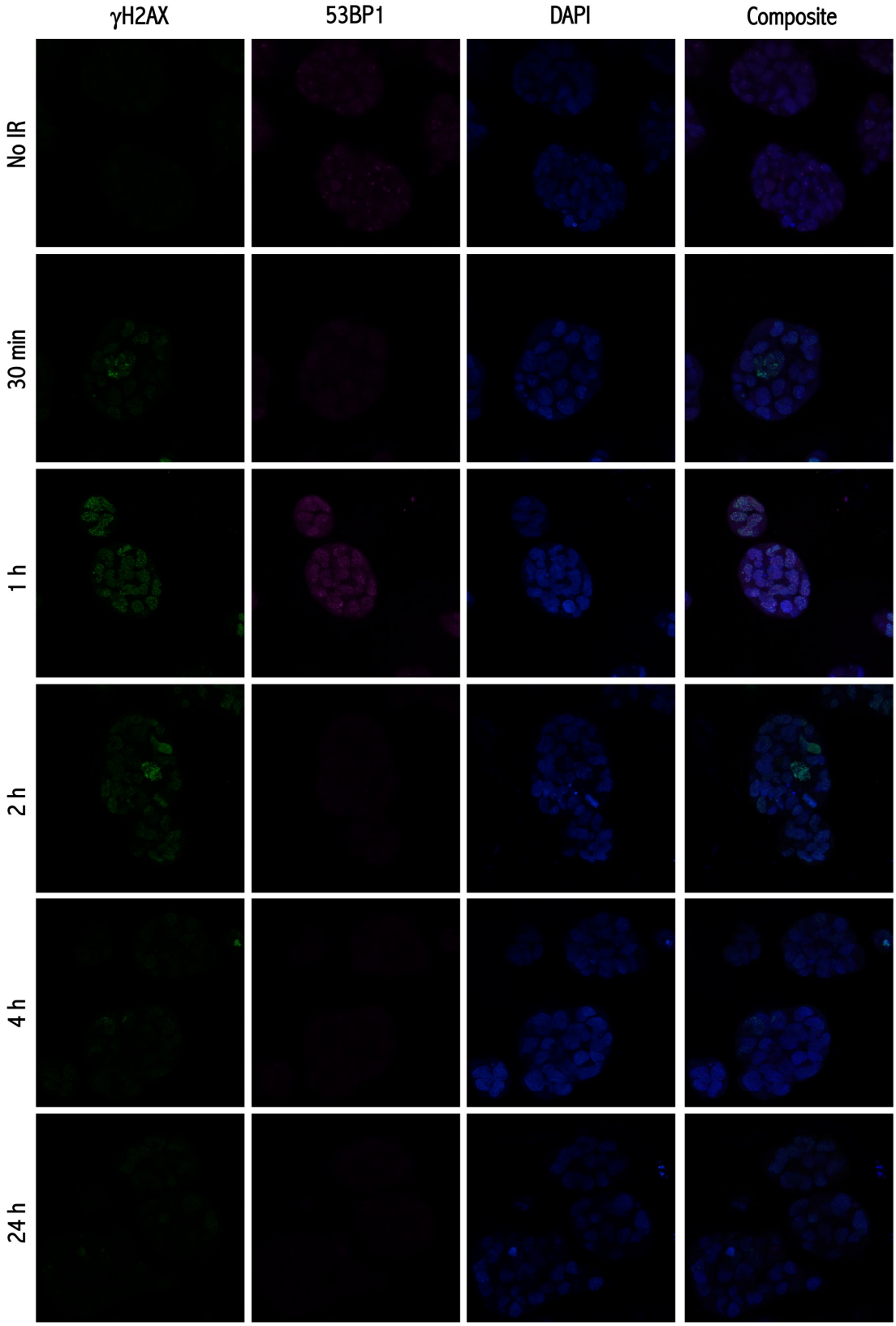

Figure S3.3. DNA damage overtime response of NSCLC spheroids in Matrigel after irradiation. Maximum projection of z-stacks on fluorescence confocal microscopy on NCI-H1299 *shGFP* NSCLC spheroids in Matrigel 30 min, 1 h, 2 h, 4 h and 24 h after 4 Gy of irradiation and a non-irradiated control. Inmunostaining was performed with γH2AX and 53 BP1 antibodies and DAPI for nuclear staining.

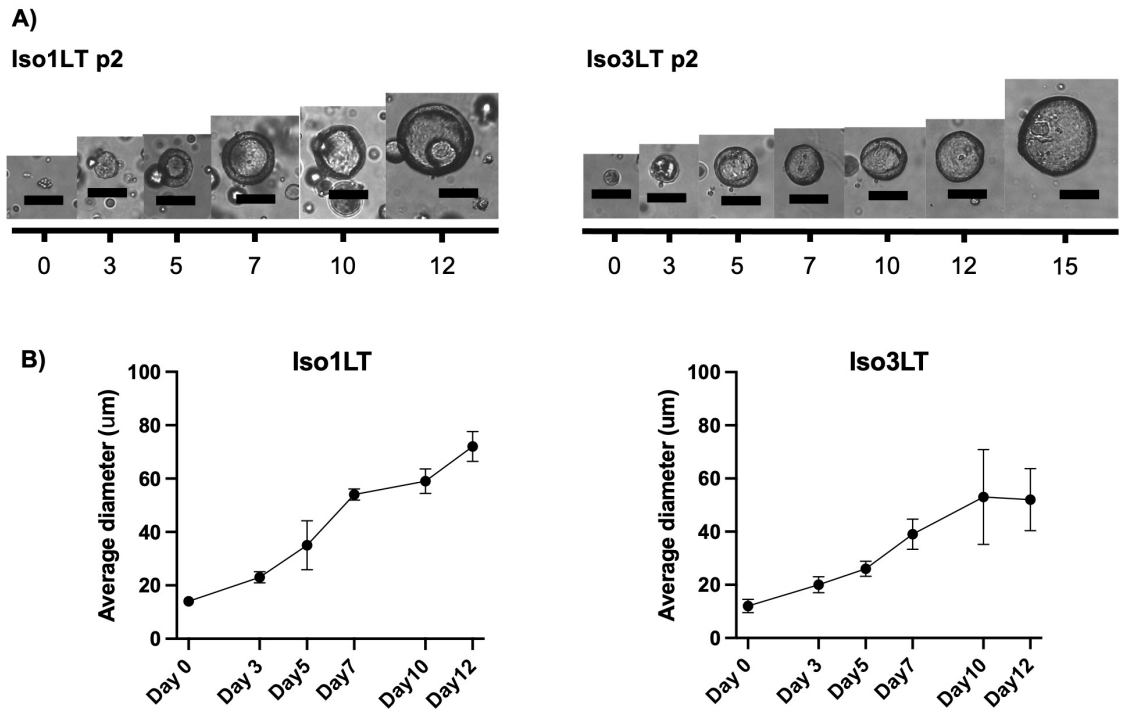

Figure S4.1. Assessing organoid growth during line-establishment. A) Representative microscopic pictures of Iso1LT and Iso3LT organoid lines at early passages (p2) over time showing organoid-growth. Scale bar: 50 μm. **B)** Average diameter of Iso1LT and Iso3LT organoid-lines over time, manually measured in FIJI. n=3. Graphs made with GrapPad Prism 9.

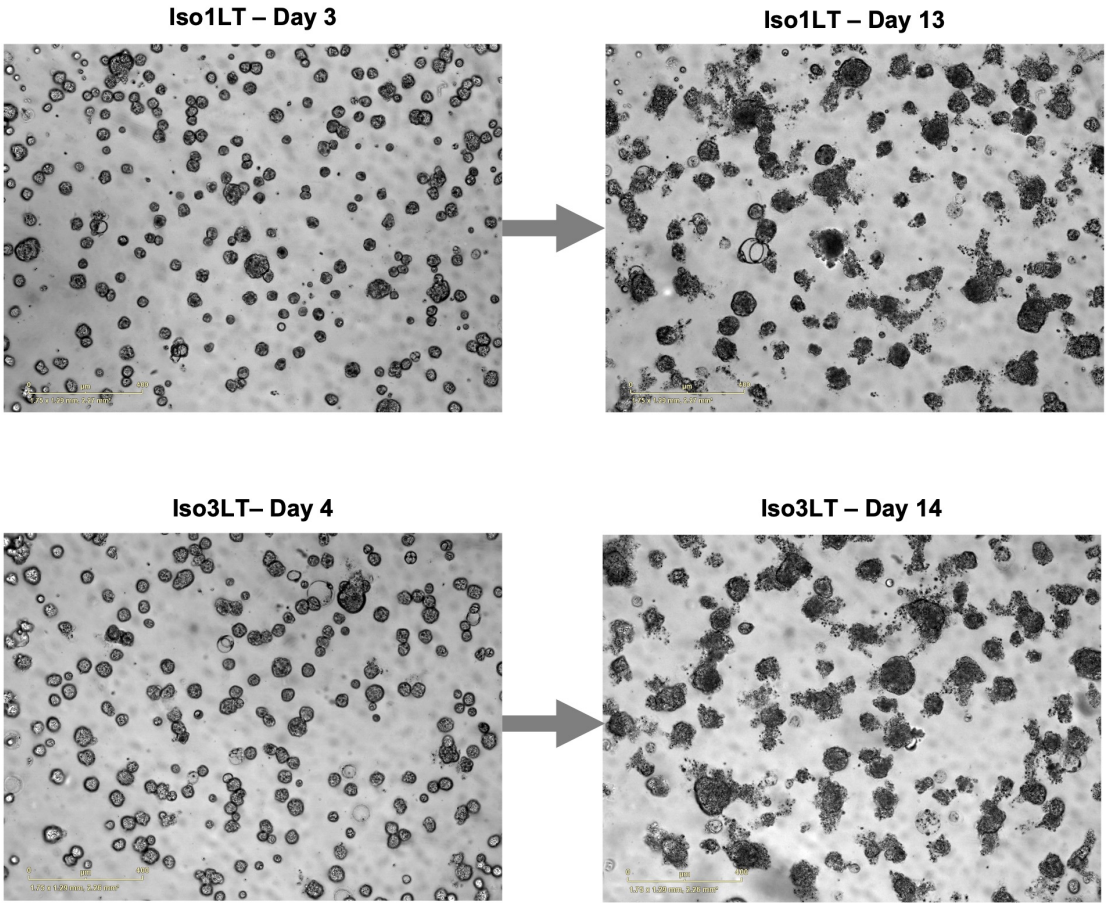

Figure S4.2. Iso1LT and Iso3LT patient-derived organoids in Kim et al. 2019 medium. Organoids, previously grown in growth-factor enriched *Sachs et al.* 2019 medium, were cultured and life-imaged in the IncuCyte®S3 in growth-factor restrictive *Kim et al.* 2019 tumour medium.

Table S4.1. Details of tumour-growth monitoring on mice taken by Transcure Bioservices for the PDXs.

Date			20-Mar-20		31-Mar-20		14-Apr-20		22-Apr-20		05-May-20		15-May-20		09-Jun-20		23-Jun-20	
Day post engraftment			15		26		40		50		61		71		96		110	
Tumour Localisation			Right	Left	Right	Left	Right	Left	Right	Left	Right	Left	Right	Left	Right	Left	Right	Left
Model	Pass age	Group	Vol. (mm^3)	Vol. (mm^3)	Vol. (mm^3)	Vol. (mm^3)	Vol. (mm^3)	Vol. (mm^3)	Vol. (mm^3)	Vol. (mm^3)	Vol. (mm^3)	Vol. (mm^3)	Vol. (mm^3)	Vol. (mm^3)	Vol. (mm^3)	Vol. (mm^3)	Vol. (mm^3)	Vol. (mm^3)
CTG-1878	p6	1st implant	0	50	0	48	0	39	0	0	0	0	0	0	0	0		
CTG-1885	p6	1st implant	123	77	79	219	174	761	Sent to Cardiff									
CTG-19555	p5	1st implant	43	32	152	77	772	204	Sent to Cardiff									
CTG-2557	p7	1st implant	28	42	37	40	91	125	161	183	222	273	289	471	1158	Sent to Cardiff		
		2nd implant	44	43	28	33	19	85	21	161	32	285	38	351	679	127	223	1006
		3rd implant	30	41	24	36	83	22	139	51	276	91	396	117	353	740	1051	742

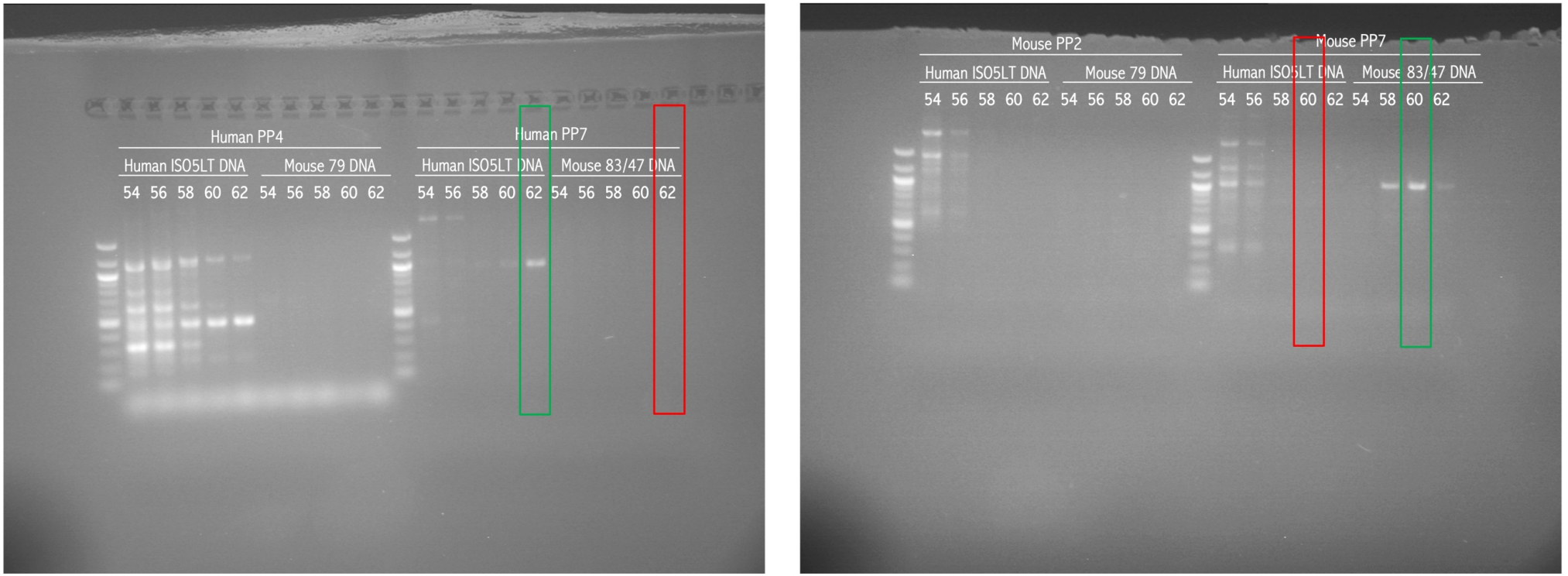

Figure S4.3. Gel electroforesis of PCR primer tests for mouse vs human genotyping of PDX-derived organoids. A) Human actin (Human PP4 – Human Primer Pair 4) and Human PP7 and **B)** 2 primer pairs for mouse (Mouse PP2 and PP7) were designed. PCR and gel electrophoresis was carried out for both human and mouse samples at different annealing temperatures with human or mouse amplified DNA. Green rectangle: positive result. Red rectangle: negative result, showing the specificity of the primers.

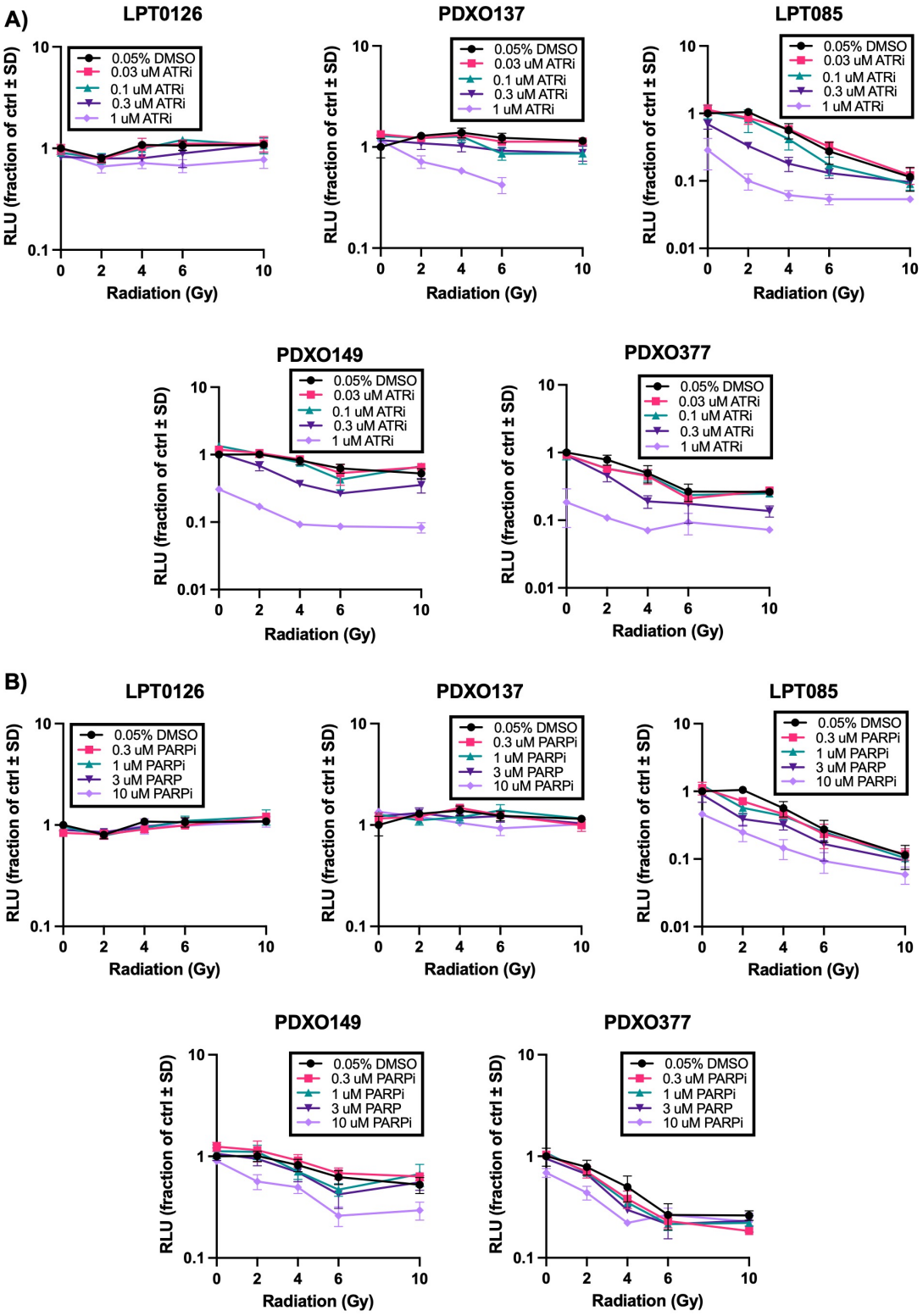

Figure S5.1. NSCLC organoid lines' viability after treatment with ionising radiation and/or a DNA Damage Repair inhibitor. Relative ATP levels as Relative Luminescence (RLU), measured with endpoint CellTiter-Glo® 3D ATP live-cell assay, of organoids (as per graph titles) treated with 2-10Gy of single dose ionising radiation or sham irradiation and 0.5 % DMSO control or a titration of and **A)** ATRi or an **B)** PARPi as per the legends in the figure. ATP measured 5 days post-IR. Drug added 1 h pre-IR and culture medium replaced 24 h post-IR with drug-free medium. n=3. ATRi: Ataxia Telangiectasia and Rad3-related inhibitor, *VE-822*. PARPi: Poly (ADP) Polymerase inhibitor, *Olaparib*. Graphs made with GrapPad Prism.

Table S5.1. Plating efficiency calculations per replicate for NSCLC organoids. Calculated plating efficiencies as number of organoids counted in sham irradiated control samples after re-seeding in the organoid re-seeding assays, normalised over the number of cells re-seeded and presented as a percentage.

Organoid Line	Drug	Replicate	N of cells seeded	N of organoids formed	Platting efficiency (%)	Mean plating efficiency (%)	SD Platting efficiency (%)
LPTO126	DMSO	R1	12500	1692	13.53	13.29	0.66
		R2	12500	-	-		
		R3	12500	1568	12.54		
		R4	12500	1723	13.78		
	ATRi	R1	12500	2530	20.24	17.88	1.86
		R2	12500	2064	16.52		
		R3	12500	2033	16.27		
		R4	12500	2313	18.50		
	PARPi	R1	12500	2313	18.50	16.70	1.41
		R2	12500	2142	17.14		
		R3	12500	1971	15.77		
		R4	12500	1925	15.40		
PDXO137	DMSO	R1	12500	1304	10.43	11.30	1.10
		R2	12500	1366	10.93		
		R3	12500	1568	12.54		
	ATRi	R1	12500	1242	9.93	11.59	1.44
		R2	12500	1568	12.54		
		R3	12500	1537	12.29		
	PARPi	R1	12500	1506	12.04	11.38	0.59
		R2	12500	1366	10.93		
		R3	12500	1397	11.18		
LPTO85	DMSO	R1	12500	900	7.20	7.53	0.92
		R2	12500	1071	8.57		
		R3	12500	854	6.83		
	ATRi	R1	12500	667	5.34	5.42	0.14
		R2	12500	667	5.34		
		R3	12500	698	5.59		
	PARPi	R1	12500	155	1.24	0.95	0.26
		R2	12500	93	0.75		
		R3	12500	109	0.87		

Table continues in the next page

PDXO149	DMSO	R1	12500	105	0.84	0.85	0.01
		R2	12500	109	0.87		
		R3	12500	106	0.85		
		R4	12500	107	0.86		
	ATRi	R1	12500	89	0.71	0.70	0.02
		R2	12500	89	0.71		
		R3	12500	87	0.70		
		R4	12500	83	0.66		
	PARPI	R1	12500	84	0.67	0.70	0.10
		R2	12500	105	0.84		
		R3	12500	85	0.68		
		R4	12500	76	0.61		
PDXO377	DMSO	R1	12500	234	1.87	1.74	0.13
		R2	12500	209	1.67		
		R3	12500	228	1.82		
		R4	12500	199	1.59		
	ATRi	R1	12500	123	0.98	0.81	0.29
		R2	12500	116	0.93		
		R3	12500	47	0.38		
		R4	12500	118	0.94		
	PARPi	R1	12500	179	1.43	1.40	0.03
		R2	12500	178	1.42		
		R3	12500	170	1.36		
		R4	12500	173	1.38		

List of references

Adjei, A. A. 2004. Pharmacology and mechanism of action of pemetrexed. *Clin Lung Cancer* 5 Suppl 2, pp. S51-55. doi: 10.3816/clc.2004.s.003

Ahnesorg, P., Smith, P. and Jackson, S. P. 2006. XLF interacts with the XRCC4-DNA ligase IV complex to promote DNA nonhomologous end-joining. *Cell* 124(2), pp. 301-313. doi: 10.1016/j.cell.2005.12.031

Ansari, J., Shackelford, R. E. and El-Osta, H. 2016. Epigenetics in non-small cell lung cancer: from basics to therapeutics. *Transl Lung Cancer Res* 5(2), pp. 155-171. doi: 10.21037/tlcr.2016.02.02

Ates, G., Vanhaecke, T., Rogiers, V. and Rodrigues, R. M. 2017. *Assaying Cellular Viability Using the Neutral Red Uptake Assay.* . Methods in Molecular Biology.

Audebert, M., Salles, B. and Calsou, P. 2004. Involvement of poly(ADP-ribose) polymerase-1 and XRCC1/DNA ligase III in an alternative route for DNA double-strand breaks rejoining. *J Biol Chem* 279(53), pp. 55117-55126. doi: 10.1074/jbc.M404524200

Azghadi, S. and Daly, M. E. 2021. Radiation and immunotherapy combinations in non-small cell lung cancer. *Cancer Treat Res Commun* 26, p. 100298. doi: 10.1016/j.ctarc.2020.100298

Badder, L. M. et al. 2020. 3D imaging of colorectal cancer organoids identifies responses to Tankyrase inhibitors. *PLoS One* 15(8), p. e0235319. doi: 10.1371/journal.pone.0235319

Bakkenist, C. J. and Kastan, M. B. 2003. DNA damage activates ATM through intermolecular autophosphorylation and dimer dissociation. *Nature* 421, pp. 499-506.

Baldassi, D., Gabold, B. and Merkel, O. 2021. Air-liquid interface cultures of the healthy and diseased human respiratory tract: promises, challenges and future directions. *Adv Nanobiomed Res* 1(6), doi: 10.1002/anbr.202000111

Ballester, B., Milara, J. and Cortijo, J. 2019. Idiopathic Pulmonary Fibrosis and Lung Cancer: Mechanisms and Molecular Targets. *Int J Mol Sci* 20(3), doi: 10.3390/ijms20030593

Basil, M. C. et al. 2022. Human distal airways contain a multipotent secretory cell that can regenerate alveoli. *Nature* 604(7904), pp. 120-126. doi: 10.1038/s41586-022-04552-0

Baumann, P., Benson, F. E. and West, S. C. 1996. Human Rad51 Protein Promotes ATP-Dependent Homologous Pairing and Strand Transfer Reactions In Vitro. *Cell* 87, pp. 757-766.

Beck, L. E. et al. 2022. Systematically quantifying morphological features reveals constraints on organoid phenotypes. *Cell Syst* 13(7), pp. 547-560 e543. doi: 10.1016/j.cels.2022.05.008

Benam, K. H. et al. 2016. Small airway-on-a-chip enables analysis of human lung inflammation and drug responses in vitro. *Nat Methods* 13(2), pp. 151-157. doi: 10.1038/nmeth.3697

Berube, K., Prytherch, Z., Job, C. and Hughes, T. 2010. Human primary bronchial lung cell constructs: the new respiratory models. *Toxicology* 278(3), pp. 311-318. doi: 10.1016/j.tox.2010.04.004

Beucher, A. et al. 2009. ATM and Artemis promote homologous recombination of radiation-induced DNA double-strand breaks in G2. *EMBO J* 28(21), pp. 3413-3427. doi: 10.1038/emboj.2009.276

Boettcher, M. and McManus, M. T. 2015. Choosing the Right Tool for the Job: RNAi, TALEN, or CRISPR. *Mol Cell* 58(4), pp. 575-585. doi: 10.1016/j.molcel.2015.04.028

Bolus, N. E. 2017. Basic Review of Radiation Biology and Terminology. *J Nucl Med Technol* 45(4), pp. 259-264. doi: 10.2967/jnmt.117.195230

Borghaei, H. et al. 2015. Nivolumab versus Docetaxel in Advanced Nonsquamous Non-Small-Cell Lung Cancer. *N Engl J Med* 373(17), pp. 1627-1639. doi: 10.1056/NEJMoa1507643

Borras-Fresneda, M., Barquinero, J. F., Gomolka, M., Hornhardt, S., Rossler, U., Armengol, G. and Barrios, L. 2016. Differences in DNA Repair Capacity, Cell Death and Transcriptional Response after Irradiation between a Radiosensitive and a Radioresistant Cell Line. *Sci Rep* 6, p. 27043. doi: 10.1038/srep27043

Bouleftour, W. et al. 2021. A Review of the Role of Hypoxia in Radioresistance in Cancer Therapy. *Med Sci Monit* 27, p. e934116. doi: 10.12659/MSM.934116

Boysen, G. et al. 2019. Glutaminase inhibitor CB-839 increases radiation sensitivity of lung tumor cells and human lung tumor xenografts in mice. *Int J Radiat Biol* 95(4), pp. 436-442. doi: 10.1080/09553002.2018.1558299

Brahmer, J. et al. 2015. Nivolumab versus Docetaxel in Advanced Squamous-Cell Non-Small-Cell Lung Cancer. *N Engl J Med* 373(2), pp. 123-135. doi: 10.1056/NEJMoa1504627

Burma, S., Chen, B. P., Murphy, M., Kurimasa, A. and Chen, D. J. 2001. ATM phosphorylates histone H2AX in response to DNA double-strand breaks. *J Biol Chem* 276(45), pp. 42462-42467. doi: 10.1074/jbc.C100466200

Cala, G., Sina, B., De Coppi, P., Giobbe, G. G. and Gerli, M. F. M. 2023. Primary human organoids models: Current progress and key milestones. *Front Bioeng Biotechnol* 11, p. 1058970. doi: 10.3389/fbioe.2023.1058970

Canman, C. E. et al. 1998. Activation of the ATM Kinaseby Ionizing Radiation andPhosphorylation of p53. *Science* 281,

Carballo, G. B., Honorato, J. R., de Lopes, G. P. F. and Spohr, T. 2018. A highlight on Sonic hedgehog pathway. *Cell Commun Signal* 16(1), p. 11. doi: 10.1186/s12964-018-0220-7

Cerignoli, F. et al. 2018. In vitro immunotherapy potency assays using real-time cell analysis. *PLoS One* 13(3), p. e0193498. doi: 10.1371/journal.pone.0193498

Chalmers, A. J. 2016. Science in Focus: Combining Radiotherapy with Inhibitors of the DNA Damage Response. *Clin Oncol (R Coll Radiol)* 28(5), pp. 279-282. doi: 10.1016/j.clon.2016.01.035

Chang, H. H. and Lieber, M. R. 2016. Structure-Specific nuclease activities of Artemis and the Artemis: DNA-PKcs complex. *Nucleic Acids Res* 44(11), pp. 4991-4997. doi: 10.1093/nar/gkw456

Chatterjee, N. and Walker, G. C. 2017. Mechanisms of DNA damage, repair, and mutagenesis. *Environ Mol Mutagen* 58(5), pp. 235-263. doi: 10.1002/em.22087

Chehab, N. H., Malikzay, A., Appel, M. and Halazonetis, T. D. 1999. Chk2/hCds1 functions as a DNA damage checkpoint in G1 by stabilizing p53. *Genes & Development* 14, pp. 278-288.

Chen, J. H. et al. 2020. Genomic characteristics and drug screening among organoids derived from non-small cell lung cancer patients. *Thorac Cancer* 11(8), pp. 2279-2290. doi: 10.1111/1759-7714.13542

Chen, L., Nievera, C. J., Lee, A. Y. and Wu, X. 2008. Cell cycle-dependent complex formation of BRCA1.CtIP.MRN is important for DNA double-strand break repair. *J Biol Chem* 283(12), pp. 7713-7720. doi: 10.1074/jbc.M710245200

Chen, X., Xie, Y., Liu, Z. and Lin, Y. 2021. Application of Programmable Tetrahedral Framework Nucleic Acid-Based Nanomaterials in Neurological Disorders: Progress and Prospects. *Front Bioeng Biotechnol* 9, p. 782237. doi: 10.3389/fbioe.2021.782237

Chen, Z., Fillmore, C. M., Hammerman, P. S., Kim, C. F. and Wong, K. K. 2014. Non-small-cell lung cancers: a heterogeneous set of diseases. *Nat Rev Cancer* 14(8), pp. 535-546. doi: 10.1038/nrc3775

Chou, T. C. 2010. Drug combination studies and their synergy quantification using the Chou-Talalay method. *Cancer Res* 70(2), pp. 440-446. doi: 10.1158/0008-5472.CAN-09-1947

Chung, W. S., Lin, C. L., Lin, C. L. and Kao, C. H. 2015. Bronchiectasis and the risk of cancer: a nationwide retrospective cohort study. *Int J Clin Pract* 69(6), pp. 682-688. doi: 10.1111/ijcp.12599

Colucci, R., Blandizzi, C., Tanini, M., Vassalle, C., Breschi, M. C. and Del Tacca, M. 2005. Gastrin promotes human colon cancer cell growth via CCK-2 receptor-mediated cyclooxygenase-2 induction and prostaglandin E2 production. *Br J Pharmacol* 144(3), pp. 338-348. doi: 10.1038/sj.bjp.0706053

Curtin, N. J. 2013. Inhibiting the DNA damage response as a therapeutic manoeuvre in cancer. *Br J Pharmacol* 169(8), pp. 1745-1765. doi: 10.1111/bph.12244

Cutz, E., Pan, J., Yeger, H., Domnik, N. J. and Fisher, J. T. 2013. Recent advances and contraversies on the role of pulmonary neuroepithelial bodies as airway sensors. *Semin Cell Dev Biol* 24(1), pp. 40-50. doi: 10.1016/j.semcdb.2012.09.003

Daley, J. M. and Sung, P. 2014. 53BP1, BRCA1, and the choice between recombination and end joining at DNA double-strand breaks. *Mol Cell Biol* 34(8), pp. 1380-1388. doi: 10.1128/MCB.01639-13

Däster, S. et al. 2017. Induction of hypoxia and necrosis in multicellular tumor spheroids is associated with resistance to chemotherapy treatment. *Oncotarget* 8(1), pp. 1725-1736.

Davies, A. A., Masson, J.-Y., McIlwraith, M. J., Stasiak, A. Z., Stasiak, A., Venkitaraman, A. R. and West, S. C. 2001. Role of BRCA2 in Control of the RAD51 Recombination and DNA Repair Protein. *Molecular Cell* 7, pp. 272-282.

Day, C. P., Merlino, G. and Van Dyke, T. 2015. Preclinical mouse cancer models: a maze of opportunities and challenges. *Cell* 163(1), pp. 39-53. doi: 10.1016/j.cell.2015.08.068

De Bont, R. and van Larebeke, N. 2004. Endogenous DNA damage in humans: a review of quantitative data. *Mutagenesis* 19(3), pp. 169-185. doi: 10.1093/mutage/geh025

Deben, C., Deschoolmeester, V., Lardon, F., Rolfo, C. and Pauwels, P. 2016. TP53 and MDM2 genetic alterations in non-small cell lung cancer: Evaluating their prognostic and predictive value. *Crit Rev Oncol Hematol* 99, pp. 63-73. doi: 10.1016/j.critrevonc.2015.11.019

Desai, T. J., Brownfield, D. G. and Krasnow, M. A. 2014. Alveolar progenitor and stem cells in lung development, renewal and cancer. *Nature* 507(7491), pp. 190-194. doi: 10.1038/nature12930

Dijkstra, K. K. et al. 2018. Generation of Tumor-Reactive T Cells by Co-culture of Peripheral Blood Lymphocytes and Tumor Organoids. *Cell* 174(6), pp. 1586-1598 e1512. doi: 10.1016/j.cell.2018.07.009

Dijkstra, K. K. et al. 2020. Challenges in Establishing Pure Lung Cancer Organoids Limit Their Utility for Personalized Medicine. *Cell Rep* 31(5), p. 107588. doi: 10.1016/j.celrep.2020.107588

Duarte, D. and Vale, N. 2022. Evaluation of synergism in drug combinations and reference models for future orientations in oncology. *Curr Res Pharmacol Drug Discov* 3, p. 100110. doi: 10.1016/j.crphar.2022.100110

Durham, A. L. and Adcock, I. M. 2015. The relationship between COPD and lung cancer. *Lung Cancer* 90(2), pp. 121-127. doi: 10.1016/j.lungcan.2015.08.017

Dye, B. R. et al. 2015. In vitro generation of human pluripotent stem cell derived lung organoids. *Elife* 4, doi: 10.7554/eLife.05098

El-Deiry, W. S. et al. 1994. WAF1/CIP1 Is Induced in /?53-mediated G! Arrest and Apoptosis. *Cancer Research* 54, pp. 1169-1174.

Ewels, P. A. et al. 2020. The nf-core framework for community-curated bioinformatics pipelines. *Nat Biotechnol* 38(3), p. 271. doi: 10.1038/s41587-020-0435-1

Falck, J., Mailand, N., Syljuasen, R. G., Bartek, J. and Lukas, J. 2001. The ATM-Chk2-Cdc25A checkpoint pathway guards against radioresistant DNA synthesis. *Nature* 410, pp. 842-847.

Faridounnia, M., Folkers, G. E. and Boelens, R. 2018. Function and Interactions of ERCC1-XPF in DNA Damage Response. *Molecules* 23(12), doi: 10.3390/molecules23123205

Fatima, N., Cohen, C., Lawson, D. and Siddiqui, M. T. 2011. TTF-1 and Napsin A double stain: a useful marker for diagnosing lung adenocarcinoma on fine-needle aspiration cell blocks. *Cancer Cytopathol* 119(2), pp. 127-133. doi: 10.1002/cncy.20135

Fei, P. and El-Deiry, W. S. 2003. P53 and radiation responses. *Oncogene* 22(37), pp. 5774-5783. doi: 10.1038/sj.onc.1206677

Feng, L., Fong, K. W., Wang, J., Wang, W. and Chen, J. 2013. RIF1 counteracts BRCA1-mediated end resection during DNA repair. *J Biol Chem* 288(16), pp. 11135-11143. doi: 10.1074/jbc.M113.457440

Fokas, E. et al. 2012. Targeting ATR in vivo using the novel inhibitor VE-822 results in selective sensitization of pancreatic tumors to radiation. *Cell Death Dis* 3(12), p. e441. doi: 10.1038/cddis.2012.181

Franken, N. A., Rodermond, H. M., Stap, J., Haveman, J. and van Bree, C. 2006. Clonogenic assay of cells in vitro. *Nat Protoc* 1(5), pp. 2315-2319. doi: 10.1038/nprot.2006.339

Friedl, P., Locker, J., Sahai, E. and Segall, J. E. 2012. Classifying collective cancer cell invasion. *Nat Cell Biol* 14(8), pp. 777-783. doi: 10.1038/ncb2548

Gao, L. et al. 2019. Post-Passage rock inhibition induces cytoskeletal aberrations and apoptosis in Human embryonic stem cells. *Stem Cell Res* 41, p. 101641. doi: 10.1016/j.scr.2019.101641

Geurts, M. H. and Clevers, H. 2023. CRISPR engineering in organoids for gene repair and disease modelling. *Nature Reviews Bioengineering* 1(1), pp. 32-45. doi: 10.1038/s44222-022-00013-5

Giroux-Leprieur, E., Costantini, A., Ding, V. W. and He, B. 2018. Hedgehog Signaling in Lung Cancer: From Oncogenesis to Cancer Treatment Resistance. *Int J Mol Sci* 19(9), doi: 10.3390/ijms19092835

Gottlieb, T. M. and Jackson, S. P. 1993. The DNA-Dependent Protein Kinase: Requirement for DNA ENds and Addociation with Ku Antigent. *Cell* 72, pp. 131-142.

Grawunder, U., Wilm, M., Wu, X., Kulesza, P., Wilson, T. E., Mann, M. and Lieber, M. R. 1997. Activity of DNA ligase IV stimulated by complex formation with XRCC4 protein in mammalian cells. *Nature* 388, pp. 492-495.

Gu, Y., Fu, J., Lo, P.-K., Wang, S., Wang, Q. and Chen, H. 2011. The Effect of B27 Supplement on Promoting In Vitro Propagation of Her2/neu-Transformed Mammary Tumorspheres. *Journal of Biotech Research* 3, pp. 7-18.

Guo, Q., Liu, L., Chen, Z., Fan, Y., Zhou, Y., Yuan, Z. and Zhang, W. 2022. Current treatments for non-small cell lung cancer. *Front Oncol* 12, p. 945102. doi: 10.3389/fonc.2022.945102

Hafner, A., Bulyk, M. L., Jambhekar, A. and Lahav, G. 2019. The multiple mechanisms that regulate p53 activity and cell fate. *Nat Rev Mol Cell Biol* 20(4), pp. 199-210. doi: 10.1038/s41580-019-0110-x

Haince, J. F., McDonald, D., Rodrigue, A., Dery, U., Masson, J. Y., Hendzel, M. J. and Poirier, G. G. 2008. PARP1-dependent kinetics of recruitment of MRE11 and NBS1 proteins to multiple DNA damage sites. *J Biol Chem* 283(2), pp. 1197-1208. doi: 10.1074/jbc.M706734200

Hakem, R. 2008. DNA-damage repair; the good, the bad, and the ugly. *EMBO J* 27(4), pp. 589-605. doi: 10.1038/emboj.2008.15

Hammond, E. M., Dorie, M. J. and Giaccia, A. J. 2003. ATR/ATM targets are phosphorylated by ATR in response to hypoxia and ATM in response to reoxygenation. *J Biol Chem* 278(14), pp. 12207-12213. doi: 10.1074/jbc.M212360200

Hauge, S., Eek Mariampillai, A., Rodland, G. E., Bay, L. T. E., Landsverk, H. B. and Syljuasen, R. G. 2023. Expanding roles of cell cycle checkpoint inhibitors in radiation oncology. *Int J Radiat Biol* 99(6), pp. 941-950. doi: 10.1080/09553002.2021.1913529

Heng, W. S., Gosens, R. and Kruyt, F. A. E. 2019. Lung cancer stem cells: origin, features, maintenance mechanisms and therapeutic targeting. *Biochem Pharmacol* 160, pp. 121-133. doi: 10.1016/j.bcp.2018.12.010

Heo, I. et al. 2018. Modelling Cryptosporidium infection in human small intestinal and lung organoids. *Nat Microbiol* 3(7), pp. 814-823. doi: 10.1038/s41564-018-0177-8

Herbst, R. S. et al. 2016. Pembrolizumab versus docetaxel for previously treated, PD-L1-positive, advanced non-small-cell lung cancer (KEYNOTE-010): a randomised controlled trial. *Lancet* 387(10027), pp. 1540-1550. doi: 10.1016/S0140-6736(15)01281-7

Hill, W. et al. 2023. Lung adenocarcinoma promotion by air pollutants. *Nature* 616(7955), pp. 159-167. doi: 10.1038/s41586-023-05874-3

Hoareau, L. et al. 2021. Induction of alveolar and bronchiolar phenotypes in human lung organoids. *Physiol Rep* 9(11), p. e14857. doi: 10.14814/phy2.14857

Hoffmann, K. et al. 2022. Human alveolar progenitors generate dual lineage bronchioalveolar organoids. *Commun Biol* 5(1), p. 875. doi: 10.1038/s42003-022-03828-5

Horie, M. et al. 2012. Characterization of human lung cancer-associated fibroblasts in three-dimensional in vitro co-culture model. *Biochem Biophys Res Commun* 423(1), pp. 158-163. doi: 10.1016/j.bbrc.2012.05.104

Hu, Y. et al. 2020. Wnt/beta-catenin signaling is critical for regenerative potential of distal lung epithelial progenitor cells in homeostasis and emphysema. *Stem Cells* 38(11), pp. 1467-1478. doi: 10.1002/stem.3241

Huang, R. and Zhou, P. K. 2021. DNA damage repair: historical perspectives, mechanistic pathways and clinical translation for targeted cancer therapy. *Signal Transduct Target Ther* 6(1), p. 254. doi: 10.1038/s41392-021-00648-7

Huang, R. X. and Zhou, P. K. 2020. DNA damage response signaling pathways and targets for radiotherapy sensitization in cancer. *Signal Transduct Target Ther* 5(1), p. 60. doi: 10.1038/s41392-020-0150-x

Hubert, C. G. et al. 2016. A Three-Dimensional Organoid Culture System Derived from Human Glioblastomas Recapitulates the Hypoxic Gradients and Cancer Stem Cell Heterogeneity of Tumors Found In Vivo. *Cancer Res* 76(8), pp. 2465-2477. doi: 10.1158/0008-5472.CAN-15-2402

Hui, K. P. Y. et al. 2018. Tropism, replication competence, and innate immune responses of influenza virus: an analysis of human airway organoids and ex-vivo bronchus cultures. *Lancet Respir Med* 6(11), pp. 846-854. doi: 10.1016/S2213-2600(18)30236-4

Hui, R. et al. 2019. Patient-reported outcomes with durvalumab after chemoradiotherapy in stage III, unresectable non-small-cell lung cancer (PACIFIC): a randomised, controlled, phase 3 study. *Lancet Oncol* 20(12), pp. 1670-1680. doi: 10.1016/S1470-2045(19)30519-4

Iftode, C., Daniely, Y. and Borowiec, J. A. 1999. Replication protein A (RPA): the eukaryotic SSB. *Crit Rev Biochem Mol Biol* 34(3), pp. 141-180. doi: 10.1080/10409239991209255

Iyama, T. and Wilson, D. M., 3rd. 2013. DNA repair mechanisms in dividing and non-dividing cells. *DNA Repair (Amst)* 12(8), pp. 620-636. doi: 10.1016/j.dnarep.2013.04.015

Jamal-Hanjani, M. et al. 2017. Tracking the Evolution of Non-Small-Cell Lung Cancer. *N Engl J Med* 376(22), pp. 2109-2121. doi: 10.1056/NEJMoa1616288

Jensen, R. B., Carreira, A. and Kowalczykowski, S. C. 2010. Purified human BRCA2 stimulates RAD51-mediated recombination. *Nature* 467(7316), pp. 678-683. doi: 10.1038/nature09399

Jiang, Y., Chen, C., Li, Z., Guo, W., Gegner, J. A., Lin, S. and Han, J. 1996. Characterization of the structure and function of a new mitogen-activated protein kinase (p38beta). *J Biol Chem* 271(30), pp. 17920-17926. doi: 10.1074/jbc.271.30.17920

Jiang, Y. et al. 2016. Hypoxia Potentiates the Radiation-Sensitizing Effect of Olaparib in Human Non-Small Cell Lung Cancer Xenografts by Contextual Synthetic Lethality. *Int J Radiat Oncol Biol Phys* 95(2), pp. 772-781. doi: 10.1016/j.ijrobp.2016.01.035

Kadur Lakshminarasimha Murthy, P. et al. 2022. Human distal lung maps and lineage hierarchies reveal a bipotent progenitor. *Nature* 604(7904), pp. 111-119. doi: 10.1038/s41586-022-04541-3

Kaminski, A. M., Chiruvella, K. K., Ramsden, D. A., Bebenek, K., Kunkel, T. A. and Pedersen, L. C. 2022. Analysis of diverse double-strand break synapsis with Pollambda reveals basis for unique substrate specificity in nonhomologous end-joining. *Nat Commun* 13(1), p. 3806. doi: 10.1038/s41467-022-31278-4

Kapalczynska, M. et al. 2018. 2D and 3D cell cultures - a comparison of different types of cancer cell cultures. *Arch Med Sci* 14(4), pp. 910-919. doi: 10.5114/aoms.2016.63743

Karolak, A., Poonja, S. and Rejniak, K. A. 2019. Morphophenotypic classification of tumor organoids as an indicator of drug exposure and penetration potential. *PLoS Comput Biol* 15(7), p. e1007214. doi: 10.1371/journal.pcbi.1007214

Kerksick, C. and Willoughby, D. 2005. The Antioxidant Role of Glutathione and N-AcetylCysteine Supplements and Exercise- Induced Oxidative Stress. *Journal of the International Society of Sports Nutrition* 2, pp. 38-44.

Kersten, K., de Visser, K. E., van Miltenburg, M. H. and Jonkers, J. 2017. Genetically engineered mouse models in oncology research and cancer medicine. *EMBO Mol Med* 9(2), pp. 137-153. doi: 10.15252/emmm.201606857

Khosravi, R., Maya, R., Gottlieb, T., Oren, M., Shiloh, Y. and Shkedy, D. 1999. Rapid ATM-dependent phosphorylation of MDM2
precedes p53 accumulation in response to
DNA damage. *The Proceedings of the National Academy of Sciences* 96(26), pp. 14973-14977.

Kim, C. F. et al. 2005. Identification of bronchioalveolar stem cells in normal lung and lung cancer. *Cell* 121(6), pp. 823-835. doi: 10.1016/j.cell.2005.03.032

Kim, M. et al. 2019. Patient-derived lung cancer organoids as in vitro cancer models for therapeutic screening. *Nat Commun* 10(1), p. 3991. doi: 10.1038/s41467-019-11867-6

Kiselev, V. Y., Yiu, A. and Hemberg, M. 2018. scmap: projection of single-cell RNA-seq data across data sets. *Nat Methods* 15(5), pp. 359-362. doi: 10.1038/nmeth.4644

Kitagawa, R., Bakkenist, C. J., McKinnon, P. J. and Kastan, M. B. 2004. Phosphorylation of SMC1 is a critical downstream event in the ATM-NBS1-BRCA1 pathway. *Genes Dev* 18(12), pp. 1423-1438. doi: 10.1101/gad.1200304

Kong, X., Yu, D., Wang, Z. and Li, S. 2021. Relationship between p53 status and the bioeffect of ionizing radiation. *Oncol Lett* 22(3), p. 661. doi: 10.3892/ol.2021.12922

Koyanagi, M. et al. 2008. Inhibition of the Rho/ROCK pathway reduces apoptosis during transplantation of embryonic stem cell-derived neural precursors. *J Neurosci Res* 86(2), pp. 270-280. doi: 10.1002/jnr.21502

Krasteva, G., Canning, B. J., Papadakis, T. and Kummer, W. 2012. Cholinergic brush cells in the trachea mediate respiratory responses to quorum sensing molecules. *Life Sci* 91(21-22), pp. 992-996. doi: 10.1016/j.lfs.2012.06.014

Krieger, T. G. et al. 2021. Single-cell analysis of patient-derived PDAC organoids reveals cell state heterogeneity and a conserved developmental hierarchy. *Nat Commun* 12(1), p. 5826. doi: 10.1038/s41467-021-26059-4

Kriegsmann, K. et al. 2019. Agreement of CK5/6, p40, and p63 immunoreactivity in non-small cell lung cancer. *Pathology* 51(3), pp. 240-245. doi: 10.1016/j.pathol.2018.11.009

Kwok, M. et al. 2016. ATR inhibition induces synthetic lethality and overcomes chemoresistance in TP53- or ATM-defective chronic lymphocytic leukemia cells. *Blood* 127(5), pp. 582-595. doi: 10.1182/blood-2015-05-644872

La Manno, G. et al. 2018. RNA velocity of single cells. *Nature* 560(7719), pp. 494-498. doi: 10.1038/s41586-018-0414-6

Lababede, O. and Meziane, M. A. 2018. The Eighth Edition of TNM Staging of Lung Cancer: Reference Chart and Diagrams. *Oncologist* 23(7), pp. 844-848. doi: 10.1634/theoncologist.2017-0659

Lampart, F. L., Iber, D. and Doumpas, N. 2023. Organoids in high-throughput and high-content screenings. *Frontiers in Chemical Engineering* 5, doi: 10.3389/fceng.2023.1120348

Lancaster, M. A. and Huch, M. 2019. Disease modelling in human organoids. *Dis Model Mech* 12(7), doi: 10.1242/dmm.039347

Lazzari, G., Couvreur, P. and Mura, S. 2017. Multicellular tumor spheroids: a relevant 3D model for the in vitro preclinical investigation of polymer nanomedicines. *Polymer Chemistry* 8(34), pp. 4947-4969. doi: 10.1039/c7py00559h

Lee, S. H. 2019. Chemotherapy for Lung Cancer in the Era of Personalized Medicine. *Tuberc Respir Dis (Seoul)* 82(3), pp. 179-189. doi: 10.4046/trd.2018.0068

Lekshmi, A. et al. 2017. A quantitative real-time approach for discriminating apoptosis and necrosis. *Cell Death Discov* 3, p. 16101. doi: 10.1038/cddiscovery.2016.101

Leprieur, E. G. et al. 2017. Membrane-bound full-length Sonic Hedgehog identifies cancer stem cells in human non-small cell lung cancer. *Oncotarget* 8(61), pp. 103744-103757.

Li, Z. et al. 2020. Human Lung Adenocarcinoma-Derived Organoid Models for Drug Screening. *iScience* 23(8), p. 101411. doi: 10.1016/j.isci.2020.101411

Lim, D.-S., Kim, S.-T., Xu, B., Maser, R. S., Lin, J., Petrini, J. H. J. and Kastan, M. B. 2000. ATM phosphorylates p95/nbs1 in an S-phase checkpoint pathway. *Nature* 404, pp. 613-617.

Linke, S. P. et al. 2003. p53 Interacts with hRAD51 and hRAD54, and Directly Modulates Homologous Recombination. *Cancer Research* 63, pp. 2596-2605.

Liu, K. et al. 2020. The role of CDC25C in cell cycle regulation and clinical cancer therapy: a systematic review. *Cancer Cell Int* 20, p. 213. doi: 10.1186/s12935-020-01304-w

Liu, Q. et al. 2019. Lung regeneration by multipotent stem cells residing at the bronchioalveolar-duct junction. *Nat Genet* 51(4), pp. 728-738. doi: 10.1038/s41588-019-0346-6

Liu, Y., Wu, W., Cai, C., Zhang, H., Shen, H. and Han, Y. 2023. Patient-derived xenograft models in cancer therapy: technologies and applications. *Signal Transduct Target Ther* 8(1), p. 160. doi: 10.1038/s41392-023-01419-2

Llamazares-Prada, M. et al. 2021. Versatile workflow for cell type-resolved transcriptional and epigenetic profiles from cryopreserved human lung. *JCI Insight* 6(6), doi: 10.1172/jci.insight.140443

Lomax, M. E., Folkes, L. K. and O'Neill, P. 2013. Biological consequences of radiation-induced DNA damage: relevance to radiotherapy. *Clin Oncol (R Coll Radiol)* 25(10), pp. 578-585. doi: 10.1016/j.clon.2013.06.007

Low, D. A., Moran, J. M., Dempsey, J. F., Dong, L. and Oldham, M. 2011. Dosimetry tools and techniques for IMRT. *Med Phys* 38(3), pp. 1313-1338. doi: 10.1118/1.3514120

Lucky, S. S. et al. 2021. Patient-Derived Nasopharyngeal Cancer Organoids for Disease Modeling and Radiation Dose Optimization. *Front Oncol* 11, p. 622244. doi: 10.3389/fonc.2021.622244

Lukonin, I., Zinner, M. and Liberali, P. 2021. Organoids in image-based phenotypic chemical screens. *Exp Mol Med* 53(10), pp. 1495-1502. doi: 10.1038/s12276-021-00641-8

Luo, H. et al. 2008. Regulation of intra-S phase checkpoint by ionizing radiation (IR)-dependent and IR-independent phosphorylation of SMC3. *J Biol Chem* 283(28), pp. 19176-19183. doi: 10.1074/jbc.M802299200

Ma, H. C., Zhu, Y. J., Zhou, R., Yu, Y. Y., Xiao, Z. Z. and Zhang, H. B. 2022. Lung cancer organoids, a promising model still with long way to go. *Crit Rev Oncol Hematol* 171, p. 103610. doi: 10.1016/j.critrevonc.2022.103610

Mahesh, A. N., Bhatia, K. S. and Bhatt, S. 2022. Cell cycle.*Reference Module in Biomedical Sciences*.

Mamdani, H., Matosevic, S., Khalid, A. B., Durm, G. and Jalal, S. I. 2022. Immunotherapy in Lung Cancer: Current Landscape and Future Directions. *Front Immunol* 13, p. 823618. doi: 10.3389/fimmu.2022.823618

Mantovani, F., Collavin, L. and Del Sal, G. 2019. Mutant p53 as a guardian of the cancer cell. *Cell Death Differ* 26(2), pp. 199-212. doi: 10.1038/s41418-018-0246-9

Mao, Z., Bozzella, M., Seluanov, A. and Gorbunova, V. 2008. Comparison of nonhomologous end joining and homologous recombination in human cells. *DNA Repair (Amst)* 7(10), pp. 1765-1771. doi: 10.1016/j.dnarep.2008.06.018

Matthews, H. K., Bertoli, C. and de Bruin, R. A. M. 2022. Cell cycle control in cancer. *Nat Rev Mol Cell Biol* 23(1), pp. 74-88. doi: 10.1038/s41580-021-00404-3

McMahon, J. A., Takada, S., Zimmerman, L. B., Fan, C.-M., Harland, R. M. and McMahon, A. P. 1998. Noggin-mediated antagonism of BMP signaling is required for growth and patterning of the neural tube and somite. *Genes and development* 12, pp. 1438-1452.

Mehdizadeh, R., Madjid Ansari, A., Forouzesh, F., Shahriari, F., Shariatpanahi, S. P., Salaritabar, A. and Javidi, M. A. 2023. P53 status, and G2/M cell cycle arrest, are determining factors in cell-death induction mediated by ELF-EMF in glioblastoma. *Sci Rep* 13(1), p. 10845. doi: 10.1038/s41598-023-38021-z

Mehmel, M., Jovanovic, N. and Spitz, U. 2020. Nicotinamide Riboside-The Current State of Research and Therapeutic Uses. *Nutrients* 12(6), doi: 10.3390/nu12061616

Meijering, E., Dzyubachyk, O. and Smal, I. 2012. Methods for cell and particle tracking. *Methods Enzymol* 504, pp. 183-200. doi: 10.1016/B978-0-12-391857-4.00009-4

Menegakis, A. et al. 2021. Resistance of Hypoxic Cells to Ionizing Radiation Is Mediated in Part via Hypoxia-Induced Quiescence. *Cells* 10(3), doi: 10.3390/cells10030610

Meng, X., Cui, G. and Peng, G. 2023. Lung development and regeneration: newly defined cell types and progenitor status. *Cell Regen* 12(1), p. 5. doi: 10.1186/s13619-022-00149-0

Meng, Y. et al. 2018. Nicotinamide Promotes Cell Survival and Differentiation as Kinase Inhibitor in Human Pluripotent Stem Cells. *Stem Cell Reports* 11(6), pp. 1347-1356. doi: 10.1016/j.stemcr.2018.10.023

Michael J. Evans, L. S. V. W. 2009. Cellular and Molecular Characteristics of Basal Cells in Airway Epithelium. *Experimental Lung Research* 27(5), pp. 401-415. doi: 10.1080/01902140120740

Mimori, T., Akizuki, M., Yamagata, H., Inada, S., Yoshida, S. and Homma, M. 1981. Characterization of a high molecular weight acidic nuclear protein recognized by autoantibodies in sera from patients with polymyositis-scleroderma overlap. *J Clin Invest* 68(3), pp. 611-620. doi: 10.1172/jci110295

Mindt, B. C., Fritz, J. H. and Duerr, C. U. 2018. Group 2 Innate Lymphoid Cells in Pulmonary Immunity and Tissue Homeostasis. *Front Immunol* 9, p. 840. doi: 10.3389/fimmu.2018.00840

Mithoowani, H. and Febbraro, M. 2022. Non-Small-Cell Lung Cancer in 2022: A Review for General Practitioners in Oncology. *Curr Oncol* 29(3), pp. 1828-1839. doi: 10.3390/curroncol29030150

Montoro, D. T. et al. 2018. A revised airway epithelial hierarchy includes CFTR-expressing ionocytes. *Nature* 560(7718), pp. 319-324. doi: 10.1038/s41586-018-0393-7

Motycka, T. A., Bessho, T., Post, S. M., Sung, P. and Tomkinson, A. E. 2004. Physical and functional interaction between the XPF/ERCC1 endonuclease and hRad52. *J Biol Chem* 279(14), pp. 13634-13639. doi: 10.1074/jbc.M313779200

Murray, J. F. 2010. The structure and function of the lung. *IJTLD* 14(4), pp. 391–396.

Nagle, W. P. and Coppes, P. R. 2020. Current and Future Perspectives of the Use of Organoids in Radiobiology. *Cells* 9, pp. 2469-2489. doi: 10.3390/cells9122649

Nakadate, Y., Kodera, Y., Kitamura, Y., Tachibana, T., Tamura, T. and Koizumi, F. 2013. Silencing of poly(ADP-ribose) glycohydrolase sensitizes lung cancer cells to radiation through the abrogation of DNA damage checkpoint. *Biochem Biophys Res Commun* 441(4), pp. 793-798. doi: 10.1016/j.bbrc.2013.10.134

Nicholson, A. G. et al. 2022. The 2021 WHO Classification of Lung Tumors: Impact of Advances Since 2015. *J Thorac Oncol* 17(3), pp. 362-387. doi: 10.1016/j.jtho.2021.11.003

Nie, X., Liang, Z., Li, K., Yu, H., Huang, Y., Ye, L. and Yang, Y. 2021. Novel organoid model in drug screening: Past, present, and future. *Liver Research* 5(2), pp. 72-78. doi: 10.1016/j.livres.2021.05.003

Nimonkar, A. V., Ozsoy, A. Z., Genschel, J., Modrich, P. and Kowalczykowski, S. C. 2008. Human exonuclease 1 and BLM helicase interact to resect DNA and initiate DNA repair. *Proc Natl Acad Sci U S A* 105(44), pp. 16906-16911. doi: 10.1073/pnas.0809380105

Nomori, H. et al. 2021. Differences between lung adenocarcinoma and squamous cell carcinoma in histological distribution of residual tumor after induction chemoradiotherapy. *Discov Oncol* 12(1), p. 36. doi: 10.1007/s12672-021-00431-8

Nunes, A. S., Barros, A. S., Costa, E. C., Moreira, A. F. and Correia, I. J. 2019. 3D tumor spheroids as in vitro models to mimic in vivo human solid tumors resistance to therapeutic drugs. *Biotechnol Bioeng* 116(1), pp. 206-226. doi: 10.1002/bit.26845

Osmani, L., Askin, F., Gabrielson, E. and Li, Q. K. 2018. Current WHO guidelines and the critical role of immunohistochemical markers in the subclassification of non-small cell lung carcinoma (NSCLC): Moving from targeted therapy to immunotherapy. *Semin Cancer Biol* 52(Pt 1), pp. 103-109. doi: 10.1016/j.semcancer.2017.11.019

Parry-Jones, A. and Spary, L. K. 2018. The Wales Cancer Bank (WCB). *Open Journal of Bioresources* 5, doi: 10.5334/ojb.46

Pasch, C. A. et al. 2019. Patient-Derived Cancer Organoid Cultures to Predict Sensitivity to Chemotherapy and Radiation. *Clin Cancer Res* 25(17), pp. 5376-5387. doi: 10.1158/1078-0432.CCR-18-3590

Peng, D. et al. 2021. Evaluating the transcriptional fidelity of cancer models. *Genome Med* 13(1), p. 73. doi: 10.1186/s13073-021-00888-w

Perez-Gonzalez, A., Bevant, K. and Blanpain, C. 2023. Cancer cell plasticity during tumor progression, metastasis and response to therapy. *Nat Cancer* 4(8), pp. 1063-1082. doi: 10.1038/s43018-023-00595-y

Perfetto, S. P., Chattopadhyay, P. K., Lamoreaux, L., Nguyen, R., Ambrozak, D., Koup, R. A. and Roederer, M. 2010. Amine-reactive dyes for dead cell discrimination in fixed samples. *Curr Protoc Cytom* Chapter 9, p. Unit 9 34. doi: 10.1002/0471142956.cy0934s53

Plasschaert, L. W. et al. 2018. A single-cell atlas of the airway epithelium reveals the CFTR-rich pulmonary ionocyte. *Nature* 560(7718), pp. 377-381. doi: 10.1038/s41586-018-0394-6

Powley, I. R. et al. 2020. Patient-derived explants (PDEs) as a powerful preclinical platform for anti-cancer drug and biomarker discovery. *Br J Cancer* 122(6), pp. 735-744. doi: 10.1038/s41416-019-0672-6

Puck, T. T. and Marcus, P. I. 1956. Action of x-rays on mammalian cells. *J Exp Med* 103(5), pp. 653-666.

Puschhof, J. et al. 2021. Intestinal organoid cocultures with microbes. *Nat Protoc* 16(10), pp. 4633-4649. doi: 10.1038/s41596-021-00589-z

Raavi, V., Perumal, V. and S, F. D. P. 2021. Potential application of gamma-H2AX as a biodosimetry tool for radiation triage. *Mutat Res Rev Mutat Res* 787, p. 108350. doi: 10.1016/j.mrrev.2020.108350

Rabata, A., Fedr, R., Soucek, K., Hampl, A. and Koledova, Z. 2020. 3D Cell Culture Models Demonstrate a Role for FGF and WNT Signaling in Regulation of Lung Epithelial Cell Fate and Morphogenesis. *Front Cell Dev Biol* 8, p. 574. doi: 10.3389/fcell.2020.00574

Ragupathi, A., Singh, M., Perez, A. M. and Zhang, D. 2023. Targeting the BRCA1/2 deficient cancer with PARP inhibitors: Clinical outcomes and mechanistic insights. *Front Cell Dev Biol* 11, p. 1133472. doi: 10.3389/fcell.2023.1133472

Rawlins, E. L. and Hogan, B. L. 2006. Epithelial stem cells of the lung: privileged few or opportunities for many? *Development* 133(13), pp. 2455-2465. doi: 10.1242/dev.02407

Rawlins, E. L., Ostrowski, L. E., Randell, S. H. and Hogan, B. L. 2007. Lung development and repair: contribution of the ciliated lineage. *Proc Natl Acad Sci U S A* 104(2), pp. 410-417. doi: 10.1073/pnas.0610770104

Reaper, P. M. et al. 2011. Selective killing of ATM- or p53-deficient cancer cells through inhibition of ATR. *Nat Chem Biol* 7(7), pp. 428-430. doi: 10.1038/nchembio.573

Rittmeyer, A. et al. 2017. Atezolizumab versus docetaxel in patients with previously treated non-small-cell lung cancer (OAK): a phase 3, open-label, multicentre randomised controlled trial. *Lancet* 389(10066), pp. 255-265. doi: 10.1016/S0140-6736(16)32517-X

Rock, J. R. et al. 2009. Basal cells as stem cells of the mouse trachea and human airway epithelium. *Proc Natl Acad Sci U S A* 106(31), pp. 12771-12775. doi: 10.1073/pnas.0906850106

Rogakou, E. P., Pilch, D. R., Orr, A. H., Ivanova, V. S. and Bonner, W. M. 1998. DNA double-stranded breaks induce histone H2AX phosphorylation on serine 139. *J Biol Chem* 273(10), pp. 5858-5868. doi: 10.1074/jbc.273.10.5858

Rothenberg, E., Grimme, J. M., Spies, M. and Ha, T. 2008. Human Rad52-mediated homology search and annealing occurs by continuous interactions between overlapping nucleoprotein complexes. *Proc Natl Acad Sci U S A* 105(51), pp. 20274-20279. doi: 10.1073/pnas.0810317106

Sachs, N. et al. 2018. A Living Biobank of Breast Cancer Organoids Captures Disease Heterogeneity. *Cell* 172(1-2), pp. 373-386 e310. doi: 10.1016/j.cell.2017.11.010

Sachs, N. et al. 2019. Long-term expanding human airway organoids for disease modeling. *EMBO J* 38(4), doi: 10.15252/embj.2018100300

Salwig, I. et al. 2019. Bronchioalveolar stem cells are a main source for regeneration of distal lung epithelia in vivo. *EMBO J* 38(12), doi: 10.15252/embj.2019102099

Sanchez, Y., Wong, C., Thoma, R. S., Richman, R., Wu, Z., Piwnica-Worms, H. and Elledge, S. J. 1997. Conservation of the Chk1 Checkpoint Pathway in Mammals: Linkage of DNA Damage to Cdk Regulation Through Cdc25. *Science* 277, pp. 1497-1501.

Santos-de-Frutos, K. and Djouder, N. 2021. When dormancy fuels tumour relapse. *Commun Biol* 4(1), p. 747. doi: 10.1038/s42003-021-02257-0

Satija, R., Farrell, J. A., Gennert, D., Schier, A. F. and Regev, A. 2015. Spatial reconstruction of single-cell gene expression data. *Nat Biotechnol* 33(5), pp. 495-502. doi: 10.1038/nbt.3192

Sato, T. et al. 2011. Long-term expansion of epithelial organoids from human colon, adenoma, adenocarcinoma, and Barrett's epithelium. *Gastroenterology* 141(5), pp. 1762-1772. doi: 10.1053/j.gastro.2011.07.050

Sato, T. et al. 2009. Single Lgr5 stem cells build crypt-villus structures in vitro without a mesenchymal niche. *Nature* 459(7244), pp. 262-265. doi: 10.1038/nature07935

Shaltiel, I. A., Krenning, L., Bruinsma, W. and Medema, R. H. 2015. The same, only different - DNA damage checkpoints and their reversal throughout the cell cycle. *J Cell Sci* 128(4), pp. 607-620. doi: 10.1242/jcs.163766

Shankar, A. et al. 2019. Environmental and occupational determinants of lung cancer. *Transl Lung Cancer Res* 8(Suppl 1), pp. S31-S49. doi: 10.21037/tlcr.2019.03.05

Sharick, J. T. et al. 2020. Metabolic Heterogeneity in Patient Tumor-Derived Organoids by Primary Site and Drug Treatment. *Front Oncol* 10, p. 553. doi: 10.3389/fonc.2020.00553

Shi, R. et al. 2020. Organoid Cultures as Preclinical Models of Non–Small Cell Lung Cancer. *Clinical Cancer Research* 26(5), pp. 1162-1174. doi: 10.1158/1078-0432.CCR-19-1376

Sikkema, L. et al. 2023. An integrated cell atlas of the lung in health and disease. *Nat Med* 29(6), pp. 1563-1577. doi: 10.1038/s41591-023-02327-2

Singh, A. K. et al. 2015. Tumor heterogeneity and cancer stem cell paradigm: updates in concept, controversies and clinical relevance. *Int J Cancer* 136(9), pp. 1991-2000. doi: 10.1002/ijc.28804

Sladek, T. L. 1997. E2F transcription factor action, regulation and possible role in human cancer. *Cell Proliferation* 30(3-4), pp. 97-105.

Sørensen, C. S. et al. 2003. Chk1 regulates the S phase checkpoint by coupling the physiological turnover and ionizing radiation-induced accelerated proteolysis of Cdc25A. *Cancer Cell* 3, pp. 247-258.

Spigel, D. R. et al. 2022. Five-Year Survival Outcomes From the PACIFIC Trial: Durvalumab After Chemoradiotherapy in Stage III Non-Small-Cell Lung Cancer. *J Clin Oncol* 40(12), pp. 1301-1311. doi: 10.1200/JCO.21.01308

Stackhouse, C. T., Gillespie, G. Y. and Willey, C. D. 2021. Cancer Explant Models. *Curr Top Microbiol Immunol* 430, pp. 131-160. doi: 10.1007/82_2019_157

Stadler, M. et al. 2015. Increased complexity in carcinomas: Analyzing and modeling the interaction of human cancer cells with their microenvironment. *Semin Cancer Biol* 35, pp. 107-124. doi: 10.1016/j.semcancer.2015.08.007

Stiff, T., O'Driscoll, M., Rief, N., Iwabuchi, K., Lo¨brich, M. and Jeggo, P. A. 2004. ATM and DNA-PK Function Redundantly to Phosphorylate H2AX after Exposure to Ionizing Radiation. *Cancer Research* 64, pp. 2390-2396.

Stuart, T. et al. 2019. Comprehensive Integration of Single-Cell Data. *Cell* 177(7), pp. 1888-1902 e1821. doi: 10.1016/j.cell.2019.05.031

Sung, H., Ferlay, J., Siegel, R. L., Laversanne, M., Soerjomataram, I., Jemal, A. and Bray, F. 2021. Global Cancer Statistics 2020: GLOBOCAN Estimates of Incidence and Mortality Worldwide for 36 Cancers in 185 Countries. *CA Cancer J Clin* 71(3), pp. 209-249. doi: 10.3322/caac.21660

Swanton, C. and Govindan, R. 2016. Clinical Implications of Genomic Discoveries in Lung Cancer. *N Engl J Med* 374(19), pp. 1864-1873. doi: 10.1056/NEJMra1504688

Swietach, P., Hulikova, A., Patiar, S., Vaughan-Jones, R. D. and Harris, A. L. 2012. Importance of intracellular pH in determining the uptake and efficacy of the weakly basic chemotherapeutic drug, doxorubicin. *PLoS One* 7(4), p. e35949. doi: 10.1371/journal.pone.0035949

Symington, L. S. 2016. Mechanism and regulation of DNA end resection in eukaryotes. *Crit Rev Biochem Mol Biol* 51(3), pp. 195-212. doi: 10.3109/10409238.2016.1172552

Takahashi, N. et al. 2019. An In Vitro System for Evaluating Molecular Targeted Drugs Using Lung Patient-Derived Tumor Organoids. *Cells* 8(5), doi: 10.3390/cells8050481

Teixeira, V. H. et al. 2013. Stochastic homeostasis in human airway epithelium is achieved by neutral competition of basal cell progenitors. *Elife* 2, p. e00966. doi: 10.7554/eLife.00966

Tojo, M. et al. 2005. The ALK-5 inhibitor A-83-01 inhibits Smad signaling and epithelial-to-mesenchymal transition by transforming growth factor-beta. *Cancer Sci* 96(11), pp. 791-800. doi: 10.1111/j.1349-7006.2005.00103.x

Travaglini, K. J. et al. 2020. A molecular cell atlas of the human lung from single-cell RNA sequencing. *Nature* 587(7835), pp. 619-625. doi: 10.1038/s41586-020-2922-4

Tuli, R. et al. 2014. Radiosensitization of Pancreatic Cancer Cells In Vitro and In Vivo through Poly (ADP-ribose) Polymerase Inhibition with ABT-888. *Transl Oncol* 7(3), pp. 439-445. doi: 10.1016/j.tranon.2014.04.003

Van den Berge, K. et al. 2020. Trajectory-based differential expression analysis for single-cell sequencing data. *Nat Commun* 11(1), p. 1201. doi: 10.1038/s41467-020-14766-3

van Tienderen, G. S., Groot Koerkamp, B., JNM, I. J., van der Laan, L. J. W. and Verstegen, M. M. A. 2019. Recreating Tumour Complexity in a Dish: Organoid Models to Study Liver Cancer Cells and their Extracellular Environment. *Cancers (Basel)* 11(11), doi: 10.3390/cancers11111706

Vaughan, A. E. et al. 2015. Lineage-negative progenitors mobilize to regenerate lung epithelium after major injury. *Nature* 517(7536), pp. 621-625. doi: 10.1038/nature14112

Vergen, J., Hecht, C., Zholudeva, L. V., Marquardt, M. M., Hallworth, R. and Nichols, M. G. 2012. Metabolic imaging using two-photon excited NADH intensity and fluorescence lifetime imaging. *Microsc Microanal* 18(4), pp. 761-770. doi: 10.1017/S1431927612000529

Vinod, S. K. and Hau, E. 2020. Radiotherapy treatment for lung cancer: Current status and future directions. *Respirology* 25 Suppl 2, pp. 61-71. doi: 10.1111/resp.13870

Vlachogiannis, G. et al. 2018. Patient-derived organoids model treatment response of metastatic gastrointestinal cancers. *Science* 359(6378), pp. 920-926. doi: 10.1126/science.aao2774

Vlashi, E. and Pajonk, F. 2015. Cancer stem cells, cancer cell plasticity and radiation therapy. *Semin Cancer Biol* 31, pp. 28-35. doi: 10.1016/j.semcancer.2014.07.001

Walls, G. M. et al. 2020. CONCORDE: A phase I platform study of novel agents in combination with conventional radiotherapy in non-small-cell lung cancer. *Clin Transl Radiat Oncol* 25, pp. 61-66. doi: 10.1016/j.ctro.2020.09.006

Wang, E., Xiang, K., Zhang, Y. and Wang, X.-F. 2022a. Patient-derived organoids (PDOs) and PDO-derived xenografts (PDOXs): New opportunities in establishing faithful pre-clinical cancer models. *Journal of the National Cancer Center* 2(4), pp. 263-276. doi: 10.1016/j.jncc.2022.10.001

Wang, R. et al. 2022b. Systematic evaluation of colorectal cancer organoid system by single-cell RNA-Seq analysis. *Genome Biol* 23(1), p. 106. doi: 10.1186/s13059-022-02673-3

Wang, X.-Y. et al. 2013. Musashi1 as a potential therapeutic target and diagnostic marker for lung cancer. *Oncotarget* 4, pp. 739-750.

Ward, I. M. and Chen, J. 2001. Histone H2AX is phosphorylated in an ATR-dependent manner in response to replicational stress. *J Biol Chem* 276(51), pp. 47759-47762. doi: 10.1074/jbc.C100569200

Ward, J. F. 1988. DNA damage produced by ionizing radiation in mammalian cells: identities, mechanisms of formation, and reparability. *Prog Nucleic Acid Res Mol Biol* 35, pp. 95-125. doi: 10.1016/s0079-6603(08)60611-x

Watanabe, N., Broome, M. and Hunter, T. 1995. Regulation of the human WEE1Hu CDK tyrosine 15-kinase during the cell cycle. *EMBO J* 14(9), pp. 1878-1891. doi: 10.1002/j.1460-2075.1995.tb07180.x

Weber, A. M., Drobnitzky, N., Devery, A. M., Bokobza, S. M., Adams, R. A., Maughan1, T. S. and Ryan, A. J. 2016. Phenotypic consequences of somatic mutations in the ataxiatelangiectasia mutated gene in non-small cell lung cancer. *Oncotarget* 7(38), pp. 60807-60822.

Weibel, E. R. 2015. On the tricks alveolar epithelial cells play to make a good lung. *Am J Respir Crit Care Med* 191(5), pp. 504-513. doi: 10.1164/rccm.201409-1663OE

Weigert, V., Jost, T., Hecht, M., Knippertz, I., Heinzerling, L., Fietkau, R. and Distel, L. V. 2020. PARP inhibitors combined with ionizing radiation induce different effects in melanoma cells and healthy fibroblasts. *BMC Cancer* 20(1), p. 775. doi: 10.1186/s12885-020-07190-9

Werner, R. S., Kirschner, M. B. and Opitz, I. 2021. Primary Lung Cancer Organoids for Personalized Medicine-Are They Ready for Clinical Use? *Cancers (Basel)* 13(19), doi: 10.3390/cancers13194832

Wold, M. S. and Kelly, T. 1988. Purification and characterization of replication protein A, a cellular protein required for in vitro replication of simian virus 40 DNA
. *Proceedings of the National Academy of Sciences* 85, pp. 2523-2527.

Wu, F. et al. 2021. Single-cell profiling of tumor heterogeneity and the microenvironment in advanced non-small cell lung cancer. *Nat Commun* 12(1), p. 2540. doi: 10.1038/s41467-021-22801-0

Xi, Y. et al. 2017. Local lung hypoxia determines epithelial fate decisions during alveolar regeneration. *Nat Cell Biol* 19(8), pp. 904-914. doi: 10.1038/ncb3580

Xiao, Z., Chen, Z., Gunasekera, A. H., Sowin, T. J., Rosenberg, S. H., Fesik, S. and Zhang, H. 2003. Chk1 mediates S and G2 arrests through Cdc25A degradation in response to DNA-damaging agents. *J Biol Chem* 278(24), pp. 21767-21773. doi: 10.1074/jbc.M300229200

Xu, L. et al. 2019. ATM deficiency promotes progression of CRPC by enhancing Warburg effect. *Endocr Relat Cancer* 26(1), pp. 59-71. doi: 10.1530/ERC-18-0196

Xue, W. et al. 2023. WNT ligands in non-small cell lung cancer: from pathogenesis to clinical practice. *Discov Oncol* 14(1), p. 136. doi: 10.1007/s12672-023-00739-7

Yao, Y. et al. 2020. Patient-Derived Organoids Predict Chemoradiation Responses of Locally Advanced Rectal Cancer. *Cell Stem Cell* 26(1), pp. 17-26 e16. doi: 10.1016/j.stem.2019.10.010

You, Z., Chahwan, C., Bailis, J., Hunter, T. and Russell, P. 2005. ATM activation and its recruitment to damaged DNA require binding to the C terminus of Nbs1. *Mol Cell Biol* 25(13), pp. 5363-5379. doi: 10.1128/MCB.25.13.5363-5379.2005

Yu, L., Hebert, M. C. and SZanhg, Y. E. 2002. TGF-B receptor-activated p38 MAP kinase mediates Smad-independent TGF-B responses. *The EMBO Journal* 21(14), pp. 3749-3759.

Yuan, J., Li, X. and Yu, S. 2022. Cancer organoid co-culture model system: Novel approach to guide precision medicine. *Front Immunol* 13, p. 1061388. doi: 10.3389/fimmu.2022.1061388

Zacharias, W. J. et al. 2018. Regeneration of the lung alveolus by an evolutionarily conserved epithelial progenitor. *Nature* 555(7695), pp. 251-255. doi: 10.1038/nature25786

Zhang, K., Wang, Y., Xue, J., Liang, N. and Wei, Z. 2023. Real-time monitoring ATP variation in human cancer organoids for a long term by DNA-based nanosensor. *Anal Chim Acta* 1275, p. 341608. doi: 10.1016/j.aca.2023.341608

Zhang, L. et al. 2022. Integrated single-cell RNA sequencing analysis reveals distinct cellular and transcriptional modules associated with survival in lung cancer. *Signal Transduct Target Ther* 7(1), p. 9. doi: 10.1038/s41392-021-00824-9

Zhao, L. et al. 2020. The Determinant of DNA Repair Pathway Choices in Ionising Radiation-Induced DNA Double-Strand Breaks. *Biomed Res Int* 2020, p. 4834965. doi: 10.1155/2020/4834965

Zhao, Z. et al. 2022. Organoids. *Nat Rev Methods Primers* 2, doi: 10.1038/s43586-022-00174-y